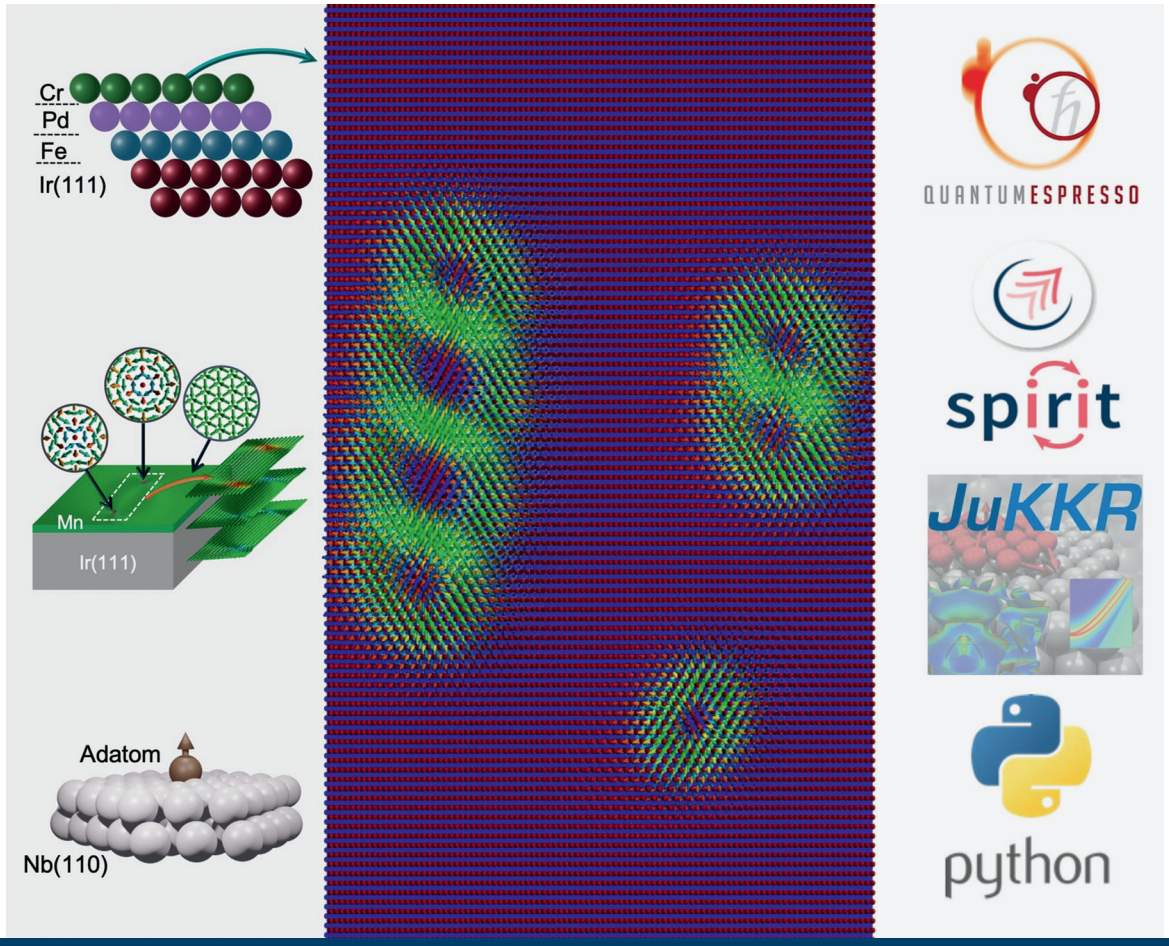

Ab initio investigation of intrinsic antiferromagnetic solitons

Amal Jawdat Nayef Aldarawsheh

Schlüsseltechnologien / Key Technologies
Band / Volume 286
ISBN 978-3-95806-785-1

Mitglied der Helmholtz-Gemeinschaft

JÜLICH
Forschungszentrum

Schriften des Forschungszentrums Jülich
Reihe Schlüsseltechnologien / Key Technologies Band / Volume 286

Forschungszentrum Jülich GmbH
Peter Grünberg Institut (PGI)
Quanten-Theorie der Materialien (PGI-1)

Ab initio investigation of intrinsic antiferromagnetic solitons

Amal Jawdat Nayef Aldarawsheh

Schriften des Forschungszentrums Jülich
Reihe Schlüsseltechnologien / Key Technologies Band / Volume 286

ISSN 1866-1807 ISBN 978-3-95806-785-1

Bibliografische Information der Deutschen Nationalbibliothek.
Die Deutsche Nationalbibliothek verzeichnet diese Publikation in der
Deutschen Nationalbibliografie; detaillierte Bibliografische Daten
sind im Internet über http://dnb.d-nb.de abrufbar.

Herausgeber und Vertrieb:	Forschungszentrum Jülich GmbH Zentralbibliothek, Verlag 52425 Jülich Tel.: +49 2461 61-5368 Fax: +49 2461 61-6103 zb-publikation@fz-juelich.de www.fz-juelich.de/zb
Umschlaggestaltung:	Grafische Medien, Forschungszentrum Jülich GmbH
Druck:	Grafische Medien, Forschungszentrum Jülich GmbH
Copyright:	Forschungszentrum Jülich 2024

Schriften des Forschungszentrums Jülich
Reihe Schlüsseltechnologien / Key Technologies, Band / Volume 286

D 464 (Diss. Duisburg-Essen, Univ., 2024)

ISSN 1866-1807
ISBN 978-3-95806-785-1

Vollständig frei verfügbar über das Publikationsportal des Forschungszentrums Jülich (JuSER)
unter www.fz-juelich.de/zb/openaccess.

Hiermit versichere ich, die vorliegende Dissertation selbstständig, ohne fremde Hilfe und ohne Benutzung anderer als den angegebenen Quellen angefertigt zu haben. Alle aus fremden Werken direkt oder indirekt übernommenen Stellen sind als solche gekennzeichnet. Die vorliegende Dissertation wurde in keinem anderen Promotionsverfahren eingereicht. Mit dieser Arbeit strebe ich die Erlangung des akademischen Grades Doktor der Naturwissenschaften (Dr. rer. nat.) an.

Ort, Datum

Author name (on the line the signature)

Acknowledgments

The journey of completing this thesis would not have been possible without the incredible support from many people. First and foremost, I wish to express my gratitude to my supervisor, Prof. Dr. Samir Lounis. His valuable guidance, relentless support, and encouragement have been the beacon that lit my path throughout this journey. He has not only honed my research skills but has also fostered a spirit of independence and teamwork in me.

I would like to extend my sincere thanks to Prof. Dr. Stefan Heinze for accepting to be the external examiner of my thesis, and I would like to thank the other members of the examination committee for agreeing to evaluate my PhD work.

I express my gratitude to Prof. Dr. Stefan Blügel for providing me with the chance to complete my thesis at his institute, "Quantum Theory of Materials," situated at PGI-1. His constant encouragement and assistance have been invaluable to my scientific ambitions.

Within the framework of my thesis funding scheme, Dr. Muayad Abusaa represents the Palestinian partner. I am incredibly appreciative of his assistance and knowledge throughout this trip. I would like to sincerely thank the German Federal Ministry of Education and Research (BMBF) and the Palestinian German Scientific Bridge (PGSB) for their financial support of this work. This research would not have been possible without their funding. Moreover, I thank the Deutsche Forschungsgemeinschaft (DFG) through SPP 2137 "Skyrmionics" for their funding. I want to thank everyone who has contributed to this project.

I would like to express my gratitude to Moritz Sallermann for his help and support during my PhD, as well as for his insightful conversations and valuable contributions that greatly enhanced my thesis. Also, I want to express my gratitude to Dr. Imara Lima Fernandes and Dr. Sascha Brinker for guiding me during the initial stages of my PhD.

My dear friend Mrs. Yasmin Ergüven has my sincere gratitude for all of our happy times together as well as for her outstanding administrative help, which made a lot of administrative obstacles easier to overcome. I express my gratitude to Mrs. Ute Winkler for her exceptional administrative assistance. My sincere gratitude also goes out to all of my colleagues at Funsilab, PGI-1, and University of Duisberg-Essen. I sincerely thank you for your contributions, as each little help has been crucial to the success of this journey.

My gratitude also goes out to Markus Hoffmann, Dr. Manuel Dos Santos, and Dr. Philipp Rüßmann, for their assistance during my PhD.

I am grateful to Hang'yu, my officemate, for her unwavering emotional support and for creating the most enjoyable work environment in the office. I would like to express my gratitude to my friends Fatima Battat and Alaa Isleem for their support and encouragement. Our happy times together will always be remembered.

I want to sincerely thank my parents for their prayers every morning, which gave me the strength to keep going and accomplish my goal. To all of my brothers and sisters, I am deeply grateful for your consistent support during my academic journey. Your support, affection, and faith in me have always been a source of motivation and inspiration. My family has stood by me through good times and bad, and I am incredibly thankful for them.

I could not have done any of this without my amazing husband, Ahmed. He has been my rock, cheering me on through thick and thin. Moving to a new country with our kids was tough, but we faced it together, turning challenges into successes. I can not thank him enough for his unlimited support. And to my kids, Oday and Sham, I am sorry for the times my work kept me away. Moving to Germany was a big change, but you guys have been incredible, rocking school and making me so darn proud. Love you all!

Amal
2024

Abstract

The field of spintronics is poised to transform technology with faster, more efficient, and energy-saving devices by exploring magnetic nanostructures for miniaturization. This thesis uses a multi-scale modeling approach, combining density functional theory and atomistic spin dynamics to study topological antiferromagnetic (AFM) spin-swirling textures in thin films. These textures are seen as ideal dynamic bits for information transmission and storage, offering advantages over ferromagnetic (FM) solitons. While progress has been made in synthetic AFM multilayers, the observation of intrinsic AFM solitons within film geometry remains elusive. The thesis predicts a realistic combination of ultrathin films capable of hosting a variety of intrinsic topological AFM solitons with unique properties, exploring their emergence mechanisms, stability, response to stimuli, and dynamics.

In our study, we choose transition metal layers that are expected to be AFM such as Cr and Mn, interfaced with Ir(111) surface, to investigate the formation of AFM solitons. We predict the emergence of intrinsic single and, surprisingly, interchained AFM skyrmions in the rowwise AFM (RW-AFM) ground state of a Cr layer on PdFe/Ir(111) surface. The stabilization mechanisms involve Heisenberg exchange interactions, Dzyaloshinskii-Moriya interactions, and magnetocrystalline anisotropy. The energy barriers and the overlap of AFM skyrmions are also explained. Then, we take a step further by developing a generic atomistic spin model with the minimum magnetic interactions required to stabilize those AFM skyrmions. This model enhances the understanding of the complex phase behavior of AFM skyrmions, showing their sensitivity to diverse magnetic interactions and external magnetic fields. When Cr is replaced with a Mn layer, a new type of AFM solitons, frustrated multi-meronic textures such as hexa-merons and tri-merons, are observed in different configurations of Mn based systems. We delve into the mechanisms underlying their emergence, investigate their properties and how different topological charges influence their response to external magnetic fields.

The study also explores the dynamics of AFM skyrmions under the influence of a spin-polarized current-perpendicular-to-plane. Anisotropic skyrmion Hall effect is observed, resulting from the elliptical shape of these AFM skyrmions. Additionally, the interaction between FM and AFM skyrmions influences the trajectories of AFM skyrmions, creating a complex hybrid interaction profile.

Finally, we propose a bottom-up approach for the construction of topological magnetic textures in diluted structures made of Cr, Mn or Fe adatoms on Nb(110) surface and demonstrate the manifestation of a rich set of topological spin-textures of FM and AFM nature.

Zusammenfassung

Die Spintronik ist ein vielversprechendes Gebiet, dass eine technologische Revolution durch die Erforschung magnetischer Nanostrukturen für die Miniaturisierung von Geräten hervorbringen könnte. In dieser Dissertation wird ein Multiskalen-Modellierungsansatz verwendet, der die Dichtefunktionaltheorie und atomistische Spindynamik kombiniert, um topologische antiferromagnetische (AFM) Spin-Wirbel-Texturen in dünnen Filmen zu untersuchen. Diese AFM-Texturen gelten als ideale dynamische Bits für Informationsübertragung und -speicherung und bieten Vorteile gegenüber ferromagnetischen (FM) Solitonen. Obwohl Fortschritte bei der Erforschung von synthetischen AFM-Multischichten gemacht wurden, ist die Beobachtung intrinsischer AFM-Solitonen innerhalb der Filmgeometrie nach wie vor schwierig. In dieser Arbeit zeigen wir jedoch, dass ultradünne Filme aus bestimmten Übergangsmetallen eine Vielzahl intrinsischer topologischer AFM-Solitonen mit einzigartigen Eigenschaften beherbergen können.

In dieser Dissertation untersuchen wir die Bildungsmechanismen, Stabilität, Reaktion auf Stimuli und Dynamik dieser AFM-Solitonen. Wir verwenden Übergangsmetallschichten wie Cr und Mn, die mit der Ir(111)-Oberfläche verbunden sind, um die Bildung von AFM-Solitonen zu untersuchen. Wir sagen das Auftreten von einzelnen und verketteten AFM-Skyrmonen in einer Cr-Schicht auf der PdFe/Ir(111)-Oberfläche voraus. Wir erklären auch die Stabilisierungsmechanismen und die Energiebarrieren dieser AFM-Skyrmionen. Darüber hinaus entwickeln wir ein generisches atomistisches Spinmodell, welches das Verständnis vom komplexen Phasenverhalten von AFM-Skyrmionen verbessert und ihre Empfindlichkeit gegenüber verschiedenen magnetischen Wechselwirkungen und externen Magnetfeldern aufweist. Wenn Cr durch eine Mn-Schicht ersetzt wird, entsteht eine neue Art von AFM-Solitonen: frustrierte multi-meronische Texturen wie Hexa-Meronen und Tri-Meronen. Diese Dissertation untersucht auch die Dynamik von AFM-Skyrmionen unter dem Einfluss eines spinpolarisierten Stroms. Es wird ein anisotroper Skyrmion-Hall-Effekt beobachtet, der sich aus der elliptischen Form dieser AFM-Skyrmionen ergibt. Darüber hinaus beeinflusst die Wechselwirkung zwischen FM- und AFM-Skyrmionen die Trajektorie der AFM-Skyrmionen, was zu einem komplexen hybriden Wechselwirkungsprofil führt.

Im letzten Teil dieser Dissertation wird ein Bottom-up-Ansatz für die Konstruktion topologischer magnetischer Texturen in verdünnten Strukturen auf der Nb(110)-Oberfläche vorgeschlagen und gezeigt, dass eine Vielzahl von topologischen Spin-Texturen mit FM- und AFM-Charakter erzeugt werden kann. Dies könnte neue Möglichkeiten für die Konstruktion von magnetischen Speicher- und Informationsübertragungsgeräten eröffnen.

List of publications

Publications in chronological order

1. *Emergence of zero-field non-synthetic single and interchained antiferromagnetic skyrmions in thin films*,
   Amal Aldarawsheh, Imara Lima Fernandes, Sascha Brinker, Moritz Sallermann, Muayad Abusaa, Stefan Blügel, and Samir Lounis, Nature Communications **13**, 7369 (2022)

2. *A spin model for intrinsic antiferromagnetic skyrmions on a triangular lattice*,
   Amal Aldarawsheh, Moritz Sallermann, Muayad Abusaa, and Samir Lounis, Frontiers in Physics **11**, 1175317 (2023)

3. *Two-dimensional Shiba lattices as a possible platform for crystalline topological superconductivity*,
   Martina O. Soldini, Felix Küster, Glenn Wagner, Souvik Das, **Amal Aldarawsheh**, Ronny Thomale, Samir Lounis, Stuart S. P. Parkin, Paolo Sessi, and Titus Neupert, Nature Physics **19**, 1848 (2023)

4. *Intrinsic Néel antiferromagnetic multimeronic spin-textures in ultrathin films*,
   Amal Aldarawsheh, Moritz Sallermann, Muayad Abusaa, and Samir Lounis, The Journal of Physical Chemistry Letters **14**, 8970 (2023)

5. *Current-driven dynamics of antiferromagnetic skyrmions: from skyrmion Hall effects to hybrid inter-skyrmion scattering*,
   Amal Aldarawsheh, Moritz Sallermann, Muayad Abusaa, and Samir Lounis, arXiv preprint arXiv:2403.01987 (2024)

6. *Manifestation of topological spin-textures in adatom-based diluted nanostructures*,
   Amal Aldarawsheh, Moritz Sallermann, Muayad Abusaa, and Samir Lounis, In preparation (2024)

Conference Contributions

1. Current-driven dynamics of antiferromagnetic skyrmions: from skyrmion Hall effects to hybrid inter-skyrmion scattering, **Amal Aldarawsheh**, Moritz Sallermann, Muayad Abusaa, and Samir Lounis, Talk, German Physical Society meeting (DPG2024), Berlin, Germany, March, 2024.

2. Intrinsic antiferromagnetic multi-meronic Néel spin-textures in thin films, **Amal Aldarawsheh**, Moritz Sallermann, Muayad Abusaa, and Samir Lounis, Talk, Skyrmionic retreat meeting, Hamburg, Germany, September, 2023.

3. Intrinsic antiferromagnetic multi-meronic Néel spin-textures in thin films, **Amal Aldarawsheh**, Moritz Sallermann, Muayad Abusaa, and Samir Lounis, Poster, Joint European Magnetic Symposia 2023 (JEMS2023), Hybrid, Madrid, Spain, August, 2023.

4. Emergence of zero-field non-synthetic single and interchained antiferromagnetic skyrmions in thin films, **Amal Aldarawsheh**, Imara Lima Fernandes, Sascha Brinker, Moritz Sallermann, Muayad Abusaa, Stefan Blügel, and Samir Lounis, Poster, 3rd CENIDE conference, Bergisch Gladbach, Germany, May, 2023. **Best poster prize**.

5. Non-synthetic antiferromagnetic multi-meronic Néel spin-textures in thin films, **Amal Aldarawsheh**, Moritz Sallermann, Muayad Abusaa, and Samir Lounis, Talk, German Physical Society meeting (DPG2023), Dresden, Germany, March, 2023.

6. Emergence of zero-field non-synthetic single and interchained antiferromagnetic skyrmions in thin films, **Amal Aldarawsheh**, Imara Lima Fernandes, Sascha Brinker, Moritz Sallermann, Muayad Abusaa, Stefan Blügel, and Samir Lounis, Talk, German Physical Society meeting (DPG2022), Regensburg, Germany, September, 2022.

7. Emergence of zero-field non-synthetic single and interchained antiferromagnetic skyrmions in thin films, **Amal Aldarawsheh**, Imara Lima Fernandes, Sascha Brinker, Moritz Sallermann, Muayad Abusaa, Stefan Blügel, and Samir Lounis, Talk, Psi-K conference, Switzerland, August, 2022.

8. Emergence of zero-field non-synthetic single and catenated antiferromagnetic skyrmions in thin films, **Amal Aldarawsheh**, Imara Lima Fernandes, Sascha Brinker, Moritz Sallermann, Muayad Abusaa, Stefan Blügel, and Samir Lounis, Talk, Joint European Magnetic Symposia 2022 (JEMS2022), Hybrid, Warsow, Poland, July, 2022.

9. Emergence of zero-field non-synthetic single and catenated antiferromagnetic skyrmions in thin films, **Amal Aldarawsheh**, Imara Lima Fernandes, Sascha Brinker, Moritz Sallermann, Muayad Abusaa, Stefan Blügel, and Samir Lounis, Talk, International Colloquium on Magnetic Films and Surfaces (ICMFS2022), Okinawa, Japan, July, 2022.

10. Ab-initio investigation of antiferomagnetic skyrmions, **Amal Aldarawsheh**, Imara Lima Fernandes, Sascha Brinker, Moritz Sallermann, Muayad Abusaa, Stefan Blügel, and Samir Lounis, Talk, Palestinian German science bridge workshop, Virtual, February, 2022.

11. Four-sublattice antiferromagnetic skyrmions on a triangular lattice, **Amal Aldarawsheh**, Imara Lima Fernandes, Sascha Brinker, Moritz Sallermann, Muayad Abusaa, and Samir Lounis, Poster, Retreat-Meeting SPP2137, Bad-Honnef (Virtual), Germany, October, 2021.

12. Ab-initio investigation of intrinsic antiferromagnetic skyrmions in magnetic thin films, **Amal Aldarawsheh**, Imara Lima Fernandes, Sascha Brinker, Moritz Sallermann, Muayad Abusaa, and Samir Lounis, Poster, German Physical Society meeting (DPG2021), Virtual, Germany, September, 2021.

List of Symbols

Abbreviations

Abbreviation	Denomination
AFM	Antiferromagnetic
FM	Ferromagnetic
DFT	Density functional theory
ASD	Atomsitic spin dynamics
SkHE	Skyrmion Hall effect
KKR	Korringa-Kohn-Rostoker
LLG	Landau-Lifshitz-Gilbert
MAE	Magnetocrystalline anisotropy energy
SOC	Spin-orbit coupling
STT	Spin transfer torque
MTJ	Magnetic tunnel junction
GNEB	Geodesic nudged elastic band method
GGA	Generalized gradient approximation
LDA	Local (spin) density approximation
DMI	Dzyaloshinskii-Moriya interaction
MC	Monte Carlo

Contents

1. Introduction

In the ever-evolving landscape of our digital age, information technology holds a dominant position. Its essence lies in the skillful manipulation, storage, and interpretation of extensive data reserves. We live in an era where we generate an astounding amount of data daily, emphasizing the vital need to find new ways of storing and manipulating this torrent of information effectively. In the realm of technological advancement, particularly over the last few decades, commercially-used devices have undergone significant transformations. This evolution has been driven by the persistent pursuit of making electronic circuit elements smaller, with the transistor leading the way. However, there is a fundamental limit to how small these components can become because they depend on the charge of electrons [1, 2]. This constant miniaturization now approaches a critical point. Evidence of this slowdown is apparent in Moore's Law [3], which raises concerns about the future of charge-based electronic progress. An ever-growing worry accompanies this trend: as transistors become faster and smaller, they produce more heat due to increased energy dissipation through Joule heating [4]. Over the last few decades, the scientific community has been exploring not only the charge but also the spin of electrons in electronic devices, giving rise to the field of spintronics. In spintronics, information is transported via the spin of electrons, rather than the electrons themselves, thus mitigating the generation of Joule heat. This principle has led to the development of various applications, including logic devices in the data storage field. The monumental breakthrough in spintronics came with the revelation of the giant magnetoresistance (GMR), independently discovered by Grünberg et al. [5] and Fert et al. [6]. This important discovery marked the beginning of spintronics and won Grünberg and Fert the Nobel Prize in 2007. GMR's core principle hinges on the strong dependence of the resistance on the relative magnetic orientation of two ferromagnetic (FM) layers, separated by a non-magnetic spacer. In modern magnetic hard disk drives (HDDs), this ingenious concept finds practical application. Here, a single bit of information is encoded in the alignment of FM domains, which can be read via the remarkable GMR effect and its close relative, tunnel magnetoresistance (TMR) [7, 8, 9], where the spacer is insulating instead of being metallic.

The traditional method of storing data in HDDs relies on the concept of magnetic domains, where regions of opposite magnetization, known as FM domains, define magnetic bits. This conventional approach necessitates a considerable number of atoms to create a single domain. This requirement not only limits storage capacity but also results in significant energy consumption, primarily due to the intricate movement of the hard disks magnetic tip. Recent interest has been directed toward alternative forms of magnetic order that offer advantages

over ferromagnets. Antiferromagnetic (AFM) materials, where the magnetic moments of adjacent atoms are antiparallel rather than parallel, exhibit much faster spin dynamics and are resilient to potentially destabilizing external magnetic fields, absence of stray fields and general abundance in nature [10, 11, 12]. Experimental evidence has demonstrated that lower electric currents are required to manipulate the magnetic state in such materials [11].

Moreover, in the pursuit of miniaturizing magnetic bits, a new frontier emerges – the realm of complex magnetic textures. These intricate magnetic structures hold great potential for future spintronic devices as they enable the control of increasingly smaller magnetic domains. Among these complex textures are localized twists in the orientation of magnetic moments within FM materials, distinguished by non-trivial winding numbers. Notable examples include skyrmions [13, 14], biskyrmions [15, 16, 17], hopfions [18, 19, 20], chiral bobbers [21, 22], skyrmionic cocoons [23], and even merons [24, 25]. What sets them apart is their inherent mobility, their stability and compact size, sometimes down to a few nanometers or atomic distances [26, 27], which allow them to serve as carriers for magnetic bits. [28, 29]. Indeed, these noncollinear structures, characterized by their intriguing topology, exhibit remarkable transport properties and can be propelled by electric currents [30, 31, 32, 33, 34], akin to domain walls. These concepts have given rise to innovative racetrack-like devices [28, 35, 36], expanding upon the original idea based on FM domain walls [37].

Skyrmions, named after British physicist Tony Skyrme [38], were initially conceived as topologically protected particles to explain phenomena in nuclear physics. Surprisingly, these exotic entities found their place not only in the microscopic world of hadrons but also in the realm of magnetic materials [39, 13, 14, 40, 41]. Their origins are attributed to several microscopic mechanisms. These mechanisms include the competition between FM Heisenberg exchange interaction and the antisymmetric exchange interaction, commonly known as the Dzyaloshinskii—Moriya interaction (DMI) [42, 43], which emerges in inversion-symmetry-broken systems with large spin-orbit coupling (SOC) either at interfaces of thin-film layers [40, 44, 27] or in bulk materials with chiral or polar structures [13, 14, 45, 46]. Magnetic frustration [47, 48, 49], and magnetic dipolar interactions [50] also contribute to their formation. One defining characteristic of skyrmions is their topological charge (N), often referred to as the "winding number" [51, 41]. In contrast to topologically trivial magnetic textures like ferromagnets or spin spirals where their topological charge is zero, skyrmions possess a finite integer charge N, endowing them with topological non-triviality and protection [52]. The latter leads to a topological barrier that prevents continuous deformation into magnetic textures of a different topological nature. Skyrmions exhibit a solitonic nature, combining finite extension with particle-like motion and interaction, rendering them appealing for future spintronics devices [41, 53, 54]. Moreover, skyrmions offer energy-efficient mobility and excitations, requiring orders of magnitude lower current densities compared to moving magnetic domain walls [30, 55]. Their non-collinear spin texture gives rise to emergent electromagnetic fields [56], leading to phenomena like the topological Hall effect (THE), which provides an

electric signature of magnetic skyrmions [57, 58]. These intriguing properties make skyrmions a captivating subject of research with significant potential in various technological applications. Skyrmions, with their unique properties, have ignited a blaze of scientific curiosity. These structures, first envisioned in the work of Bogdanov and Yablonskii [59, 39], have since become the subject of extensive research [13, 60, 14, 40, 55, 28, 61, 62, 63, 54, 64, 65].

However, as the landscape of future nanotechnologies comes into focus, it becomes apparent that the requirements are stringent. The generation of information bits, though a crucial step, is just one facet. Efficiency in reading, control, and power consumption stands as equally vital considerations [54, 66]. The miniaturization of FM skyrmions, for instance, faces hurdles due to the presence of dipolar interactions [67, 68]. The stabilization of these structures often necessitates the application of external magnetic fields [62], rendering them less desirable for certain applications. The unwanted skyrmion Hall effect (SkHE), a consequence of the Magnus force deflecting FM skyrmions when driven with a current, complicates the precise control of their motion where FM skyrmions exhibit a complex dynamical behavior in response to applied currents, further accentuating the challenges [41, 69, 32, 70, 33]. The presence of defects introduces an additional layer of complexity, hindering the practical implementation of FM skyrmions in real-world devices [71, 72]. It is against this backdrop of challenges and limitations that we turn our attention to an alternative: AFM skyrmions.

AFM skyrmions are expected to resolve several of the previous issues and offer various advantages. Indeed, AFM materials being at the heart of the rapidly evolving field of AFM spintronics [11] are much more ubiquitous than ferromagnets. The compensated spin structure of AFM skyrmions inherently forbids dipolar interactions, which should allow the stabilization of rather small skyrmions while enhancing their robustness against magnetic perturbations. Moreover, the predicted disappearance of the Magnus force, which triggers the SHE, would then enable a better control of the skyrmions motion [73, 74], which has been partially illustrated experimentally in a ferrimagnet [64, 75]. AFM skyrmions were predicted early on using continuum models [76], followed with multiple phenomenology-based studies on a plethora of properties and applications, see e.g. Refs. [77, 78, 73, 79, 80, 81, 82, 83, 84, 85, 86, 87, 88].

The landscape of topological magnetism took a significant step forward with the experimental stabilization of synthetic AFM skyrmions [89, 68] just before I started my PhD in 2020. Synthetic AFM skyrmions are composed of two FM skyrmions realized in distinct magnetic layers and antiferromagnetically coupled through a non-magnetic spacer layer [89, 68, 90, 91, 92]. In contrast to the synthetic ones, an intrinsic AFM skyrmion is a unique magnetic entity since it is entirely located in a single layer. However, the observation of intrinsic AFM skyrmions has so far been elusive, in particular at surfaces and interfaces, where they are highly desirable for racetrack concepts. Whereas, intrinsic complexes involving AFM meronic spin-textures (complexes made of half-skyrmions) were recently detected in bulk phases [93, 94, 95].

In the realm of two-dimensional FM systems, merons exhibit a unique behavior, primarily

existing in pairs or groups [96, 97, 98, 99], hence, offering more topological states than conventional skyrmions, which makes them an important focus in fundamental quasi-particle research as well as topology-based computing approaches, distinguishing them from their skyrmionic counterparts. These merons, in essence, enrich our understanding of topological spin textures, offering a different perspective on their formation and behavior. Regular FM merons are in-plane magnetized textures with magnetization that curls around a stable core pointing out-of-plane (OOP), and are topologically equivalent to one half of a skyrmion [96, 97, 100, 98, 101, 25, 102, 103, 104, 105]. The topological charge of a single FM meron equals $\pm\frac{1}{2}$.

Despite the extensive research on topological AFM solitons, a pristine ultrathin film material that hosts AFM skyrmions remains challenging to find. It is the aim of this PhD thesis to investigate the emergence of intrinsic AFM spin textures in ultrathin magnetic films utilizing the density functional theory (DFT) principles in combination with atomistic spin dynamics (ASD) simulations. We carried out a systematic procedure to investigate the formation of such AFM solitons in magnetic layered systems grown on Ir(111) surface with face-centered cubic (fcc) stacking, which is known to facilitates the formation of FM skyrmions, such as when PdFe bilayer is deposited over (see Fig. **1-1**).

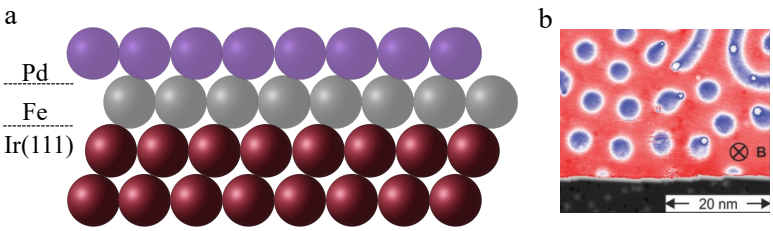

Figure **1-1**.: **PdFe/Ir(111) system.** Schematic representation of PdFe/Ir(111) magnetic layered system **a**, where nm-sized FM skyrmions have been experimentally observed to emerge in the Fe layer as depicted in **b**. Panel **b** has been adapted from Ref. [106], with permission from the American Physical Society.

Our strategy involves interfacing the Ir(111) surface with thin magnetic layers composed of 3d elements (V, Cr, and Mn), which are expected to be of AFM nature. We explored various combinations of these layers (as depicted in Fig. **1-2**). The AFM layers could be directly interfaced with the Ir substrate, covered with a Pd overlayer, or separated with a PdFe bilayer and Pd_2Fe trilayer. Among the 3d elements, Cr and Mn emerged as promising candidates to host topological AFM spin-textures, which is the key focus of this thesis. The V ultrathin film turned to host magnetic interactions favoring ferromagnetism, and therefore it is disregarded in our reported investigations.

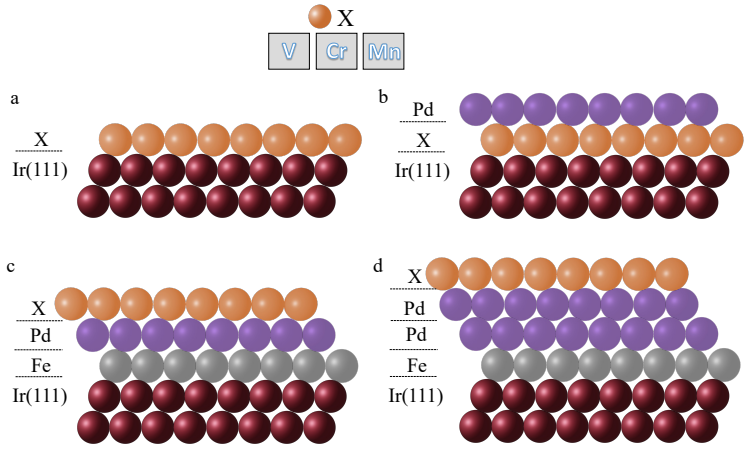

Figure **1-2**.: **Configurations of the different inspected magnetic layered thin films potentially hosting AFM spin-textures. a-d** Representation of **X**/Ir(111), Pd**X**/Ir(111), **X**PdFe/Ir(111), and **X**Pd_2Fe/Ir(111), respectively. Where X is either V, Cr or Mn layer.

The thesis is structured in the following manner. In chapter 2 we introduce the topological solitons discussed in this PhD thesis (skyrmion and merons). First, we discuss some fundamental concepts in magnetism. Then we delve into aspects pertaining to non-collinear magnetism, where we introduce in more detail skyrmions and merons.

Chapter 3 serves as the theoretical foundation for this thesis, introducing essential concepts and methods employed in our investigations. This chapter is twofold, the first section sheds light into the main *ab initio* principles utilized in the thesis, which are implemented in the widely used pseudo-potential DFT code, Quantum Espresso, and the all-electron full-potential Korringa-Kohn-Rostoker green function method based code (KKR), which has been developed in our institute (PGI-1) in Jülich research center. Subsequently, we elucidate the multi-scale modelling approach, which hinges on the mapping of the magnetic interactions pertaining to an extended Heisenberg Hamiltonian from our *ab initio* simulations. This is realized via the connection between the system's Green function, exchange splitting and spin-orbit coupling, to the parameters governing the Heisenberg exchange interaction and the DMI through the application of the infinitesimal rotations method [107, 108]. In the second section, we introduce the ASD principles, implemented in the Spirit code, which are utilized to handle the extended Heisenberg Hamiltonian and its minimization via the Landau-Lifshitz-Gilbert (LLG) equation. Additionally, we present the scheme simulating the spin transfer torque (STT) method that we used to investigate the spin-polarized in-

duced dynamics of AFM skyrmions.

In chapter 4, we predict the emergence of single and interchained intrinsic AFM skyrmions in a Cr layer deposited over PdFe/Ir(111). The lattice of triangular nature is characterized by a row-wise AFM (RW-AFM) ground state, which is dictated by the underlying competing magnetic interactions. The building-blocks of the unveiled AFM skyrmions emerge within four sublattices associated to the two-dimensional hexagonal lattice. We analyse the mechanisms giving rise to the skyrmions and their overlapping. Additionally, we investigate the impact of external magnetic fields and explore their thermal stability. Phase diagrams are presented, illustrating the range and influence of Heisenberg exchange interaction strengths, DMI, and magnetocrystalline anisotropy energy.

Moving to chapter 5, motivated by our findings in chapter 4 we develop a generic Heisenberg spin model that encapsulates the minimum magnetic interactions required for the formation of single and interchained AFM skyrmions on a triangular lattice. This model serves as a valuable tool to design materials capable of hosting these AFM solitons. The model enables the exploration of phase diagrams of a larger parameters range than done in chapter 4.

Chapter 6 is devoted to the investigation of a Mn layer interfaced with Ir(111). In contrast to the Cr case, here different interface combinations involving the presence of Pd, PdFe or Pd_2Fe films, show the emergence of topological AFM states. The ground state is found to be a Néel state with an in-plane orientation of the magnetic moments due to magnetic frustration and the presence of a finite perpendicular component of the DMI vector, which enforces the moments to rotate in the surface plane. This Néel state hosts a unique type of frustrated AFM multi-meronic spin textures, which spread into three FM sublattices, each hosting FM meron pairs, giving rise to rich combinations of topological charges, which differentiates them from the AFM skyrmions discussed in chapter 4. We discuss the stabilizing mechanisms of the frustrated multi-merons and their response to an external magnetic field before providing a simple model with the minimum set of magnetic interactions.

In chapter 7, we delve into the intricate dynamics of single and interchained AFM skyrmions reported in chapter 4. In contrast to the usual expectations, our AFM skyrmions are found to show a finite SkHE, which we trace back to their elliptical shape. By injecting perpendicular-to-plane spin currents, we demonstrate the controllability of both SkHE magnitude and skyrmion velocity based on the polarization direction of the applied current. Notably, we identify specific orientations where AFM skyrmions remain unaffected by the Magnus force. Additionally, we discuss the hybrid AFM-FM skyrmion interactions, which is of an attractive nature, due to the presence of FM skyrmions at the Fe-interface. This gives rise to the scattering of the AFM skyrmions in the Cr layer. The Fe skyrmions trigger effective traps that enrich the energy profile felt by the AFM skyrmions.

In chapter 8, we propose a bottom-up approach for the construction of topological magnetic

textures in diluted structures made of Cr, Mn or Fe adatoms on Nb(110) surface and demonstrate the emergence of topological spin-textures of FM and AFM nature.

Finally, the last chapter draws conclusions and summarizes the results presented in the thesis.

2. Topological spin textures: Skyrmions and merons

2.1. Origin of magnetism

The study of magnetism has deep historical roots, with magnetic phenomena known since ancient times. Magnetic materials have played an essential role in technological advancements, revolutionizing fields from navigation with the magnetic compass to data storage such as hard disk drives. Despite these early practical applications, the fundamental understanding of the origin of magnetism came much later, in the 19th century. To comprehend the origin of magnetism, it is essential to explore the microscopic world of atoms and their magnetic properties.

Magnetism emerges from the quantum properties of electrons that carry a spin and an orbital angular momentum, which give rise to, respectively, a spin and orbital magnetic moments

$$\mathbf{m} = \mathrm{m}^{\mathrm{S}} + \mathrm{m}^{\mathcal{L}} = -\frac{1}{\hbar}\mu_{\mathrm{B}}\left(\mathcal{L} + g_{\mathrm{e}}\mathbf{S}\right), \tag{2-1}$$

where μ_{B} is Bohr magneton, given by $\frac{e\hbar}{2m_e}$ in SI units with m_e, $\hbar$ represent the electron mass and reduced Planck constant separately, while g_{e} is the Landé g-factor. The magnetic moments follow Hund's rules at the atomic level. First, electrons must occupy the orbitals that maximize the spin angular momentum S. Consequently, each orbital in a subshell is initially occupied by a single electron with parallel spins before any orbital is doubly occupied. This principle minimizes Coulomb repulsion among electrons within the same subshell. For a given value of S, the orbital angular momentum $\mathcal{L}$ is maximized. The total angular momentum J is determined by the relationship $J = |\mathcal{L} - \mathrm{S}|$ if the subshell is less than half-full, or $J = \mathcal{L} + \mathrm{S}$ if it is more than half-full. When the subshell is half-full, $\mathcal{L}$ equals zero, leading to $J = \mathrm{S}$. Thus atoms with half-filled d-shells as those explored in this thesis are expected to carry weak orbital magnetic moments.

Once atoms are brought together to form a solid, the tendency to form a magnetic material is less common than for isolated atoms. Hybridization phenomena of the electronic states enable the delocalization of electrons, which reduces the ability of a material to become magnetic. In a metal, for example, the Stoner criterion [109] relates the emergence of magnetism to the condition $I\rho(\varepsilon_F) > 1$, meaning that the product of density of states at the Fermi energy $\rho(\varepsilon_F)$ of the non-magnetic phase with the intra-atomic exchange interaction I,

which is tightly connected to electronic correlations, must be larger than one. If the criterion is fulfilled, a magnetic instability occurs, driving the system to magnetic ordering, which induces an exchange splitting in the electronic states between the majority and minority spin-channels given by $\Delta = I\mathrm{m}^{\mathrm{S}}$. Moreover, in a solid made of transition elements for example, orbital magnetic moments tend to be quenched and are much weaker than the spin moments.

While the focus of the thesis is based on an atomistic description of magnetism, it is important to highlight that another common concept utilized in micromagnetism is that of the magnetization, which is defined as the volumetric density of magnetic moments and it can be written as:

$$\mathbf{M}(\mathbf{r}) = \frac{\mathrm{d}\mathbf{m}}{\mathrm{d}V}, \tag{2-2}$$

and used at much larger length scales than that of atoms.

Magnetic materials exhibit different types of magnetic arrangements. The most fundamental one is the ferromagnetic (FM) state where all magnetic moments are parallel to each other and point along the same direction. In the antiferromagnetic (AFM) case, adjacent moments ($\mathbf{m}_1$ and $\mathbf{m}_2$) with equal magnitudes are antiparallel. That is the atoms are spread int two sublattices (L_1, and L_2). Transition elements with half-filled d-shells tend to be AFM [110, 111] and are therefore at the heart of the investigations carried in the thesis.

Some materials have even more intricate structures, like canted magnetic moments creating a noncollinear configuration as seen in spin spirals and skyrmion lattices, which will be further discussed in this chapter. In spin spirals, the magnetic moments rotate around a fixed axis along a given direction. A skyrmion lattice [39, 13], on the other hand, emerges by combining multiple spin spirals, each having a distinct rotational axis. Additionally, isolated skyrmions can manifest as localized disruptions in a uniform magnetic field. Non-collinear magnetic structures can be found in various systems characterized by competing magnetic interactions. Chiral magnets are of particular interest among these non-collinear structures, marked by the presence of the antisymmetric exchange interaction known as Dzyaloshinskii-Moriya interaction (DMI) [42, 43], which is finite whenever spin-orbit coupling (SOC) is present and inversion symmetry is broken as it happens at various interfaces involving heavy elements and magnetic films. These materials exhibit a unique feature—fixed sense rotation of magnetization tied to the crystal lattice's chirality, resulting from the competition between the Heisenberg exchange interaction (J_{ij}) favoring parallel spin alignment and the DMI. Under specific conditions, chiral spin spirals can undergo a transition to form non-trivial topological entities denoted as magnetic skyrmions. In our study, we are discussing the emergence of non-collinear magnetic solitons namely skyrmions and merons in AFM materials.

2.2. Skyrmions

The concept of "skyrmion" finds its origin in baryonic field theories, initially representing solitonic solutions proposed by Tony Skyrme within his model describing low-energy interactions between mesons and baryons [38]. In the realm of condensed matter physics, the term "magnetic skyrmion" was later introduced by Bogdanov and his colleagues [39]. These magnetic skyrmions are two-dimensional, non-collinear magnetic spin structures localized in space, often enabled by the DMI [42, 43]. DMI is present in systems with large SOC and broken inversion symmetry, favors non-collinear spin configurations. Notably, DMI can also be induced in centrosymmetric crystals if their symmetry is disrupted by external factors, such as interfaces in thin magnetic films [112]. Based on the nature of the DMI present in the material, several types of skyrmions are stabilized, including Néel [40], Bloch [13], and antiskyrmions [113] as shown in Fig. **2-1**. These different skyrmion types offer versatile platforms for studying various aspects of condensed matter physics and magnetism, making skyrmions intriguing objects of study. The experimental observation of skyrmions occurred 15 years ago, initially in bulk chiral magnets, followed quickly with their discovery in magnetic thin films [40]. Magnetic skyrmions exhibit unique behaviors. They can be manipulated by spin torques driven by spin-polarized currents [28, 31, 36, 35], making them promising candidates for applications in spintronics, data storage, and logic devices. Their stability and robustness, stemming from topological properties, make them compelling choices for future technological advancements in spintronics. The concept of topology plays a central role in understanding the stability of skyrmions by providing effectively an energy barrier that protects them from a continuous deformation into a topologically trivial state, e.g. the FM state, similar to a knot in a rope that cannot be untied without cutting. Topology is quantified by the winding number or topological charge [51] discussed in the next subsection.

2.2.1. Topological definition of skyrmions

In the micromagnetic limit, the topological charge (N) is defined by the mixed product involving the magnetization [51], which quantifies a solid angle summed up over the whole two-dimensional spin-texture:

$$\mathrm{N} = \frac{1}{4\pi} \int \boldsymbol{n} \cdot \left(\frac{\partial \boldsymbol{n}}{\partial x} \times \frac{\partial \boldsymbol{n}}{\partial y} \right) \mathrm{d}x\mathrm{d}y \,, \tag{2-3}$$

which measures how often the non-collinear magnetization texture wraps around a unit sphere. Here, $\boldsymbol{n} = \frac{\mathbf{M}}{|\mathbf{M}|}$ is the normalized magnetization vector. This vector may be represented in spherical coordinates utilizing the symmetry of skyrmionic textures as:

$$\boldsymbol{n}(\mathbf{r}) = [\cos\Phi(\varphi)\sin\Theta(r), \sin\Phi(\varphi)\sin\Theta(r), \cos\Theta(r)], \tag{2-4}$$

where the polar angle $\Phi(\varphi)$ of the magnetization depends on the polar angle φ of the position vector $\mathbf{r}$ and $\Theta(r)$ depends on the length r of the position vector $\mathbf{r}$. We can rewrite the

equation of topological charge from Eq. (2-3) as [41]:

$$\mathrm{N} = \frac{1}{4\pi}\int_0^{\infty}\mathrm{d}r\int_0^{2\pi}\mathrm{d}\varphi\frac{\partial\Phi(\varphi)}{\partial\varphi}\frac{\partial\Theta(r)}{\partial r}\sin\Theta(r) = -\frac{1}{2}\cos\Theta(r)\Big|_{r=0}^{\infty}\cdot\frac{1}{2\pi}\Phi(\varphi)\Big|_{\varphi=0}^{2\pi} \quad (2\text{-}5)$$

$$= \mathrm{p}\ .\ \mathrm{w} \quad (2\text{-}6)$$

p, known as polarity, and w, referred to as vorticity, jointly determine the topological charge. Polarity specifies the orientation of the magnetization at the core of the spin texture, indicating whether it points upward, or downward. On the other hand, vorticity characterizes the sense of rotation within the in-plane magnetic texture. Therefore:

- Polarity: p can take values of +1 or -1, representing either an upward or downward core magnetization orientation.
- Vorticity: w can have values of 0, ±1, ±2, and so on, indicating various degrees of in-plane magnetic rotation.

This implies that the value of N can vary between 0, ±1, ±2, and so on, contingent upon the particular interplay of polarity and vorticity. Examples of skyrmions carrying different topological charges together with the associated projection of the underlying spin-texture on the surface of a unit sphere are illustrated in Fig. **2-1**.

In the case of a discrete atomic lattice, the topological charge defined in the micromagnetic limit as presented in Eq. (2-3) needs to be replaced by:

$$\mathrm{N} = \frac{1}{4\pi}\sum_l A_l \quad (2\text{-}7)$$

with

$$\cos\left(\frac{A_l}{2}\right) = \frac{1+\boldsymbol{n}_i\cdot\boldsymbol{n}_j+\boldsymbol{n}_i\cdot\boldsymbol{n}_k+\boldsymbol{n}_j\cdot\boldsymbol{n}_k}{\sqrt{2\left(1+\boldsymbol{n}_i\boldsymbol{n}_j\right)\left(1+\boldsymbol{n}_j\boldsymbol{n}_k\right)\left(1+\boldsymbol{n}_k\boldsymbol{n}_i\right)}}, \quad (2\text{-}8)$$

where l runs over all elementary triangles of any triangulated regular lattice and A_l is the solid angle, i.e., the area of the spherical triangle with vertices $\boldsymbol{n}_i, \boldsymbol{n}_j$, and $\boldsymbol{n}_k$; see Fig. **2-2** as described in [114]. $\boldsymbol{n}_i, \boldsymbol{n}_j$, and $\boldsymbol{n}_k$ are the unit vectors of the magnetic moments associated to the building-blocks triangles. The sign of A_l is determined as sign $(A_l) = \mathrm{sign}\left[\boldsymbol{n}_i\cdot(\boldsymbol{n}_j\times\boldsymbol{n}_k)\right]$.

Two magnetic configurations are considered to be topologically equivalent if they share the same topological charge. This implies that it is possible to continuously transform one into the other without having to overcome an infinite energy barrier. The uniformly magnetized state, like the FM or AFM state, holds a topological number of zero, so it is coined as topologically trivial state. In contrast, different types of skyrmions exhibit an integer topological charge of 1 or -1, designating them as "topologically non-trivial." As a result, they cannot be continuously transformed into the uniform state by continuous deformation. This property

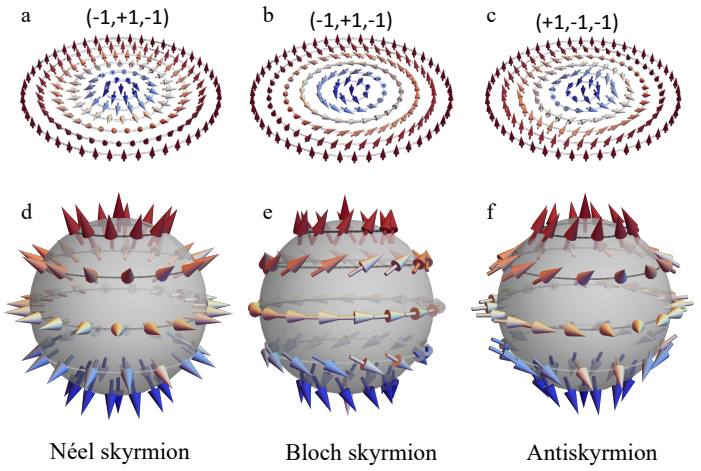

Figure **2-1**.: **Different types of skyrmions.** Schematic illustration of **a** Néel, **b** Bloch and **c** antiskyrmion with their associated topological charge, polarity and vorticity, i.e. (N, w, p). **d, e, f** Projection of the different skyrmionic spin-textures onto the surface of a unit sphere.

is what classifies them as "topologically stable".

Skyrmions emerging in a FM background, FM skyrmions, characterized by a distinct topological charge, exhibit the skyrmion Hall effect (SkHE) directly proportional to the topological charge under the influence of spin-polarized currents (Fig. **2-3** a). When skyrmions are subjected to an electric current, the skyrmions do not simply move along the direction of the current; instead, they also exhibit a transverse motion perpendicular to the direction of the current, which arises due to the interplay between the unique spin structure of skyrmions and the flow of electric charges. In essence, as the electric current flows through the material, it interacts with the magnetic moments of the skyrmions, exerting a force perpendicular to both the current and the magnetic orientations of the skyrmions (Magnus force). This force causes the skyrmions to drift sideways, leading to their transverse motion [41, 115, 33, 70]. This phenomenon has spurred considerable interest in exploring the AFM counterparts of skyrmions [76, 77, 11, 78, 73, 79, 80, 86, 87, 88, 81, 82, 83, 84, 85], wherein two oppositely cored FM skyrmions combine in an AFM arrangement (see Fig. **2-3** b and Fig. **2-4**), resulting in a total topological charge of zero. This renders them as 'Topologically neutral' entities [116]. The concept of topological neutrality pertains to magnetic structures with an effective net zero topological charge. It involves summing two opposing individual skyrmion numbers, each scaled by its corresponding saturation magnetization. AFM skyrmions can

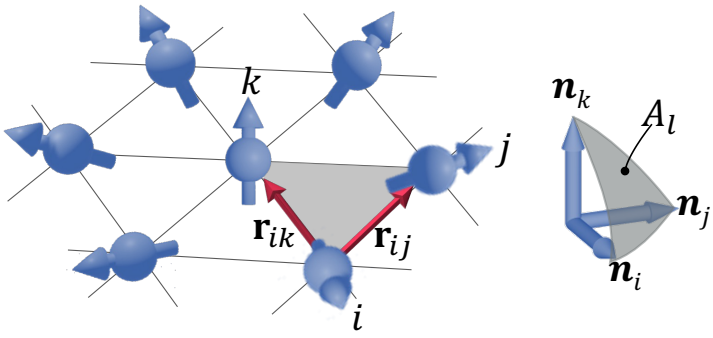

Figure **2-2**.: **Topological charge on a discrete lattice.** An illustration of a portion of a hexagonal magnetic spin lattice that exemplifies how the elementary topological charges are defined on a discrete lattice. The solid angle A_l is defined by the unit vectors $\boldsymbol{n}_i, \boldsymbol{n}_j$, and $\boldsymbol{n}_k$ associated to the atomic magnetic moments carried by atoms defining the vertices of a triangle of lattice points (shaded).

manifest in two configurations: synthetic and intrinsic. In the synthetic scenario [117], the two FM skyrmions forming the AFM structure reside in distinct magnetic layers, separated by a non-magnetic spacer (depicted in Fig. **2-4** a). Conversely, intrinsic AFM skyrmions involve the coexistence of the two FM skyrmions within the same magnetic layer [73, 80, 86] (illustrated in Fig. **2-4** b).

Besides integer topological solitons, spin-swirling textures carrying half-integer charges can exist. They are called merons, which are topologically equivalent to half skyrmions [96, 97, 100, 98, 101, 25, 102, 103, 104, 105], by exhibiting a topological charge of $\pm\frac{1}{2}$ and effectively wrapping half of the unit sphere (refer to Fig. **2-5**). The latter indicates that they emerge in a magnetic background with a magnetization pointing in-plane. Merons come in four distinct types, depending on their vorticity and polarity, as illustrated in Fig. **2-5**. Due to their unique half-integer topological charge, merons can only exist in infinite systems as pairs, forming either a bi-meron or a meron-antimeron pair [97, 98, 99].

To ensure the stability of AFM skyrmions or merons, various magnetic interactions within the energy functional of the skyrmion play a crucial role. In the upcoming sections, we delve into the specifics of these interactions in the context of the atomistic model. Exploring these terms is essential for understanding the intricate factors that contribute to the stability of these fascinating magnetic structures.

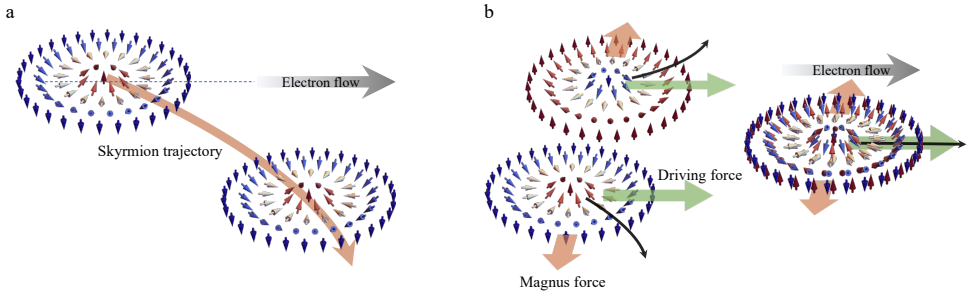

Figure **2-3**.: **Skyrmion Hall effect. a** An illustration of the skyrmion Hall effect when FM skyrmion is subjected to spin currents. **b** An illustration of the cancellation of the Magnus force for AFM skyrmions, where the skyrmion Hall angle is suppressed.

2.3. Magnetic interactions in atomistic models

The magnetic interactions, essential for establishing magnetic order, originate from diverse sources. This includes the electron-electron Coulomb interaction, SOC, and magnetic dipole-dipole interactions. Typically, the dominant exchange interaction is primarily driven by Coulomb interactions. Furthermore, the spin-orbit interaction couples spin to the lattice, which gives rise to preferred magnetic orientations through the magnetocrystalline anisotropy energy (MAE) and breaking of magnetic chirality via the DMI. The long-range dipole-dipole interaction is responsible in creating magnetic domains. However, in the scope of this thesis, we are not discussing the dipolar interactions, as our focus centers on AFM materials, known for their insensitivity to such dipolar influences.

This section provides a brief overview of the crucial interactions within the magnetic systems studied in this thesis using an atomistic model. Of particular significance is the interplay involving the frustration of Heisenberg exchange interactions (J_{ij}), along with the influence of DMI, MAE parameter K, and external magnetic field.

2.3.1. Exchange interaction

The isotropic exchange interaction is a quantum mechanical phenomenon that stems from the Coulomb repulsion between electrons, and from the Pauli exclusion principle. It was recognized independently by Heisenberg and Dirac [118, 119]. Mathematically, the interaction energy between two neighbouring sites i, j can be expressed in its atomistic form as $-J_{ij}\, \boldsymbol{n}_i \cdot \boldsymbol{n}_j$, where J_{ij} is the exchange integral between sites i and j. Isotropic Heisenberg exchange is referred to as FM if it favours parallel spins, i.e., if $J_{ij} > 0$, and AFM if $J_{ij} < 0$, which favours anti-parallel spins. The interaction is symmetric upon interchanging i and j,

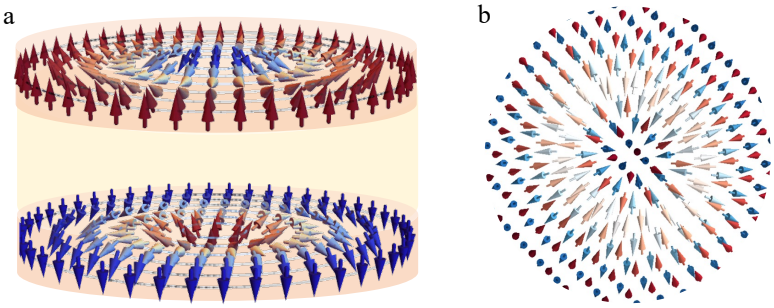

Figure **2-4**.: **AFM skyrmions.** Schematic representation of **a** synthetic and **b** intrinsic AFM skyrmion.

and isotropic as it is independent of the direction of the change relative to the magnetization direction. The total Heisenberg exchange energy of a system of $\mathcal{N}$ interacting spins is expressed as:

$$\mathcal{H}_{\text{Exc}} = -\sum_{<ij>} \mathrm{J}_{ij}\, \boldsymbol{n}_i \cdot \boldsymbol{n}_j \tag{2-9}$$

in which the summation is done over pairs of neighbouring spins $< ij >$, with $i; j = 1 \ldots \mathcal{N}$ and $i \neq j$. (see Fig. **2-6**).

2.3.2. Spin-orbit coupling induced magnetic interactions

Dirac's relativistic theory of the atom introduces the SOC correction to the energy: $E_{\text{SOC}} = -\frac{e}{m_e^2 c^2}\left(\frac{1}{r}\frac{\mathrm{d}\phi}{\mathrm{d}r}\right)\mathcal{L}\cdot\mathbf{S}$, where ϕ is the electric potential due to the nucleus, c is the speed of light in vacuum. This term couples the electron spin with its orbital motion due to the electric field of the nucleus. Although typically small, the strength of the SOC is proportional to the square of the atomic number, making it particularly crucial for heavier elements [120].

Magnetocrystalline anisotropy

The magnetocrystalline anisotropy (MAE) arises from SOC. Because of the SOC in an isolated isotropic atom, a change in the spin direction pulls the orbital angular momentum along. However, the spatial isotropy is disrupted in a crystal, causing the systems energy to be contingent upon the alignment of spherically asymmetric orbitals with the crystal's major axes. The resulting dependence on the magnetic moment orientation defines the MAE. In instances favoring the alignment of the magnetic moment along a specific direction, the system exhibits uniaxial anisotropy. In this simple case, the corresponding spin Hamiltonian

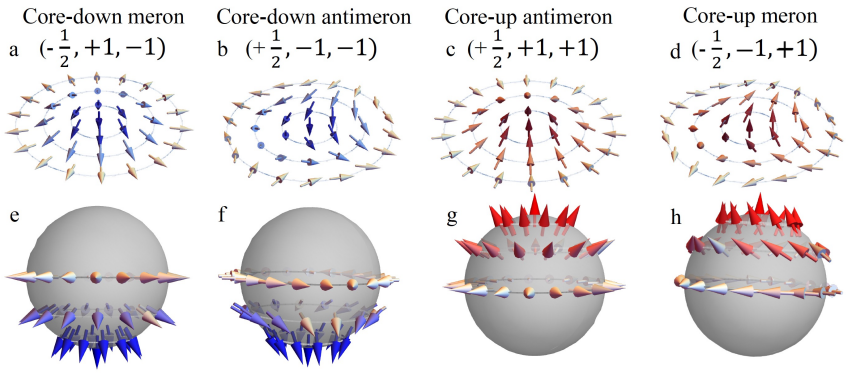

Figure **2-5**.: **Different types of merons.** Schematic representation of **a** Core-up meron, **b** core-up antimeron, **c** core-down antimeron, and **d** core-down meron associated with their distinct topological charge, polarity and vorticity (N, w, p). **e, f, g, h** Projection of the meronic spin-textures onto the surface of the unit sphere.

for this interaction is expressed as:

$$\mathcal{H}_{\text{Ani}} = -\sum_{i} \mathrm{K}_i(\boldsymbol{n}_i \cdot \mathbf{e}_{an})^2, \tag{2-10}$$

where $\mathbf{e}_{an}$ is a unity vector along the preferred direction, and K represents the MAE parameter. If $\mathrm{K} > 0$, the system possesses an easy-axis, minimizing energy when magnetic moments align parallel to $\mathbf{e}_{an}$. Conversely, a negative K implies an easy-plane, where the is energy minimized with magnetic moments perpendicular to $\mathbf{e}_{an}$.

The Dzyaloshinksii-Moriya Interaction

Dzyaloshinskii-Moriya Interaction (DMI), also referred to as antisymmetric exchange interaction, emerges as an exchange interaction between adjacent spins, originating from SOC. In the Heisenberg model, the total DMI energy for a system of N interacting spins is expressed as:

$$\mathcal{H}_{\text{DMI}} = -\sum_{<ij>} \mathbf{D}_{ij} \cdot (\boldsymbol{n}_i \times \boldsymbol{n}_j). \tag{2-11}$$

The existence of DMI is confined to systems with broken inversion symmetry, with the direction of $\mathbf{D}_{ij}$ dictated by the underlying structure, guided by Moriya's symmetry rules [43]. Typically, the DMI manifests in regions like surfaces, interfaces, or low-symmetry bulk materials. The introduction of heavy elements such as Ir is often employed to amplify the effects of SOC. The DMI in the systems explored in the current thesis is typically one order of magnitude lower than the Heisenberg exchange interaction (J_{ij}). The energy contribution associated with the DMI is minimized when neighboring spins are oriented perpendicularly

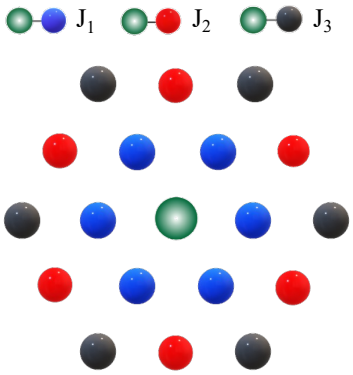

Figure **2-6**.: **Nearest neighboring isotropic exchange interactions in a two-dimensional triangular (hexagonal) lattice.** J_1, J_2, J_3 are the Heisenberg exchange interactions between the central atom with the first (blue), second (red), and third (black) nearest neighboring atoms, respectively.

to each other, determined by the rotation sense specified by $\mathbf{D}_{ij}$. Consequently, the DMI induces non-collinear magnetic configurations, such as spin spirals and skyrmions, and some frustrated magnets.

Initially theorized by Dzyaloshinskii [42] and Moriya [43], the DMI is a consequence of low crystal symmetry and SOC, prevalent in non-centrosymmetric magnetic crystals. This interaction was first observed in weak ferromagnetism in AFM compounds like Fe_2O_3 and CrF_3. Its effects were later identified in chiral bulk magnets such as MnSi (Bulk DMI) [13]. The DMI of this form stabilizes Bloch skyrmion in which spins are rotated in the tangential plane. Another type of DMI arises for systems where the inversion symmetry is broken due to explicit formation of interfaces by two different grown layers (Interfacial DMI) [121, 122, 40]. This form of DMI stabilizes Néel skyrmions such that the rotation of spin is in the radial plane and attributed to the cycloid propagation. Fig. **2-7** illustrates the various types of DMI alongside the corresponding skyrmion types they stabilize.

2.3.3. Zeeman Energy

The Zeeman energy contribution arises from the interaction between the magnetic moments and an external magnetic field $\mathbf{B}$. It can be formulated as follows:

$$\mathcal{H}_{\text{Zeem}} = -\sum_i m_i \mathbf{B} \cdot \boldsymbol{n}_i, \tag{2-12}$$

and favors parallel alignment of the spins with the magnetic field.

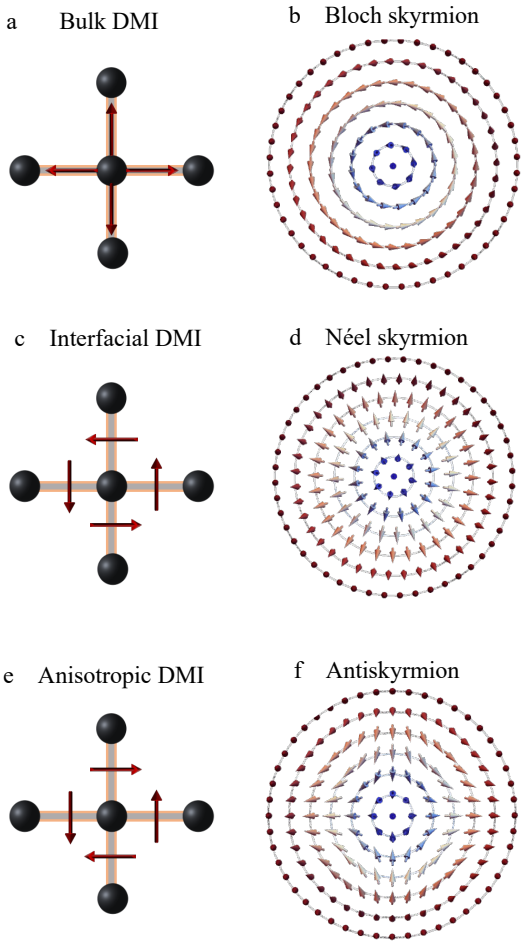

Figure **2-7**.: **Distinct skyrmions resulting from different types of DMI vectors**. Schematic representation of **a** Bulk DMI and **b** the corresponding Bloch skyrmion. **c** Interfacial DMI and **d** the resulting Néel skyrmion. **e** and **f** are for the anisotropic DMI

2.4. The extended Heisenberg Hamiltonian

The extended Heisenberg Hamiltonian is obtained by taking into account all of the interactions previously mentioned. We can now formulate the generalized Heisenberg Hamiltonian

utilized in the thesis:

$$\mathcal{H} = \mathcal{H}_{\text{Exc}} + \mathcal{H}_{\text{DMI}} + \mathcal{H}_{\text{Ani}} + \mathcal{H}_{\text{Zeem}}. \tag{2-13}$$

In this dissertation, as mentioned in chapter 1 and illustrated in Fig. **1-2**, we are investigating several magnetic layered systems involving mainly films of potentially AFM transition metals X (Cr, Mn, V) interfaced with an Ir surface involving the presence or not of Fe, Pd and FePd layers so that, Eq. (2-13) can be dissected as follows:

$$\mathcal{H}_{\text{Exc}} = -\sum_{<ij>} \text{J}_{ij}^{\text{X-X}}\, \boldsymbol{n}_i \cdot \boldsymbol{n}_j - \sum_{<ij>} \text{J}_{ij}^{\text{Fe-X}}\, \boldsymbol{n}_i \cdot \boldsymbol{n}_j - \sum_{<ij>} \text{J}_{ij}^{\text{Fe-Fe}}\, \boldsymbol{n}_i \cdot \boldsymbol{n}_j, \tag{2-14}$$

the term $\mathcal{H}_{\text{Exc}}$ accounts for the isotropic Heisenberg exchange coupling strengths, represented by $\text{J}_{ij}^{\text{X-X}}$ and $\text{J}_{ij}^{\text{Fe-Fe}}$ (if an Fe-film is present). These parameters dictate the interactions between the AFM transition metal (X) and Fe atoms, playing a pivotal role in shaping the magnetic behavior of the system. Similarly, the DMI term is given by:

$$\mathcal{H}_{\text{DMI}} = -\sum_{<ij>} \mathbf{D}_{ij}^{\text{X-X}} \cdot (\boldsymbol{n}_i \times \boldsymbol{n}_j) - \sum_{<ij>} \mathbf{D}_{ij}^{\text{Fe-X}} \cdot (\boldsymbol{n}_i \times \boldsymbol{n}_j) - \sum_{<ij>} \mathbf{D}_{ij}^{\text{Fe-Fe}} \cdot (\boldsymbol{n}_i \times \boldsymbol{n}_j), \tag{2-15}$$

while the contribution from the MAE valid for both easy axis and easy plane cases reads:

$$\mathcal{H}_{\text{Ani}} = -\text{K}^{\text{X}} \sum_i (n_i^z)^2 - \text{K}^{\text{Fe}} \sum_i (n_i^z)^2, \tag{2-16}$$

and finally the Zeeman interaction:

$$\mathcal{H}_{\text{Zeem}} = -\sum_i m_i \mathbf{B} \cdot \boldsymbol{n}_i. \tag{2-17}$$

The aforementioned magnetic interactions are extracted from first-principles using an approach elucidated in the subsequent chapter.

3. Multi-scale modelling – DFT in combination with atomistic spin dynamics

In chapter 2, we introduced a generalized Heisenberg Hamiltonian that, once parameterized, enables the exploration of the magnetic properties of materials with localized magnetic moments at atomic sites. To predict the magnetic properties of a material, we need to extract the system-specific parameters associated with the Hamiltonian's interactions. *Ab initio* simulations provide means to extract these parameters, allowing the determination of model parameters through a fundamental quantum-mechanical description of the crystal's electronic structure. Consequently, we obtain a parametrized Heisenberg Hamiltonian utilizing Density functional theory (DFT) principles, facilitating realistic predictions for material behavior. After the *ab initio* simulations and the extraction of magnetic interactions, atomistic spin dynamics (ASD) calculations are employed to minimize the parameterized Heisenberg Hamiltonian, which enables the exploration of complex and large spin-textures unattainable with pure *ab initio* simulations. In this chapter, we discuss this multi-scale modelling approach we carried out in this thesis.

The following sections commence with an exploration of the quantum-mechanical many-body problem for electrons within a crystal. Subsequently, we delve into DFT [123, 124], that deals with the many-body problem by tackling the electronic system's charge density rather than its wavefunction. The DFT-based methodologies utilized in the thesis are introduced: (i) first we introduce the pseudopotential-based plane wave basis method, Quantum Espresso [125, 126], to solve the single-particle eigenstates of the Kohn-Sham equations; (ii) then, we discuss the fundamentals of the Korringa-Kohn-Rostoker method (KKR) [127, 128, 129, 130], which incorporates multiple-scattering theory and Green functions. Access to the Green function provides access to the tensor of magnetic interactions using the infinitesimal-rotation approach [107, 131, 132]. The aim of this chapter is to offer a concise overview of the essential theoretical concepts utilized in our thesis. It does not aim to provide an exhaustive descriptions to either the KKR formalism or DFT. Comprehensive introductions to DFT can be found in standard textbooks (e.g., [133, 134]). The KKR formalism is thoroughly presented in the textbook Ref. [135] and in the PhD thesis of Bauer [136].

3.1. The many-body Schrödinger equation

In order to describe a condensed matter system consisting of nuclei and electrons, the Schrödinger equation, expressed here in Rydberg atomic units, is the fundamental equation that can describe the stationary states:

$$\mathcal{H}\psi\left(\mathbf{r}_1, \mathbf{r}_2, .., \mathbf{r}_N, \mathbf{R}_1, \mathbf{R}_2, .., \mathbf{R}_M\right) = E\psi\left(\mathbf{r}_1, \mathbf{r}_2, .., \mathbf{r}_N, \mathbf{R}_1, \mathbf{R}_2, .., \mathbf{R}_M\right). \tag{3-1}$$

It consists of a Hamiltonian $\mathcal{H}$ and the many-body wave function $\psi\left(\mathbf{r}_1, \mathbf{r}_2, .., \mathbf{r}_N, \mathbf{R}_1, \mathbf{R}_2, .., \mathbf{R}_M\right)$, which contains all information about physical observables of the system with N interacting electrons and M nuclei (we disregarded the spins in this notation). In this chapter, we use the atomic Rydberg units, where $\hbar = 2m_e = e^2/2 = 1$, where m_e is the rest mass of the electron and e its charge. Neglecting relativistic corrections, the general form of the full many-body Hamiltonian takes the following general form:

$$\mathcal{H} = \underbrace{-\sum_{i}^{N} {\nabla_i}^2}_{\mathcal{T}_\mathrm{e}} \underbrace{-\sum_{I}^{M} \frac{1}{M_I} {\nabla_I}^2}_{\mathcal{T}_{\boldsymbol{n}}} \underbrace{-\sum_{i,I} \frac{Z_I}{|\mathbf{r}_i - \mathbf{R}_I|}}_{\mathcal{V}_{\mathrm{e}-\boldsymbol{n}}} + \underbrace{\sum_{i \neq j} \frac{1}{|\mathbf{r}_i - \mathbf{r}_j|}}_{\mathcal{V}_{\mathrm{e}-\mathrm{e}}} + \underbrace{\sum_{I \neq J} \frac{Z_I Z_J}{|\mathbf{R}_I - \mathbf{R}_J|}}_{\mathcal{V}_{\boldsymbol{n}-\boldsymbol{n}}}. \tag{3-2}$$

The first two terms represent the kinetic energy operators of respectively the electrons and ions. The third term, $\mathcal{V}_{\mathrm{e}-\boldsymbol{n}}$, describes the attractive interaction between an electron located at $\mathbf{r}_i$ and an ion positioned at $\mathbf{R}_I$. The fourth term, $\mathcal{V}_{\mathrm{e}-\mathrm{e}}$, accounts for the repulsion between electrons, and the last term, $\mathrm{V}_{\boldsymbol{n}-\boldsymbol{n}}$, reflects the repulsion between ions. Here, M_I and Z_I represent the mass and atomic number of ion I, respectively. The practicality of solving the Schrödinger equation diminishes rapidly as the number of electrons in a system increases. Even a single Fe atom poses computational challenges, rendering an exact solution unattainable. To clarify that, consider that we want to calculate the wavefunction of an iron atom with its 26 electrons, in three dimensions, we have $3 \times 26 = 78$ degrees of freedom. If we want to solve Eq. (3-1) on a real space grid of $10 \times 10 \times 10$ points, this corresponds to 10^{78} potential configurations, and for each of these configurations, we need to evaluate the wavefunction. Simply storing this function requires physical memory with the mass of the observable universe [137], which illustrates part of the challenge to address even before considering how to solve the Schrödinger equation for such a problem!

3.2. Born-Oppenheimer approximation

The high velocity of light electrons compared to the much slower nuclei, which are at least a thousand times heavier, allows us to consider the nucleus as stationary in the study of electron motion. By neglecting the nucleus velocity, we can separate the electrons motion from that of the nucleus, which is a principle known as the Born-Oppenheimer approxima-

tion [138] or adiabatic approximation. This approximation decouples the motion of nuclei and electrons. Consequently, the electrostatic potential from the nucleus can be treated as an external potential, akin to other externally applied fields, allowing for the expression of the Hamiltonian as:

$$\mathcal{H} = \mathcal{T}_{\mathrm{e}} + \mathcal{V}_{\mathrm{ee}} + \mathcal{V}_{ext}, \tag{3-3}$$

where $\mathcal{V}_{ext}$ is the external potential which includes the nuclear electrostatic potential. This is the first simplification towards an effective description of a system of interacting particles, since it leaves only the electron-electron interaction responsible for all the difficulties. The electronic problem, however, is a quantum many-body problem; due to the mutual interaction of all the electrons in the system, where the system's wavefunction $\psi(\mathbf{r}_1, \mathbf{r}_2, .., \mathbf{r}_N)$ depends on the coordinates of all the electrons, and hence, can not be separated into a single particle contribution, making it too complicated to get the exact solution of the problem.

The idea of DFT is to use the electronic charge density $\rho(\mathbf{r})$ instead of the wave function to determine all observables of a given system.

3.3. Density functional theory

3.3.1. Hohenberg-Kohn theorems

The Hohenberg-Kohn theorems, which were introduced in 1964 [123], provide the essential framework for DFT. The fundamental concept of DFT is to address the many-body electronic problem by focusing on the ground state probability density $\rho_{\mathrm{gs}}(\mathbf{r})$, rather than calculating the intricate many-body wavefunction $\psi(\mathbf{r}_1, \mathbf{r}_2, .., \mathbf{r}_N)$.

For a system of N interacting electrons governed by the Hamiltonian in Eq. (3-3), the expression for $\rho_{\mathrm{gs}}(\mathbf{r})$ is given by:

$$\rho_{\mathrm{gs}}(\mathbf{r}) = \int |\psi(\mathbf{r}_1, \mathbf{r}_2, ..., \mathbf{r}_N)|^2 \mathrm{d}\mathbf{r}_2 \mathrm{d}\mathbf{r}_3 ... \mathrm{d}\mathbf{r}_N. \tag{3-4}$$

The first Hohenberg-Kohn theorem states [123]: *Given the Hamiltonian described by Eq.* (3-3) *and an arbitrary external potential, if the ground state is non-degenerate, a unique correspondence exists between the external potential (up to a constant), the ground-state wavefunction, and the electron density of the ground state.* Thus, each observable as well as the total energy are given as a functional of the ground state density:

$$E[\rho] = \langle \psi[\rho] | \mathcal{H} | \psi[\rho] \rangle = \mathcal{T}[\rho] + \mathcal{U}[\rho] + \mathcal{V}_{ext}[\rho]. \tag{3-5}$$

Further, Hohenberg and Kohn established their second theorem [123], which states: *the*

ground state density $\rho_{\mathrm{gs}}(\mathbf{r})$ *minimizes the total energy functional* $E[\rho]$. This suggests that one can use the variational principle to calculate the ground state density.

For magnetic materials, the energy is written as a functional of the charge density $\rho_{\mathrm{gs}}(\mathbf{r})$ and of the spin density $\mathrm{m}_{\mathrm{gs}}(\mathbf{r})$, which for collinear magnetic materials can be written as:

$$\rho_{\mathrm{gs}}(\mathbf{r}) = \rho^{\uparrow}_{\mathrm{gs}}(\mathbf{r}) + \rho^{\downarrow}_{\mathrm{gs}}(\mathbf{r}), \tag{3-6}$$

where $\rho^{\uparrow}_{\mathrm{gs}}(\mathbf{r})$, $\rho^{\downarrow}_{\mathrm{gs}}(\mathbf{r})$ denote the charge density for respectively the majority and minority spin electrons. The spin density is expressed as:

$$\mathrm{m}_{\mathrm{gs}}(\mathbf{r}) = \rho^{\uparrow}_{\mathrm{gs}}(\mathbf{r}) - \rho^{\downarrow}_{\mathrm{gs}}(\mathbf{r}). \tag{3-7}$$

Hence, the energy, that can now be written as $E\left[\rho_{\mathrm{gs}}, \mathrm{m}_{\mathrm{gs}}\right]$, should be minimized with respect to the charge and spin densities.

Although the Hohenberg-Kohn theorems are very powerful, they do not provide a practical scheme for minimizing Eq. (3-5), which is required to obtain the ground state density. This has been further elaborated by by Kohn and Sham [124] as summarized below.

3.3.2. Kohn-Sham equations

The Hohenberg-Kohn theorems enable us to deduce the ground state characteristics of a system with multiple electrons by focusing on the ground state charge density instead of the wave function. Nevertheless, solving the many-body problem remains a significant challenge. In 1965, Kohn and Sham introduced a systematic method to minimize the total energy functional, laying the groundwork for modern DFT calculations [124]. They suggested creating an auxiliary imaginary system of noninteracting particles with the same ground state density as the many-body interacting system of study, and hence, the same ground state energy. The solutions for this noninteracting problem can be determined by solving the Kohn-Sham equation:

$$\left(-\nabla^2 + \mathcal{V}_{\mathrm{eff}}\ (\mathbf{r})\right) \phi_i(\mathbf{r}) = \varepsilon_i \phi_i(\mathbf{r}), \tag{3-8}$$

which has the form of a single-particle Schrödinger equation, and ϕ_i are known as Kohn-Sham orbitals with orbital eigenvalues ε_i, while the density can be easily calculated using the Kohn-Sham orbitals:

$$\rho(\mathbf{r}) = \sum_{i=1}^{N} \left|\phi_i(\mathbf{r})\right|^2. \tag{3-9}$$

The mapping between the many-body and the noninteracting problems is obtained through

the effective potential $\mathcal{V}_{\text{eff}}$, which is an *unknown* functional of the ground state density.

The potential $\mathcal{V}_{\text{eff}}(\mathbf{r})$ is split into:

$$\mathcal{V}_{\text{eff}}(\mathbf{r}) = \mathcal{V}_{\text{ext}}(\mathbf{r}) + \mathcal{V}_{\text{H}}(\mathbf{r}) + \mathcal{V}_{\text{xc}}(\mathbf{r}), \tag{3-10}$$

where $\mathcal{V}_{\text{ext}}$ is the external potential, $\mathcal{V}_{\text{H}}$ is the Hartree potential given by:

$$\mathcal{V}_{\text{H}}(\mathbf{r}) = \int \frac{2\rho\left(\mathbf{r}'\right)}{|\mathbf{r} - \mathbf{r}'|} \mathrm{d}\mathbf{r}', \tag{3-11}$$

which represents a noninteracting mean-field electrostatic contribution from the electrons in the system, and $\mathcal{V}_{\text{xc}}$ is called the exchange-correlation potential, which is unknown and accounts for the many-body effects, such as the exchange coupling due to Pauli's exclusion principle and electronic correlations. Thus, the energy functional of the Kohn-Sham system, which needs to be minimized, can be written as:

$$E[\rho] = T_{\text{s}}[\rho] + E_{\text{H}}[\rho] + E_{\text{xc}}[\rho] + E_{\text{ext}}\left[\rho\right], \tag{3-12}$$

where the first terms ($T_{\text{s}}[\rho]$) is the kinetic energy associated to the noninteracting Kohn-Sham orbitals:

$$T_{\text{s}}[\rho] = -\sum_{i=1}^{N} \int \phi_i^*(\mathbf{r}) \nabla^2 \phi_i(\mathbf{r}) \mathrm{d}\mathbf{r}. \tag{3-13}$$

$E_{\text{H}}[\rho]$ is the Hartree term, which describes the Coulomb interaction between electrons

$$E_{\text{H}}[\rho] = \iint \frac{\rho(\mathbf{r})\rho\left(\mathbf{r}'\right)}{|\mathbf{r} - \mathbf{r}'|} \mathrm{d}\mathbf{r}\ \mathrm{d}\mathbf{r}'. \tag{3-14}$$

The third term E_{xc} is the exchange-correlation energy, which remains unknown, and it is connected to $\mathcal{V}_{\text{xc}}$ by:

$$\mathcal{V}_{\text{xc}}(\mathbf{r}) = \frac{\delta E_{\text{xc}}[\rho]}{\delta \rho(\mathbf{r})}. \tag{3-15}$$

3.3.3. Exchange-correlation energy

The exchange-correlation energy remains to be evaluated. Various approaches and approximations have been proposed since the seminal paper of Kohn and Sham. In this section, we introduce simple yet highly valuable approximations for the exchange-correlation energy.

Local (spin) density approximation

One of the earliest and simplest approximations of the exchange-correlation energy is the local density approximation (LDA) [124], where the exchange-correlation energy is given by:

$$\mathrm{E}_{\mathrm{xc}}^{\mathrm{LDA}}[\rho] = \int \rho(\mathbf{r}) \varepsilon_{\mathrm{xc}}^{\mathrm{hom}}(\rho(\mathbf{r}))\, \mathrm{d}\mathbf{r}, \tag{3-16}$$

where $\varepsilon_{\mathrm{xc}}^{\mathrm{hom}}\left(\rho^{\uparrow}(\mathbf{r}), \rho^{\downarrow}(\mathbf{r})\right)$ is the exchange-correlation energy density of a homogeneous electron gas.

An extension of the approximation known as the local spin density approximation (LSDA) is utilized here, accounting for distinct spin channels [139]. In both the LDA and LSDA methods, the exchange-correlation energy is approximated using the energy of a "homogeneous" electron gas, with its density assumed to be identical to the local electron density.

$$\mathrm{E}_{\mathrm{xc}}^{\mathrm{LSDA}}\left[\rho^{\uparrow}, \rho^{\downarrow}\right] = \int \rho(\mathbf{r}) \varepsilon_{\mathrm{xc}}^{\mathrm{hom}}\left(\rho^{\uparrow}(\mathbf{r}), \rho^{\downarrow}(\mathbf{r})\right) \mathrm{d}\mathbf{r}. \tag{3-17}$$

The exchange-correlation energy comprise a correlation and an exchange component:

$$\varepsilon_{\mathrm{xc}}\left(\rho^{\uparrow}(\mathbf{r}), \rho^{\downarrow}(\mathbf{r})\right) = \varepsilon_x\left(\rho^{\uparrow}(\mathbf{r}), \rho^{\downarrow}(\mathbf{r})\right) + \varepsilon_c\left(\rho^{\uparrow}(\mathbf{r}), \rho^{\downarrow}(\mathbf{r})\right), \tag{3-18}$$

in which ε_x represents the exchange term, which can be computed for the homogeneous electron gas using the Hartree-Fock method. On the other hand, ε_c, the correlation term, can be calculated through Quantum Monte Carlo simulations [139, 140]. For materials like metals, which have slowly varying densities, LSDA exhibits remarkable performance. Additionally, it provides reasonable outcomes for inhomogeneous systems in other materials due to a systematic error cancellation. Specifically, while LSDA tends to underestimate the exchange energy, it compensates by overestimating the correlation energy, and these errors exhibit opposite signs [141].

Generalized gradient approximation

The Generalized Gradient Approximation (GGA) is a more advanced method than the LDA [142]. It improves accuracy by considering not only the local electron density but also its gradient. When taking the spin into account, the energy functional can be formulated as follows:

$$\mathrm{E}_{\mathrm{xc}}^{\mathrm{GGA}}\left[\rho^{\uparrow}, \rho^{\downarrow}\right] = \int \rho(\mathbf{r}) \varepsilon_{\mathrm{xc}}\left(\rho^{\uparrow}(\mathbf{r}), \rho^{\downarrow}(\mathbf{r}), \nabla\rho^{\uparrow}(\mathbf{r}), \nabla\rho^{\downarrow}(\mathbf{r})\right) \mathrm{d}\mathbf{r}. \tag{3-19}$$

Various GGA formulations, such as PBE [142] and PBEsol [143], are widely used for the approximation of the exchange-correlation energy. Ongoing efforts aim to explore more accu-

rate approximations to enhance the precision of these calculations. However, it is important to note that the increased accuracy achieved with such methods is often accompanied by higher computational complexity.

As discussed earlier, DFT in practice involves intricate models and approximations designed to represent interactions within many-body systems realistically. To apply this theory to actual calculations on real systems, we need to acknowledge specific numerical constraints. It is crucial to choose a suitable basis set for the Kohn-Sham orbitals to practically solve the DFT equations. In our thesis, we employed DFT calculations utilizing the KKR Green function method [127, 128, 129, 130], as elaborated in the following sections. However, atomic relaxations with the KKR Green function method is computationally cumbersome. An alternative is provided by Quantum Espresso [125, 126] DFT code. This code, which is a plane wave pseudo-potential method, was employed specifically for obtaining the relaxed positions of the magnetic materials explored in our study.

3.4. Ab initio method I: Plane waves basis and pseudo-potentials (Quantum Espresso)

3.4.1. Plane waves

Using Bloch's theorem [144], the Kohn-Sham orbitals (Eq. (3-8)) can be expanded on a basis set of plane waves as follows:

$$\phi_{\mathbf{k}u}(\mathbf{r}) = \sum_{\mathbf{G}} a_{u,\mathbf{G}+\mathbf{k}} \times \frac{1}{\sqrt{V}} e^{i(\mathbf{G}+\mathbf{k})\cdot\mathbf{r}}, \tag{3-20}$$

where the expansion coefficients of the wavefunction, now expressed in terms of orthonormal plane waves, are $a_{u,\mathbf{G}+\mathbf{k}}$, and the sum runs over the reciprocal lattice vector $\mathbf{G}$, where V is the unit cell's volume. The Kohn-Sham equations in reciprocal space for the expansion coefficient $a_{u,\mathbf{G}+\mathbf{k}}$ are obtained by substituting this expansion into Eq. (3-8). The plane wave expansion is exact in the limit of infinite G-vectors. Eq. (3-20) of the wave functions is truncated in practical calculations by retaining only those plane wave vectors $(\mathbf{G}+\mathbf{k})$ whose kinetic energy is less than a specified cutoff value E_{cut}:

$$|\mathbf{G}+\mathbf{k}|^2 \leq \mathrm{E}_{cut}. \tag{3-21}$$

To find the minimum number of wave functions (or minimum energy cut-off) in practical calculations that allows the total energy to converge, one should first conduct a preliminary investigation. The expansion of all electronic states on a plane wave basis is required after E_{cut} has been determined. Because many plane waves are needed to fully describe the system—especially when localized states are involved—this is computationally inconvenient.

The problem can be avoided by making a distinction between the valence electrons and core electrons and assuming that the valence electrons account for the majority of the relevant physics, while the core electrons being considered as fixed in their atomic configuration [145] (frozen core approximation). Consequently, a pseudo-potential (PP) [146, 147] can be introduced in place of directly treating the core electrons in order to replicate the interaction between the real atomic potential and the outermost states.

In addressing core electrons, a pseudo-wavefunction is employed, designed to be smooth within a specified core cut-off radius and aligned with the scattering properties of the entire system beyond this radius. Essentially, the Kohn-Sham orbitals derived from a comprehensive all-electron calculation beyond the core-shell should coincide with the single-particle orbitals originating from the PP. There are different families of PPs depending on the shape, the conditions placed on the pseudo-wavefunction, the location of the core cut-off radius, and the mathematical structure of the PPs. One example is the Norm-conserving PPs [148, 149] which is contingent upon the preservation of the original full-potential wavefunction norm. However, this condition poses a drawback, particularly in systems like transition metals, where an extensive number of plane waves is required for wave function expansion, incurring high computational costs. This constraint is alleviated in Projector-Augmented Waves PPs (PAW) [150, 151], minimizing the G-vectors needed to describe the pseudo-wavefunction's variation in the core region and subsequently reducing computational expenses. PAW presents a potentially more reliable alternative, providing comparable results to other PPs but with enhanced accuracy for specific materials.

3.4.2. Quantum Espresso

The many-body Hamiltonian within the framework of DFT is mapped into self-consistent single-particle Kohn-Sham equations, where the single-particle eigenstates of the Kohn-Sham equations are determined using the open-source computer codes Quantum Espresso [125, 126, 152]. The electron-ion interactions were modeled using pseudopotentials (PPs) from the PSLibrary, applying the frozen-core approximation [146, 147, 153, 145]. For determining the electronic structures and geometrical details of our magnetic systems, the Projector Augmented Wave (PAW) method was employed [150, 151].

To conduct PAW calculations using Quantum Espresso, the process involves several steps:

1. Define the system structure by specifying the arrangement, positions, and types of atoms in the material.

2. Perform the PAW self consistent calculations: Use the Quantum Espresso pw.x code with the PAW option to perform the self consistent DFT calculations with the PAW method to converge the system allowing the vertical relaxations of the atoms.

3. Extract the relaxed positions of the magnetic atoms to be plugged in KKR DFT calculations.

After establishing the relaxed positions of our magnetic systems, our next goal is to calculate material-specific magnetic properties using the KKR Green function-based method, which is described in the following section.

3.5. Ab initio method II: Korringa-Kohn-Rostoker Green function method (KKR)

In solid state physics and quantum chemistry, a wide range of approaches and implementations for solving the Kohn-Sham equation of DFT are currently available on the market with a comparable level of accuracy, enabling the creation of quantitative predictions for experimentally observable quantities [154]. The all-electron approaches, which handle valence and core electrons equally, are recognized as the gold standard. The KKR Green function method is a full-potential relativistic implementation made possible by the KKR code developed in Jülich [155, 156, 129, 136, 157]. The KKR method was first proposed by Korringa, Kohn, and Rostoker [127, 128], and it was used for the majority of first-principles calculations in this thesis. Using this technique, the space is divided into Voronoi cells, each of which defines a scattering center. In a solid, the scattering centers typically correspond to the atoms. The basic idea behind the KKR Green function method is to split the process of accurately describing a solid's electronic structure into two tasks:

1. Solve the problem for a single scattering center.

2. Incorporate the structural environment of this particular scatterer by use of a multiple scattering ansatz.

The condition that the outgoing wave function from one scattering center equals the sum of all incoming wave functions to this scatterer formally fulfils the second request. The Green function formulation of the KKR method imparts it with considerable power, characterized by certain non-standard features, some of which (pertinent to this thesis) will be elucidated below. This section presents a brief introduction to the fundamental properties of Green functions in solid-state physics and delves into the multiple scattering theory to the KKR formalism. While providing a concise overview of the theory, we recommend a more in-depth exploration through standard literature, such as Gonis' book [158], or KKR-specific references like those in the introductions of publications such as Refs. [159, 136].

3.5.1. Definition and general properties of a Green function

Suppose a system is described by the time-independent Hamiltonian $\mathcal{H}_0$ for which a complete basis set of eigenfunctions $|\psi_0\rangle$ with eigenvalues ε_0 exists, satisfying:

$$\mathcal{H}_0|\psi_0\rangle = \varepsilon_0|\psi_0\rangle\,. \tag{3-22}$$

When the system is subject to a perturbation given by potential $\mathcal{V}$, the Schrödinger equation

reads:

$$\begin{aligned} \mathcal{H}|\psi\rangle &= \varepsilon|\psi\rangle \\ (\mathcal{H}_0 + \mathcal{V})|\psi\rangle &= \varepsilon|\psi\rangle \\ (\varepsilon - \mathcal{H}_0)|\psi\rangle &= \mathcal{V}|\psi\rangle\,. \end{aligned} \tag{3-23}$$

Instead of solving the eigenvalue problem the usual way by calculating the density from the eigenfunctions, one can utilize the Green function $\mathcal{G}$ associated with the precedent Hamiltonian.

The Green function of the unperturbed system is defined as:

$$(z\mathcal{I} - \mathcal{H}_0)\mathcal{G}_0(z) = \mathcal{I}, \tag{3-24}$$

where z is a complex energy with a finite imaginary part ($z \equiv \varepsilon + \mathrm{i}\eta$) and $\mathcal{I}$ is the identity operator. Similarly, the Green function $\mathcal{G}(z)$ of the perturbed system described by $\mathcal{H}$ is given by:

$$(z\mathcal{I} - \mathcal{H})\mathcal{G}(z) = \mathcal{I}. \tag{3-25}$$

The Green function is also called resolvent of the Hamiltonian and can be characterized as its inverse,

$$\mathcal{G}(z) = (z\mathcal{I} - \mathcal{H})^{-1}. \tag{3-26}$$

Using the eigenvalues ε_n and the complete set of the Hamiltonians eigenfunctions $\{|\psi_n\rangle\}$, the Green function can be written as a sum over all eigenstates. This is called the spectral or Lehmann-representation of the Green function:

$$\mathcal{G}(z) = \sum_n \frac{|\psi_n\rangle\langle\psi_n|}{z - \varepsilon_n}. \tag{3-27}$$

From Eq. (3-25), the Green function of the perturbed system $\mathcal{G}$ can be expressed by means of $\mathcal{G}_0$ (the Green function of the unperturbed system) according to:

$$\begin{aligned} (z\mathcal{I} - \mathcal{H}_0 - \mathcal{V})\mathcal{G}(z) &= \mathcal{I} \\ (z\mathcal{I} - \mathcal{H}_0)\mathcal{G}(z) &= \mathcal{I} + \mathcal{V}\mathcal{G}(z) \\ \mathcal{G}(z) &= (z\mathcal{I} - \mathcal{H}_0)^{-1} + (z\mathcal{I} - \mathcal{H}_0)^{-1}\mathcal{V}\mathcal{G}(z) \\ \mathcal{G}(z) &= \mathcal{G}_0(z) + \mathcal{G}_0(z)\mathcal{V}\mathcal{G}(z). \end{aligned} \tag{3-28}$$

The last equation is known as the Dyson equation and plays a central role in the KKR Green

function theory. One can formally expand Eq. (3-28) by subsequently inserting the left-hand side into $\mathcal{G}(z)$:

$$\begin{aligned}\mathcal{G}(z) &= \mathcal{G}_0(z) + \mathcal{G}_0(z)\mathcal{V}\mathcal{G}(z) \\ &= \mathcal{G}_0(z) + \mathcal{G}_0(z)VG_0(z) + \mathcal{G}_0(z)\mathcal{V}\mathcal{G}_0(z)\mathcal{V}G(z) \\ &= \mathcal{G}_0(z) + \mathcal{G}_0(z)\mathcal{V}\mathcal{G}_0(z) + \mathcal{G}_0(z)\mathcal{V}\mathcal{G}_0(z)\mathcal{V}\mathcal{G}_0(z) + \ldots \\ &= \mathcal{G}_0(z) + \mathcal{G}_0(z)(\mathcal{V} + \mathcal{V}\mathcal{G}_0(z)\mathcal{V} + \ldots)\mathcal{G}_0(z).\end{aligned} \tag{3-29}$$

Such a series allows to express the requested Green function $\mathcal{G}(z)$ exclusively by the two operators $\mathcal{G}_0(z)$ and $\mathcal{V}$.

The term in brackets in Eq. (3-29) is the *transition matrix* (t-matrix), defined as:

$$\mathcal{T}(z) = \mathcal{V} + \mathcal{V}\mathcal{G}_0(z)\mathcal{V} + \mathcal{V}\mathcal{G}_0(z)\mathcal{V}\mathcal{G}_0(z)\mathcal{V} + \ldots. \tag{3-30}$$

Then, Eq. (3-29) can be written as:

$$\mathcal{G} = \mathcal{G}_0 + \mathcal{G}_0\mathcal{T}\mathcal{G}_0. \tag{3-31}$$

A similar approach can be followed for the solutions of the differential equations (Eq. (3-22), and Eq. (3-23)) resulting in the *Lippmann-Schwinger* equation. It connects the wave functions of a perturbed ($|\psi\rangle$) and an unperturbed ($|\psi_0\rangle$) system:

$$(z\mathrm{I} - \mathcal{H}_0)|\psi_0\rangle = 0 \tag{3-32}$$

$$(z\mathrm{I} - \mathcal{H}_0)|\psi\rangle = \mathcal{V}|\psi\rangle. \tag{3-33}$$

Multiplying Eq. (3-33) with the resolvent, $\mathcal{G}_0 = (z\mathcal{I} - \mathcal{H}_0)^{-1}$, we get:

$$|\psi\rangle = |\psi_0\rangle + \mathcal{G}_0\mathcal{V}|\psi\rangle. \tag{3-34}$$

However, the desired solution $|\psi\rangle$ appears in both side of this equation. We can iteratively insert the above equation into itself to produce a Born series:

$$\begin{aligned}|\psi\rangle &= |\psi_0\rangle + \mathcal{G}_0(z)\mathcal{V}|\psi_0\rangle + \mathcal{G}_0(z)\mathcal{V}\mathcal{G}_0(z)\mathcal{V}|\psi_0\rangle + \ldots \\ &= |\psi_0\rangle + \mathcal{G}_0(z)\mathcal{T}|\psi_0\rangle.\end{aligned} \tag{3-35}$$

The *Lippmann-Schwinger* equation is, besides the Dyson equation, the second central equa-

tion which is used in KKR theory.

A convenient attribute of the Green function formalism is that observables $\mathcal{A}$, which depend only on single particle properties, can be extracted from $\mathcal{G}(\varepsilon)$ by making use of the algebraic connection:

$$\langle \mathcal{A} \rangle = -\frac{1}{\pi} \mathrm{Im} \int_{-\infty}^{\varepsilon_F} \mathrm{d}\varepsilon \mathrm{Tr}[\mathcal{A}\mathcal{G}(\varepsilon)], \tag{3-36}$$

where ε_F is the Fermi energy of the system and the is trace over the degrees of freedom (e.g. position, spin and orbital angular momenta). The integration is performed along the energy contour up to the Fermi energy ε_F of the electronic structure. This allows for the straightforward calculation of the electronic density, a key ingredient in DFT. It can be easily computed in the position representation by taking the trace of the Green function via:

$$\rho(\mathbf{r}) = -\frac{1}{\pi} \mathrm{Im} \int_{-\infty}^{\varepsilon_F} \mathrm{d}\varepsilon \mathrm{Tr}[\mathcal{G}(\mathbf{r}, \mathbf{r}'; \varepsilon)]. \tag{3-37}$$

3.5.2. Full potential

In the Green function formalism of the KKR method, a Voronoi decomposition is used to partition the space containing the material. Typically, in this process, the decomposition starts at the center of each atom. Next, we locate the area in space whose points are nearest a given atom. Every area is referred to as a Voronoi cell, which contains either a single atom or vacuum. Centered in each Voronoi seed, we construct a Wigner–Seitz cell which is a sphere with the same volume as the Voronoi cell. The purpose of these cell divisions is to be able to separate the calculation of the Green function into local problems (on-site), which each can be solved independently, and a global part in which all local solutions are connected (multiple-scattering). The Voronoi cells collectively occupy the entire space. Nevertheless, within the KKR framework, two distinct approaches are employed for handling the geometry. The first is the atomic sphere approximation (ASA), which represents each cell as a sphere encompassing a spherically symmetric potential, and therefore neglects any inter-cell region. The second is the full potential method which makes no shape approximations of the potential and describes correctly the interstitial region between the atoms. In this thesis, we opted for the full potential approach.

Due to the cell construction, the corresponding sites i and j at $\mathbf{R}_i$ and $\mathbf{R}_j$, respectively, serve as the center of the spatial coordinates of the KKR Green function:

$$\mathcal{G}(\mathbf{x}, \mathbf{x}'; \varepsilon) = \mathcal{G}(\mathbf{r} + \mathbf{R}_i, \mathbf{r}' + \mathbf{R}'_j; \varepsilon) = \mathcal{G}_{ij}(\mathbf{r}, \mathbf{r}'; \varepsilon), \tag{3-38}$$

as depicted in Fig. **3-1**. With this separation, the Green function can be dissected into an on-site contribution and a structural contribution, addressing multiple scattering, as elucidated

in the subsequent sections.

$$\mathcal{G}_{ij}(\mathbf{r},\mathbf{r}';\varepsilon) = \mathcal{G}_{ij}^{\text{on-site}}(\mathbf{r},\mathbf{r}';\varepsilon)\delta_{ij} + \mathcal{G}_{ij}^{\text{str}}(\mathbf{r},\mathbf{r}';\varepsilon). \tag{3-39}$$

A site i's potential is only defined within the volume V_i of the corresponding cell because of the Voronoi construction:

$$\mathcal{V}_i(\mathbf{r}) = \begin{cases} \mathcal{V}_i(\mathbf{r}), & \text{if } \mathbf{r} \in \mathrm{V}_i \\ 0, & \text{else} \end{cases}. \tag{3-40}$$

This results in the definition of the so-called shape function $\Theta_i(\mathbf{r})$,

$$\Theta_i(\mathbf{r}) = \begin{cases} 1, & \text{if } \mathbf{r} \in \mathrm{V}_i \\ 0, & \text{else} \end{cases}. \tag{3-41}$$

For every site i, the potential is treated in the local frames and expanded in real spherical harmonics (refer to Fig. **3-1**).

$$\mathcal{V}_i(\mathbf{r})\Theta_i(\mathbf{r}) = \sum_{\mathcal{L}} \mathcal{V}_{\mathcal{L}}(r) Y_{\mathcal{L}}(\hat{r}). \tag{3-42}$$

The spherical harmonics carry an index $\mathcal{L} = (\ell, m)$ combining the orbital quantum number and the magnetic quantum number, the absolute distance is denoted by $r = |\mathbf{r}|$, while the unit direction is indicated by $\hat{r} = \mathbf{r}/r$. Keep in mind that real spherical harmonics, not complex spherical harmonics, are employed throughout the thesis. According to this convention, $\mathcal{V}_{\mathcal{L}}(r)$ is convoluted with the shape function.

$$\mathcal{V}_{\mathcal{L}}(r) = \sum_{\mathcal{L}'\mathcal{L}''} C_{\mathcal{L}'\mathcal{L}''}^{\mathcal{L}} \mathcal{V}_{i\mathcal{L}}^{0}(r')\, \Theta_{\mathcal{L}''}(r). \tag{3-43}$$

The Gaunt coefficient $C_{\mathcal{L}'\mathcal{L}''}^{\mathcal{L}}$ is expressed as

$$C_{\mathcal{L}'\mathcal{L}''}^{\mathcal{L}} = \int \mathrm{d}\hat{r} Y_{\mathcal{L}}(\hat{r}) Y_{\mathcal{L}'}(\hat{r}) Y_{\mathcal{L}''}(\hat{r})\,. \tag{3-44}$$

represents the potential expansion in spherical harmonics, excluding spatial constraints, while $\Theta_{\mathcal{L}}(r)$ stands as the shape functions expansion coefficient. In the full potential context, the radial argument r extends up to the radius of the bounding sphere. This sphere is the smallest one that encompasses the entire Wigner-Seitz cell, as depicted in Fig. **3-1**.

In the subsequent sections, we apply the Green function formalism to address the Schrödinger equation, beginning with the free electron gas, reaching the multiple scattering problem.

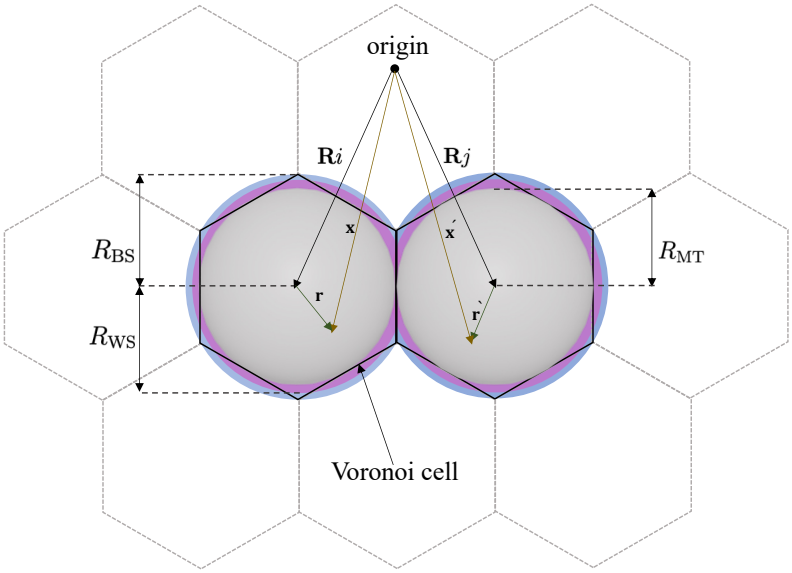

Figure **3-1**.: **Visualization of the Voronoi construction for a hexagonal lattice.** The Voronoi cell associated with site i is centered at $\mathbf{R}i$, establishing a local frame $\mathrm{x} = \mathbf{r} + \mathbf{R}j$. Each cell features key parameters, including the muffin tin radius R_{MT}, defined as the largest sphere fully contained within the Wigner-Seitz cell, the Wigner-Seitz radius R_{WS} corresponding to a sphere with equivalent volume to the Wigner-Seitz cell, and the bounding sphere's radius R_{BS}, representing the smallest sphere encompassing the entire Wigner-Seitz cell.

3.5.3. Green function for free electrons

In the following it is explained how the propagation of a single electron in a finite potential can be described by a Green function. But before that, we introduce the Green function for the simple case of a three-dimensional free electron gas (i.e. $\mathcal{V}(\mathbf{r}) = 0$). The electronic wave function $\psi_k^0(\mathbf{r})$ is a plane wave and is expanded in the real spherical harmonics basis $Y_{\mathcal{L}}(\hat{r})$:

$$\begin{aligned}\psi_k^0(\mathbf{r}) &= e^{i\mathbf{k}.\mathbf{r}} \\ &= \sum_{\mathcal{L}} 4\pi \mathrm{i}^l j_l(\sqrt{\varepsilon} r) Y_{\mathcal{L}}(\hat{r}) Y_{\mathcal{L}}(\hat{k})\,.\end{aligned} \tag{3-45}$$

The energy ε is connected to the wave vector $\mathbf{k}$ through the equations $k = |\mathbf{k}| = \sqrt{\varepsilon}$ and $r = |\mathbf{r}|$. $j_l(kr)$ is the spherical Bessel function of first kind. The Green function, for an energy ε, that connects a point at position $\mathbf{r}$ in space with a point at $\mathbf{r}'$ in a free electron gas is provided by:

$$g\left(\mathbf{r},\mathbf{r}',\varepsilon\right) = -\frac{1}{4\pi}\frac{e^{\mathrm{i}k|\mathbf{r}-\mathbf{r}'|}}{|\mathbf{r}-\mathbf{r}'|}\,. \tag{3-46}$$

$g\left(\mathbf{r},\mathbf{r}',\varepsilon\right)$ is expanded in its turn in a real spherical harmonics basis as:

$$g\left(\mathbf{r},\mathbf{r}',\varepsilon\right) = \sum_{\mathcal{L}} Y_{\mathcal{L}}(\hat{r}) g_l\left(r,r',\varepsilon\right) Y_{\mathcal{L}}\left(\hat{r}'\right) \tag{3-47}$$

$$= -\mathrm{i}k \sum_{\mathcal{L}} Y_{\mathcal{L}}(\hat{r}) j_l\left(kr_<\right) h_l\left(kr_>\right) Y_{\mathcal{L}}\left(\hat{r}'\right)\,, \tag{3-48}$$

where $r_{<(>)}$ is the smaller (larger) of the radii r and r' respectively. The Hankel function $h_l(kr)$ is irregular in the limit of $r \to 0$, while the Bessel function $j_l(kr)$ is regular in the same limit. The Green function fulfills the translational invariance of the free electron gas and depend therefore only on the relative distance $|\mathbf{r}-\mathbf{r}'|$.

3.5.4. Single site problem

We now consider the presence of a finite potential $\mathcal{V}$ and solve the Schrödinger equation to determine the electronic wave function ψ_k. Based on the wavefunction of the free electron gas, Eq. (3-45), an ansatz for the wavefunction of the full system is

$$\psi_k(r) = \sum_{\mathcal{L}} 4\pi i^{\ell} Y_{\mathcal{L}}(\hat{k}) R^{\mathcal{L}}(r;\varepsilon), \tag{3-49}$$

where $R^{\mathcal{L}}(r;\varepsilon)$ is the regular solution of the Schrödinger equation, which can be expressed as follows in a basis of spherical harmonics:

$$R^{\mathcal{L}}(\mathbf{r};\varepsilon) = \sum_{\mathcal{L}'} \frac{1}{r} R^{\mathcal{L}}_{\mathcal{L}'}(r;\varepsilon) Y_{\mathcal{L}'}(\hat{r}), \tag{3-50}$$

generally reliant on two angular indices: $\mathcal{L}$, which represents the partial wave component of the original free-electron plane wave, and $\mathcal{L}'$, which describes the spatial shape that the partial wave takes on when it is scattered by a non-spherical potential. Eq. (3-34) can be substituted with Eq. (3-45), Eq. (3-49), and Eq. (3-50) to obtain a set of coupled radial *Lippmann-Schwinger* equations:

$$R^{\mathcal{L}'}_{\mathcal{L}}(r;\varepsilon) = r j_\ell(kr)\delta_{\mathcal{L}\mathcal{L}'} + \int \mathrm{d}r' g_\ell\left(r,r';E\right) \sum_{\mathcal{L}''} \mathcal{V}_{\mathcal{L}\mathcal{L}''}\left(r'\right) R^{\mathcal{L}'}_{\mathcal{L}''}\left(r';\varepsilon\right), \tag{3-51}$$

where two spherical harmonics were employed as matrix elements of the non-spherical potential,

$$\mathcal{V}(r) = \sum_{\mathcal{L}\mathcal{L}'} Y_{\mathcal{L}}(\hat{r}) \mathcal{V}_{\mathcal{L}\mathcal{L}'}(r) Y_{\mathcal{L}'}(\hat{r}) \quad \text{with} \quad \mathcal{V}_{\mathcal{L}\mathcal{L}'}(r) = \sum_{\mathcal{L}''} C^{\mathcal{L}''}_{\mathcal{L}\mathcal{L}'} \mathcal{V}_{\mathcal{L}''}(r). \tag{3-52}$$

To construct the on-site Green function, a few more basis functions are required in addition to the regular solution. The first one, denoted as $S_{\mathcal{L}}^{\mathcal{L}'}(r;\varepsilon)$, is the irregular solution based on the Hankel functions. Moreover, if the potential is non-diagonal in spin space, the Schrödinger equation, which is a system of coupled second-order linear differential equations, allows for left and right solutions (refer to Ref. [136] for specifics). The right solutions were previously discussed, while the left solutions, denoted as $\bar{R}_{\mathcal{L}}^{\mathcal{L}'}$ and $\bar{S}_{\mathcal{L}}^{\mathcal{L}'}$ for the regular and irregular solutions, respectively, are two-dimensional row vectors in spin space. One can obtain the radial wave functions from:

$$\begin{aligned} S_{\mathcal{L}}^{\mathcal{L}'}(r;\varepsilon) &= r h_\ell(kr)\beta_{\mathcal{L}}^{\mathcal{L}'} + \int \mathrm{d}r' g_\ell(r,r';\varepsilon) \sum_{\mathcal{L}''} \mathcal{V}_{\mathcal{L}\mathcal{L}''}(r')\, S_{\mathcal{L}''}^{\mathcal{L}'}(r';\varepsilon)\,, \\ \bar{R}_{\mathcal{L}}^{\mathcal{L}'}(r;\varepsilon) &= r j_\ell(kr)\delta_{\mathcal{L}\mathcal{L}'} + \int \mathrm{d}r' \sum_{L''} \bar{R}_{\mathcal{L}''}^{\mathcal{L}'}(r';\varepsilon)\, \mathcal{V}_{\mathcal{L}''\mathcal{L}}(r')\, g_\ell(r',r;\varepsilon)\,, \\ \bar{S}_{\mathcal{L}}^{\mathcal{L}'}(r;\varepsilon) &= \bar{\beta}_{\mathcal{L}}^{\mathcal{L}'} r h_\ell(kr) + \int \mathrm{d}r' \sum_{\mathcal{L}''} \bar{S}_{\mathcal{L}''}^{\mathcal{L}'}(r';\varepsilon)\, \mathcal{V}_{\mathcal{L}''\mathcal{L}}(r')\, g_\ell(r',r;\varepsilon)\,, \end{aligned} \tag{3-53}$$

with

$$\beta_{\mathcal{L}}^{\mathcal{L}'} = \delta_{\mathcal{L}\mathcal{L}'} - k \int \mathrm{d}r' r j_\ell(kr') \sum_{\mathcal{L}''} \mathcal{V}_{\mathcal{L}\mathcal{L}''}(r')\, S_{\mathcal{L}''}^{\mathcal{L}'}(r';\varepsilon)\,, \tag{3-54}$$

$$\bar{\beta}_{\mathcal{L}}^{\mathcal{L}'} = \delta_{\mathcal{L}\mathcal{L}'} - k \int \mathrm{d}r' \sum_{\mathcal{L}''} \bar{S}_{\mathcal{L}''}^{\mathcal{L}'}(r';\varepsilon)\, \mathcal{V}_{\mathcal{L}''\mathcal{L}}(r')\, r j_\ell(kr')\,. \tag{3-55}$$

Using the right and left solutions (see, for example, [136]), the on-site Green function can be obtained as follows:

$$\mathcal{G}_{\mathcal{L}\mathcal{L}}^{\text{on-site}}(r,r';\varepsilon) = -\mathrm{i}k \sum_{\mathcal{L}''} \begin{cases} R_{\mathcal{L}}^{\mathcal{L}''}(r;\varepsilon)\bar{S}_{\mathcal{L}'}^{\mathcal{L}''}(r';\varepsilon) & , \quad \text{if} \quad r' > r \\ S_{\mathcal{L}}^{\mathcal{L}''}(r;\varepsilon)\bar{R}_{\mathcal{L}'}^{\mathcal{L}''}(r';\varepsilon) & , \quad \text{if} \quad r > r' \end{cases}. \tag{3-56}$$

3.5.5. Multiple scattering theory

Following the computation of the single-site Green function, the subsequent critical step involves calculating the structural part of the Green function which takes into account the multiple scatterings induced by the presence of neighboring atoms in addition to the geometrical details. In this section, we explore how insights derived from the single-site problem inform the computation of the globally defined Green function. By expanding the Green function, we separate its calculation into a localized part, addressing the single-site problem, and a globally defined part, forming the structural Green function. The Green function between the two distinct sites i and j, starting from the free electron gas, can be expanded as follows:

$$g(\mathbf{r}+\mathbf{R}_i,\mathbf{r}'+\mathbf{R}_j;\varepsilon) = \sum_{\mathcal{L}\mathcal{L}'} Y_{\mathcal{L}}(\hat{r}) j_\ell(kr) g_{\mathcal{L}\mathcal{L}'}^{ij}(\varepsilon) j_{\ell'}(kr')\, Y_{\mathcal{L}'}(\hat{r}')\,, \tag{3-57}$$

where a transformation theorem for Hankel functions can be used to derive the coefficient

$g^{ij}_{\mathcal{L}\mathcal{L}'}(\varepsilon)$,

$$g^{ij}_{\mathcal{L}\mathcal{L}'}(\varepsilon) = -(1-\delta_{ij})\,4\pi \mathrm{i} k \sum_{\mathcal{L}''} \mathrm{i}^{\ell-\ell'+\ell''} C^{\mathcal{L}''}_{\mathcal{L}\mathcal{L}'} h_{\ell''}\left(k\,|\mathbf{R}_i-\mathbf{R}_j|\right) Y_{\mathcal{L}''}\left(\frac{\mathbf{R}_i-\mathbf{R}_j}{|\mathbf{R}_i-\mathbf{R}_j|}\right). \tag{3-58}$$

Utilizing a suitable assumption for the total Green function of the system,

$$\mathcal{G}_{ij}\left(\mathbf{r},\mathbf{r}';\varepsilon\right) = G_i^{\mathrm{on-site}}\left(\mathbf{r},\mathbf{r}';\varepsilon\right)\delta_{ij} + \sum_{\mathcal{L}\mathcal{L}'} R^i_{\mathcal{L}}(\mathbf{r};\varepsilon)\mathcal{G}^{ij}_{\mathcal{L}\mathcal{L}'}(\varepsilon)\bar{R}^j_{\mathcal{L}'}\left(\mathbf{r}';\varepsilon\right), \tag{3-59}$$

where the first term is the single-site Green function at site i, and the second term is a multiple scattering term including a structural Green function, which by utilizing both Eq. (3-59) and the Dyson Eq. (3-28) can be written as (Refer to [136] for details),

$$\mathcal{G}^{ij}_{\mathcal{L}\mathcal{L}'}(\varepsilon) = g^{ij}_{\mathcal{L}\mathcal{L}'}(\varepsilon) + \sum_m g^{im}_{\mathcal{L}\mathcal{L}''}(\varepsilon) t^m_{\mathcal{L}''\mathcal{L}'''}(\varepsilon)\mathcal{G}^{mj}_{\mathcal{L}'''\mathcal{L}'}(\varepsilon), \tag{3-60}$$

with the t-matrix

$$t^m_{\mathcal{L}\mathcal{L}'}(\varepsilon) = \int \mathrm{d}\mathbf{r}\, r j_\ell(kr)\mathcal{V}^m(\mathbf{r})R^m_{\mathcal{L}'}(\mathbf{r};\varepsilon), \tag{3-61}$$

describing the scattering at the potential of site k. The essence of multiple scattering theory is therefore described by successively iterating the Dyson equation as shown in Eq. (3-45), which describes free waves being scattered at different potentials corresponding to different sites. It turns out that the structural Green functions decay slowly as function of distance, which enlarges the size of the matrices used in solving Eq. 3-60. One then introduces a new reference system with repulsive potentials, which enable an exponential decay of the Green function and permit a faster sparse and smaller matrix inversion [160, 161].

3.5.6. Energy integration

To minimize computational expenses in the Green function KKR method, energy integrations like the one in Eq. (3-36) are carried out by splitting the integration interval into two halves:

$$\int_{-\infty}^{\varepsilon_F} \mathrm{d}\varepsilon = \sum_{\text{core states}} + \int_{\varepsilon_B}^{\varepsilon_F} \mathrm{d}\varepsilon. \tag{3-62}$$

Finding an energy ε_B that is higher than the energies of the core states but lower than the energies of the valence states is necessary to accomplish this. We also utilize the Green function's analytic continuity properties. Consequently, rather than following the real axis, we carry out the integration using an energy contour integration in the complex plane [162]. This increases the calculation's accuracy because the Green function is smoother when it is

away from the real axis. In addition to that, this method is computationally cheap since it requires a small number of complex energy points.

3.5.7. Spin-orbit coupling in KKR

The coupling between the spin and orbital angular momenta of the electrons, as discussed in section 2.3.2, is a very significant relativist effect in magnetism and can be described by the following spin-orbit Hamiltonian:

$$\mathcal{H}_{SOC} = \mathcal{V}_{SOC} = \underbrace{\frac{1}{M(r)^2c^2}\frac{1}{r}\frac{\partial \mathcal{V}(r)}{\partial r}}_{\chi(r)} \mathcal{L}\cdot\mathbf{S}\,, \tag{3-63}$$

where c represents the speed of light in a vacuum, and $M(r)$ stands for the relativistic mass, defined as $M(r) = \frac{1}{2} + \frac{\varepsilon - \mathcal{V}(r)}{2c^2}$. Here, $\mathcal{V}(r)$ denotes the Kohn-Sham potential, specifically chosen as the average of the spin-up and spin-down potentials, $\mathcal{V}(r) = \frac{\mathcal{V}^{\uparrow}+\mathcal{V}^{\downarrow}}{2}$. Given its dependence on the potential's derivative, it is anticipated to be more pronounced as electrons approach the nuclei. Additionally, since the spin-orbit coupling operator is proportional to the nuclear charge, it becomes more prominent for heavy elements. We treat the SOC as an addition to the Hamiltonian. Consequently, the complete potential entering the Schrödinger equation can be broken down into components as follows

$$\mathcal{V}^{\text{tot}} = \begin{pmatrix} \mathcal{V}^{\uparrow\uparrow} & 0 \\ 0 & \mathcal{V}^{\downarrow\downarrow} \end{pmatrix} + \begin{pmatrix} \mathcal{V}^{\uparrow\uparrow}_{\text{SOC}} & \mathcal{V}^{\uparrow\downarrow}_{\text{SOC}} \\ \mathcal{V}^{\downarrow\uparrow}_{\text{SOC}} & \mathcal{V}^{\downarrow\downarrow}_{\text{SOC}} \end{pmatrix}. \tag{3-64}$$

Calculating the SOC potential requires determining the prefactor $\chi(r)$ in Eq. (3-63), which incorporates a potential derivative. To enhance the accuracy of the derivative calculation, we can separate the potential into components: one stemming from the nucleus charge Z, characterized by an analytical form of $-2Z/r$, and the other originating from the electronic contribution:

$$\frac{\partial \mathcal{V}(r)}{\partial r} = \frac{2Z}{r^2} + \frac{\partial \mathcal{V}_e(r)}{\partial r}\,. \tag{3-65}$$

The numerical differentiation is applied to the electrons' contribution to the potential, which encompasses the exchange-correlation and Hartree terms.

Since, the single-site solutions are expanded in real spherical harmonics the same basis is used for $\mathcal{L}\cdot\mathbf{S}$. One way to express the SOC potential is as follows:

$$\mathcal{V}^{2\times2}_{\text{SOC}} = -\frac{1}{M(r)^2c^2}\left(\frac{1}{r}\frac{\mathrm{d}\mathcal{V}(r)}{\mathrm{d}r}\right)\begin{pmatrix} \mathcal{L}^z & \mathcal{L}^- \\ \mathcal{L}^+ & -\mathcal{L}^z \end{pmatrix}, \tag{3-66}$$

where $\mathcal{L}^{\pm}$ are the ladder operators defined as $\mathcal{L}^{\pm} = \mathcal{L}^{x} \pm i\mathcal{L}^{y}$. Their decomposition in terms of complex spherical harmonics $\mathcal{Y}_{lm}$ is straightforward, as we already understand the action of these operators on them:

$$\mathcal{L}^{z}\,|\mathcal{Y}_{lm}\rangle = m\,|\mathcal{Y}_{lm}\rangle \quad , \quad \mathcal{L}^{\pm}\,|\mathcal{Y}_{lm}\rangle = \sqrt{l(l+1) - m(m\pm 1)}\,|\mathcal{Y}_{lm}\rangle\,. \tag{3-67}$$

Finally, the matrix elements can be re-expressed in the usual basis using the transformation from complex to real spherical harmonics. Then, the Dyson and Lippmann-Schwinger equations can be solved to obtain the total Green function once we have the SOC potential. Further details can be found in Refs. [159, 136].

3.5.8. KKR self-consistent cycle

In order to wrap up this overview of the Green function KKR method, we outline the procedural steps for its practical implementation [163]:

1. First, we identify the Voronoi cells that surround the atoms. The vacuum regions that come into contact with the material are also divided into Voronoi cells for surface calculations, just like atomic layers would be.

2. An initial potential $\mathcal{V}^{\text{in}}$ is selected. We usually use a potential that has previously been calculated for isolated atoms in bulk calculations. The converged potential of a corresponding bulk material could be initially used for subsequent simulations of a thin film.

3. Using Eq. (3-51) and Eq. (3-61), solve the single-site problem for each cell to get $R_{\mathcal{L}}$ and $t_{\mathcal{L}}$.

4. Establish the reference system $g_{\mathcal{L}\mathcal{L}'}$ through Eq. (3-58).

5. Solve the Dyson equation in Eq. (3-60) and integrate over the k-space to obtain the real-space Green function, thereby acquiring the on-site elements $\mathcal{G}_i^{\text{on-site}}(E)$ necessary for charge density computation.

6. Calculate the charge density by integrating along the energy contour.

7. Determine the new potential $\mathcal{V}^{\text{out}}$ by solving Poisson's equation and compute the exchange-correlation potential $\mathcal{V}_{xc}$.

8. Check convergence by comparing $\mathcal{V}^{\text{out}}$ and $\mathcal{V}^{\text{in}}$. If they differ beyond a set tolerance, mix $\mathcal{V}^{\text{out}}$ with $\mathcal{V}^{\text{in}}$ and use the result as new $\mathcal{V}^{\text{in}}$ to start again from step 3.

3.6. Mapping procedure from ab initio of interaction parameters of an extended Heisenberg Hamiltonian

Introduced in Sec. 2.4, the generalized Heisenberg Hamiltonian offers an apparent simplified tool to describe magnetism for materials possessing localized magnetic moments.

Throughout the remainder of this section, our goal is to introduce the method used to extract both the Heisenberg exchange interaction and the Dzyaloshinskii-Moriya interaction (DMI) using the Green function KKR method. Additionally, we will address the calculation of the magnetocrystalline anisotropy energy (MAE). The Zeeman energy, which connects the spin moments to an external magnetic field, is the simplest term, which requires to determining the net magnetic moment m_i at each atomic site.

3.6.1. Infinitesimal rotations method for calculating magnetic interactions

We use the infinitesimal rotation method to derive magnetic interactions from first-principles computations and use them to parametrize the extended Heisenberg Hamiltonian. The change in DFT total energy with respect to a spin-dependent perturbative potential, which corresponds to a rotation of the magnetic moment, can be used to determine the magnetic interactions. Since the KKR Green function technique offers direct access to the Green function, it is especially well-suited for this use. A formalism for computing J_{ij} was first presented by Liechtenstein et al.[107]. Udvardi et al.[108] later improved this formalism to take into account new contributions to the extended Heisenberg model. The method enables the extraction of the distance-dependent magnetic interactions starting from one single converged collinear magnetic state.

The method is based on the Andersen's magnetic force theorem [164, 165], which offers an approximation of the change of the total energy upon rotation of the magnetic moments that simplifies into the alteration of the the one-particle energies (band energies):

$$\delta\varepsilon = \int_{-\infty}^{\varepsilon_\mathrm{F}} (\varepsilon - \varepsilon_\mathrm{F})\, \delta\rho(\varepsilon)\mathrm{d}\varepsilon = -\int_{-\infty}^{\varepsilon_\mathrm{F}} \delta\mathcal{N}(\varepsilon)\mathrm{d}\varepsilon, \tag{3-68}$$

where $\mathcal{N}(\varepsilon)$ is the number of electronic states (integrated density of states) with energy smaller than or equal to ε, and $\rho(\varepsilon) = \frac{\mathrm{d}\mathcal{N}}{\mathrm{d}\varepsilon}$ is the density of states, while $\delta\rho(\varepsilon)$, $\delta\mathcal{N}(\varepsilon)$ stand for, respectively, the change in $\rho(\varepsilon)$, $\mathcal{N}(\varepsilon)$ due to the rotation of magnetic moments from the reference collinear magnetic state.

Next, Lloyd's formula [166] is used to associate the single-particle energy (ε_{sp}) variation upon

the rotation of the magnetic moments with the system's T-matrix as:

$$\varepsilon_{sp} = -\frac{1}{\pi}\int_{-\infty}^{\varepsilon_{\mathrm{F}}} \mathrm{Im}\,\mathrm{Tr}\ln\mathbf{T}(\varepsilon)\mathrm{d}\varepsilon, \tag{3-69}$$

where the inverse of $\mathbf{T}$ is provided by

$$\left(\delta\mathbf{T}^{-1}\right)^{ij}_{\mathcal{L}\sigma,\mathcal{L}'\sigma'} = \left(\delta\mathbf{t}^{-1}\right)^{i}_{\mathcal{L}\sigma\sigma'}\delta_{ij}\delta_{\mathcal{L}\mathcal{L}'} - \mathcal{G}^{ij}_{\mathcal{L}\mathcal{L}'}\delta_{\sigma\sigma'}, \tag{3-70}$$

which shows the connection to the Green function $\mathcal{G}$ and single-site t-matrix.

Upon an infinitesimal rotation of two magnetic moments at sites i and j simultaneously, the change in energy with respect to an infinitesimal change in the t-matrix can be written as:

$$\delta\varepsilon_{ij} = -\frac{1}{\pi}\int \mathrm{Im}\,\mathrm{Tr}[\delta\mathbf{t}_i\mathcal{G}_{ij}\delta\mathbf{t}_j\mathcal{G}_{ji}]\mathrm{d}\varepsilon, \quad i \neq j\,, \tag{3-71}$$

where

$$\delta\mathbf{t}_i = (\delta\mathbf{t}_i^x, \delta\mathbf{t}_i^y, \delta\mathbf{t}_i^z)\cdot\delta\boldsymbol{n}_i \tag{3-72}$$

with $\mathbf{t}_i^\alpha(\varepsilon)$ is the derivative of $\mathbf{t}_i(\varepsilon)$ with respect to $\boldsymbol{n}_i^\alpha$ ($\mathbf{t}_i^\alpha(\varepsilon) = \frac{\partial\mathbf{t}_i(\varepsilon)}{\partial\boldsymbol{n}_i^\alpha}$) and $\alpha = (x, y, z)$.

Inserting Eq. (3-72) into Eq. (3-71) leads to the form

$$\begin{aligned}\delta\varepsilon_{ij} &= -(\delta\boldsymbol{n}_i^x, \delta\boldsymbol{n}_i^y, \delta\boldsymbol{n}_i^z)\begin{pmatrix} \mathcal{J}_{ij}^{xx} & \mathcal{J}_{ij}^{xy} & \mathcal{J}_{ij}^{xz} \\ \mathcal{J}_{ij}^{yx} & \mathcal{J}_{ij}^{yy} & \mathcal{J}_{ij}^{yz} \\ \mathcal{J}_{ij}^{zx} & \mathcal{J}_{ij}^{zy} & \mathcal{J}_{ij}^{zz} \end{pmatrix}\begin{pmatrix} \delta\boldsymbol{n}_j^x \\ \delta\boldsymbol{n}_j^y \\ \delta\boldsymbol{n}_j^z \end{pmatrix} \\ &= -\delta\boldsymbol{n}_i^T\cdot\mathcal{J}_{ij}\cdot\delta\boldsymbol{n}_j\,,\end{aligned} \tag{3-73}$$

where $\boldsymbol{n}_i$ is the column unit vector and the 3×3 matrix $\mathcal{J}_{ij}$ is defined as:

$$(\mathcal{J}_{ij})^{\alpha\beta} = \frac{1}{\pi}\,\mathrm{Im}\int \mathrm{Tr}\,\delta\mathbf{t}_i^\alpha\mathcal{G}_{ij}\delta\mathbf{t}_j^\beta\mathcal{G}_{ji}\mathrm{d}\varepsilon\,. \tag{3-74}$$

What we have done is to identify the tensor of magnetic exchange interactions of an extended Heisenberg model that can be evaluated from first-principles [131]:

$$\mathcal{H} = -\sum_{<ij>}\boldsymbol{n}_i^{\mathrm{T}}\mathcal{J}_{ij}\boldsymbol{n}_j\,. \tag{3-75}$$

The tensor of magnetic interactions can be decomposed into three parts,

$$\mathcal{J}_{ij} = \mathcal{J}_{ij}^{tr} + \mathcal{J}_{ij}^{\mathrm{S}} + \mathcal{J}_{ij}^{\mathrm{A}} \,. \tag{3-76}$$

The first part, is the isotropic part corresponding to the conventional Heisenberg exchange interaction, given by:

$$\mathcal{J}_{ij}^{tr} = J_{ij}\mathcal{I}, \tag{3-77}$$

where $\mathcal{I}$ is the identity matrix, and the isotropic exchange interaction describing the average diagonal value,

$$\mathrm{J}_{ij} = \frac{1}{3}\,\mathrm{Tr}\,\mathcal{J}_{ij} \,. \tag{3-78}$$

The third part of Eq. (3-76) represents the anisotropic antisymmetric exchange contribution corresponding to the DMI. It can be expressed as:

$$\mathcal{J}_{ij}^{\mathrm{A}} = \left(\mathcal{J}_{ij} - \mathcal{J}_{ij}^{\mathrm{T}}\right) = \begin{pmatrix} 0 & D_{ij}^{z} & -D_{ij}^{y} \\ -D_{ij}^{z} & 0 & D_{ij}^{x} \\ D_{ij}^{y} & -D_{ij}^{x} & 0 \end{pmatrix}, \tag{3-79}$$

where the three components of a Cartesian vector $\mathbf{D}_{ij} = (D_{ij}^{x}, D_{ij}^{y}, D_{ij}^{z})$ are given by:

$$D_{ij}^{x} = \frac{1}{2}\left(\mathcal{J}_{ij}^{yz} - \mathcal{J}_{ij}^{zy}\right) \quad , \quad D_{ij}^{y} = \frac{1}{2}\left(\mathcal{J}_{ij}^{xz} - \mathcal{J}_{ij}^{zx}\right) \quad , \quad D_{ij}^{z} = \frac{1}{2}\left(\mathcal{J}_{ij}^{xy} - \mathcal{J}_{ij}^{yx}\right) . \tag{3-80}$$

The antisymmetric part of Eq. (3-76) can then be reformulated into a vector product by:

$$\mathcal{H}_{\mathrm{DMI}} = -\sum_{<ij>} \mathbf{D}_{ij} \cdot (\boldsymbol{n}_i \times \boldsymbol{n}_j) \,. \tag{3-81}$$

Finally, the second term in Eq. (3-76) is given by the remaining symmetric traceless contributions,

$$\mathcal{J}_{ij}^{\mathrm{S}} = \left(\mathcal{J}_{ij} + \mathcal{J}_{ij}^{\mathrm{T}}\right) - J_{ij}\mathcal{I}, \tag{3-82}$$

where $\mathcal{J}_{ij}^{\mathrm{T}}$ is the transpose of $\mathcal{J}_{ij}$. The latter turns out to be small in the materials investigated in this thesis and therefore, we do not consider its effect in the present work. Essentially, in order to obtain every element of the interaction matrix, the computation must be done with the magnetization aligned along three orthogonal directions, such as x, y,

and z.

3.6.2. Extraction of the magnetocrystalline anisotropy energy

A general formulation of the magnetic anisotropy in second order is given by:

$$\mathcal{H}_{\mathrm{Ani}} = -\boldsymbol{n}_i^{\mathrm{T}} \mathcal{K}_i \boldsymbol{n}_i \qquad \text{with} \qquad \mathcal{K} = \begin{pmatrix} \mathrm{K}_{xx} & \mathrm{K}_{xy} & \mathrm{K}_{xz} \\ \mathrm{K}_{xy} & \mathrm{K}_{yy} & \mathrm{K}_{yz} \\ \mathrm{K}_{xz} & \mathrm{K}_{yz} & \mathrm{K}_{zz} \end{pmatrix} \quad , \tag{3-83}$$

where $\mathcal{K}$ is a symmetric traceless matrix.

To extract the tensor elements defining MAE one needs to compute the energy of the material for different magnetization-rotated directions and proceed to energy differences.

In general, taking the energy difference between the cases where the magnetization points along the x and z axis gives:

$$\varepsilon^x - \varepsilon^z = \mathrm{K}_{zz} - \mathrm{K}_{xx}, \tag{3-84}$$

while considering the magnetization along the x and y axis leads to:

$$\varepsilon^x - \varepsilon^y = \mathrm{K}_{yy} - \mathrm{K}_{xx}. \tag{3-85}$$

If there is no anisotropy in the xy-plane, the magnetic anisotropy energy matrix takes a simple diagonal form with only one free parameter, K_{zz}. Depending on the sign of K_{zz} the anisotropy is called easy-axis ($\mathrm{K}_{zz} > 0$) or easy-plane ($\mathrm{K}_{zz} < 0$) anisotropy. In this case, the MAE adopts the form,

$$\mathcal{H}_{\mathrm{Ani}} = \mathrm{K}_{zz} \cos^2(\vartheta) \quad , \tag{3-86}$$

where one notices that there is no need to specify K_{xx} and K_{yy}.

When employing this approach to calculate the MAE, it is crucial to consider that these energy differences are significantly smaller than the total energy, posing a numerical challenge. Instead of proceeding to self-consistency in the first-principles simulations, another approach consists in utilizing the magnetic force theorem, as illustrated in [167]. This theorem justifies substituting the difference in self-consistent total energies with the difference in band energies $\varepsilon_{\mathrm{band}}$ by proceeding to a single iteration after rotating the moments from an initially converged calculation along a given direction of the magnetization.

3.7. Atomistic Spin dynamics

DFT inherently operates within a static framework, as exemplified by the Kohn-Sham equations (Eq. (3-8)), where time dependence is conspicuously absent. While Time-Dependent DFT (TD-DFT) exists to address dynamic effects, such as atomistic magnetic precession, its computations are intricate and resource-intensive, constrained to short time scales (typically within femtoseconds [168, 169]). In response to these challenges, ASD are introduced as a more affordable approach compared to the computationally expensive real-time solutions of TD-DFT equations. One main method of ASD is the simulation of dynamical spin trajectories, by solving the Landau-Lifshitz-Gilbert (LLG) equation. This section introduces ASD methods, LLG, the Geodesic Nudged Elastic Band (GNEB), and Monte Carlo (MC) methods, all implemented in the Spirit code [114, 170]. In particular, LLG is instrumental in our exploration of metastable magnetic states in materials, while GNEB and MC are used to inspect transition mechanisms and the properties of the thermal ensemble of our magnetic states, respectively. For a more comprehensive understanding of this subject, additional insights can be found in pertinent textbooks [171] and PhD theses [170, 172] within the field.

3.7.1. Landau-Lifshitz-Gilbert equation (LLG)

Upon extracting the magnetic interactions of the system from first-principles and incorporating them into the extended Heisenberg Hamiltonian (Eq. (2-13)), our next step involves investigating the magnetic states that can be stabilized by these extracted interactions. To accomplish this, we employ a spin relaxation method based on the LLG equation of motion, which describes the magnetization dynamics of a material and can be expressed as follows:

$$\frac{\mathrm{d}\boldsymbol{n}_i}{\mathrm{d}t} = -\frac{\gamma}{(1+\alpha^2)m_i}\boldsymbol{n}_i \times \mathbf{B}^i_{\text{eff}} - \frac{\gamma\alpha}{(1+\alpha^2)m_i}\boldsymbol{n}_i \times \left(\boldsymbol{n}_i \times \mathbf{B}^i_{\text{eff}}\right), \tag{3-87}$$

where α is the Gilbert damping controlling the dissipation of angular momentum and energy from the magnetic subsystem, γ is the gyromagnetic ratio, and $\mathbf{B}^i_{\text{eff}}$ is the effective field related to the energy gradient,

$$\mathbf{B}^i_{\text{eff}} = -\frac{\partial \mathcal{H}}{\partial \boldsymbol{n}_i}. \tag{3-88}$$

The first term in LLG Eq. (3-87) is called the precessional term, it accounts for the moment's precession that is directed perpendicular to the direction of the moment and the direction of the effective field, i.e. it causes the moment to precess on a circular path which means that an effective field perpendicular to the spins sets them into precession. The second term, parametrized by α, is called the damping term as it yields a vector that damps the precession of $\mathbf{n}_i$ and eventually causes it to realign with the effective magnetic field.

In order to evolve a spin system in time and drive it towards a minimum of the energy landscape, various well-established numerical solvers [173, 174, 175] implemented in the Spirit code [114, 170] can be employed. In our energy minimization simulations, we utilized the limited-memory Broyden–Fletcher–Goldfarb–Shanno (LBFGS) method, known for significantly accelerating the convergence [176]. The ASD methods consist of starting from a initial spin configuration, e.g., a random configuration, then use an energy minimization to evolve the spin in time at zero temperature until an equilibrium configuration is reached. Once identified, this equilibrium configuration's spin matrix allows us to scrutinize its properties and explore how it responds to external stimuli, such as the presence of an external magnetic field or its reaction to spin-polarized currents.

An additional significant facet of ASD involves studying the motion induced by spin currents. When subjected to a current perpendicular to plane (CPP), The dynamics of the magnetization $\mathbf{n}_i$ at the lattice site i is then governed by the extended LLG equation taking into account the spin transfer torque (STT) term [177, 178, 117, 73, 179],

$$\begin{aligned}\frac{\mathrm{d}\boldsymbol{n}_i}{\mathrm{d}t} = &-\frac{\gamma}{(1+\alpha^2)m_i}\boldsymbol{n}_i \times \mathbf{B}^i_{\text{eff}} - \frac{\gamma\alpha}{(1+\alpha^2)m_i}\boldsymbol{n}_i \times \left(\boldsymbol{n}_i \times \mathbf{B}^i_{\text{eff}}\right) \\ &- \frac{\gamma\alpha\eta}{(1+\alpha^2)}\boldsymbol{n}_i \times \boldsymbol{n}_p + \frac{\gamma\eta}{(1+\alpha^2)}\boldsymbol{n}_i \times (\boldsymbol{n}_i \times \boldsymbol{n}_p)\,,\end{aligned} \tag{3-89}$$

where $\boldsymbol{n}_p$ is the current polarisation direction with the current amplitude monitored by the parameter η which is related to the current density j_e by:

$$\eta = \frac{jPg\mu_B}{2edM_s\gamma}, \tag{3-90}$$

where P is the polarization, g the Landé factor, μ_B the Bohr magneton, e the electronic charge, d the film thickness and M_s the saturation magnetization.

Eq. (3-89) models the effect of a perpendicular to thin film spin current onto the magnetization structure [180]. With the ability to simulate these effects, the current induced motion of magnetic configurations such as skyrmions, and therefore potential racetrack memory designs, can be studied numerically.

3.7.2. Geodesic nudged elastic band method (GNEB)

To determine the energy barrier required for the annihilation of a magnetic configuration from a local minimum state to the system's ground state, the GNEB method is utilized [181, 182, 114]. This method is employed for computing minimum energy transition paths between two predefined configurations. The path is discretized into several spin configurations, referred to as images. Convergence from an initial guess (starting configuration) to a stable, energy-minimized path (ground state configuration) is achieved by applying spring forces along the

path tangents, while energy gradient forces are applied orthogonal to the path tangents. The total force is expressed as:

$$F_{\nu}^{\mathrm{tot}} = F_{\nu}^{\mathrm{s}} + F_{\nu}^{\mathrm{g}}, \tag{3-91}$$

where F^{s} represents a spring force given by:

$$F_{\nu}^{\mathrm{s}} = \left(d_{\nu-1,\nu} - d_{\nu,\nu+1}\right)\tau_{\nu}, \tag{3-92}$$

with $d_{\nu,\nu\prime}$ is a measure of distance between images ν and $\nu\prime$. F^{g} denotes a force related to the energy gradient, acting to pull each image towards the minimum energy path while keeping the distances to other images constant:

$$F_{\nu}^{\mathrm{g}} = -\nabla E_{\nu} + \left(\nabla E_{\nu} \cdot \tau_{\nu}\right)\tau_{\nu}, \tag{3-93}$$

where and ν is the image index along the chain, $\nabla_{=}\partial/\partial \boldsymbol{n}_i$, and τ_{ν} is the (normalized) path tangent at image ν. To accurately locate the highest energy point along the minimum energy path, known as the saddle point, a climbing image (CI) can be employed [181]. After identifying the saddle point, the energy barrier can be calculated by determining the energy difference between the saddle point and the initial configuration, as illustrated in Fig. **3-2**.

3.7.3. Monte Carlo (MC) simulations

In our study, we employed the Monte Carlo (MC) method to calculate the critical temperature of the magnetic systems. The MC method is well known in physics and has a broad range of applications [183]. MC requires only the calculation of the energy, making it the most straightforward method of those implemented in Spirit. While it is a useful tool to calculate equilibrium properties, the drawback is that it cannot resolve time-dependent processes. One iteration of the METROPOLIS algorithm will sequentially—but in random order—pick each spin in the system once and perform a trial step. Trial steps are performed by defining a relative basis in which the current spin is the z axis and choosing a new spin direction by uniformly distributed random variables $\phi \in [0, 2\pi]$ and $\cos\theta \in [0, \cos\theta_{\mathrm{cone}}]$, where θ_{cone} is the opening angle of the cone. The trial step is accepted with a probability

$$\mathcal{P} = e^{-\Delta E/K_B T}, \tag{3-94}$$

where ΔE is the energy difference between the previous spin configuration and the trial step. The cone angle can be set by an adaptive feedback algorithm according to a desired acceptance-rejection ratio. Using this method, one can, for example, calculate the critical

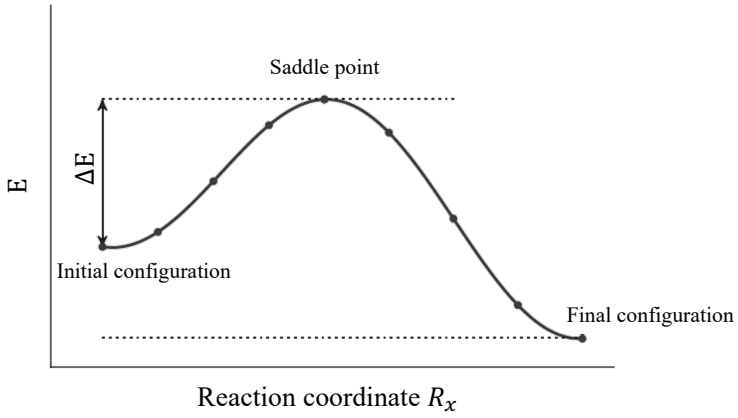

Figure **3-2**.: **Schematic energy barrier.** An energy path is shown schematically, with the energy barrier ΔE of a metastable state (initial configuration) with respect to the ground state (final configuration). The path is discretized by a set of configurations, often referred to as images. R_x is the reaction coordinate, which is simply a measure of distance along the transition.

temperature of a spin system, T_c [183], which for a ferromagnetic system is the Curie temperature of the transition from the collinear phase at low temperature to the paramagnetic phase at high temperature. For antiferromagnets, T_c is the Néel temperature at which the antiferromagnetic order is lost. In general, as with other transitions, for example between non-collinear and paramagnetic states, the low-temperature order will at some point be destroyed by fluctuations, when the temperature is increased. In order to calculate T_c, the average total magnetization $M(T) = \frac{1}{N}|\sum_i \boldsymbol{n}_i|$ is evaluated at each temperature, then by fitting the results with,

$$M(T) = \begin{cases} (1 - T/T_\mathrm{c})^b, & T < T_\mathrm{c} \\ 0 & \text{else} \end{cases} \tag{3-95}$$

T_c can be calculated once the critical exponent is defined.

4. Intrinsic AFM skyrmions in Cr films interfaced with PdFe/Ir(111)

Antiferromagnetic (AFM) skyrmions, with their topological spin structures, offer potential as localized magnetic bits in future technology. They differ from ferromagnetic (FM) skyrmions in their expected immunity to the skyrmion Hall effect, which is advantageous for applications. While they have been observed in synthetic AFM structures and as complex meronic textures in intrinsic AFM bulk materials, their realization in non-synthetic AFM films has been elusive. Here, we unveil their presence in a row-wise AFM (RW-AFM) Cr film deposited on a PdFe bilayer grown on a face-centered cubic (fcc) Ir(111) surface. Using first-principles in combination with atomistic spin dynamics (ASD), we demonstrate the emergence of single and strikingly interpenetrating chains of AFM skyrmions, which can co-exist with the rich inhomogeneous exchange field, including that of FM skyrmions, hosted by PdFe. Besides identifying an ideal platform for intrinsic AFM skyrmions, we anticipate these knotted solitons to be promising in AFM spintronics.

The results discussed in this chapter have been previously published in the following reference [184]:
"Emergence of zero-field non-synthetic single and interchained antiferromagnetic skyrmions in thin films".

4.1. Introduction

As elaborated in the introduction chapter 1, AFM skyrmions both synthetic and intrinsic have been at the heart of extensive research for their potential as promising candidates for replacing the FM skyrmions in spintronic devices [77, 11, 78, 73, 79, 80, 86, 87, 88, 83, 84], due to their ultrafast dynamics, robustness against magnetic perturbations, and insensitivity to dipolar fields, which should allow the stabilization of rather small skyrmions. On the one hand, synthetic AFM skyrmions consist of two FM skyrmions realized in two different magnetic layers, which are antiferromagnetically coupled through a non-magnetic spacer layer [117, 185, 89, 68]. On the other hand, an intrinsic AFM skyrmion is a unique magnetic entity since it is entirely located in a single layer [73, 74, 80]. Recently, and just before starting this PhD study, synthetic AFM skyrmions have been successfully engineered experimentally [68]. However, the experimental observation of intrinsic AFM skyrmions has proven challenging, especially at surfaces and interfaces, which are of significant interest for racetrack concepts and various applications.

We predict here, utilizing first-principles and atomic spin dynamics (ASD), see the section on computational details 4.2, the emergence of intrinsic AFM skyrmions in a monolayer of Cr deposited on a surface known to host FM skyrmions: A PdFe bilayer grown on Ir(111) fcc surface [27] as illustrated in Fig. **4-1** a. The AFM nature of Cr coupled antiferromagnetically to PdFe remarkably offers the right conditions for the emergence of a rich set of complex AFM textures. The ground state is collinear RW-AFM within the Cr layer (see inset of Fig. **4-2** a). The emergence of the RW-AFM magnetic spin order on a triangular lattice is an unexpected magnetic configuration. Typically, one expects that with the AFM first nearest neighbours (n.n.) interactions on a triangular lattice, magnetic frustration would lead to the formation of an AFM Néel state. However, the introduction of the next n.n. interactions becomes influential. In particular, when the second and third n.n. interactions being of AFM and FM nature, respectively, which happens to be the case for the interactions among Cr atoms as depicted in Fig. **4-3** b. The competition between those three first n.n. interactions leads to the formation of the RW-AFM spin alignment as shown in the three dimensional phase diagram depicted in Fig. **4-4**. This magnetic state was first theoretically predicted by Kurz [186] and has been so far observed experimentally only in Mn/Re(0001) [187, 188]. The difference to the latter, however, is that although being collinear, the Cr layer interfaces with a magnetic surface, the highly non-collinear PdFe bilayer.

A plethora of localized chiral AFM-skyrmionic spin textures (Fig. **4-2** a) and metastable AFM domain walls (see Fig. **A-1** of Appendix A) emerge in the Cr overlayer. Besides isolated topological AFM solitons, we identify strikingly unusual interpenetrating AFM skyrmions, which are reminiscent of crossing rings (see schematic Fig. **4-2** c), the building blocks of knot theory where topological concepts such as Brunnian links are a major concept [189]. The latter has far reaching consequences in various fields of research, not only in mathematics or physics but extends to chemistry and biology. For instance, the exciting and intriguing process of interchaining is paramount in carbon-, molecular-, protein- or DNA-based assemblies [190, 191, 192]. We discuss the mechanisms enforcing the stability of the unveiled catenated topological objects, their response to magnetic fields and the subtle dependence on the underlying magnetic textures hosted in PdFe bilayer.

4.2. Computational details

4.2.1. First-principles calculations

Our investigation is based on first-principles calculations within the framework of density functional theory (DFT). Details of the concepts and methodologies were introduced in chapter 3. These *ab initio* calculations unfolded through a two-stage process. In the initial phase, our focus was on obtaining the relaxed geometry of the various interfaces. This was accomplished by employing the Quantum Espresso computational package [125]. To describe the electronic structure, we utilized pseudopotentials sourced from the PSLibrary [153] consid-

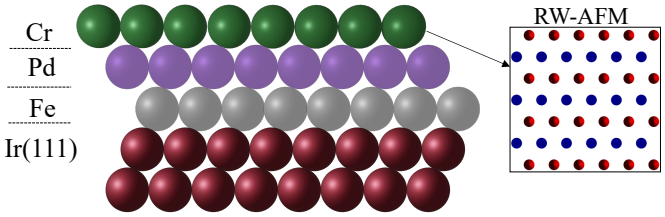

Figure **4-1**.: **Schematic representation of the investigated trilayer deposited on Ir(111) following fcc stacking, with illustration of the RW-AFM order of spins emerging at Cr layer**.

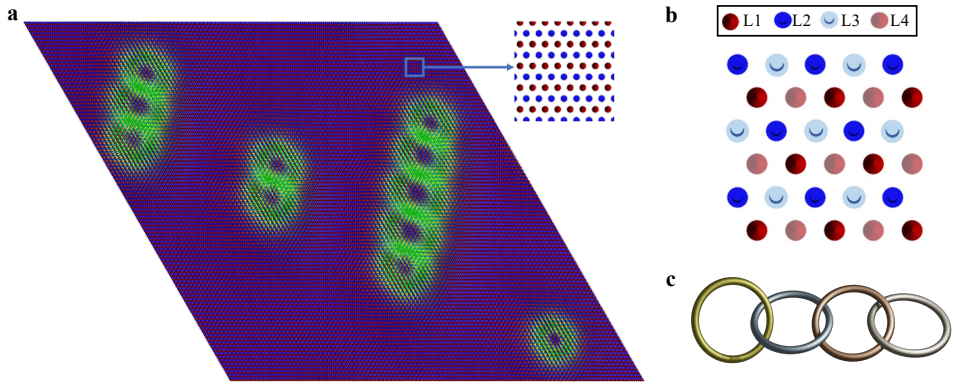

Figure **4-2**.: **Interchained AFM skyrmions in Cr layer atop PdFe bilayer on Ir(111).** **a** The ground state of Cr layer being RW-AFM (see inset) can host AFM skyrmions that can be isolated or interchained to form multimers of skyrmions. Here we show examples ranging from dimers to pentamers. The AFM skyrmions can be decomposed into FM skyrmions living in sublattices illustrated in **b**. **c** The interchaining of skyrmions is reminiscent of interpenetrating rings, which realize topologically protected phases.

ering a $28 \times 28 \times 1$ k-mesh. The kinetic energy cutoff for the wavefunction and for the charge density were set to 70 Ry and 700 Ry, respectively.

For our multi-layered system, visually depicted in Fig. **4-1**, the interlayer relaxations are presented in Table **4-1**. These layers, encompassing Cr, Pd, Fe, and Ir, were arranged in an fcc stacking configuration along the [111] direction. The interlayer relaxation with respect to the one characterizing the ideal bulk of Ir were found to be 4%, 5.8%, 8.1%, and -1%.

It is worth noting that positive and negative values signify atomic relaxations toward and away from the Ir surface, respectively.

In the subsequent stage of our investigation, we delve into the electronic structure and magnetic properties. This was achieved through simulations employing the all-electron full-potential Koringa-Kohn-Rostoker (KKR) Green function method [129, 136], which incorporates SOC self-consistently within the local spin density (LDA) approximation. The slab configuration for this stage consisted of 30 layers, comprising 3 vacuum layers, 1 Cr layer, 1 Pd layer, 1 Fe layer, 20 Ir layers, and 4 vacuum layers.

In the mathematical treatment, the momentum expansion of the Green function was truncated at $\ell_{\max} = 3$. Self-consistent calculations were executed using a k-mesh comprising 30×30 points. Furthermore, the energy contour was constructed with 23 complex energy points situated in the upper complex plane, incorporating 9 Matsubara poles. The tensor of magnetic exchange interactions were quantified using the infinitesimal rotation method [107, 131], with a 200×200 k-mesh.

Table **4-1**.: Vertical relaxations or Cr, Pd, Fe layers and the first layer of Ir towards (positive sign) or away from the (negative sign) Ir(111) surface. The values are expressed as a change with respect to the ideal bulk Ir interlayer distances.

Atom nature	Relaxation(%)
Cr	4
Pd	5.8
Fe	8.1
Ir	-1

4.2.2. Hamiltonian model and atomistic spin dynamics

To uncover the magnetic properties and the emergence of complex states at Cr layer as well as Fe layer, we employ the Landau-Lifshitz-Gilbert equation (LLG) [173] implemented in the Spirit code [114], to minimize the extended Heisenberg Hamiltonian discussed in chapter 2 section 2.4. For CrPdFe/Ir(111) magnetic layered system, the Heisenberg Hamiltonian reads:

$$\mathcal{H} = \mathcal{H}_{\text{Exc}} + \mathcal{H}_{\text{ DMI}} + \mathcal{H}_{\text{Ani}} + \mathcal{H}_{\text{Zeem}}, \tag{4-1}$$

with:

$$\mathcal{H}_{\text{Exc}} = -\sum_{<ij>} \mathrm{J}_{ij}^{\text{Cr-Cr}}\, \boldsymbol{n}_i \cdot \boldsymbol{n}_j - \sum_{<ij>} \mathrm{J}_{ij}^{\text{Fe-Cr}}\, \boldsymbol{n}_i \cdot \boldsymbol{n}_j - \sum_{<ij>} \mathrm{J}_{ij}^{\text{Fe-Fe}}\, \boldsymbol{n}_i \cdot \boldsymbol{n}_j,$$
$$\mathcal{H}_{\text{DMI}} = \sum_{<ij>} \mathbf{D}_{ij}^{\text{Cr-Cr}} \cdot [\boldsymbol{n}_i \times \boldsymbol{n}_j] + \sum_{<ij>} \mathbf{D}_{ij}^{\text{Fe-Cr}} \cdot [\boldsymbol{n}_i \times \boldsymbol{n}_j] + \sum_{<ij>} \mathbf{D}_{ij}^{\text{Fe-Fe}} \cdot [\boldsymbol{n}_i \times \boldsymbol{n}_j],$$
$$\mathcal{H}_{\text{Ani}} = -\mathrm{K}^{\text{Cr}} \sum_i (n_i^z)^2 - \mathrm{K}^{\text{Fe}} \sum_i (n_i^z)^2,$$
$$\mathcal{H}_{\text{Zeem}} = -\sum_i h_i n_i^z,$$

where i and j are site indices carrying each magnetic moments. $\boldsymbol{n}$ is a unit vector of the magnetic moment. $\mathrm{J}_{ij}^{\text{X-Y}}$ is the Heisenberg exchange coupling strength, being < 0 for AFM interaction, between an X atom on site i and a Y atom on site j. A similar notation is adopted for the Dzyaloshinskii-Moriya interaction (DMI) vector $\mathbf{D}$ and the magnetocrystalline anisotropy energy (MAE) parameter K (0.5 meV per magnetic atom). The latter favors the out-of-plane (OOP) orientation of the magnetization, and $h_i = m_i B$ describes the Zeeman coupling to the atomic spin moment m at site i assuming an OOP field.

The magnetic interactions involving Cr and Fe, which are extracted from first-principles, are shown in Fig. **4-3** for both the Heisenberg exchange interactions and DMI.

In this chapter we also inspect the phase diagram resulting from changing the magnitude of the magnetic interactions among Cr atoms (J, D and K) after multiplication with renormalization factor, and explore the magnetic state forming with the new set of magnetic interactions as explained later in this chapter in section 4.7.

Moreover, the investigations of the thermal stability of the AFM solitons were carried out utilizing the GNEB method [181] implemented in the Spirit code as well. In our analysis, we consider periodic boundary conditions, effectively modeling an extended two-dimensional system with cells containing 100^2, 200^2, 300^2, and 400^2 sites.

4.3. RW-AFM state and emergence of intrinsic AFM skyrmions

In the well-known system of PdFe/Ir(111), homo-chiral spin spiral emerges as its ground state [27, 62], arising from the intricate interplay between Heisenberg exchange interactions and the DMI. This DMI is induced by the heavy Ir substrate, characterized by a strong spin-orbit coupling (SOC). When subjected to a magnetic field, sub-10-nanometer FM skyrmions emerge [27, 62, 61, 106, 193, 194, 195]. Following the deposition of the Cr overlayer, significant modifications in the magnetic interactions governing Fe become apparent, as evidenced by the comparison depicted in Fig. **4-3**. These changes stem from alterations in the elec-

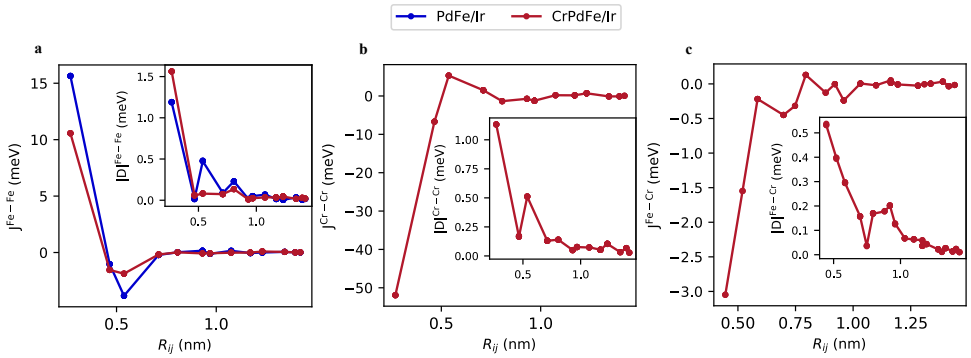

Figure **4-3**.: **Distance-dependent magnetic interactions in CrPdFe and PdFe deposited on Ir(111). a** The Heisenberg exchange interactions as function of distance among Fe atoms ($J^{Fe\text{-}Fe}$) in PdFe/Ir(111) (blue) and in CrPdFe/Ir(111) (red), with inset indicating the corresponding magnitude of DMI. **b** The Heisenberg exchange interactions between Cr atoms ($J^{Cr\text{-}Cr}$) with DMI depicted in the inset. Similarly to **b**, the interactions between Cr and Fe atoms are shown in **c**.

tronic structure, illustrated in Fig. **A-2** of Appendix A. Specifically, the Heisenberg exchange interaction among Fe n.n. undergoes a substantial reduction of 5.5 meV, corresponding to a decrease of 33%. This reduction in Heisenberg exchange interaction enhances the non-collinear magnetic behavior of Fe, enabling the spontaneous formation of FM skyrmions even in the absence of an external magnetic field, as demonstrated in Fig. **A-3** of Appendix A.

The first n.n. Cr atoms exhibit strong AFM coupling (-51.93 meV). This strong AFM coupling within the first n.n. on a triangular lattice is expected to favor the AFM Néel spin alignment due to magnetic frustration. However, the subtle interplay between magnetic interactions beyond the first n.n. becomes crucial in determining the ultimate spin alignment. In our case, the AFM interaction of the second n.n. (-6.69 meV) further reinforces the formation of the Néel state. Intriguingly, a subtle competition arises from the FM Heisenberg exchange interactions of the third n.n. (5.32 meV) on the triangular lattice. This competition stabilizes the RW-AFM state as established in a prior study [186] and illustrated in the phase diagram Fig. **4-4**.

In Fig. **4-4**, we are showing the three dimensional magnetic phase diagram of the Heisenberg model on a triangular lattice including only the Heisenberg exchange interactions up to the third n.n. Here, J_1, J_2 and J_3, denote the Heisenberg exchange interactions with the first, second, and third nearest neighbors, respectively. The values of J_2 and J_3 are normalized to the absolute value of J_1, while J_1 is being of AFM nature (< 0). If only J_1 is considered ($J_2 = J_3 = 0$), the magnetic frustration leads to the AFM Néel state, whereas negative J_2

and J_3, both favoring an AFM coupling, would trigger an AFM spin-spiraling state. However, the FM values of J_3 stabilize the RW-AFM state. Notably, when both J_2 and J_3 exceed $|J_1|$ while being positive, the FM state becomes the ground state. The interactions among the first three n.n. among Cr atoms position our system within the RW-AFM region as illustrated in the figure. Remarkably, the stability of the RW-AFM state at Cr layer remains independent of the AFM interaction with the Fe substrate.

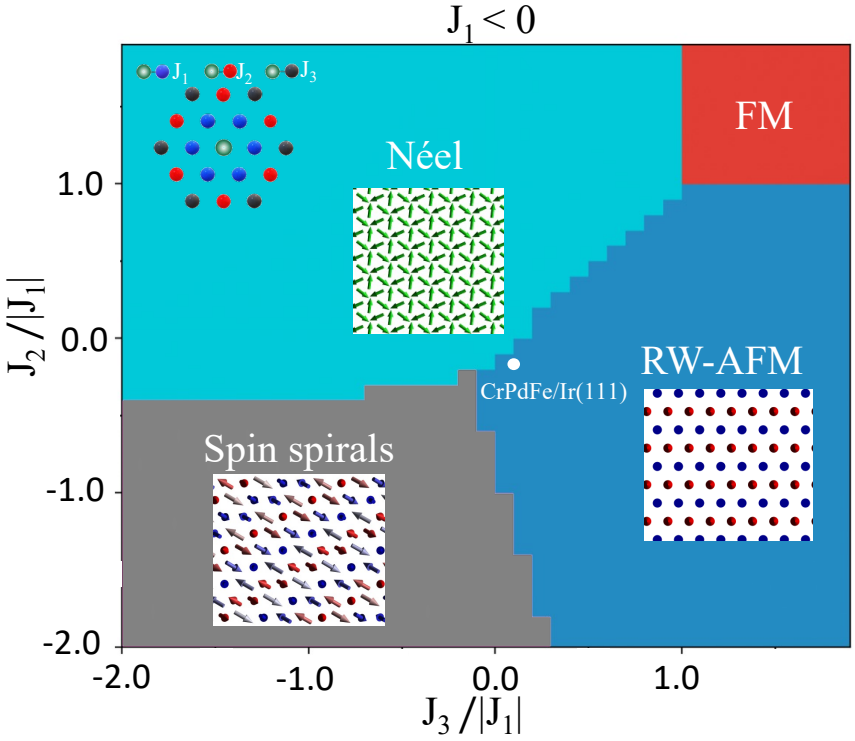

Figure **4-4**.: **Phase diagram of the Heisenberg model for a hexagonal two-dimensional lattice including magnetic interactions up to the third n.n.** The impact of magnetic interactions up to the third n.n. is considered while neglecting the DMI as illustrated in upper left inset, assuming an AFM coupling J_1 among first n.n. The circled point represents the position of our magnetic system (CrPdFe/Ir(111)).

As depicted in Fig. **4-2** a, the RW-AFM configuration is characterized by parallel magnetic moments along a close-packed atomic row, with antiparallel alignment between adjacent

rows. The hexagonal symmetry of the atomic lattice allows for the rotation of the AFM rows in three symmetrically equivalent directions. Importantly, the magnetic moments point OOP due to the presence of an MAE reaching 0.5 meV per magnetic atom.

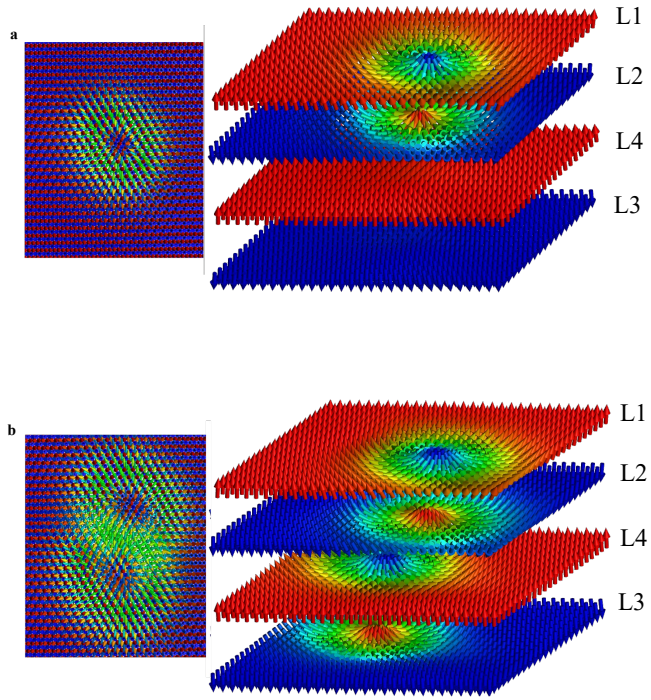

Figure **4-5**.: **Single and double AFM skyrmions.** In case of the single AFM skyrmion, two of the sublattices, L1 and L2, are occupied by the FM skyrmions shown in **a**. L3 and L4 host quasi-collinear AFM spins in contrast to the FM skyrmions emerging in the case of the double AFM skyrmion presented in **b**. Note that the separation of sublattices L1, L2, L3 and L4 shown in **a** and **b** is only done for illustration.

The DM interactions among Cr atoms arise due to the broken inversion symmetry and is mainly induced by the underlying Pd atoms hosting a large SOC. The n.n. Cr DMI (1.13 meV) is of the same chiral nature and order of magnitude as that of Fe atoms (1.56 meV), which gives rise to the chiral non-collinear behavior illustrated in Fig. **4-2** a. We note that the solitons are only observed if Cr magnetic interactions beyond the n.n. are incorporated, which signals the significance of the long-range coupling in stabilizing the observed textures. Since the Heisenberg exchange interaction among the Cr atoms is much larger than that of

Fe, the AFM solitons are bigger, about a factor of three larger than the FM skyrmions found in Fe.

While the RW-AFM state is defined by two sublattices, the different AFM skyrmions, isolated or interchained, can be decomposed into interpenetrating FM skyrmions living in 4 sublattices (L1, L2, L3 and L4) as illustrated in Fig. **4-2** b and Fig. **4-5**. In the RW-AFM phase, L1 and L4 are equivalent and likewise for L2 and L3. It is evident that the moments in L1 and L4 are antiparallel to the ones in L2 and L3. Taking a closer look at the isolated AFM magnetic texture, one can dismantle it into two FM skyrmions with opposite topological charges anchored in the distinct antiparallel FM sublattices L1 and L2, while L3 and L4 carry rather collinear magnetization (Fig. **4-5** a). In the case of the overlapped AFM skyrmions, however, no sublattice remains in the collinear state. As an example, the dimer consists of two couples of antiferromagnetically aligned skyrmions, each being embedded in one of the four sublattices (Fig. **4-5** b). One can clearly demonstrate that within a given sublattice, say L1, the magnetic interaction among the n.n. is mediated via J_3, which is of FM nature and the associated DMI $\mathbf{D}_3$. Both together with the OOP MAE are responsible for the emergence of FM skyrmions in each sublattice. Then J_1 and J_2 taking care of the inter-sublattice AFM coupling enforce the AFM alignment of the sublattice skyrmions.

Our investigation uncovers a notable disparity between the behavior of single AFM skyrmions and their interchained counterparts in response to the magnetic environment originating from the underlying PdFe bilayer. In the subsequent sections, we delve into a more detailed analysis of the stability mechanisms governing single and overlapping AFM skyrmions.

4.4. Elucidating the stabilization mechanisms of interchained AFM skyrmions

The occurrence of overlapped solitons is an unusual phenomenon as conventional FM skyrmions tend to repel each other. This phenomenon arises from the intricate interplay of competing interactions among skyrmions residing in different sublattices, which is rooted in the inherent AFM coupling between n.n. magnetic moments. Depending on the hosting sublattice (L1 to L4), the four skyrmions shown in Fig. **4-5** b experience attraction or repulsion. The sublattices are arranged such that n.n. within a sublattice correspond to third n.n. in the overall system. This arrangement results in the Heisenberg exchange coupling favoring the parallel alignment of spins within a given sublattice.

When looking at any sublattice in isolation, this effective FM-like exchange interaction enables the existence of skyrmions in a collinear background. In the overall system, however, pairs of sublattices interact via the first and second n.n. exchange interactions, which prefers anti-parallel spin alignments. Therefore, the exchange interaction between skyrmions formed at sublattices with a parallel background, such as (L1, L4) and (L2, L3), and denoted in

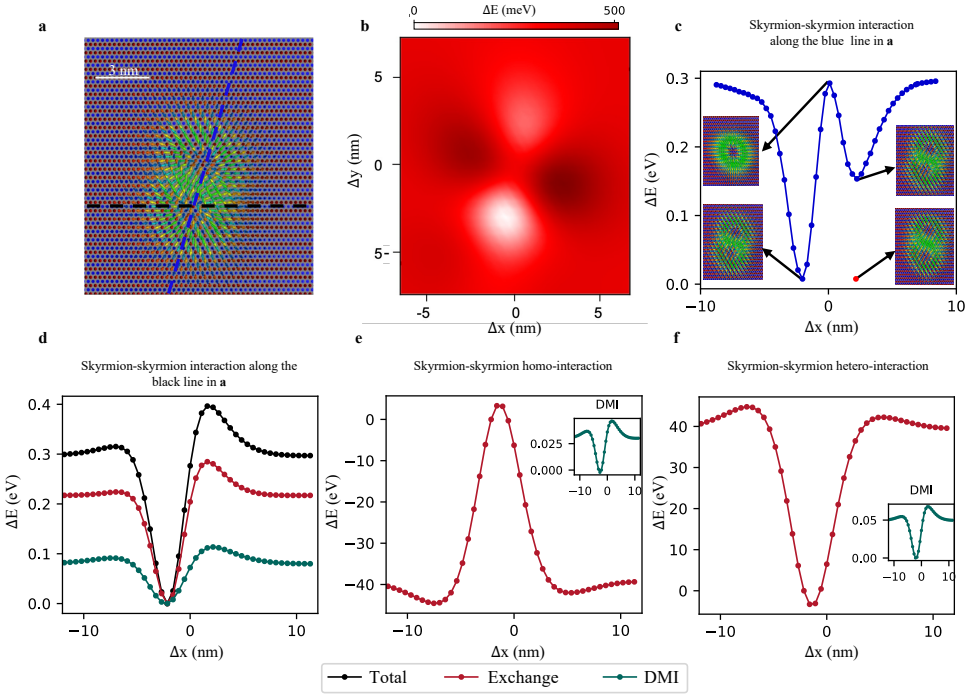

Figure **4-6**.: **Energetics of two interchained AFM skyrmions. a** Two overlapping AFM skyrmions decoupled from the PdFe bilayer with black and blue line representing two examples of paths along which the lower skyrmion is rigid-shifted with respect to the upper one, which is pinned. **b** Two-dimensional map of the total energy difference with respect to the magnetic state shown in **a** as a function of the distance between the skyrmion centers. **c** Energy profile along the blue line shown in **a**. A double minimum is found once the skyrmions swap their positions and become truly degenerate once the rigidity of the spin state is removed (see the red circle). **d** The Heisenberg exchange is the most prominent contribution to the skyrmion stabilization, as shown along the path hosting a single minimum. The total skyrmion-skyrmion repulsive homo-interaction is dominated by the attractive hetero-interaction, red curves in **e** and **f**, respectively. The DMI contribution, shown in insets, is smaller and sublattice independent. It favors the overlap of AFM skyrmions.

the following as skyrmion-skyrmion homo-interactions, are repulsive as usually experienced by FM skyrmions. In contrast, and for the same reasons, interaction between skyrmions in sublattices with oppositely oriented background spins, denoted as hetero-interactions, are attractive as it is for (L1, L2), (L2, L4), (L3, L4) and (L1, L3). Detailed illustration of the

interactions among sublattices spins is depicted in Fig. **A-4** of Appendix A. Clearly, the set of possible hetero-interactions, enforced by the attractive nature induced by the DMI, outnumbers the homo ones. The interchained AFM skyrmion is simply the superposition of the sublattice skyrmions at the equilibrium distance, here 2.58 nm between the two AFM skyrmions, where both interactions (attraction and repulsion) are equal.

To substantiate the proposed mechanism, we quantify the skyrmion-skyrmion interaction. We simplify the analysis by neglecting the Cr-Fe magnetic interactions, which puts aside the impact of the rich non-collinear magnetic behavior hosted by the PdFe bilayer. In this case, only the overlapping AFM skyrmions are observed, and single AFM skyrmions disappear. We note that be reducing the MAE from 0.5 to 0.4 meV for the Cr atoms helps maintaining the single AFM skyrmion even when switching-off the Cr-Fe interaction. We take the skyrmion dimer illustrated in Fig. **4-6** a, and proceed to a rigid shift of the lower AFM skyrmion while pinning the upper one at the equilibrium position. We extract the skyrmion-skyrmion interaction map as a function of distance, as shown in Fig. **4-6** b, which clearly demonstrates that as soon as the AFM skyrmions are pulled away from each other, the energy of the system increases. Note that within this procedure, the sublattice interactions (L1, L2) and (L3, L4) do not contribute to the plots since they are assigned to each of the AFM skyrmions moved apart from each other. Two minima are identified along a single direction as favored by the symmetry reduction due to the AFM arrangement of the magnetic moments in which the skyrmions are created. Indeed, one notices in Fig. **4-2** b that due to the sublattice decomposition symmetry operations are reduced to C_2, i.e. rotation by 180°, while mirror symmetries, for example, originally present in the fcc(111) lattice are broken.

Fig. **4-6** c-d depict the skyrmion-skyrmion interaction, which hosts either one or two minima, as a function of distance along two directions indicated by the dashed lines, blue and black, in Fig. **4-6** a. The two minima found along the blue line should be degenerate and correspond to the swapping of the two AFM skyrmions. The breaking of degeneracy is an artifact of the rigid shift assumed in the simulations, which can be corrected by allowing the moments to relax (see red circle in Fig. **4-6** c). The maximum of repulsion is realized when the two AFM skyrmions perfectly overlap (see inset). The interaction profile shown in Fig. **4-6** d is decomposed into two contributions: the skyrmion-skyrmion homo- and hetero-interactions, which we plot in Fig. **4-6** e and f, respectively. The data clearly reveals the strong repulsive nature of the homo-interaction mediated by the Heisenberg exchange, which competes with the attractive hetero-interaction driven by both the Heisenberg exchange coupling and DMI. The latter skyrmion-skyrmion interaction is strong enough to impose the unusual compromise of having strongly overlapping solitons.

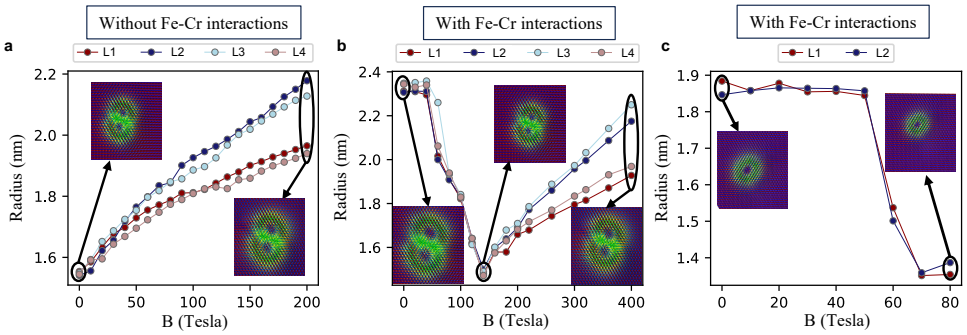

Figure **4-7**.: **Impact of magnetic field on the AFM skyrmion radius.** Radius of the sublattice FM skyrmions for two-interchained AFM skyrmions **a** decoupled from and **b** coupled to the Fe magnetization. **c** A single case is shown for the isolated AFM skyrmion since it disappears without the inhomogeneous magnetic field emerging from the substrate. Examples of snapshots of the AFM skyrmions are illustrated as insets of the different figures. In Fe, the amount of FM skyrmions and antiskyrmions increases once applying a magnetic field, which erases the ground state spin-spiral. The coupling to the Fe magnetization affects the evolution of the AFM skyrmions as function of the magnetic field dramatically.

4.5. Impact of magnetic field

Before delving into an in-depth exploration of stability aspects concerning single AFM skyrmions, we apply a magnetic field perpendicular to the substrate and disclose pivotal ingredients for the formation of the isolated solitons. In general, the reaction of FM and AFM skyrmions to an external magnetic field is expected to be deeply different. When applied along the direction of the background magnetization, FM skyrmions reduce in size while recent predictions expect a size expansion of AFM skyrmions [86, 87, 77], thereby enhancing their stability.

To inspect the response of AFM skyrmions to a magnetic field perpendicular to the substrate, we first remove, as done in the previous section, the Cr-Fe interactions since they give rise to a non-homogeneous and strong effective exchange field. In this particular case, we explored the case of AFM skyrmion dimers. As illustrated in Fig. **4-7** a, the size of each of the sublattice skyrmions, which together form the AFM skyrmion dimer, increases with an increasing magnetic field. The type of the hosting sublattice, with the magnetization being parallel or antiparallel to the applied field, seems important in shaping the skyrmions dimension.

Strikingly, and in strong contrast to what is known for FM skyrmions, the AFM skyrmions, single and multimers, were found to be stable up to extremely large magnetic fields. Al-

though the assumed fields are unrealistic in the lab, they can be emulated by the exchange field induced by the underlying magnetic substrate. Indeed, the magnetic interaction between Cr and its nearest neighboring Fe atoms, carrying each a spin moment of 2.51 μ_B, reaches -3.05 meV, which translates to an effective field of about 21 Tesla. At this value, the average skyrmion radius is about 1.6 nm, which is 30% smaller than the one found once the Cr-Fe magnetic coupling is enabled (see Fig. **4-7** b). We note that since the skyrmions are not circular in shape, their radius is defined as the average distance between the skyrmions center and the position where the spin moments lie in-plane. The significant size difference is induced by the strong inhomogenous exchange field emanating from the Fe sub-layer, which can host spirals, skyrmions and antiskyrmions.

If the Cr-Fe interactions are included, the size dependence changes completely. Instead of the rather monotonic increase with the field, the size of the skyrmion is barely affected until reaching about 50 Tesla, which is accompanied by substantial miniaturization of the AFM skyrmions. Here, a phase transition occurs in Fe, which initially hosts spin spirals that turn into FM skyrmions (see Fig. **A-5** of Appendix A). After being squeezed down to an average radius of 1.48 nm at 140 Tesla, the size expansion observed without the Cr-Fe interactions is recovered because the substrate magnetization is fully homogeneous and parallel to the Zeeman field. Likewise, single AFM skyrmions, found only once the coupling to the substrate is enabled, react in a similar fashion to the field as depicted in Fig. **4-7** c. The substantial difference, however, is that fields larger than 80 Tesla destroy the AFM skyrmions due to the annihilation of the Fe FM skyrmions. This highlights an enhanced sensitivity to the underlying magnetic environment and clearly demonstrates the robustness enabled by skyrmion interchaining.

4.6. Stabilization mechanism for single AFM skyrmions

We learned that single AFM skyrmions can be deleted after application of an external magnetic field or by switching off the exchange coupling to the magnetic substrate. Both effects find their origin in the magnetization behavior of the PdFe bilayer. To explore the underlying correlation, we consider as an example the magnetic configuration obtained with a field of 70 Tesla and delete one after the other the skyrmions and antiskyrmions found in Fe, then check whether the AFM skyrmion in Cr survives (see example in Fig. **4-8**). We notice that the AFM skyrmion disappears by deleting the FM solitons located directly underneath or even a bit away. Fig. **A-6** of Appendix shows that when shifted across the lattice, the AFM skyrmion disappears if fixed above a magnetically collinear Fe area.

We proceed in Fig. **4-9** to an analysis of the Fe-Cr interaction pertaining to the lower-right snapshot presented in Fig. **4-8** c by separating the Heisenberg exchange contribution from that of DMI and plotting the corresponding heat maps of the site-dependent of these two contributions for each sublattice. Here, we consider as reference energy that of the RW-AFM

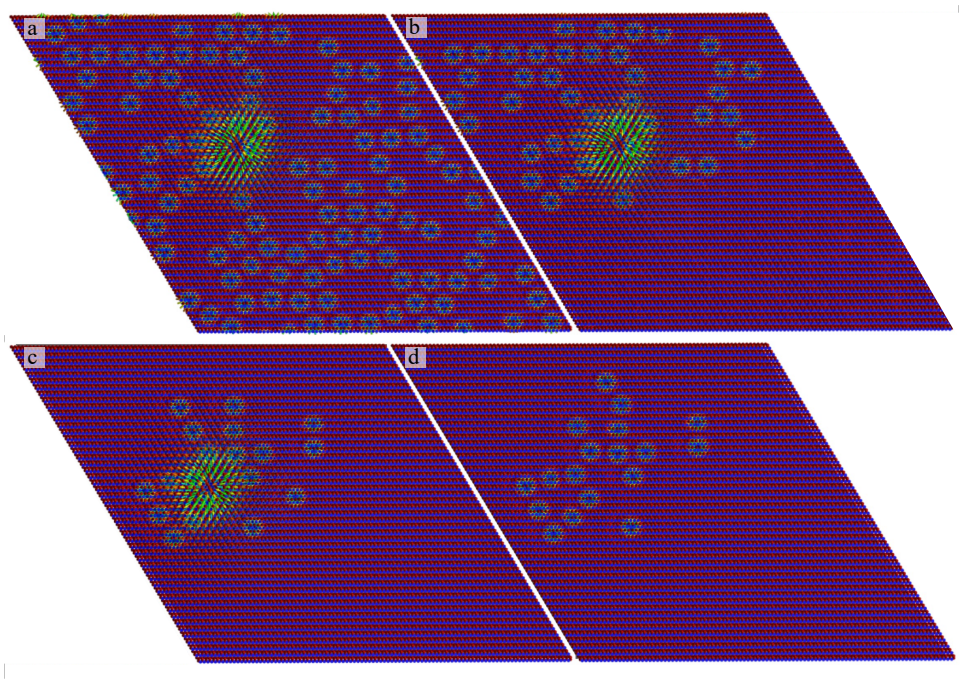

Figure **4-8**.: **Impact of Fe FM skyrmions on the stability of single AFM skyrmion. a-d** snapshots depicting the dependence of the AFM skyrmion under a magnetic field of 70 Tesla on the surrounding magnetic environment, by sequentially deleting one FM skyrmion or antiskyrmion in the Fe layer and relaxing the spin structure. At some point, removing any of the single FM skyrmions in **c** annihilates the AFM skyrmion.

collinear state surrounding the non-collinear states in Fig. **4-8** c. The building-blocks of the AFM skyrmion are shown in Fig. **4-9** a and d, where one can recognize the underlying Fe FM skyrmions in the background. The latter are more distinguishable in the sublattices free from the AFM skyrmion as illustrated in Figs. **4-9** g and j. The order of magnitude of the interactions clearly indicates that the DMI plays a minor role and that one can basically neglect the interactions arising in the skyrmion-free sublattices, namely L3 and L4. It is the Heisenberg exchange interaction emerging in the sublattices L1 and L2 that dictates the overall stability of the AFM skyrmion.

In L2, the core of the magnetization of the Cr FM skyrmion points along the same direction as that of the underlying Fe atoms, which obviously is disfavored by the AFM coupling between Cr and Fe (-3.05 meV for the first n.n.). This induces the red exchange area surrounding the core of the AFM skyrmion (black circle in Fig. **4-9** e), which is nevertheless sputtered with

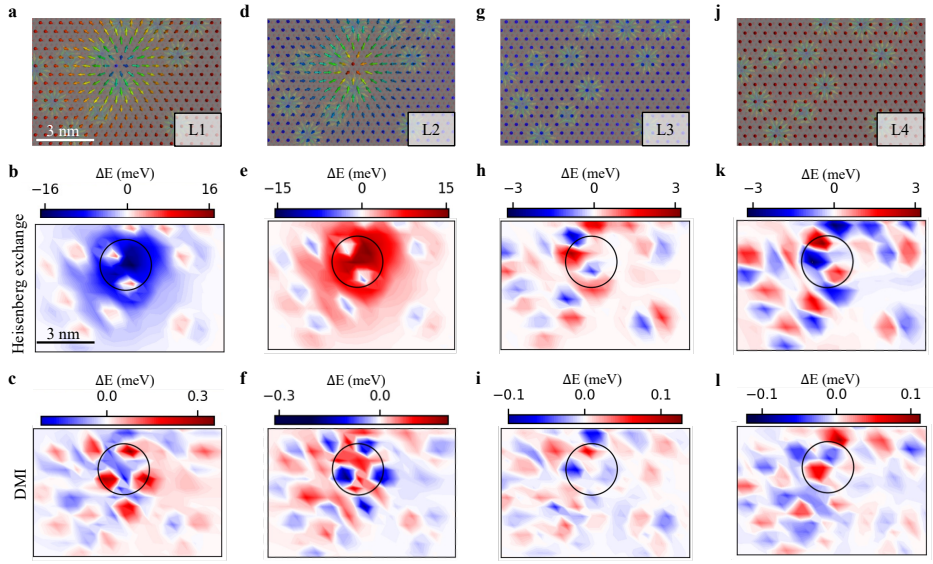

Figure **4-9**.: **Interaction map of the single AFM skyrmion with the magnetic substrate.** In the first row of figures, sublattice decomposition of a Cr skyrmion including the underlying Fe skyrmions shown in four columns **a**, **d**, **g** and **j**, corresponding respectively to L1, L2, L3 and L4. The AFM skyrmion is made of two FM skyrmions hosted by sublattices L1 and L2. In Fe, FM skyrmions and antiskyrmions can be found in all four lattices. The second row (**b**, **e**, **h** and **k**) illustrates the sublattice dependent two dimensional Heisenberg exchange energy map corresponding to the areas plotted in the first row, followed by the third row (**c**, **f**, **i** and **l**) corresponding to DMI. Note that the energy difference ΔE is defined with respect to the RW-AFM background.

blue spots induced by the magnetization of the core of the Fe FM skyrmions pointing in the direction opposite to that of the Cr moments in L2. The latter is a mechanism reducing the instability of the Cr skyrmion. Overall, the total energy cost in having the Cr skyrmion in L2 reaches +693.7 meV and is compensated by the Heisenberg exchange energy of -712.4 meV generated by the one living in sublattice L1. Here, the scenario is completely reversed since the core of the Cr skyrmion has its magnetization pointing in the opposite direction than that of the neighboring Fe atoms and therefore the large negative blue area with the surrounding area being sputtered by the Fe skyrmions, similar to the observation made in L2 (see Fig. **4-9** d). Overall, the Cr AFM skyrmion arranges its building blocks such that the energy is lowered by the skyrmion anchored in sublattice L1. Here, the details of the non-collinear magnetic textures hosted by Fe play a primary role in offering the right balance to enable stabilization. This explains the sensitivity of the single AFM skyrmion to the number and location of the underlying FM Fe skyrmions. Removing non-collinearity in Fe makes both building blocks of the AFM skyrmion equivalent without any gain in energy from the Cr-Fe interactions, which facilitates the annihilation of the Cr skyrmion.

4.7. Phase diagrams

Exploring the phase diagrams of AFM skyrmions in relation to the underlying magnetic interactions offers valuable insights. The magnetic interactions among Cr atoms shown in Fig. **4-3** b are multiplied by a factor renormalizing the initial parameters. In Fig. **4-10** we illustrate the impact of DMI vectors magnitude (D), Heisenberg exchange (J) and MAE parameter (K) on the formation of various phases including the one hosting double interchained AFM skyrmions. For simplicity, we consider the case where the interaction between Cr and the underlying Fe layer is switched off. A color code is amended to follow the changes induced on the distance between the AFM skyrmions. From this study, we learn that in contrast to the DMI, which tend to increase the size of the structures, J and K tend to miniaturize the skyrmions, ultimately favoring their annihilation. The phase hosting AFM skyrmions is sandwiched between the RW-AFM state and a phase hosting stripe domains. It is convenient to analyse the unveiled overall behavior in terms of the impact of DMI. The latter protects the AFM skyrmions structure from shrinking, similarly to FM skyrmions [35, 196]. So for small values of DMI compared to J in Fig. **4-10** a, or compared to K in Fig. **4-10** b, the AFM skyrmions shrink and disappear. In contrast, large values of the DMI increase the size of the skyrmions till reaching a regime where stripe domains are formed. Within the phase hosting AFM skyrmions, increasing J or K results in smaller skyrmions.

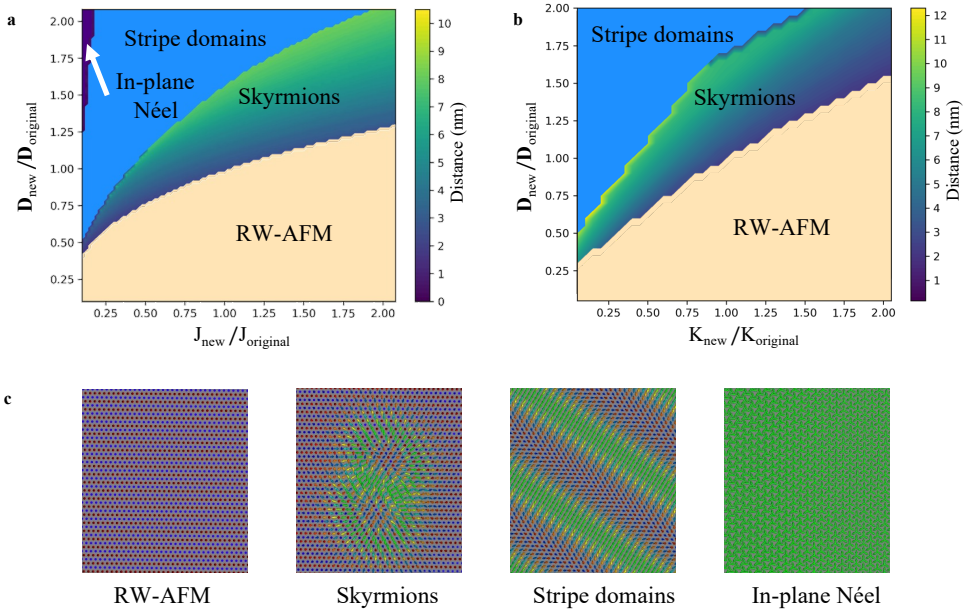

Figure **4-10**.: **Phase diagrams of the free double interchained AFM skyrmions.** **a** Phase diagram obtained by fixing K while changing the set of DMI and Heisenberg exchange interaction J, or **b** by fixing J while modifying K and DMI. The color gradient pertaining to the skyrmion phase indicates the distance between two AFM skyrmions. **c** Illustration of the states shown in the phase diagrams. Note that an in-plane Néel state is predicted for large DMI and small J.

4.8. Thermal stability with geodesic nudged elastic band (GNEB) method

Up to this point, we have demonstrated the existence of interchained AFM skyrmion multimers as localized energy minima within the framework of the Heisenberg Hamiltonian (Eq. (4-1)). However, a critical question arises regarding the stability of these structures against thermal excitations. To address this, we need to assess the depth of these energy minima, quantified as the minimum energy barrier that must be overcome for the system to transition out of a minimum state. It is important to note that the Néel temperature of the RW-AFM ground state is approximately 310 °K, a value we determined through our Monte Carlo (MC) simulations [197, 173, 114]. To investigate this issue, we systematically carried out a series of GNEB simulations [181, 182, 114] for AFM multimers, containing initially 10 interchained skyrmions not interacting with the Fe film. We then calculate the energy bar-

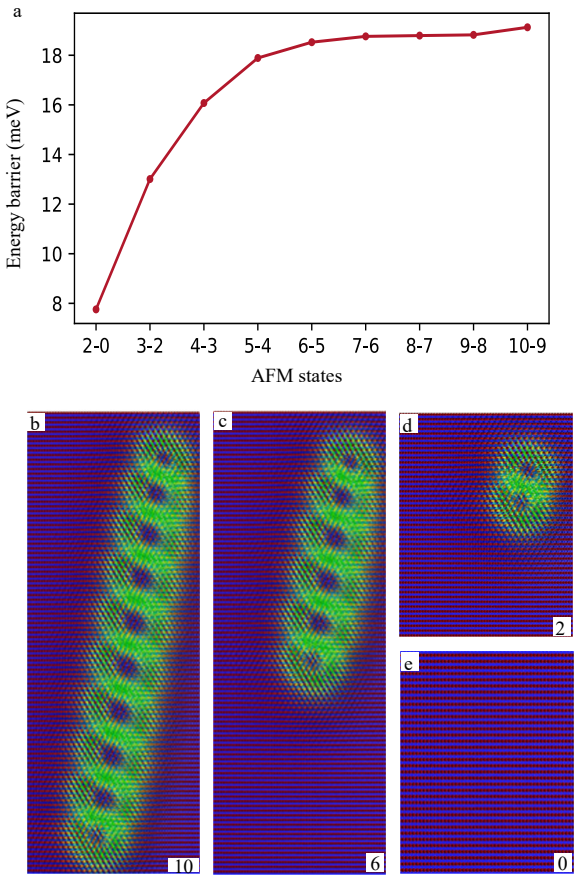

Figure **4-11**.: **Energy barriers for chains of free interchained AFM skyrmions. a** The energy barrier obtained with GNEB simulations for deleting a single AFM skyrmion from the lower edge of the free (not interacting with PdFe) chains, the x-axis shows the magnetic states between which the energy barrier is calculated. For example, (6-5) means that the energy barrier needed to annihilate one AFM skyrmion from the chain containing initially 6 AFM skyrmions as depicted in **c**. **b-e** Snapshots of some of the explored skyrmion chains, with the number of AFM skyrmion in each chain clarified at the bottom right corner.

rier needed to annihilate one AFM skyrmion at a time as depicted in Fig. **4-11** b-e, showing the successive magnetic states between which, the energy barrier has been calculated. The energy barrier is given by the energy difference between the n^{th} AFM skyrmions state local

minimum (hosting n AFM interchained skyrmions) and the relevant saddle point located on the minimum energy path connecting the initial state with the $(n-1)^{th}$ AFM skyrmions state. The energy barrier increases from about 8 meV ($\approx$ 90 °K) for the double interchained AFM skyrmions to 13 meV ($\approx$ 150 °K) for three interchained ones, reaching a saturation value of $\approx$ 18.5 meV ($\approx$ 214 °K) for chains containing more than five AFM skyrmions, see Fig. **4-11** a. Hence, increasing the number of interchained skyrmions enhances their stability, which is further amplified when enabling the interaction with the PdFe substrate.

Instead of 8 meV pertaining to the free skyrmion dimer, the barrier reaches 45.7 meV ($\approx$ 530 °K) owing to the interaction with the underlying substrate while the single AFM skyrmion experiences a barrier of 10 meV ($\approx$ 113 °K). Thus, the exchange field emanating from the PdFe substrate promotes the use of interchained AFM skyrmions in room temperature applications. By analysing how the different interactions contribute to the barrier, we identified the DMI as a key parameter for the thermal stability of the interchained AFM skyrmions. For example, in the case of free double interchained AFM skyrmions, the Heisenberg exchange interactions contribution is -87 meV, MAE contribution is -150 meV while the DMI provides a barrier of 245 meV. Interestingly and as expected, it is the magnetic Heisenberg exchange interaction between Cr and Fe that is mainly responsible for the thermal stability of the single AFM skyrmion.

4.9. Conclusion

Following a two-pronged approach based on first-principles simulations combined with ASD, we identify a thin film that can host intrinsic, i.e. non-synthetic, AFM skyrmions at zero magnetic field. A Cr monolayer deposited on a substrate known to host FM skyrmions, PdFe/Ir(111), offers the right AFM interface combination enabling the emergence of a rich set of AFM topological solitons [184]. The ground state among Cr atoms is the RW-AFM configuration, a magnetic configuration sought after for so long. The explored AFM skyrmions, whether single or interchained, showcase remarkable stability and open the door for potential applications in room temperature racetrack memory devices, driven by currents with potential to suppress the skyrmion Hall effect. The prospects of utilizing the underlying FM substrate to control and manipulate these AFM solitons present an exciting opportunity to design novel materials and devices for AFM spintronics.

Since the experimental observation of intrinsic AFM skyrmions has so far been elusive at interfaces and ultrathin films, our predictions open the door for their realization in well-defined materials and offer the opportunity to explore them in thin film geometries. The robustness of the single and interchained skyrmions qualifies them as ideal particles spintronic devices to be driven with currents while avoiding the skyrmion Hall effect.

We anticipate that our work will facilitate the search and the identification of single or overlapping AFM skyrmions while contributing to the detailed understanding of their various

properties, which is a cornerstone in the field of topological antiferromagnetism and its potential use in devices for information technology.

5. Spin model for intrinsic AFM skyrmions

Following our first-principles simulations predicting the emergence in an intrinsic antiferromagnetic (AFM) skyrmions within a RW-AFM single monolayer of Cr deposited on PdFe bilayer grown on Ir(111) surfaces (chapter 4), here, we explore the minimal Heisenberg model enabling the occurrence of such AFM solitons and the underlying phase diagrams by accounting for the interplay between the Dzyaloshinskii-Moriya interactions (DMI) and Heisenberg exchange interactions, as well as the magnetocrystalline anisotropy energy (MAE) parameter (K) and impact of magnetic field. By providing the fundamental basis to identify and understand the behavior of intrinsic AFM skyrmions, we expect our model to serve as powerful tool for exploring and designing new topological magnetic materials to conceptualize devices for AFM spintronics.

The results discussed in this chapter, have been previously published in [198]:
"A spin model for intrinsic antiferromagnetic skyrmions on a triangular lattice".

5.1. Introduction

The findings from our previous first-principles investigations reported in chapter 4 showed that intrinsic single and interchained AFM skyrmions can emerge on a triangular lattice hosting a RW-AFM out-of-plane (OOP) state. These results motivated us to take a step further and construct a generic spin model that is capable of describing the underlying physics. In this chapter, we introduce a Heisenberg model that incorporates the essential magnetic interactions required to form AFM skyrmions, single and interchained ones, on a triangular lattice. As done in the previous chapter, we perform atomistic spin simulations on the basis of the Landau-Lifshitz-Gilbert (LLG) equation [173] as implemented in the Spirit code [114]. We consider the interplay between the Heisenberg exchange interactions, DMI, K and the impact of an external magnetic field to establish the phase diagrams of the intrinsic AFM skyrmions while inspecting their stability via simulations based on Geodesic nudged elastic band method (GNEB) method [181, 182, 114].

Our model offers a robust approach to comprehend the behavior of AFM skyrmions in a triangular lattice with the aim of understanding the required ingredients for their stabilization and to create novel materials and devices for AFM spintronics.

5.2. Computational details

For completeness we present once more the tow-dimensional Heisenberg model that we consider for the hexagonal lattice, which is equipped with the Heisenberg exchange coupling, DMI, K, and Zeeman term. The energy functional reads as follows:

$$\mathcal{H} = -\sum_{<ij>} \mathrm{J}_{ij}\, \boldsymbol{n}_i \cdot \boldsymbol{n}_j - \sum_{<ij>} \mathbf{D}_{ij} \cdot (\boldsymbol{n}_i \times \boldsymbol{n}_j) - \mathrm{K} \sum_i (n_i^z)^2 - \sum_i m_i \mathbf{B} \cdot n_i^z, \tag{5-1}$$

where we consider only the first, second and third neighboring atoms for the Heisenberg exchange interactions and just the third nearest neighboring DMI. The motivation behind our assumptions will be discussed in the upcoming section. we assume $m = 1\ \mu_B$ and an OOP field.

The LLG simulations were carried out with 100^2, 200^2 and 300^2 sites assuming periodic boundary conditions at zero Kelvin.

5.3. Minimal generic model for the RW-AFM state and emergence of AFM skyrmions

To explore the conditions required for the formation of single and interchained AFM skyrmions within a triangular lattice, the initial step involves determining the prerequisites for establishing the RW-AFM state. We recall that the latter configuration can be separated into four sublattices L1, L2, L3 and L4, carrying each ferromagnetic (FM) moments which are aligned antiferromagnetically with respect to each other when considering the inter-sublattice magnetization direction. As established in Refs. [186, 199] the minimum set of Heisenberg exchange interactions involves the interactions with first (J_1), second (J_2) and third (J_3) nearest neighboring atoms. The formation of the FM skyrmions building up our AFM skyrmions requires, as demonstrated in chapter 4, a third nearest neighbors (n.n.) interaction J_3, which should mediate an FM coupling between magnetic moments hosted by the same sublattice.

Fig. **4-4** in chapter 4 illustrates the underlying phase diagram, where we expect four regions that can host either a Néel, FM, AFM spin spiraling and RW-AFM states. If too weak with respect to J_1 or if it is of an AFM nature, either spin spirals or a Néel state are favored depending on the strength of J_2. We observe that the RW-AFM configuration occupies a larger phase area when J_2 is of AFM nature. In the RW-AFM state, J_3 is thus positive, which together with the DMI vector $\mathbf{D}_3$, that is connecting the third n.n. similarly to J_3, enables the formation of sublattice FM skyrmions. Therefor in our model, we do not need further DM interactions and it is enough to assume that $\mathbf{D}_3$ lies in-plane while being perpendicular to the bond connecting neighboring atoms as shown in Fig. **B-1** of Appendix B. The AFM interaction among the FM skyrmions is mediated by J_1 such that the presence of J_2 is not requested. As discussed in the previous chapter, the single AFM skyrmion consists of FM

skyrmions present in two sublattices (L1 and L2) with the other two sublattices remaining collinear, while for the double AFM skyrmions, the building blocks FM skyrmions reside in each of the four sublattices (L1, L2, L3 and L4). The MAE should favor an OOP orientation of the magnetic moments, therefore $K > 0$.

5.4. Phase diagrams of the AFM skyrmions in a hexagonal lattice

After setting the base for the magnetic interactions needed to realize our AFM solitons, we inspect the range of parameters (J_2, J_3, D_3 and K) normalized to the absolute value of the AFM J_1, within which the single and double interchained AFM skyrmions can be stabilized (Fig. **5-1** a-d). The region hosting the skyrmions, color coded in terms of their radius, is sandwiched between the RW-AFM and stripe domains phases. Since the building blocks of the AFM solitons are FM skyrmions, the impact of the underlying interactions is similar to what is expected from the FM topological objects. For instance increasing J_3 (Fig. **5-1** a-b), which defines the FM interaction among the spins of the FM skyrmions, or increasing the OOP K (Fig. **5-1** c-d) shrinks the size of the spin-texture by ultimately leading to its annihilation, while the DM interaction D_3 induces the opposite behavior (Figs. **5-1** c-d). Interestingly, J_2 counteracts J_3 by amplifying the skyrmion size, which at some point can be deformed into stripe domains. For completeness, snapshots of skyrmions, labelled from A to L in Fig. **5-1**, are presented in Fig. **B-2** of Appendix B.

5.5. The shape of the AFM skyrmions

The shape of the AFM skyrmions is determined by the specific interaction parameters involved. While the interactions between spins in one sublattice Li, characterized by J_3 and D_3, lead to the formation of a FM skyrmion in that sublattice, the interactions with spins in the other FM skyrmion hosting sublattice, governed by J_1 and J_2, have a significant impact on shaping the resulting AFM skyrmion, as illustrated in Fig. **5-2**. If the two FM skyrmions building up the AFM skyrmion are hosted by sublattices L1 and L2 as shown in Fig. **5-2** b and d, then their centers will be located at positions **M** and **N**. As depicted in Fig. **5-2** a, **M** interacts with **N** through J_1, and with $\mathbf{N}'$ through J_2. For the skyrmion depicted in Fig. **5-2** b, **M** will only be affected by **N**, and, since $J_2/|J_1| = 0$, **M** will not notice $\mathbf{N}'$ while its response to **P**, and **O** will cancel out since sublattices L3 and L4 are oppositely collinearly oriented. As a result, this unbalanced interaction leads to the elongation of the AFM skyrmion along **MN** direction. Whereas if the two centers are positioned at **M** and **P** as shown in Fig. **5-2** c, the elongation will be along **MP** direction. The shape of the AFM skyrmion becomes more symmetric when **M** reaches out $\mathbf{N}'$ ($\mathbf{P}'$), i.e. for larger values of $J_2/|J_1|$ as depicted in Fig. **5-2** d (e), where $J_2/|J_1| = 0.28$.

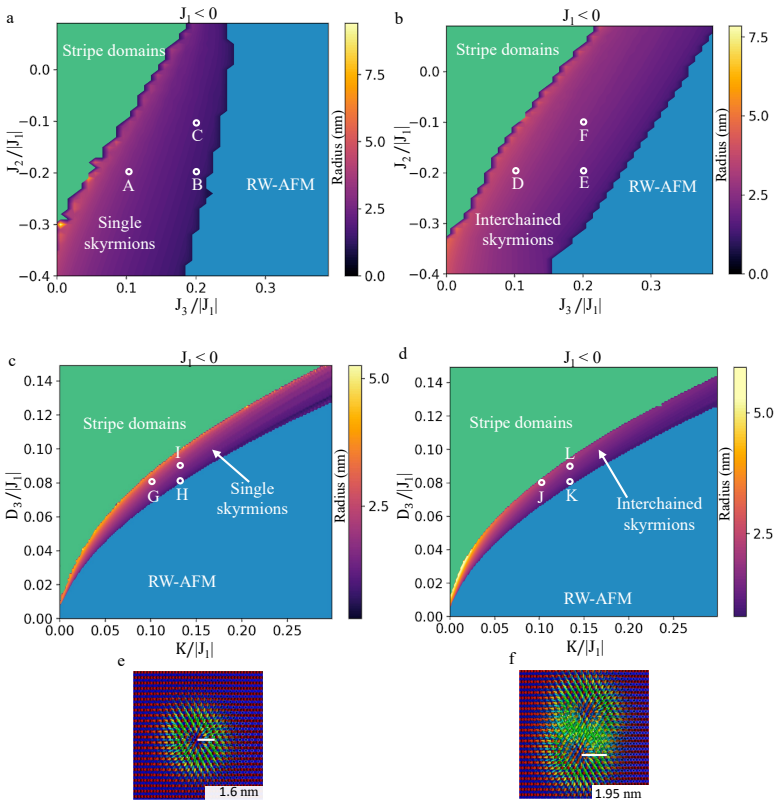

Figure **5-1**.: **Phase diagrams for AFM skyrmions.** Phase diagram showing the range of interactions $J_2/|J_1|$ and $J_3/|J_1|$ at which the single **a** and double **b** AFM skyrmions can be stabilised with $D_3/|J_1|$ =0.03, and $K/|J_1|$=0.024. The color code indicates the radius of the stabilized AFM skyrmion. **c** and **d** Phase diagrams obtained by changing the $D_3/|J_1|$ magnitude along with that of $K/|J_1|$ while fixing $J_2/|J_1|$ at -0.2, and $J_3/|J_1|$ at 0.2, for single and double AFM skyrmions, respectively. The letters A-L shown in the diagrams indicate skyrmions which are plotted in Fig. **B-2** of Appendix B. **e, f** Snapshots of the single and interchained AFM skyrmions

It is worth mentioning that the size of the single AFM skyrmion is smaller than those participating in the formation of the interchained magnetic textures (see for example the radius given in Fig. **5-1** e-f), which impacts on the details of the phase diagrams. On the one hand, the window in which the double AFM skyrmions are stabilised while varying $J_2/|J_1|$ and $J_3|J_1|$ is larger than that of the single magnetic objects (Fig. **5-1** a-b). On the

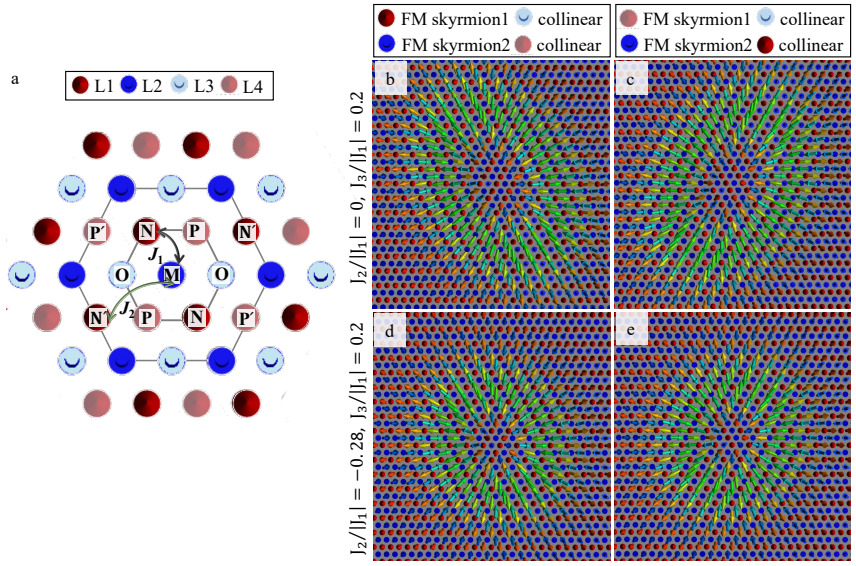

Figure **5-2**.: **The shape of AFM skyrmions.** **a** Schematic representation of the four sublattices distribution on the triangular lattice. The shape of the single AFM skyrmion is elongated along the line connecting the centers of the two FM skyrmions building up the single AFM skyrmion, in **b** the elongation is along **MN** where the centers of the two FM skyrmions reside, with **M** not interacting with $\mathbf{N}'$, while in **c** the elongation is along **MP**, where the the centers are positioned at **M** and **P**, and **M** does not interact with $\mathbf{P}'$. **d, e** The shape of the AFM skyrmion becomes more symmetric when the value of $J_2/|J_1|$ increases.

other hand, the single skyrmion phase seems wider and shifted to the upper region of the diagram while tuning $D_3/|J_1|$ and $K/|J_1|$.

5.6. Response to an external OOP magnetic field

We have investigated in chapter 4 section 4.5, the effect of the external magnetic field on the single and interchained AFM skyrmions formed with the realistic interactions among Cr atoms. We demonstrated how the size of both single and interchained AFM skyrmions changes with the magnetic field, revealing that they can withstand high magnetic fields. Here, we show the effect of changing the values of $K|/J_1|$ and $D_3/|J_1|$ affect the critical magnetic field up to which the AFM skyrmions survive. In addition to that, we investigate the response of the single and double AFM skyrmions with different values of $D_3/|J_1|$ and $K/|J_1|$ to magnetic fields perpendicular to the lattice. Within our model, as theoretically

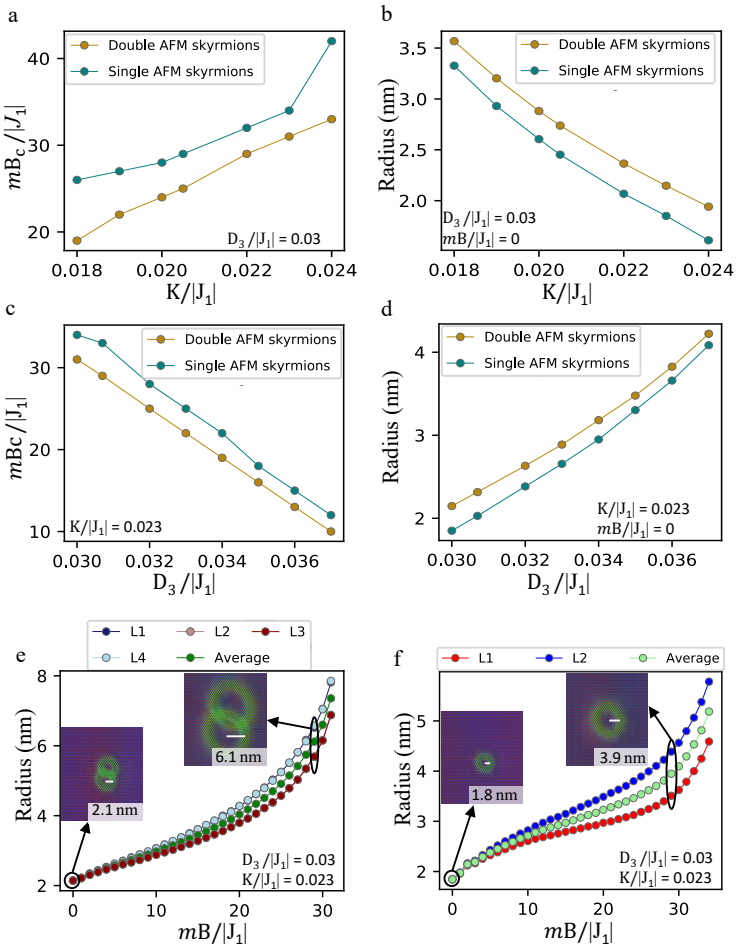

Figure **5-3**.: **AFM skyrmions response to an external OOP magnetic field.** The critical magnetic field $mB_c/|J_1|$ tolerated by the single (green dots) and double (golden dots) AFM skyrmions as a function of **a** the normalized values of $K/|J_1|$, and **c** the normalized values of DMI $D_3/|J_1|$. The critical field is defined by the largest field to which the skyrmion survives. **b** Increasing $K/|J_1|$ shrinks the radii of both the double and single AFM skyrmions, while **d** increasing $D_3/|J_1|$ expands them. **e, f** Impact of the external magnetic field on the radii of both types of AFM skyrmions.

expected [77, 86, 87, 184], and in contrast to their FM counterparts, the size of the AFM skyrmions increases with the external magnetic field, until its magnitude approaches a critical value (B_c), after which, the skyrmion deforms into the stripe domain phase.

The critical value of the normalized magnetic field ($mB_c/|J_1|$) can be enhanced by increasing $K/|J_1|$ magnitude, as depicted in Fig. **5-3** a, for both single and double AFM skyrmions. In contrast, the DMI lessens the highest magnetic field survived by the AFM solitons, as shown in Fig. **5-3** c. Various formulas have been proposed to describe the impact of DMI and K magnitude on the radius of the FM skyrmions [196, 200, 54, 201]. Inspired by Ref. [201], and utilizing the fact that $|J_1| >> D_3, K$, our results on the dependence of the AFM skyrmion radius R on K (Fig. **5-3** b) and DMI (Fig. **5-3** d) when the external field is switched-off can be fitted with $R_0 = a\frac{D_3}{K}\left(1 + b\frac{D_3^2}{|J_1|K}\right)$, where a and b are fitting parameters.

Upon application of the magnetic field, we found that the form proposed in Ref. [86] has to be amended with a linear field-dependent term. After a Taylor expansion in the regime where the field is smaller than the rest of the magnetic interactions, we find $R = a\frac{D_3}{K}\left(1 + b\frac{D_3^2}{|J_1|K}\right)\left(1 + \alpha\frac{B}{|J_1|} + \beta\frac{B^2}{|J_1|^2} + \gamma\frac{B^3}{|J_1|^3}\right)$, where α, β and γ are additional fitting parameters, grasps reasonably the dependencies reported in Figs. **5-3** e-f (with $D_3/|J_1| = 0.03$ and $K/|J_1| = 0.023$). Overall, the magnetic interactions that decrease (increase) the size of the skyrmions, such as K (DMI), contribute to an enhanced (reduced) stability in the presence of an external magnetic field.

5.7. Effect of magnetic field on the thermal stability of single and double AFM skyrmions

Next, we delve into the stability of AFM skyrmions when subjected to thermal fluctuations by quantifying the energy barrier protecting the single and double interchained AFM skyrmions from collapsing into the RW-AFM ground state utilizing the GNEB method [181, 182, 114]. We assume $J_2/|J_1| = -0.2$, $J_3/|J_1| = 0.2$, $D_3/|J_1| = 0.03$, and $K/|J_1| = 0.024$. The barrier is determined by the energy difference between the local minimum magnetic state hosting the AFM skyrmion and its relevant saddle point, which lies on the path of minimum energy connecting the skyrmion configuration to the RW-AFM ground state. In the absence of external magnetic field, the double AFM skyrmions with radius of 1.95 nm, has an energy barrier of 0.67 meV, which translates to $\approx$ 7.8 °K, while for the single AFM skyrmion with radius of 1.6 nm, the energy barrier is 0.055 meV ($\approx$ 0.64 °K). For both cases, the major key for the stability of the AFM skyrmions is the DMI which contributes with ΔE_{DMI} = 15.66 meV to the energy barrier of the double AFM skyrmion and 4.33 meV for the single case, while K and Heisenberg exchange interactions prefer the collapse of the AFM solitons by contributing with ΔE_K = -9.21 meV (-2.53 meV), and ΔE_J = -5.79 meV (-1.71 meV) for double (single) AFM skyrmions. Moreover, we addressed another important aspect, the impact of the magnetic field, by carrying out a systematic study with results illustrated in

Fig. **5-4**. The thermal stability is obviously enhanced with the magnetic field, which impacts more efficiently the double than the single AFM skyrmion (Fig. **5-4** a). For $m\mathrm{B}/|\mathrm{J}_1| = 1$, the energy barrier of the double (single) AFM skyrmions increased to 0.81 meV (0.12 meV) $\approx$ 9.4 °K (1.3 °K). By increasing the magnetic field, the skyrmions expand (Fig. **5-4** f), which in contrast to the DMI and Zeeman contributions (Figs. **5-4** c-d) is disfavored by those of the Heisenberg exchange and K (Figs. **5-4** b, e). Snapshots of the various states prospected in defining the energy barriers are presented in Fig. **B-3** of Appendix B.

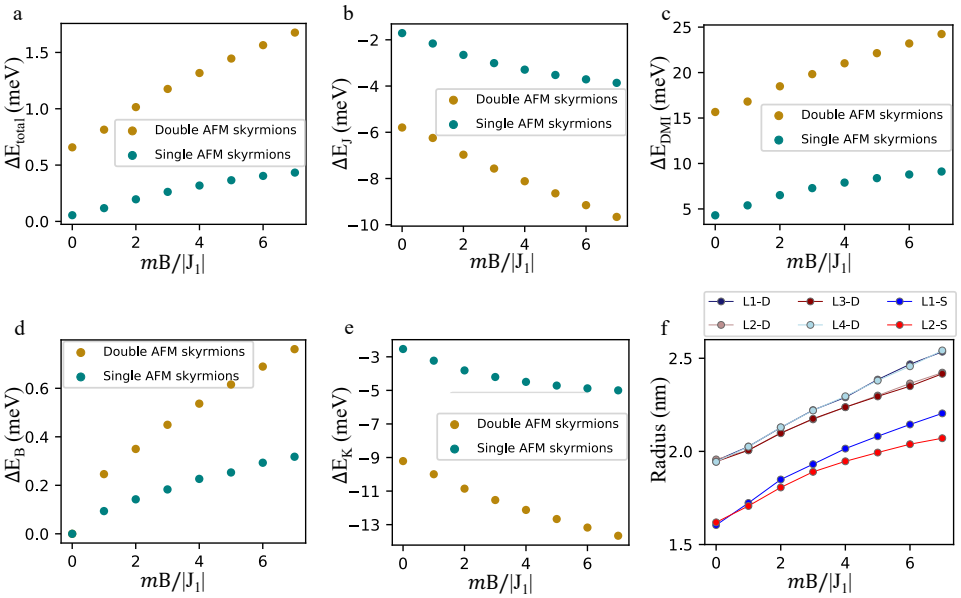

Figure **5-4**.: **Thermal stability of the single and double AFM skyrmions in the presence of an external magnetic field.** **a** The total energy barrier for double (golden) and single (green) AFM skyrmions as a function of the normalized value of the external magnetic field. The different contribution to the energy barrier as shown in **b** Heisenberg exchange, **c** DMI, **d** Zeeman and **e** K. **f** The Radii of the single and double AFM skyrmions are plotted as function of the magnetic field.

5.8. Conclusion

Inspired by our first-principles findings on the emergence of single and interchained AFM skyrmions on a triangular lattice, we propose here a spin model with the minimum set of

magnetic interactions needed to realize such intriguing solitons. This model is carefully constructed to represent the essential magnetic interactions required for the emergence of intrinsic AFM skyrmions, single and interchained, on a triangular lattice. They form in an RW-AFM state, which can be decomposed into four sublattices. The exchange interaction within each sublattice, mediating the coupling between the third n.n., is of FM nature which along with the associated DMI and OOP MAE permits the formation of FM skyrmions within the sublattices. The first n.n. has to be of an AFM nature to impose the emergence of AFM skyrmions. We identify the phase diagrams of the latter entities as well as their dependencies on the magnitude of various magnetic interactions and sensitivity to an external magnetic field. We anticipate that our work will facilitate the search and the identification of single or overlapping AFM skyrmions while contributing to the detailed understanding of their various properties, which is a cornerstone in the field of topological antiferromagnetism and its potential use in devices for information technology.

6. Intrinsic Néel AFM multi-meronic solitons

In this chapter, we proceed further with our investigation of AFM solitons in thin films. We predict an intriguing exchange-frustrated multi-meronic spin-textures that emerge within a Néel magnetic order of spins by replacing the Cr layer addressed in the previous chapters with Mn. The frustrated multi-merons are topological entities, which are intrinsic to the AFM Mn film and showcase remarkable stability against external magnetic fields. The discovery of the frustrated Néel AFM multi-meronic spin-textures opens doors to a new frontier in AFM solitons, offering tantalizing prospects for innovative spintronic devices based on non-synthetic AFM quantum materials.

The results discussed in this chapter, have been previously published in [202]:
"Intrinsic Néel antiferromagnetic multi-meronic spin textures in ultrathin films".

6.1. Introduction

Since this chapter deals with meronic textures, it is order to recapitulate what has been achieved in the FM topological world regarding merons. Regular FM merons are in-plane magnetized textures with magnetization that curls around a stable core pointing out-of-plane (OOP), and are topologically equivalent to one half of a skyrmion with a topological charge (N) = $\pm\frac{1}{2}$ [96, 97, 100, 98, 101, 25, 102, 103, 104, 105]. They have been observed experimentally in thin films [25, 203] and in bulk as cross sections of vortex-antivortex three-dimensional rings [204]. Antiferromagnetically coupled merons emerge synthetically in confined geometries [100, 101] or nucleate across domain walls [205, 206]. They were identified in hybrid complexes involving various magnetic objects in intrinsic bulk (thick films) phases [207, 93, 95], following a large body of phenomenology-based simulations [208, 209, 210, 211, 212]. However, a pristine ultrathin film material that hosts AFM merons remains unattainable.

6.2. Computational details

In this study, we conducted a systematic investigation to explore the magnetic structures that can be hosted by the magnetic layers of our four layered systems depicted in Fig. **6-1**. For instance, we considered the case where the Mn layer: (i) is directly interfaced with the Ir(111) surface; (ii) covered with a Pd overlayer; (iii) separated from Ir with a PdFe bilayer

or with (iv) a Pd_2Fe trilayer. Similar to chapter 4, we follow a two-fold procedure, combining *ab initio* calculations with atomistic spin dynamics. The details of this procedure are similar to what has been already discussed in computational details section(section 4.2 in chapter 4).

The investigated thin films were arranged in an fcc-stacked configuration along the [111] direction. The relaxed atomic positions were then extracted and presented in table **6-1** in terms of their relative difference with respect to the ideal inter-layer Ir distance, where positive (negative) values indicate atomic relaxations towards (away from) the Ir surface.

After establishing the geometries of the various magnetic systems, we conducted in a second step a detailed investigation of their magnetic properties and interactions similar to the procedure conducted in chapter 4.

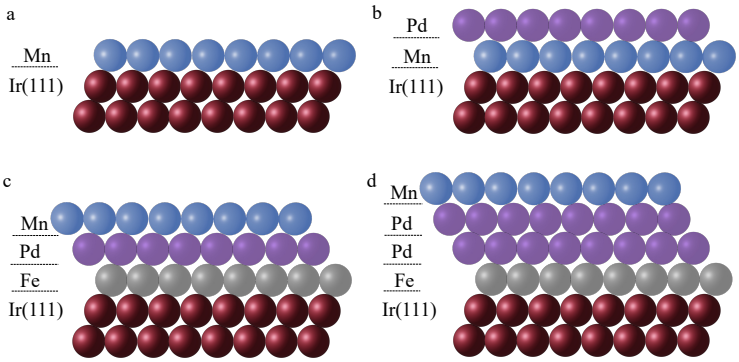

Figure **6-1**.: **Mn-based magnetic systems under investigation.** We explore several scenarios where topological spin-textures emerge: **a** Mn layer interfaced directly with Ir(111) surface; **b** Mn layer covered with a Pd overlayer; **c** Mn layer separated from Ir by a PdFe bilayer; **d** Mn layer separated from Ir by a Pd_2Fe trilayer.

a

Mn/Ir(111)	
	Relaxation (%)
Mn	2.3
Ir	-3.4

b

PdMn/Ir(111)	
	Relaxation (%)
Pd	8.6
Mn	10.3
Ir	-2.3

c

MnPdFe/Ir(111)	
	Relaxation (%)
Mn	4
Pd	5.2
Fe	8.1
Ir	-1

d

$MnPd_2Fe$/Ir(111)	
	Relaxation (%)
Mn	5.9
Pd	-4
Pd	8.2
Fe	8.2
Ir	-0.7

Table **6-1**.: Relative vertical relaxations of the magnetic layers for the different investigated scenarios of Mn interfaced with Ir(111) surface. Positive and negative values correspond to respectively relaxations towards and away from the Ir surface.

6.3. Magnetic interactions and ground state of Mn-based thin films on Ir(111)

When Cr serves as our AFM layer deposited on Ir(111) based surfaces, the interactions among the Cr atoms in CrPdFe/Ir(111), particularly the interactions among first, second and third nearest neighbors (n.n.) as discussed in chapter 4, stabilize the RW-AFM state as the ground state. Mn film provides important changes with respect to Cr. The first Mn n.n. Heisenberg exchange interactions are in general strongly AFM but smaller than those of Cr: J_1^{Cr-Cr}= -51.9 meV in CrPdFe/Ir(111), while J_1^{Mn-Mn}= -41.7 meV, -19.6 meV, -37.4 meV, and -32.1 meV in Mn/Ir(111), PdMn/Ir(111), MnPdFe/Ir(111), and $MnPd_2Fe$/Ir(111), respectively. Importantly, the third Mn n.n. interaction favors an AFM coupling (except for PdMn/Ir(111), where it is extremely weak) in contrast to the FM nature found for the Cr layer. This, together with the strong AFM couplings of the first n.n. compared to the second and third ones (see Fig. **6-2**) for Mn-based films, lead to the emergence of the AFM Néel state as the ground state due to magnetic frustration.

It is instructive to locate the ground state for Mn in the phase diagram presented in chapter 4 (Fig. **4-4**) when analysing the case of CrPdFe/Ir(111) surface. As illustrated in Fig. **6-3**, assuming only the three n.n. isotropic Heisenberg interactions, we find that all the points pertaining to the Mn-based films are located in the Néel phase. The n.n. DMI is found to be significant for Mn/Ir(111) and PdMn/Ir(111) surfaces and experiences a significant decrease when Mn is separated from Ir with the PdFe bilayer of Pd_2Fe trilayer. Except for Mn/Ir surface, the magnetocrystalline anisotropy energy (MAE) favors an OOP orientation of the magnetic moments. The incorporation of the DMI and MAE maintained the Néel

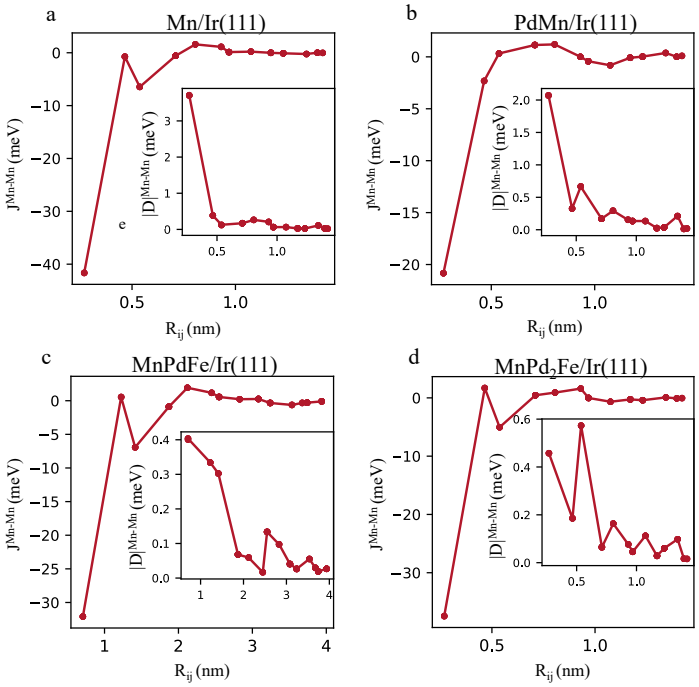

e

	MnIr	PdMnIr	MnPdFeIr	$MnPd_2FeIr$
m_{Mn}	3.4	2	3.7	3.8
K_{Mn}	-0.21	0.76	0.5	0.18
Magnetic moment m is in μ_B and magnetic anisotropy strength (K) is in meV				

Figure **6-2**.: **Magnetic interactions among Mn atoms for the investigated systems.** The Heisenberg exchange interactions values as a function of distance for Mn/Ir(111) **a**, PdMn/Ir(111) **b**, MnPdFe/Ir(111) **c** and $MnPd_2Fe/Ir(111)$ **d**. Insets show the DM interaction values as a function of distance. **e** The spin moment per Mn atom (m) in μ_B and the magnetocrystalline anisotropy energy (K) for Mn layer for the inspected systems.

configuration as the ground state. Intriguingly, however, the Néel state is found to be in-plane, which means that the moments rotate in the surface plane. As mentioned before, the MAE in general favors an OOP orientation of the moments. It turns out that the z-component of the DMI is strong enough to compete against the MAE and enforces the in-plane orientation of the Mn moments. We are thus dealing with a chirality-induced

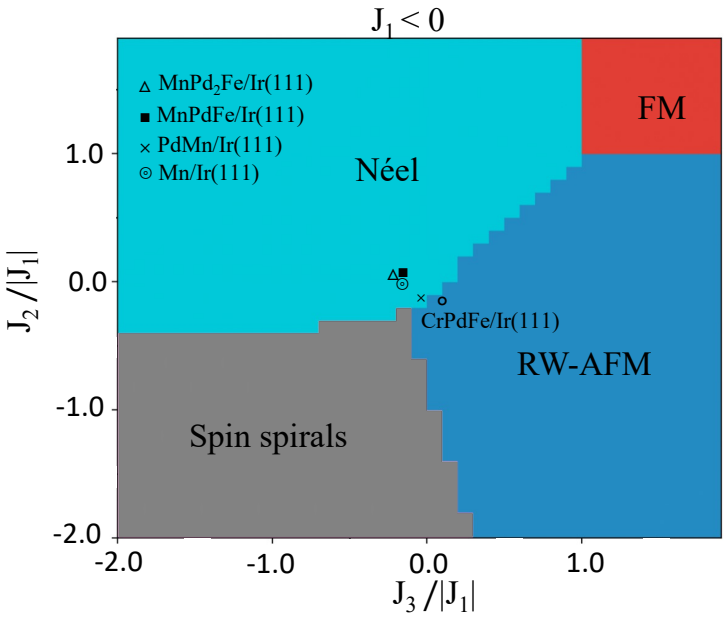

Figure **6-3**.: **The magnetic phase diagram of the hexagonal two-dimensional lattice including magnetic interactions up to the third n.n.** Besides the case of CrPdFe/Ir(111) surface, which is lying in the RW-AFM phase (see Fig. **4-4** in chapter 4), the cases of Mn-based films are all positioned in the Néel phase.

stabilization of an in-plane Néel state. The associated critical temperatures range from 130°K for PdMn bilayers to about 600°K or more for the rest of thin films.

6.4. Topological magnetic states in frustrated Mn ultrathin films

A thorough investigation of the potential emergence of intrinsic topological states in the different Mn-based films demonstrated the existence of a plethora of AFM Néel meronic magnetic states forming metastable states emerging in the Mn layer as depicted in Fig. **6-4** a, Fig. **6-5** and Fig. **C-1** of Appendix C.

The spins forming the AFM Néel order are segmented into three sublattices L1, L2 and L3, each hosting FM spin alignment (Fig. **6-4** j). At each sublattice, FM meronic pair can be stabilized, so in total, in the case of single AFM Néel meronic pair (Fig. **6-4** a), we have

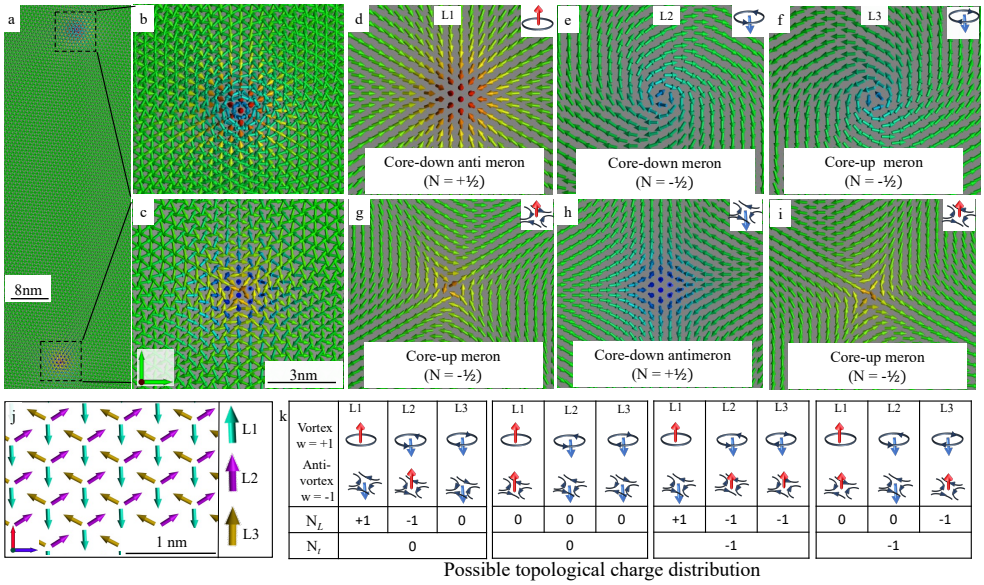

Figure **6-4**.: **Frustrated Néel AFM meronic topology. a** AFM hexa-meronic state composed of vortex-antivortex pair that emerges in a frustrated triangular Mn layer on e.g. Ir(111) surface with zoom into the vortex **b**, and antivortex **c** components. The frustrated AFM meronic texture is decomposed into three FM vortix-antivortex pairs residing at sublattices L1 **d, g**, L2 **e, h**, and L3 **f, i**. **j** illustration of the Néel AFM ground state with colors indicating the decomposition into three sublattices L1, L2 and L3. **k** Schematic representation of the set of sublattices for the possible topological magnetic structures, with w represents vorticity and N stands for the topological number (N = wp/2 with p = +1 for up and p = -1 for down polarity of the core).

six FM merons (antimerons), as shown in Fig. **6-4** d-i, which we refer to as a hexa-meronic state. By zooming in into the two spin-swirling extremities of the hexa-meron(Figs. **6-4** b-c) and their respective sublattice decomposition (Figs. **6-4** d-i), we identify a vortex (Fig. **6-4** d) and an antivortex (Fig. **6-4** h) whose cores reside on an Mn lattice site, around which the spins of the remaining meronic textures precess, as dictated by the magnetic frustration induced by the underlying AFM magnetic interactions.

Each of the FM building blocks of our AFM explored solitons holds a topological charge (N) defined as: N = wp/2 [96] (see discussion in section 2.2.1 in chapter 2), where w = +1 (-1) for the vortex (antivortex) is the vorticity describing the rotational direction of the in-plane magnetization, and p is the polarity which defines the OOP magnetization of the

center being +1 (-1) when pointing up (down) [213]. Since the merons and antimerons carry a topological charge of -1/2 and +1/2, respectively [25, 203, 93], the sublattice charge N_L is either -1 (+1) for a meron-meron (antimeron-antimeron) pair, as the case of L3 (Fig. **6-4** f, i), or 0 for a hybrid (see L1 and L2 in Fig. **6-4** d, g, e, h) meron-antimeron pair. By summing up the total charge N_t for a hexa-meron, one can end up with three possible values -1, 0 and +1 (see Fig. **6-4** k), which interestingly are energetically degenerate in the absence of an external magnetic field.

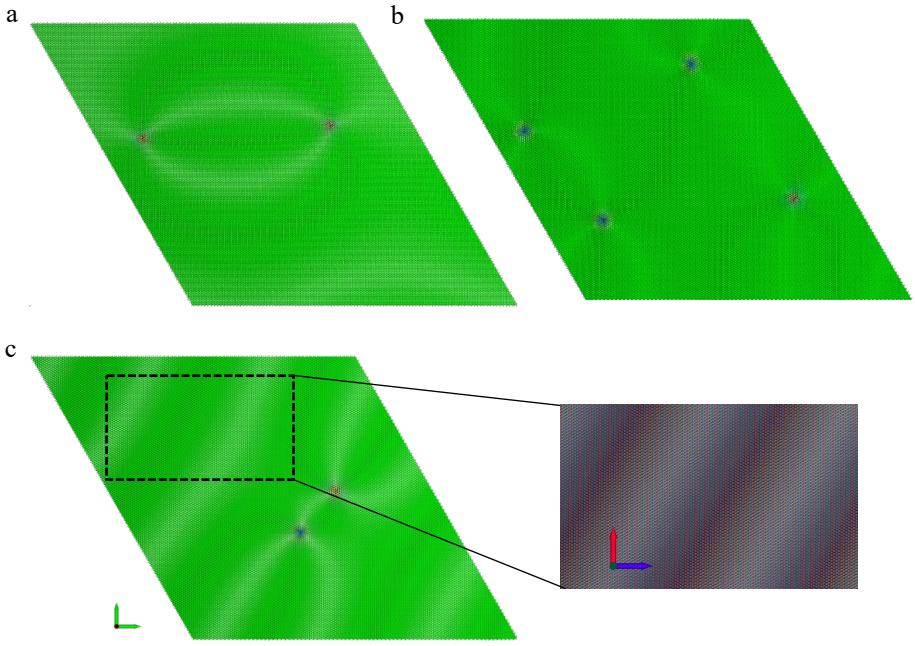

Figure **6-5**.: **Plethora of AFM magnetic states emerges at Mn layer.** Snapshots of hexa-meronic state **a**, dodeca-meronic state **b** with Néel AFM order of spins at the background. **c** Hexa-meronic state with AFM Néel spirals at the background, while inset shows the spiral at the background.

Besides the hexa-meronic frustrated AFM Néel state, we identified a rich set of other meronic textures, such as the dodeca-meron, hosting 12 merons, shown in Fig. **6-5** b. Further examples of complex multi-merons are presented in Fig. **C-1** of Appendix C. Similarly to the purely FM counterparts, in confined geometries (see Fig. **C-1** b-c of Appendix C) a "single" AFM Néel meronic state can be stabilized. This object is a tri-meron resulting from three frustrated merons with overlapping cores, carrying in total a half integer topological charge.

6.5. Stability against external magnetic fields

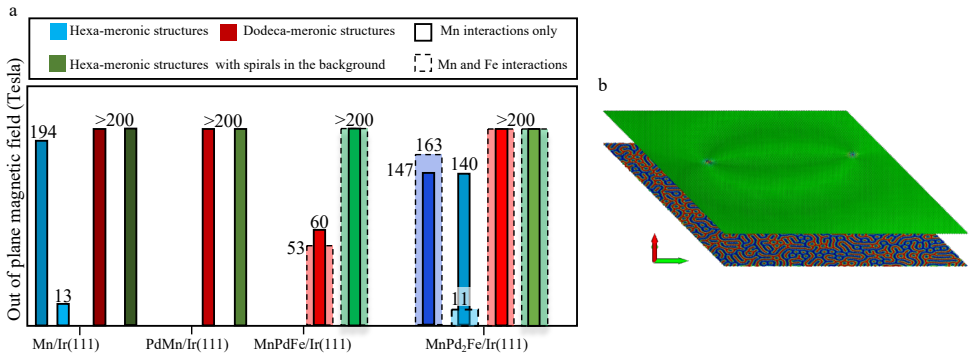

Figure **6-6**.: **Impact of external magnetic field. a** The critical OOP magnetic field annihilating. Blue and red bars refer to respectively hexa- and dodeca-merons emerging in AFM Néel order, while green bars correspond to hexa-merons hosted by initially spiraling Néel states. Bars with solid versus dashed lines distinguish the cases without and with Mn-Fe interactions. **b** Snapshot showing the blue dashed bar representing the Mn layer(upper layer) interfaced with the Fe layer (lower layer) in $MnPd_2Fe$.

Investigating how topologically paired AFM Néel meronic pairs respond to magnetic fields is a crucial aspect to understand their stability and potential non-trivial topological transitions. Remarkably, these frustrated meronic textures exhibit robustness even when subjected to extremely high in-plane magnetic fields exceeding 200 Tesla. However, when an OOP magnetic field is applied, it has a multifaceted impact on the explored spin textures. Therefore, in this context, we conduct a detailed examination of the latter scenario, with a particular focus on three distinct AFM Néel meronic states, as illustrated in Fig. **6-5** a-c and Fig. **6-6** b.

As a prototypical chiral magnetic object, we consider the hexa-meron emerging either in the AFM Néel (Fig. **6-5** a) or in the spiraling AFM Néel states (Fig. **6-5** c) as well as the dodeca-meron (Fig. **6-5** b). For interfaces hosting the Fe layer, MnPdFe/Ir(111) and $MnPd_2Fe$/Ir(111), we examined both cases: switching-off (solid bars in Fig. **6-6** a) and -on (dashed bars in Fig. **6-6** a) the Mn-Fe magnetic interactions. A snapshot for the Mn-hexa-meron interfaced with ferromagnetic Fe spirals and skyrmion is illustrated in Fig. **6-6** b.

While we were expecting the robustness of the unveiled meronic textures against external magnetic fields, we were intrigued by the annihilation of some hexa-merons emerging in an AFM Néel background with experimentally accessible OOP fields, e.g. 10 Tesla, in contrast to dodeca-merons and hexa-merons arising in a Néel spiraling state (red and green bars in

Fig. **6-6** a).

To get insight into the origin of the sensitivity of these magnetic states, hexa-merons forming in an AFM Néel background, we scrutinize the sublattices topological distribution along with the spin orientation at each sublattice of the different hexa-meronic states shown in Fig. **6-7** (see Fig. **C-2** of Appendix C illustrating snapshots of the different hexa-merons). As introduced earlier, there is a quadruple degeneracy for each hexa-meron in the absence of a magnetic field. The four states, denoted Hexa A–D and illustrated in Fig. **6-7**, can be distinguished by the vortex nature of their core constituents and the orientation of the core spins (see Fig. **6-4** k). A finite OOP field lifts partially the degeneracy and favors the hexa-meron, here Hexa D, with most spins pointing along the field direction (see also Fig. **C-2** of Appendix C). Among the four hexa-merons, Hexa D will be the most robust to the applied field and therefore survives gigantic fields. The remaining hexa-merons experience at some point magnetization switching to reach the optimal sublattice topological distribution defined by Hexa D. This requires a flip of the spins for at least one meron (antimeron) implying going through a topological charge transition, being a non trivial process, during which, the AFM meronic structure might encounter an unstable spin distribution, leading to the annihilation of the AFM meronic structure where the AFM vortex and antivortex start rolling towards each other and then collapse at a rather low magnetic field. If the transition occurs, however, the new magnetic state would be capable of surviving large magnetic fields similar to Hexa D.

However, the presence of Néel spirals in the background or additional pairs of AFM meronic textures (leading for example to dodeca-merons) prevent the formation of unstable states within the topological transition induced by the magnetic field, which would lead to the collapse of the frustrated soliton. Effectively, a barrier is provided by enabling the rearrangement of the spins to acquire the desired topological state, which would withstand immense magnetic fields.

6.6. Emergence mechanism of the frustrated multi-merons

The ingredient requested to stabilize the frustrated multi-merons is the stabilization of an in-plane Néel state. A minimal Heisenberg model consists then of a hexagonal two-dimensional lattice with AFM Heisenberg exchange coupling among the first n.n. atoms (J_1). The in-plane orientation of the moments can be enforced by either the in-plane MAE, $K < 0$, as observed in Mn/Ir(111) or by the z-component of the DMI vector (D_z).

The minimal Heisenberg model can be then written as:

$$\mathcal{H} = -\sum_{<ij>} J_1 \, \boldsymbol{n}_i \cdot \boldsymbol{n}_j - \sum_{<ij>} D_1^z (\boldsymbol{n}_i \times \boldsymbol{n}_j)^z, \tag{6-1}$$

which involves D_z only, since the latter played the main role in stabilizing the meronic tex-

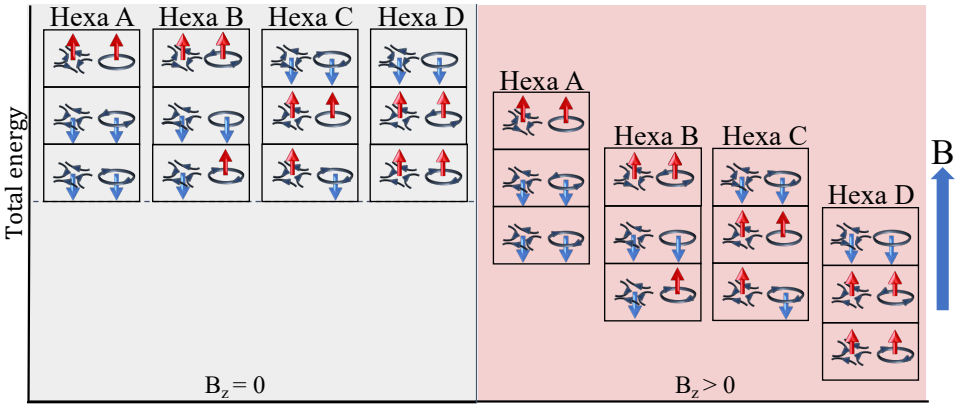

Figure **6-7**.: **Topologically-dependent response to the external magnetic field.** Lifting the quadrupole degeneracy of the hexa-meron (Hexa A–D) upon application of an OOP magnetic field. Each hexa-meron is decomposed into the three sublattices with the illustration of the vortex nature of the meronic core constituents together with the core spin-direction. Hexa D is the frustrated hexa-meron satisfying the ideal stability criterion against the magnetic field.

tures in the four investigated Mn-based interfaces.

To inspect the range of J_1 and D_z values within which the multi-meronic spin textures are stabilized, we change the values of J_1 and D_z and analyze the resulting magnetic states in the phase diagram shown in Fig. **6-8** a. Increasing D_z enforces a stronger in-plane alignment of the spins, which reduces the size of the meronic constituents (Fig. **6-8** b and Fig. **C-3** of Appendix C). Clearly, the size of merons is dictated by a competition between the Heisenberg exchange interaction and DMI. Keeping D_z fixed while increasing the AFM J_1 counteracts the effect of DMI and enlarges the meron core (Fig. **6-8** c).

Fig. **6-8** d presents the critical OOP magnetic field upon which the meronic texture, here Hexa D similar to that shown in Fig. **6-7**, is annihilated as function of the OOP DMI component all normalized by the n.n. AFM Heisenberg exchange interaction. The obtained curve follows a quadratic dependence, highlighting that the DMI enhances the stability of the frustrated merons. In fact, the application of an OOP magnetic field counteracts the influence of the OOP DMI component by tilting the spins to the OOP direction. This causes disruption to the in-plane alignment of the spins, imposed by the OOP DMI component, throughout the surrounding area, including the region spanning between the extremities of the hexa-meron, ultimately leading to its collapse. Consequently, the larger the OOP DMI component (smaller meronic cores), the larger the critical field required to destroy the AFM

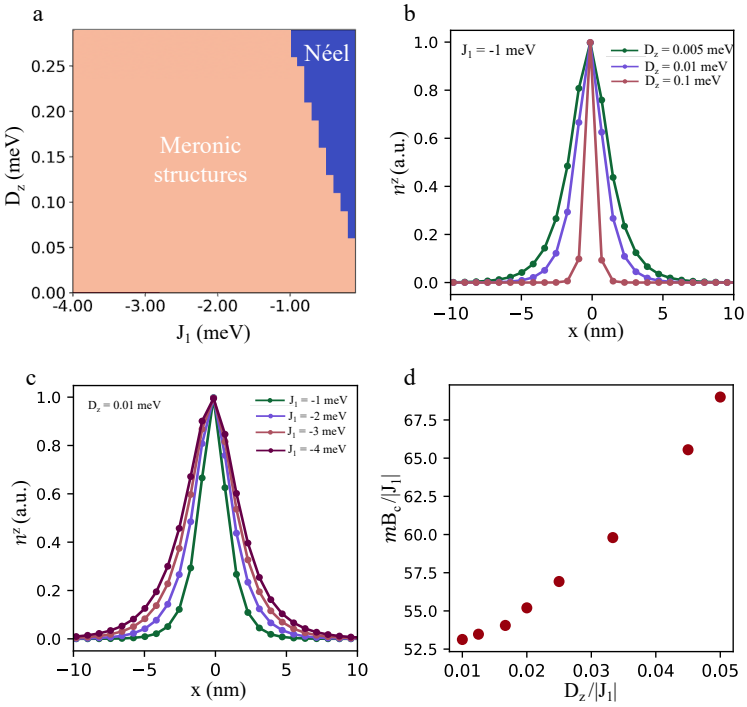

Figure **6-8**.: **Minimal spin model for frustrated AFM Néel multi-merons. a** Phase diagram showing immediate emergence of hexa-merons requiring an AFM n.n. magnetic interaction, J_1, and an OOP DMI component, D_z. **b, c** Mutual impact of magnetic Heisenberg exchange interactions and DMI on the z-component of the magnetization (n^z) profile of one of the vortices. **d** The associated critical field required for the annihilation of the multi-meron as function of the DMI.

spin-swirling textures.

6.7. Conclusion

Our *ab initio* simulations uncovered nonsynthetic Néel-frustrated AFM meronic textures emerging in a realistic set of materials and interfaces. The newly unveiled nanoscale magnetic objects are hosted by a triangular Mn layer interfaced with an Ir(111) surface alone, or covered with a Pd overlayer, or separated from Ir by either a PdFe bilayer or a Pd_2Fe trilayer, which all represent substrates that can readily be grown experimentally. We note that at the time of finishing writing this thesis, spin-polarized STM experiments confirmed our simulations in detected a Néel state in a single Mn layer deposited on Ir(111) surface [214].

The frustrated AFM states form hexa-merons, composed of three FM meronic pairs each located at one of the three FM sublattices building up the AFM Néel background. Other solitons can emerge such as dodeca-merons (12 merons) while confined geometries enable the stabilization of a frustrated tri-meron.

We have observed that these AFM Néel meronic solitons survive high values of magnetic fields if the majority spins align in the direction of the OOP magnetic field. Otherwise, a transition of the sublattice topological charge occurs, leading to the potential annihilation of the AFM solitons at experimentally accessible values of magnetic fields. To gain a better understanding of the characteristics of these AFM solitons, we provided a spin model that outlines the minimum set of magnetic interactions necessary to generate the detected AFM solitons.

We anticipate the integration of these intricate AFM meronic spin-textures into future spintronic devices, where a major aspect to be addressed is the ability to manipulate them, since in general AFM spin-textures are robust to magnetic fields. We expect that the AFM meronic structures, similar to the AFM topological solitons, despite their inherent immunity to magnetic fields, remain amenable to manipulation through external stimuli such as spin currents. For conventional AFM solitons, this was proposed either theoretically [74, 73, 211, 215], or realized experimentally in the synthetic scenario [89, 95, 216]. Moreover, our demonstration of the sensitivity of certain hexa-meronic states to experimentally attainable magnetic fields suggests that the latter can be utilized as an external stimuli to control these frustrated AFM multi-meronic spin-textures, contingent upon the distribution of sequential topological charges across the sublattices.

The discovery of novel AFM solitons with a realistic existence scenario is at the heart of AFM topological magnetism. Our predictions can initiate the experimental discovery of the intriguing intrinsic frustrated multi-meronic textures, which can delineate in various topological sequences. It remains to be explored how such spin states can be implemented and designed in AFM spintronic devices. Certainly, the thin films being proposed provide a solid platform for AFM meronic textures with a potential impact in information technology.

7. Current-driven dynamics of AFM skyrmions

In chapter 4, we unveiled the emergence of intrinsic single and interchained antiferromagnetic (AFM) skyrmions on Cr layer when deposited on PdFe/Ir(111). Understanding the response of these skyrmions to external stimuli, particularly spin-polarized currents, is crucial for their potential application in spintronic devices. A distinguishing feature of AFM skyrmions is their zero topological charge and hence anticipated zero skyrmion Hall effect (SkHE). In this chapter we unveil that the latter is surprisingly finite under the influence of spin-transfer torque, depending on the direction of the injected current impinging on intrinsic AFM skyrmions emerging in CrPdFe trilayer on Ir(111) surface. Hinging on first-principles combined with atomistic spin dynamics (ASD) simulations, we identify the origin of the SkHE and uncover that ferromagnetic (FM) skyrmions in the underlying Fe layer act as effective traps for AFM skyrmions, confining them and reducing their velocity. These findings hold significant promise for spintronic applications, the design of multi-purpose skyrmion-tracks, advancing our understanding of AFM-FM skyrmion interactions and hybrid soliton dynamics in heterostructures.

7.1. Introduction

Building upon the findings revealed in chapter 4 regarding the emergence of intrinsic of single and interchained AFM skyrmions, it becomes motivating to further explore the impact of spin-polarized currents on the dynamical behavior of these magnetic entities, when applying a perpendicular to plane currents (CPP).

Various methods have been proposed to drive magnetic skyrmions, encompassing electric currents [28, 31, 36, 35], spin waves [217], magnetic field gradients [218], temperature gradients [219], and voltage-controlled magnetic anisotropy [220, 221, 222, 223]. However, one significant challenge that arises during their manipulation via electrical means or magnetic field gradient [224] is the SkHE, wherein skyrmion trajectories deviate from the driving current direction due to the Magnus force [225, 56, 70] proportional to the topological charge [41]. This undesired effect hampers the precise control and movement of skyrmions in spintronic devices. In contrast, AFM skyrmions are expected to be transparent to the SkHE since the building-blocks skyrmions carry opposite topological charge, which enforce the motion along the direction of the applied current, as predicted theoretically [73, 117, 74] and observed for significant distances experimentally [89].

Here, we explore the dynamical response of intrinsic AFM skyrmions to an applied current. We consider the scenario of a magnetic tunnel junction (MTJ), where a magnetic electrode injects a perpendicular-to-plane spin-polarized current (SP-CPP) with in-plane polarization on the row-wise AFM (RW-AFM) CrPdFe thin film deposited on Ir(111) surface (Fig. **7-1**). Counter-intuitively, we demonstrate that the AFM skyrmions present in the thin film exhibit a significant SkHE, which is strongly anisotropic, i.e. that is dependent on the polarization direction of the applied spin-current. We identify the origin of the SkHE and its vanishing conditions while unveiling complex interactions when interfacing intrinsic AFM skyrmions hosted in Cr with the spin-textures, including individual FM skyrmions, found in Fe. This unique hybrid scenario enables the exploration of AFM-FM inter-skyrmion dynamics. The mutual inter-skyrmion interactions design a non-trivial two-dimensional energetical map, with pinning and repulsive centers, which impact both the trajectory and velocity of AFM skyrmions and provide pinning and deflection processes. These findings pave the way for further exploration and control of skyrmion-based devices and applications in AFM storage systems.

7.2. Computational details

The *ab initio* part of the simulations as well as the conventional investigation of the magnetic behavior of the emerging skyrmionic states were detailed in the computational details section in chapter 4. We assumed periodic boundary conditions to model the extended two-dimensional system with cells containing 200^2.

We apply the SP-CPP injection to induce transitional motion of AFM skyrmions. In the CPP case, the current is perpendicular to the film plane, but polarized in in-plane direction (Fig. **7-1** a-d). The dynamics of the magnetization $\boldsymbol{n}_i$ at the lattice site i is then governed by the extended LLG equation taking into account the STT term [177, 178, 117, 73, 179], which was introduced in chapter 3 section 3.7. To ease the readability of the current chapter, we reproduce the STT term in the following:

$$\begin{aligned}\frac{\mathrm{d}\boldsymbol{n}_i}{\mathrm{d}t} = &-\frac{\gamma}{(1+\alpha^2)m_i}\boldsymbol{n}_i \times \mathbf{B}^i_{\text{eff}} - \frac{\gamma\alpha}{(1+\alpha^2)m_i}\boldsymbol{n}_i \times \left(\boldsymbol{n}_i \times \mathbf{B}^i_{\text{eff}}\right) \\ &- \frac{\gamma\alpha\eta}{(1+\alpha^2)}\boldsymbol{n}_i \times \boldsymbol{n}_p + \frac{\gamma\eta}{(1+\alpha^2)}\boldsymbol{n}_i \times \left(\boldsymbol{n}_i \times \boldsymbol{n}_{\mathrm{P}}\right),\end{aligned} \tag{7-1}$$

with γ, α and $\mathbf{B}^i_{\text{eff}}$ being respectively the gyromagnetic ratio, Gilbert damping, and the effective field given by $(-\frac{\partial\mathcal{H}}{\partial\boldsymbol{n}_i})$. $\mathcal{H}$ is the Heisenberg Hamiltonian in Eq. (4-1), while the current polarisation direction is defined by $\boldsymbol{n}_{\mathrm{P}}$ and the current amplitude is quantified by $\eta = \frac{j_s P g \mu_B}{2edM_s\gamma}$. Here j_s is the current density, P the polarization, M_s the saturation magnetization in each sublattice and g the Landé factor while d is the film thickness.

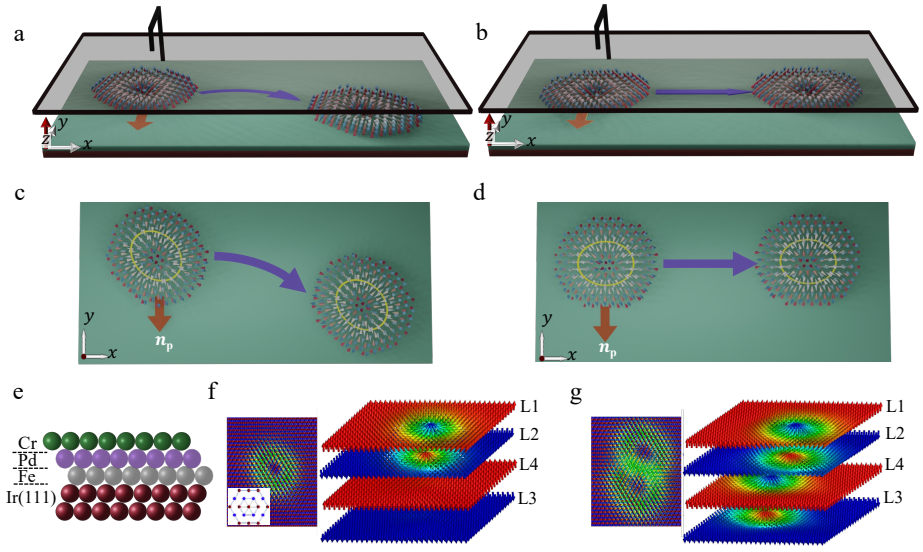

Figure **7-1**.: **Current-driven dynamics of AFM skyrmions. a, b** Schematic representations of CPP induced motion of an elliptical AFM skyrmion showing the SkHE **a** or not **b** depending on the alignment of the polarization of the applied current $\boldsymbol{n}_{\mathrm{P}}$ with respect to the skyrmion. **c, d** Top view of **a** and **b**, respectively. **e** Schematic representation of the material hosting intrinsic AFM skyrmions at the triangular lattice of a Cr layer grown on PdFe film deposited on an fcc(111) surface of Ir. As discussed in chapter 4 the ground state in the Cr layer is the RW-AFM configuration illustrated in the top view of the surface as red and blue spheres for different orientation of the spins shown in inset of **f**. For completeness, snapshots of single **f** and double **g** overlapping AFM skyrmions emerging in the Cr film with the spins distribution among four sublattices L1-L4.

7.3. Trajectories of AFM skyrmions driven by perpendicular-to-plane currents

When injecting the SP-CPP as illustrated in Fig. **7-1**, one expects a straight motion of an AFM skyrmion along the direction perpendicular to the polarization $\boldsymbol{n}_{\mathrm{P}}$ of the applied spin current j_s [117, 73], as illustrated in Fig.**7-1** b-d.

We initiate our study by investigating the case of single AFM skyrmions and consider two possibilities: either (i) by neglecting the Cr-Fe magnetic exchange interactions, which corresponds to a free standing Cr film (Fig. **7-2** a), or (ii) not by scrutinizing various magnetic

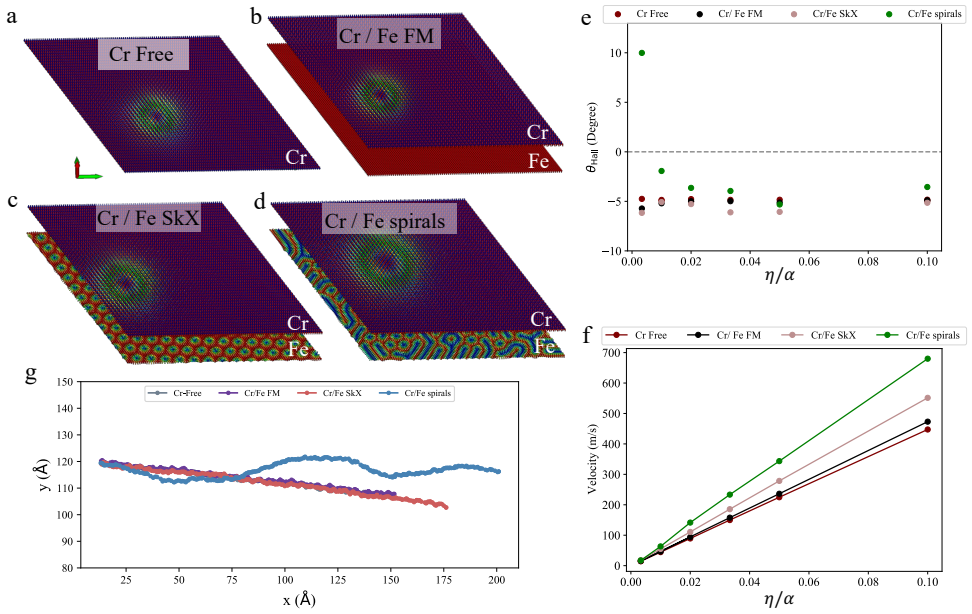

Figure **7-2**.: **Transitional motion of elliptical AFM skyrmion driven by SP-CPP currents. a-d** Snapshots of the AFM skyrmion at Cr layer in four different cases: **a** Cr-free case, where the magnetic interactions with Fe layer are not included (AFM skyrmion radius is 2 nm); **b** Fe interactions are included with a finite magnetic field saturating Fe into an FM state (AFM skyrmion radius is 2.1 nm) while **c** a weaker magnetic field leads to a skyrmion lattice (SkX) which slightly enlarges the AFM skyrmion (radius of 2.5 nm); **d** in the absence of a magnetic field spirals emerge at Fe layer (AFM skyrmion reaches a radius of 3.2 nm). **e** Impact of the current parameter ratio η/α on the skyrmion Hall angle, and **f** on velocity. **g** The trajectories of the AFM skyrmion for cases in **a-d** with η/α =0.01 meV.

states in PdFe, which can be tuned by applying a magnetic field (Fig. **7-2** b-d). For the latter, we consider the case of a saturated FM state in the Fe film (Fig. **7-2** b), which is obtained upon application of a large magnetic field, while a moderate field can transition the spin-spiraling state shown in Fig. **7-2** d to a skyrmion lattice (SkX) illustrated in Fig. **7-2** c [27, 106]. The effective impact of the spin current can be monitored via the current parameter η, which is directly proportional to j_s (see computational details section).

As mentioned before, AFM skyrmions exposed to spin-polarized currents via STT, typically do not experience a SkHE [117, 73, 185, 74, 89] while their velocity is expected to be proportional to η/α in the case of CPP injection [185]. Surprisingly, our AFM skyrmions exhibit an

unexpected dynamical behavior, deviating from conventional expectations. Independently from the Cr-Fe interaction and the nature of the magnetic state pertaining to the PdFe film, the Hall angle is found overall to be around -5° (negative sign means the deviation is clockwise), which remains consistent across various η/α values (Fig. **7-2** e). Deviations occur, however, for weak driving forces (small η/α) when Cr is placed atop Fe spin spirals. Indeed, the AFM skyrmions display then an irregular 'Brownian-like' motion as depicted in Fig. **7-2** g, due to uncontrolled scattering at various spin-textures emerging in Fe. In this particular case, the extraction of the Hall angle is not trivial, since the skyrmion trajectories are not straight. Impressively, the Fe spirals can strongly deflect the AFM skyrmions, which can lead to effective Hall angles that are larger than 10°, as calculated up to average distances of about 90 nm. Overall, the Hall angles are found to be the smallest (largest) atop the SkX Fe (Fe spirals).

The velocity of the skyrmions is linear with η/α, with the largest speed found when Fe host a spirals state (Fig. **7-2** f). Intriguingly, the Cr-Fe interaction in general favors large skyrmion velocities, which can be traced back to the size of the skyrmions. Indeed the Cr-Fe interaction enlarges the diameter of the AFM skyrmion, which is known to increase its velocity [226, 227], as unveiled in the upcoming analysis.

Fig. **7-2** e-f is just the tip of the iceberg. By scrutinizing the skyrmion dynamics as function of the direction of the applied current, we unveil a rich anisotropic response: both the Hall angles and velocities are modified and we identify directions along which the SkHE cancels out. Before discussing the anisotropic current-driven dynamical response, we briefly address the origin of this behavior, which is induced by the ellipticity of the AFM skyrmions emerging in CrPdFe/Ir(111) surface. By carefully scrutinizing the AFM skyrmions, one can identify an elliptical shape. For instance the single AFM skyrmion shown in Fig. **7-3** c has a major and minor axis of 2.2 nm, and 1.8 nm, respectively. Upon formation of a double AFM skyrmion, the shape of the skyrmions remains elliptical. The size of the skyrmions forming the solitonic dimer, experiences a significant increase, enlarging both the major and minor axes of the skyrmion building-blocks to 3 nm and 2.4 nm, respectively. The origin of the observed ellipticity can be traced back to the interplay between the neighboring exchange interactions as elaborated in chapter 5 section 5.5. Phenomenologically, one can demonstrate that by tuning the underlying interactions, the skyrmions can be reshaped into an isotropic form. We note that this is clearly a material dependent property.

7.4. Directionality of the current-driven elliptical AFM skyrmions

To explore the anisotropic current-driven response of the AFM skyrmions, we focus here on the case of the free-standing Cr layer, i.e. with the Cr-Fe interaction switched-off, which is also representative of the behavior found when the interaction is switched on while the Fe

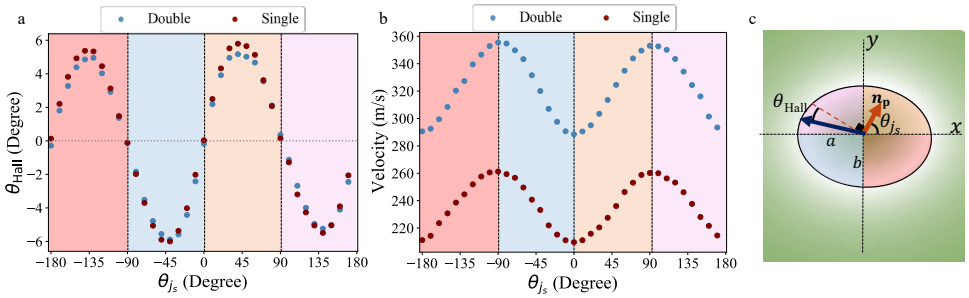

Figure **7-3**.: **Influence of the direction of current polarization on the skyrmion Hall angle and velocity of elliptical AFM skyrmions. a** The skyrmion Hall angle and **b** velocity of AFM skyrmions as a function of the angle θ_{j_s} between the current polarization direction and the major ellipse axis, for single (brown) and double(blue) AFM skyrmions, with $\eta/\alpha = 0.05$ meV. **c** Schematic representation of the AFM skyrmion showing an elliptical shape, with a long (short) axis defining the x-axis (y-) axis. The angles associated with the spin-polarization of the current $\boldsymbol{n}_{\text{P}}$ and the SkHE are displayed. The colored regions within the ellipse correspond to those shown in **a** and **b**.

film hosts either the skyrmion lattice or the saturated FM state. As an example, we inject a current with $\eta/\alpha = 0.05$ meV, but varying systematically the angle θ_{j_s} between the in-plane current and the major axis of the ellipse, which is represented by the orange dashed line in Fig. **7-3** c.

The skyrmion Hall angle as function of θ_{j_s} is illustrated in Fig. **7-3** a, which clearly shows an oscillating behavior for both the single (brown) and double (blue) AFM skyrmions, with color coded regions corresponding to colored areas depicted in Fig. **7-3** c. From Fig. **7-3** a, one can notice that θ_{Hall} is suppressed when the current is polarized along the two ellipse axes, and reaches its maximum value of about 6° when $\theta_{j_s} = 42°$. Notably, it is not only the Hall angle that changes with θ_{j_s}; the velocity of AFM skyrmions also varies as shown in Fig. **7-3** b, exhibiting the maximum (minimum) velocity when the skyrmions move along the ellipse major (minor) axis. Interestingly as depicted in Fig. **7-3** a, double and single AFM skyrmions show the same Hall angle when subjected to the same polarized currents, however the double AFM skyrmion moves faster than the single (Fig. **7-3** b).

7.5. Thiele equation for elliptical AFM skyrmions

To comprehend these intriguing findings, we analyze the Thiele equation governing skyrmions driven by CPP [228, 29, 117, 73, 70]:

$$\mathbf{G} \times \mathbf{v} - \alpha \mathcal{D} \cdot v + \mathcal{B} \cdot \boldsymbol{n}_{\text{P}} = 0, \tag{7-2}$$

where, $\mathbf{G} = (0, 0, Q)$, with Q is the topological charge of the skyrmion being $+1, -1$ for core up, core down FM skyrmions, respectively. $\mathbf{v}$ is the skyrmion velocity, $\mathcal{D}$ is the dissipative tensor, where $\mathcal{D}_{\mu\nu} = \int d^2\mathbf{r}\left(\partial_\mu \boldsymbol{n} \cdot \partial_\nu \boldsymbol{n}\right)/4\pi$, and $\boldsymbol{n}(\mathbf{r})$ is the magnetic skyrmion profile can be expressed as, $\boldsymbol{n}(\mathbf{r}) = \boldsymbol{n}(\theta, \phi) = (\sin\theta\cos\phi, \sin\theta\sin\phi, \cos\theta)$. $\boldsymbol{n}_{\mathrm{P}} = (\cos\theta_{j_s}, \sin\theta_{j_s})$ stands for the unit vector defining the spin polarization direction of the injected current. Note that the x and y axes are defined respectively by the large (semi-major) and small (semi-minor) axes of the elliptical skyrmion (see Fig. **7-3** c). $\mathcal{B}$ is the driving force related tensor, where $\mathcal{B}_{\mu\nu} = \gamma\eta \int d^2\mathbf{r}\left(\partial_\mu \boldsymbol{n} \times \boldsymbol{n}\right)_\nu /4\pi$.

For each building-block FM skyrmion i forming the AFM skyrmion, the associated components of the dissipative tensor [229], assuming skyrmions of identical size and shape, are given by: $(\mathcal{D}^i_{xx}, \mathcal{D}^i_{yy}) = \frac{\pi^2}{8}\left(\frac{b}{a}, \frac{a}{b}\right)$, where a, and b are the semi-major and semi-minor ellipse axes, while $\mathcal{D}^i_{yx} = \mathcal{D}^i_{xy} = 0$. The components of the driving force tensor are $(\mathcal{B}^i_{xy}, \mathcal{B}^i_{yx}) = \frac{\gamma\pi}{8}\eta(-b, a)$ and $\mathcal{B}^i_{xx} = \mathcal{B}^i_{yy} = 0$.
So, Eq. (7-2) for elliptical AFM skyrmion reads,

$$-\alpha\mathcal{D}^i_{xx}v_x\hat{\imath} - \alpha\mathcal{D}^i_{yy}v_y\hat{\jmath} + \mathcal{B}^i_{xy}\sin\theta_{js}\hat{\imath} + \mathcal{B}^i_{yx}\cos\theta_{js}\hat{\jmath} = 0, \tag{7-3}$$

The skyrmion velocity is then given by:

$$\mathbf{v} = \frac{1}{\alpha}\left(\frac{\mathcal{B}_{xy}}{\mathcal{D}_{xx}}\sin\theta_{j_s}, \frac{\mathcal{B}_{yx}}{\mathcal{D}_{yy}}\cos\theta_{j_s}\right) = \frac{\gamma\eta a}{\pi\alpha}\left(-\sin\theta_{j_s}, \frac{b}{a}\cos\theta_{j_s}\right), \tag{7-4}$$

$$|\mathbf{v}| = \frac{\gamma\eta a}{\pi\alpha}\sqrt{\sin^2\theta_{j_s} + \frac{b^2_{sk}}{a^2_{sk}}\cos^2\theta_{j_s}}, \tag{7-5}$$

where one immediately notices that if the skyrmions were circular isotropic, the polarization of the spin-current is perpendicular to the velocity since $\mathbf{v}\cdot\boldsymbol{n}_p = 0$. The propagation direction associated to the isotropic case case defines the reference angle from which the skyrmion Hall angle is measured $\theta_{\mathrm{ref}} = \tan^{-1}\frac{v_y}{v_x} = \theta_{j_s} + \frac{\pi}{2}$. Therefore, the Hall angle is evaluated from:

$$\theta_{\mathrm{Hall}} = \arctan\left[\frac{b}{a}\tan\left(\theta_{j_s} + \frac{\pi}{2}\right)\right] - \left(\theta_{j_s} + \frac{\pi}{2}\right). \tag{7-6}$$

With these findings at hand, we can explain the behavior of the AFM skyrmions. If the current is polarized along the major or minor axes of the spins, i.e. θ_{j_s} is a multiple of $\frac{\pi}{2}$, the Hall angle cancels out, which define the extrema of the velocity given by $\frac{\gamma\eta b}{\pi\alpha}$ for $\theta_{j_s} = 0, \pi$ (minimum) and $\frac{\gamma\eta a}{\pi\alpha}$ for $\theta_{j_s} = \frac{\pi}{2}, \frac{3\pi}{2}$ (maximum). The ratio $\frac{b}{a}$, which is about 0.8 for both the single and double AFM skyrmions, defines the magnitude of the Hall angle as well as the range of oscillations in the velocity. This means with elliptical AFM skyrmions, we have two more degrees of freedom to manipulate the CPP induced motion of the AFM skyrmions, where the skyrmion exhibits its maximum velocity when injecting currents polarized along its minor axis, resulting in a Hall free motion along the major axis. This analysis goes along with our findings depicted in Fig. **7-3** b, where the double AFM skyrmion with dimensions

of $(a, b) = (3, 2.4)$ nm moves with maximum velocity of 355 m/s while the single AFM skyrmion with smaller size (dimensions of $(2.2, 1.8)$ nm), and hence slower motion according to Eq. (7-4), where its maximum velocity reaches 260 m/s. The maximum Hall angle is expected for $\theta_{j_s} + \pi/2 = \arccos\sqrt{\frac{b}{a+b}}$, which leads to $\theta_{j_s} = 42°$ and $\theta_{\text{Hall}} = 6.2°$ in agreement with the numerical findings of the previous section. Notably, the impact of ellipticity of FM skyrmions subjected to spin currents was discussed in Refs. [230, 229, 231].

7.6. Current-driven dynamics of AFM skyrmions interacting with FM skyrmions

When the Fe substrate hosts spirals with an inhomogeneous distribution of FM skyrmions, we unveiled in Fig. **7-2** g that the intrinsic AFM skyrmions driven in the Cr overlayer exhibit typical dynamics pertaining to interactions with defects. In this section, we explore the synthetic configuration of an AFM skyrmion interacting with a FM one through a Pd film. This scenario is trivially realized in CrPdFe/Ir(111) surface by applying an out-of-plane magnetic field, which reduces the size of the FM skyrmions and transforms the lattice configuration into individual topological objects. By applying spin-polarized current, as done previously, we drive an AFM skyrmion living in the Cr film towards a pinned FM skyrmion hosted by the Fe layer. We consider two cases, either the planned skyrmion trajectory passes trough the FM skyrmion, or it is shifted (see Fig. **7-4** a-b). We notice that when the applied current is not strong enough, the AFM skyrmion gets pinned at the FM skyrmion, which clearly indicates the attractive nature of the FM-AFM skyrmion interaction. This scenario is evident when $\eta/\alpha = 0.001$ meV, where the AFM skyrmion gets trapped by the FM skyrmions, as shown in Fig. **7-5**. When the applied current is larger, e.g. $\eta/\alpha = 0.017$ meV, the AFM skyrmion experiences a velocity increase from the initial 75 m/s to reach 130 m/s once getting close to the FM skyrmion, which leads to a "speeding up zone" as shown in Fig. **7-4** c. Conversely, if the driving force surpasses the attraction force, the AFM skyrmion overtakes the FM skyrmion, and experiences a velocity reduction of about 88% down to around 15 m/s due to FM-AFM skyrmion interaction that opposes the driving force and leads to a "slowing-down zone". As the AFM skyrmion moves away from the proximity of the FM skyrmion, it is no longer influenced by the attraction force. In this phase, only the driving force dictates its motion, resulting in a "constant motion regime", depicted in Fig. **7-4** c and Fig. **D-1** c of Appendix D, where the velocity stabilizes at approximately 75 m/s.

If the AFM skyrmion is off-centered with respect to the FM one, their mutual attractive interaction is capable of deviating the underlying trajectory to bring the AFM skyrmion to the vicinity of the FM one as depicted schematically in Fig. **7-4** b and demonstrated systematically for different paths illustrated in Fig. **7-4** d and Figs. **D-1**, **D-2**, and **D-3** of Appendix D. Due to the AFM-FM skyrmion attraction the AFM skyrmion deflects at the vicinity of the FM one and then continues its motion along a straight line with a velocity

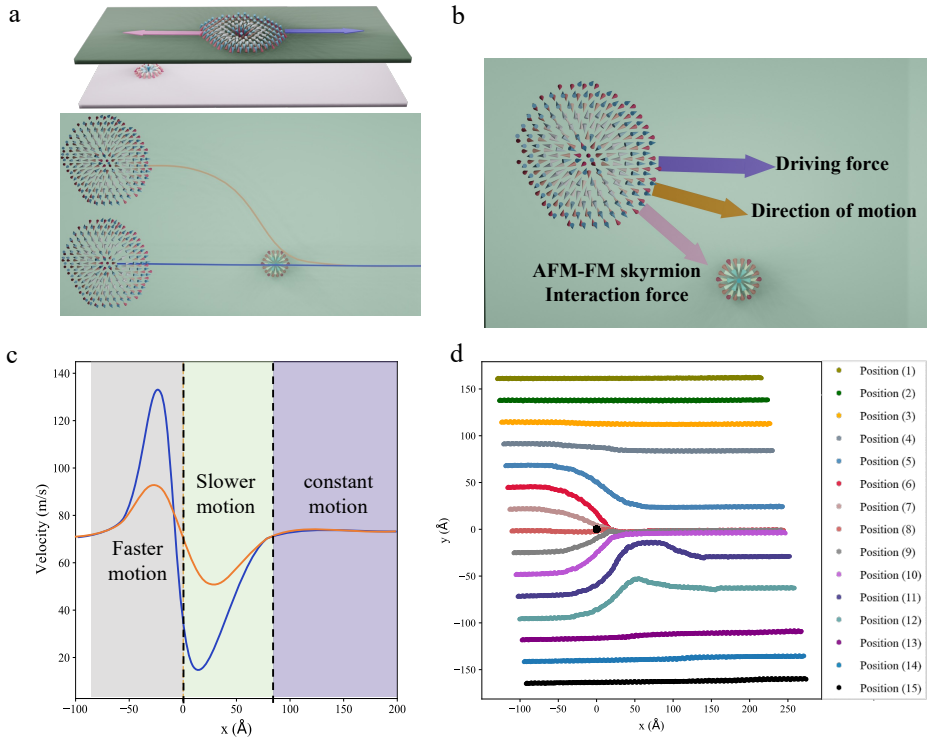

Figure **7-4**.: **Position dependent deflection of AFM skyrmions due to the AFM-FM skyrmionic interaction.** **a, b** Schematic representation of the forces acting on the AFM skyrmion: The driving force due to the applied spin current and the AFM-FM skyrmionic interacting induced by the FM skyrmion in the Fe layer through the Pd-spacer. In **a** two trajectories with different starting points are illustrated. **c** Schematic representation of the effect of the Fe FM skyrmion on the velocity of the AFM skyrmion with the blue and orange lines corresponding to the paths shown in **a**. **d** The trajectory of the AFM skyrmion shown in **a** when current-driven toward a pinned FM skyrmion considering different initial positions (motion from left to right). Deflection in the motion direction occurs depending on the relative position between the AFM and FM skyrmions.

of 75 m/s. Intriguingly, a second deflection manifests when the AFM skyrmion starts an approach from positions (11) and (12) after passing the FM skyrmion, which signals a non-trivial energy profile of the hybrid AFM-FM skyrmionic interaction.

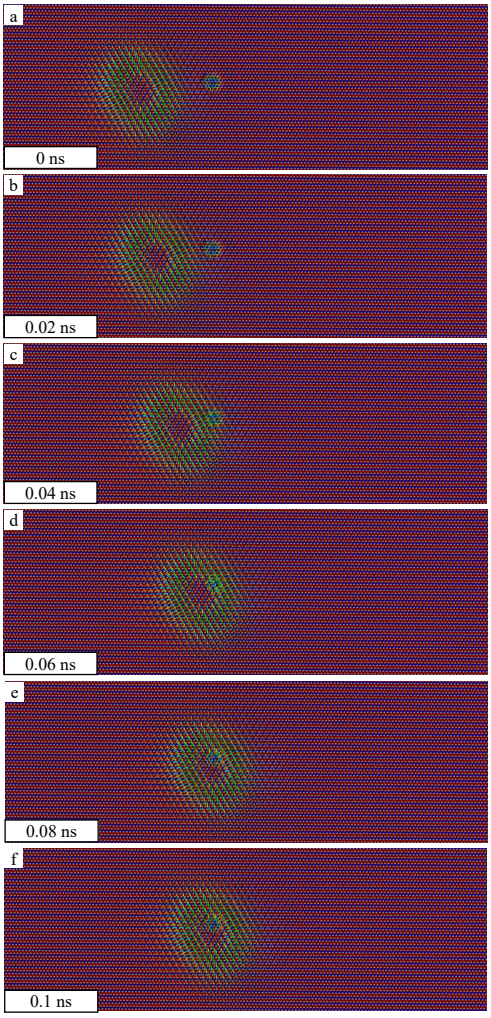

Figure **7-5**.: **AFM skyrmion trapped by a FM skyrmion at Fe layer. a-f** Snapshots showing how AFM skyrmion got trapped by FM skyrmion at low driving force, with η/α=0.001 meV.

7.7. AFM-FM skyrmion interaction profile

To elucidate the underlying reason for the unanticipated second deflection mentioned in the previous section, we analyse the AFM-FM skyrmion interaction profile. Since the AFM skyrmion in Cr film is made of two FM skyrmions oppositely oriented with respect to each

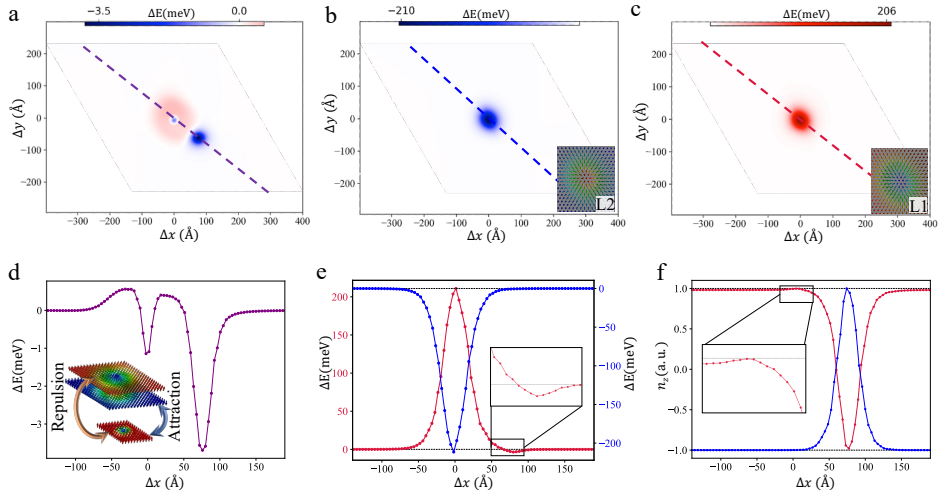

Figure **7-6**.: **AFM-FM skyrmion interaction profile.** **a** Two-dimensional heat map of the total energy difference resulting when rigid-shifting the AFM skyrmion all over the lattice with the presence of Fe-FM skyrmion at the center of the Fe layer. The energy difference is taken with respect to the case when the two skyrmions are not interacting. This energy difference is further decomposed into the interaction with the AFM skyrmions building-blocks: the red-cored FM skyrmion residing at sublattice L2 **b**, which is of attractive nature, and the interaction with the blue-cored skyrmion residing at sublattice L1 **c**, which is of repulsive nature. **d** Energy profile along the purple line indicated in **a**, decomposed in **e** into the L2 blue and L1 red contributions. **f** The z component of the spin in the two sublattices L1 (blue) and L2 (red) along the purple line when the AFM skyrmion positioned at the second minimum shown in **a**. Inset in **d** is a schematic representation of the nature of the interaction between the building blocks of the AFM skyrmion and the FM Fe-skyrmion.

other, we expect two competing interactions with the FM skyrmion in Fe layer, as shown in the inset of Fig. **7-6** d. The FM skyrmions having their cores pointing in the same direction and residing in the same FM background would repel each other, while those having an opposite magnetic alignment would attract each other. This is clearly illustrated in Fig. **7-6** b, and c, respectively, which shows the energy contribution of both types of coupling to the energy profile, that is obtained by rigidly shifting the AFM skyrmion all over the Cr lattice atop the FM skyrmion pinned in center of the Fe film. The total interaction heat map depicted in Fig. **7-6** a exhibits a minimum when the AFM skyrmion overlaps with the FM skyrmion, signifying their mutual attraction. A second minimum appears when the AFM skyrmion is positioned in the lower right part of the FM skyrmion, which explains the

aforementioned second deflection experienced by the AFM skyrmion as noted in the previous section.

The surprising second minimum finds its origin in the intrinsic asymmetric shape of the AFM skyrmion with respect to the skyrmion core residing in one of the sublattices, as illustrated in Fig. **D-4** of Appendix D. When interfaced with the Fe FM spins, the Cr spins residing in the background of sublattice L1 tilt away from their initial direction, while those residing in sublattice L2 get more collinear and antiferromagnetically aligned with respect to the Fe-magnetization, see the red and blue plots respectively in Fig. **7-6** f obtained along the purple line in Fig. **7-6** a when positioning the Cr skyrmion at the second minimum. At the vicinity of the Fe FM-skyrmion, the interaction picture gets reversed, which leads to the sublattice-dependent interaction profile shown in Fig. **7-6** e. In particular, the asymmetric profile of the AFM skyrmions together with the magnetic interaction across the sublattices enable an energy gain in an area of sublattice L1, where the Cr spins benefit from the AFM coupling with the core of the Fe skyrmion, see the kink in the spin profile highlighted in the inset of Fig. **7-6** f. Unveiling the interaction profile between AFM and FM skyrmions holds significant importance, as it offers an opportunity for manipulating and regulating the trajectories and dynamics of AFM skyrmions by strategically positioning pinned FM skyrmions at the Fe layer.

7.8. Conclusion

In this chapter, we uncovered the intricate dynamics of intrinsic AFM skyrmions subjected to perpendicular to plane spin polarised currents, with a particular attention to the impact of FM skyrmions emerging in a hybrid heterostructure (CrPdFe/Ir(111) surface) made of an AFM layer (Cr) separated from an FM layer (Fe) by a Pd spacer layer. In contrast to expectations, even in AFM skyrmions we demonstrate the emergence of the SkHE stemming from the elliptical shape of the topological states. Both the SkHE and skyrmion velocity are anisotropic and follow well defined dependencies with respect to the polarization direction of the applied currents. The ability to manipulate the polarization direction of impinging spin currents provides a clear avenue for designing tracks where the SkHE either diminishes or persists.

The presence of non-trivial magnetic states in the FM film can impact the dynamics of the AFM skyrmions by tuning both their velocity and trajectory. For instance, FM skyrmions act as pinning centers, which depending on the applied current can deflect AFM skyrmions. The seeding of FM skyrmions modifies non-trivially the emergent hybrid AFM-FM skyrmionic interaction profile, which can host several minima, offering the potential of customizing pathways for the motion of AFM skyrmions (see examples illustrated in Fig. **D-5** of Appendix D).

In summary, our study advances the understanding of AFM skyrmion dynamics and their interplay with FM skyrmions. These insights hold great promise for the development of in-

novative spintronic devices that harness the unique properties of AFM and FM spin textures. As the field of AFM spintronics continues to evolve, this research contributes to the foundation for efficient information processing and storage schemes, potentially revolutionizing the realm of next-generation spintronic technologies.

8. Topological magnetism in diluted artificial adatom lattices

In the previous chapters, we addressed conventional scenarios for the emergence of topological spin-textures. By conventional, we mean that we have explored magnetic films interfaced with heavy metallic substrates. In this chapter, we propose a bottom-up approach for the construction of topological magnetic textures by considering magnetic adatoms forming diluted structures deposited on a non-magnetic substrate. We choose as a substrate Nb(110) surface, which is heavily investigated as a superconducting platform on which adatom-based nanostructures trigger trivial and potentially non-trivial states in the superconducting gap of Nb. Our goal, however, is not aiming at studying topological superconductivity but at demonstrating that topological spin-textures of FM and AFM nature can emerge in diluted adatom-based lattices, wherein the magnetic interactions are mainly mediated by the substrate, which enables exploration of a portion of the magnetic phase diagram not reachable with conventional magnetic thin films.

8.1. Introduction

The bottom-up construction of artificial nanostructures offers an exceptional framework for investigating synthetic quantum states of matter, meticulously engineered atom by atom [232, 233]. The groundbreaking creation of the inaugural quantum corral [234], enabling the visualization of confined electronic states, propelled scanning tunneling microscopy (STM) and spectroscopy (STS) into indispensable tools for crafting and customizing the electronic and magnetic characteristics of materials at the atomic level.

Arranging atoms into chains and clusters facilitates the exploration of a rich array of quantum phenomena, including quantum-confined electrons [235, 236, 237], Dirac bands [238, 239], flat bands [240], and topological defects [241, 242]. The magnetic states exhibited by such nanostructures exhibit intriguing complexity influenced by underlying competing interactions [243, 244, 245, 246, 247, 248]. Atomic impurities possess the capacity to influence the stability of large spin textures by either pinning or deflecting them [72, 249, 250, 65, 251]. Man-engineered nanostructures can induce chiral orbital magnetism [252, 253, 254] and give rise to novel magnetoresistance effects [255]. Superlattices of adatoms can emerge through interactions mediated by surface-state electrons [256, 257], which are influenced by Friedel charge oscillations [258, 259] leading to long-range magnetic interactions known as Ruderman-Kittel-Kasuya-Yosida (RKKY) interactions [260, 261, 262]. These interactions,

such as the isotropic Heisenberg interaction and the spin-orbit induced Dzyaloshinskii-Moriya interaction (DMI) [42, 43], oscillate and decay as a function of distance. They play a dominant role when magnetic atoms are placed directly atop a metal surface and have been quantified through measurements and electronic simulations in various diluted nanostructures [263, 264, 265, 266, 267, 268].

The capability to fabricate artificial atomic lattices with adjustable inter-atomic distances presents a unique opportunity to explore a vast magnetic phase diagram, a feat unattainable with conventional materials without altering their chemical compositions and structures. One remarkable example that hinges on the delicate balance of various magnetic interactions is the emergence of magnetic skyrmions [269, 28, 41, 270, 54, 271, 272, 66].

By adjusting the separation between magnetic atoms, it becomes possible to toggle the magnetic coupling from FM to AFM, manipulate the chirality governed by the DMI, or even access a regime where the Heisenberg magnetic interaction is eclipsed by the DMI [264, 265, 266, 267]. This motivates the design of artificial lattices capable of realizing topological magnetic textures. Herein, we examine the case of Cr, Mn, or Fe adatoms deposited on a Nb(110) surface, renowned for its superconducting properties and extensively utilized in cutting-edge experiments [273]. These experiments aim to probe the potential emergence of topological Majorana boundary states [274, 275, 276] or trivial ones [277, 278, 279, 280, 281]. Recently, it was demonstrated that two-dimensional diluted lattices comprising Cr adatoms atop a Nb(110) surface host two types of mirror-symmetry-protected topological superconductors [282].

Hinging on first-principles simulations combined with atomic spin-dynamics (ASD) (see computational details section), we illustrate that the magnetic interactions among the adatoms on various lattices give rise to diverse magnetic states, such as domain walls, skyrmions, and antiskyrmions. Noting that skyrmions, being FM or AFM, have been proposed to trigger the formation of Majorana states once interfaced with a superconductor [283, 284], the proposed diluted lattices provide an appealing playground for the exploration of topological superconductivity.

8.2. Computational details

As explained in the previous chapters and outlined in chapter 3, our approach involves a two-fold procedure, combining *ab initio* calculations with ASD. Similarly to the experimental construction of the adatoms-based diluted structures reported in our article [282], we consider two possible lattices denoted as (A) and (B), visually depicted in Fig. **8-1**. We assume a slab configuration consisting of 5 Nb layers and 1 diluted adatoms-based layer. In each layer we have 8 atoms per unit cell for lattice A, and 9 atoms per unit cell for system B. We place the diluted magnetic layer (the magnetic adatoms are either Cr, Mn or Fe) such that the adatoms reside on the hollow stacking site as depicted in Fig. **8-1**.

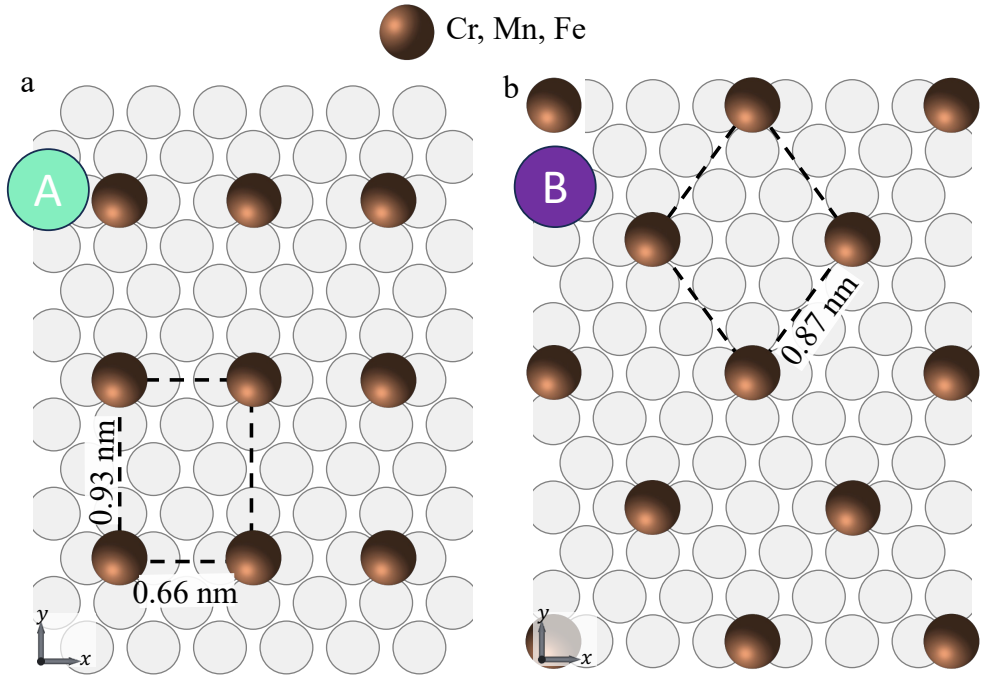

Figure **8-1**.: **Diluted lattices. a, b** Schematic representation of the magnetic adatoms positioned in both investigated lattice types, (A) the rectangular lattice with the first (second) nearest neighbours atoms separated by 0.66 nm (0.93 nm), and (B) the rhombic lattice with the first nearest neighbors set 0.87 nm apart.

After extracting the magnetic interactions characterizing the adatoms, we solve, as done in the previous chapters, the Landau-Lifshitz-Gilbert (LLG) equation to minimize the underlying extended Heisenberg Hamiltonian (see section 2.4 in chapter 2).

8.3. Magnetic interactions among the magnetic adatoms on Nb(110)

The magnetic interactions among the magnetic adatoms (Cr, Mn, and Fe) as a function of distance are shown in Fig. **8-2**, **8-3**, and **8-4**, for Cr, Mn and Fe, respectively. Our first-principles calculations reveal that the magnetic interactions among the first nearest neighbors (n.n.), and beyond depend strongly on the types of the considered adatom lattices. For instance, the first n.n. Heisenberg exchange interactions among Mn adatoms transition from

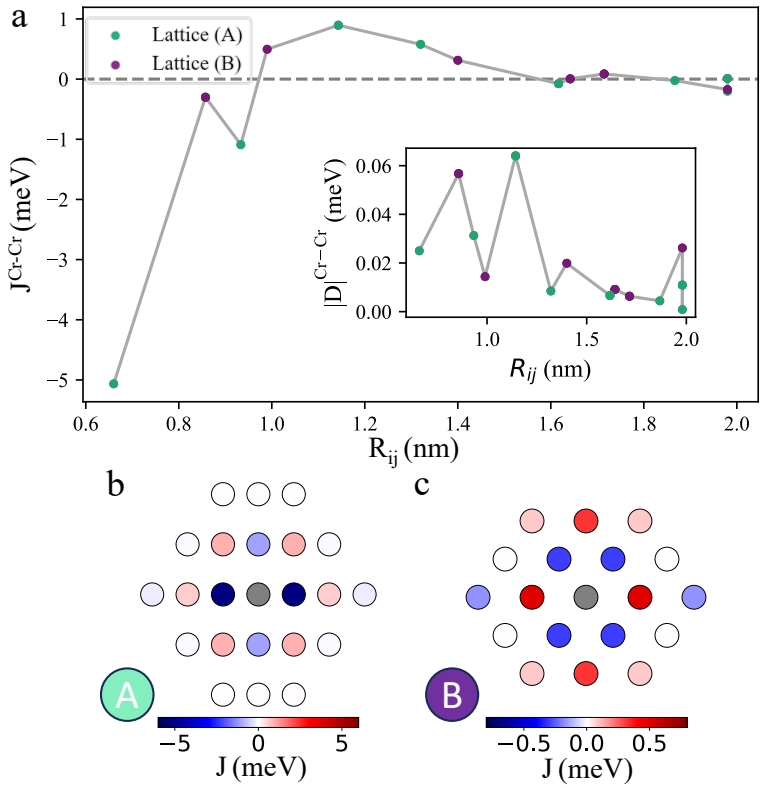

Figure **8-2**.: **Magnetic interactions among Cr adatoms on Nb(110). a** Heisenberg exchange interactions among Cr atoms as a function of the distance, with the DMI values in inset. The values obtained for both lattices are plotted in the same curve. The lines serve as a guide for the eye. **b, c** Illustration of the simulated lattices, where each circle is coloured as a function of the size of J with respect to the central atom (grey colour). The positive (negative) values correspond to FM (AFM) coupling.

FM coupling (J_1= 2 meV) in the rectangular lattice (lattice (A)) to AFM coupling (J_1= -0.43 meV) in the rhombic lattice (lattice (B)). For Cr adatoms, the n.n. AFM coupling is reduced by 94%, decreasing from -5 meV to -0.3 meV. While the Fe adatoms experience a cancellation of the magnetic interaction, initially FM, when placing them in lattice (B) instead of (A). The DMI is found to be finite and can be of the same order of magnitude than the Heisenberg exchange interactions (e.g. Mn in lattice (B)). Alternatively, in the other cases, it can be one to two orders of magnitude smaller than the Heisenberg exchange

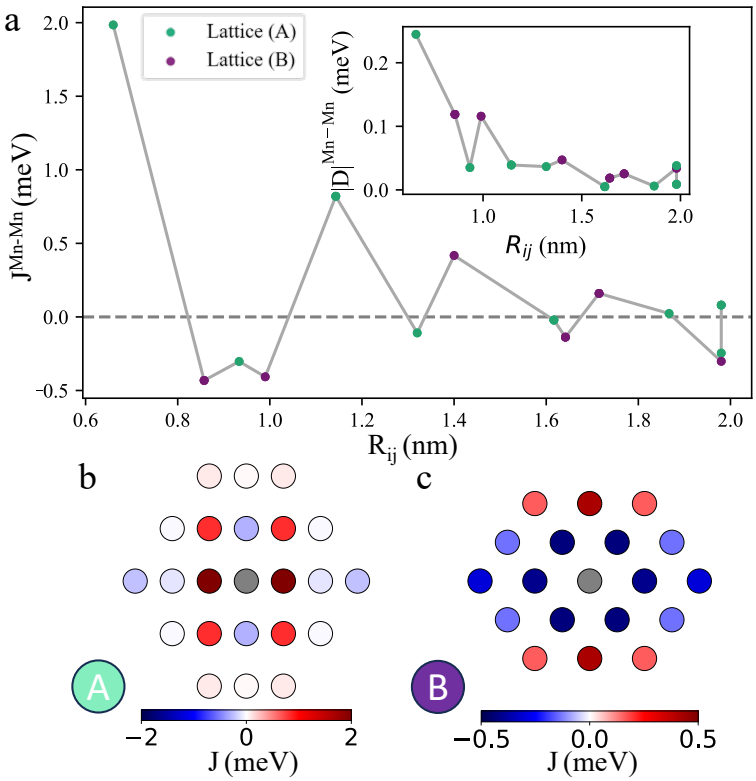

Figure **8-3**.: **Magnetic interactions among Mn adatoms on Nb(110). a** Heisenberg exchange interactions among Mn atoms as a function of the distance, with the DMI values in inset. The values obtained for both lattices are plotted in the same curve. The lines serve as a guide for the eye. **b, c** Illustration of the simulated lattice, where each circle is coloured as a function of the size of J with respect to the central atom (grey colour).

interactions.

Notably, not only the Heisenberg exchange interactions and DMI vary across different adatom lattices, but the magnetocrystalline anisotropy energy (MAE) also changes, as shown in Table **8-1**. In contrast to what we have experienced in the previous chapters, where we had either OOP easy-axis (CrPdFe/Ir(111)) or easy-plane cases (Mn/Ir(111)), here the MAE tensor gets more complex. The energy differences are shown in terms of the MAE tensor elements introduced in Eq.3-83 in chapter 3. For Mn adatoms, the MAE exhibits a distinct shift between lattice (A) and lattice (B). The OOP spin orientation is favored in lattice (A)

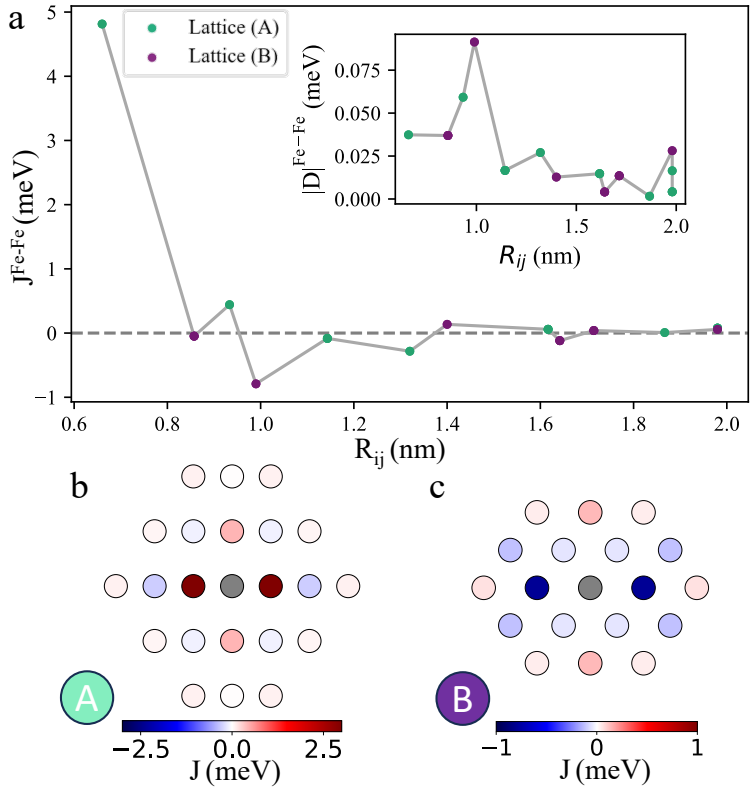

Figure **8-4**.: **Magnetic interactions among Fe adatoms on Nb(110). a** Heisenberg exchange interactions among Fe atoms as a function of the distance, with the inset showing the DMI. The values obtained for both lattices are plotted in the same curve. The lines serve as a guide for the eye. **b, c** Illustration of the two simulated lattices, where each circle is coloured as a function of the size of J with respect to the central atom (grey colour).

by 0.1 meV with respect to the in-plane magnetization case ($K_{zz} - K_{xx} = K_{zz} - K_{yy} = 0.1$ meV). Here, there is no in-plane anisotropy in contrast to all cases investigated in this chapter. Conversely, in lattice (B), there is a transition to anisotropic spin alignment in the xz plane with $(K_{yy} - K_{xx}, K_{yy} - K_{zz}) = -(0.24$ meV, 0.18 meV). Moving to Cr adatoms lattices, the MAE prefers anisotropic in-plane (xy plane) spin orientation for both lattices, but with different values $((K_{zz} - K_{xx}, K_{zz} - K_{yy}) = -(0.31$ meV, 0.15 meV), $-(0.49$ meV, 0.21 meV)) for lattice (A), lattice (B), respectively). Similarly, both Fe adatoms lattices MAEs prefer anisotropic spin alignment in yz plane with $((K_{xx} - K_{yy}, K_{xx} - K_{zz}) = -(0.44$ meV,

0.32 meV), −(0.58 meV, 1.28 meV)) for lattice (A), lattice (B), respectively). The rich set of MAEs underscores the tunability of the adatoms magnetic properties depending on the lattice configurations.

The observed modifications in the magnetic interactions induced by the two types of diluted lattices considered in our study impacts on the ground states and metastable states emerging spin-textures, which will be discussed in the next section.

MAEs (in meV)	Cr (A)	Cr (B)	Mn (A)	Mn (B)	Fe (A)	Fe (B)
K_{zz} - K_{xx}	-0.31	-0.49	0.1	-0.06	0.32	1.28
K_{zz} - K_{yy}	-0.15	-0.21	0.1	0.18	-0.12	0.70

Table **8-1**.: Tensor elements associated to the magnetocrystalline anisotropy energies for the different adatoms lattices.

8.4. Complex magnetic states emerging at the two types of diluted adatom-lattices

After extracting the magnetic interactions among the adatoms for each lattice type, the next step is to investigate the underlying magnetic states.

Starting with the case of Cr adatoms, the ground states are the in-plane AFM magnetic states for both lattice (A) and (B), as depicted in the insets of Fig. **8-5** a, b, where the spins are oriented in-plane due to the underlying in-plane MAE. AFM domain walls emerge across both types of lattices, as shown in Fig. **8-5** a, b. Since the values of the MAEs are found to be rather small, it is educational to explore the impact of their magnitude on the magnetic states characterizing the Cr-adatoms-based lattices. When reducing the MAE down to 0.01 meV but with an isotropic in-plane magnetization ($K_{zz} - K_{xx} = K_{zz} - K_{yy} = -0.01$ meV), an in-plane AFM antiskyrmion with a size of 15.8 nm emerges as a metastable state (Fig. **8-6** a). This AFM antiskyrmion is composed of in-plane FM antiskyrmions (Fig. **8-6** b and c) residing at two FM sublattices with an inter-sublattice coupling of AFM nature. Similarly, when flipping the sign of the MAE while keeping the value of 0.01 meV, the OOP AFM configuration is stabilized (see Fig.**8-6** d), which can host an elliptical AFM antiskyrmion. The major and minor axes of the elliptical AFM antiskyrmion measure 7.6 nm and 4.6 nm, respectively. The constituents of this AFM antiskyrmion are two FM antiskyrmions emerging at FM sublattices, as depicted in Fig.**8-6** e and f. The manifestation of antiskyrmions rather than skyrmions, is due to the DMI vectors that favor a directional dependence of the chirality, with the latter being of opposite sign along the x-direction than that along the y-direction (see e.g. Fig. **2-7** in chapter 2). The same scenario holds for the (B) lattice of Cr adatoms. Initially, with an isotropic in-plane MAE ($K_{zz} - K_{xx} = K_{zz} - K_{yy} = -0.2$

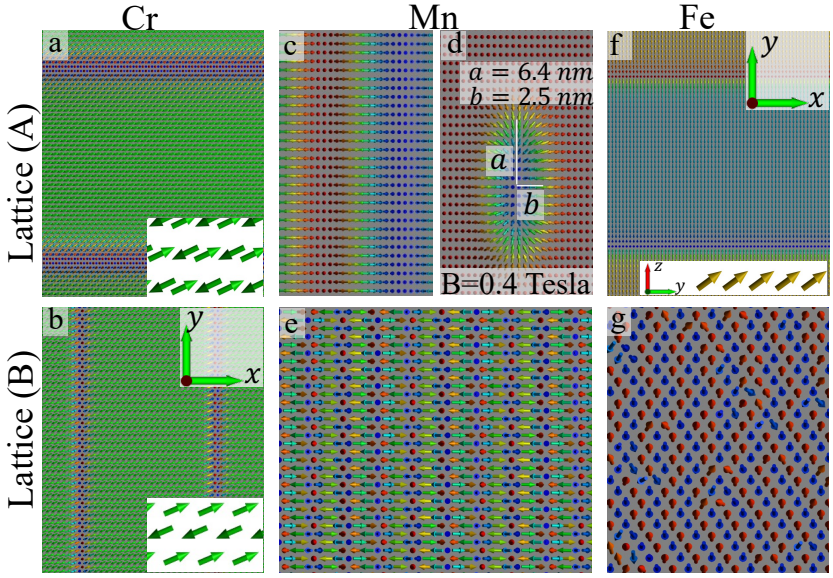

Figure **8-5**.: **Magnetic states emerging at Cr, Mn, Fe lattices. a, b** Snapshots of the AFM domain walls forming on the in-plane (xy plane) AFM ground state with the in-plane anisotropic MAE $(K_{zz} - K_{xx}, K_{zz} - K_{yy}) = -(0.31$ meV, 0.15 meV), $-(0.49$ meV, 0.21 meV)) for Cr (A) and (B) lattices, respectively. For Mn (A) lattice, MAE favors an OOP spin alignment $(K_{zz} - K_{xx}, K_{zz} - K_{yy} = 0.1$ meV). The magnetic interactions, however, induce FM spin spirals as the ground state **c**. The application of an OOP magnetic field of 0.4 T enables the stabilization of FM skyrmions **d**. **e** For Mn (B) lattice, MAE prefers anisotropic spin alignment in the xz plane $((K_{yy} - K_{xx}, K_{yy} - K_{zz}) = -(0.24$ meV, 0.18 meV)), and the ground state is a complex set of AFM spin spirals. **f** Snapshot of the FM domains forming at the FM ground state, shown in inset, for the Fe (A) lattice, where the MAE prefers anisotropic spin orientation in the yz plane $((K_{xx} - K_{yy}, K_{xx} - K_{zz}) = -(0.44$ meV, 0.32 meV)). **g** For Fe (B) lattice the magnetic interaction among the adatoms, with an anisotropic MAE in the yz plane $((K_{xx} - K_{yy}, K_{xx} - K_{zz}) = -(0.58$ meV, 1.28 meV)), gives rise to an irregular AFM order of spins.

meV), we obtain an in-plane AFM state as depicted in the inset of Fig. **8-7** a. In this case, the DMI vectors stabilizes AFM skyrmion (Fig. **8-7** a). This 3.9 nm sized in-plane AFM skyrmion is built up of two in-plane FM skyrmions, residing at two FM sublattices (Fig. **8-7** b, and c). Whereas upon changing the sign of the MAE ($K_{zz} - K_{xx} = K_{zz} - K_{yy} = 0.08$ meV) to favor an OOP spin alignment, the ground state flips from the in-plane orientation to an OOP AFM state depicted in the inset of Fig. **8-7** d. Here, an OOP AFM skyrmion

emerges. This skyrmion is elliptical in shape with dimensions of (5.5 nm, 2.4 nm) as depicted in Fig. **8-7** d, and the building blocks in this case are two elliptical FM skyrmions residing at two oppositely spin oriented FM sublattices (Fig. **8-7** e, and f).

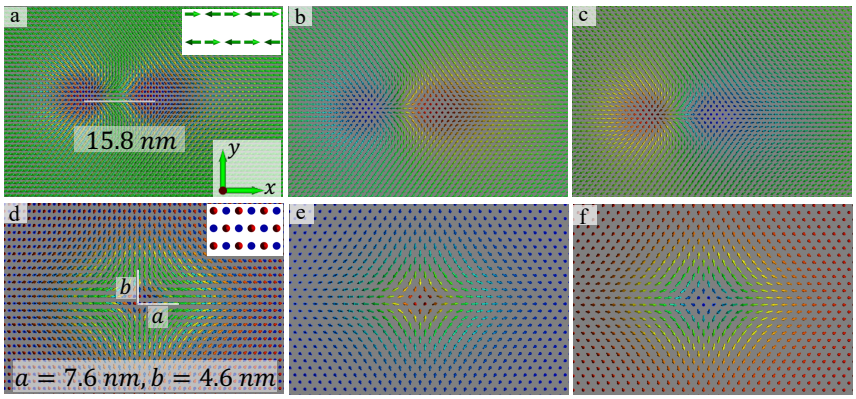

Figure **8-6**.: **Magnetic states emerging at Cr (A) lattice by tuning the MAE. a** Snapshot of the in-plane AFM Cr antiskyrmion when $K_{zz} - K_{xx} = K_{zz} - K_{yy} = -0.01$ meV. With this MAE the spins can align isotropically in-plane, with the in-plane AFM state shown in inset being the ground state. **b, c** The building blocks of the in-plane AFM antiskyrmion, which are two in-plane FM antiskyrmions coupled antiferromagnetically. **d** Snapshot of the OOP AFM Cr antiskyrmion after flipping the sign of the MAE ($K_{zz} - K_{xx} = K_{zz} - K_{yy} = 0.01$ meV), which leads to an OOP AFM order. **e, f** The building blocks of the AFM antiskyrmion, which are two FM antiskyrmions coupled antiferromagnetically.

Regarding the Mn-based (A) lattice case, the ground state is FM spin spirals in the absence of magnetic filed, as shown in Fig. **8-5** c. Upon applying an OOP magnetic field of 0.4 Tesla, the spin spirals deform into elliptical FM skyrmions surrounded by an OOP FM state (Fig. **8-5** d). In this case the ellipse has major and minor axes of 6.4 nm, and 2.5 nm. By flipping the sign of the MAE, and choosing it to prefer in-plane spin alignment ($K_{zz} - K_{xx} = K_{zz} - K_{yy} = -0.5$ meV), a 3.9 nm sized in-plane FM skyrmion emerges at the in-plane FM background (Fig. **8-8** a). For Mn-based (B) lattices, the magnetic interactions among the adatoms do not support the stabilization of topological solitons, and only complex sets of AFM spin spirals emerge as the ground state, see Fig. **8-5** e.

Finally, for the Fe adatoms lattices, the FM state in the yz plane is the ground state for the (A) lattice, which can host FM magnetic domain walls (see Fig. **8-5** f and its inset). Upon reducing the MAE value down to 0.025 meV, and choosing it to be preferring an isotropic in-plane (xy plane) orientation of spins, i.e. $K_{zz} - K_{xx} = K_{zz} - K_{yy} = -0.5$ meV, a 15.1

nm sized in-plane FM antiskyrmion emerges (Fig. **8-8** b). Whereas, when flipping the sign of the MAE, an elliptical FM antiskyrmion emerges in the OOP FM background as shown in Fig. **8-8** c, with major and minor axes of 7.9 nm, 5.1 nm, respectively. For the Fe (B) lattices, the weak magnetic interactions among the Fe adatoms ($J_1 = -0.03$ meV) do not support the stabilization of topological solitons, and only AFM irregular (kind of arbitrary) spin alignments emerge, see Fig. **8-5** g.

To summarize, we have learned from this study that Mn-based dilute lattice (A) is the most promising case to explore the emergence of topological magnetic states. The other cases, were not successful, not because of the underlying magnetic exchange interactions, but due to the complexity of the MAE tensor, which shows a third MAE axis that breaks magnetic rotation in the encompassing plane, which works against the formation of solitonic spin-textures. Restoring an isotropic in-plane rotation enables the formation of various magnetic objects such as AFM of FM skyrmions or antiskyrmions.

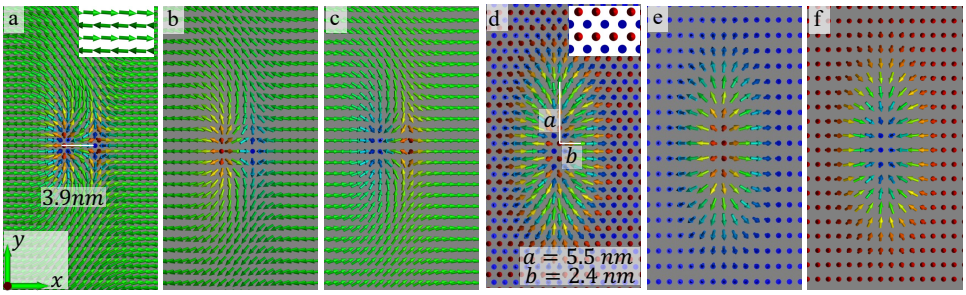

Figure **8-7**.: **Magnetic states emerging at Cr (B) lattice by tuning the MAE. a** Snapshot depicting the in-plane AFM Cr skyrmion emerging when $K_{zz} - K_{xx} = K_{zz} - K_{yy} = -0.2$ meV. The latter promotes an isotropic in-plane spin orientation and therefore, the in-plane AFM order is the ground state (inset of **a**). **b, c** The building blocks of the in-plane AFM skyrmion, consisting of two in-plane FM skyrmions that are coupled antiferromagnetically. **d** The AFM Cr skyrmion when the MAE favors an OOP spin orientation ($K_{zz} - K_{xx} = K_{zz} - K_{yy} = 0.08$ meV), with the associated OOP AFM ground state shown in inset. **e, f** Snapshots of the constituents of the AFM skyrmion, two FM skyrmions that are antiferromagnetically coupled.

8.5. Conclusion

In this study, we unveiled the emergence of a plethora of topological solitons on the diluted lattices of Cr, Fe, and Mn adatoms deposited on Nb(110) surface. We find potential stabilization of FM and AFM skyrmions, as well as antiskyrmions, which depend on the

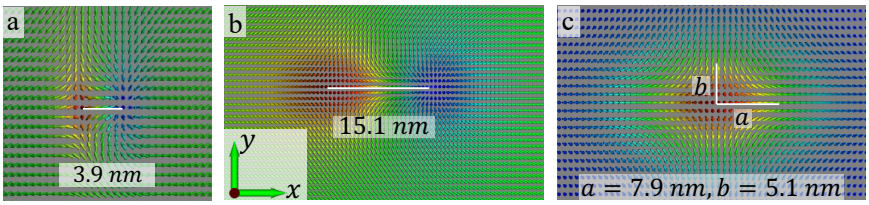

Figure **8-8**.: **Magnetic states emerging at Mn and Fe adatoms (A) lattices by tuning MAE. a** Snapshot of the in-plane FM skyrmion forming at Mn (A) lattice when the MAE is preferring in-plane spin alignment ($K_{zz} - K_{xx} = K_{zz} - K_{yy} = -0.5$ meV). **b** Snapshot of the in-plane FM antiskyrmion emerging at Fe (A) when the MAE is modified to be isotropic in the xy plane ($K_{zz} - K_{xx} = K_{zz} - K_{yy} = -0.025$ meV). Flipping the sign of the MAE ($K_{zz} - K_{xx} = K_{zz} - K_{yy} = 0.015$ meV) favors the OOP spin orientation, where the ground state is the FM state, which hosts FM antiskyrmions **c**.

lattice type of the adatom structures. Motivated by our recent collaboration involving STM experiments, demonstrating the possibility of creating diluted lattices, we assumed either a rectangular lattice (lattice (A)), or a rhombic lattice (lattice (B)).

The Heisenberg exchange interactions, DMI and MAE can be strongly modified depending on the lattice considered. For instance, the coupling between the n.n. adatoms can change from being FM to AFM such as what we observed for the case of Mn adatoms. Moreover the DMI chirality changes across the different lattices types stabilizing for example antiskyrmions in the (A) lattices of Cr and Fe adatoms, while in the Mn (A) and Cr (B) lattices, skyrmions are formed.

In conclusion, our study provides a comprehensive understanding of the magnetic interactions and topological spin textures in diluted adatom lattices. This research opens up new possibilities for exploring synthetic quantum states of matter and their potential applications in technologies. Future research could focus on the diluted lattices on several interfaces such as Ir(111), which might lead to more isotropic MAE.

9. Conclusions

In this thesis, we have conducted first-principles investigations to predict the emergence of intrinsic antiferromagnetic (AFM) solitons emergence within magnetic layered systems. Our research aimed to understand the formation, dynamics, and potential applications of these magnetic structures in various realistic combination of materials. We have carried out a systematic study, depositing magnetic layers of 3d elements, being potentially AFM (V, Cr, and Mn) on Ir(111) surface. We have explored several interfaces involving those magnetic layers with films made of Pd and Fe. We employed density functional theory (DFT) as a theoretical framework to investigate the structural, electronic, and magnetic properties of the materials under study. Subsequently, we utilized atomistic spin dynamics (ASD) using the Landau-Lifshitz-Gilbert (LLG) equation to minimize the extended Heisenberg Hamiltonian, incorporating parameters derived from *ab initio* principles. This approach allowed us to explore and analyze the magnetic states that emerge within our magnetic layered systems. Among the investigated 3d transition metal elements, Cr and Mn have emerged as promising candidates due to their inherent AFM properties, which facilitate the formation of novel types of AFM solitons. Each chapter of this thesis contributes to our comprehensive understanding of those discovered AFM solitons, revealing their intricate properties and shedding light on their profound significance in the realm of spintronics and technology.

Our study started with the prediction of intrinsic single and interchained AFM skyrmions in chapter 4. Within a Cr layer deposited on PdFe/Ir(111) substrate, we observed the emergence of single and interchained AFM skyrmions. Their formation within the Cr layer, characterized by a row-wise AFM (RW-AFM) configuration on a triangular lattice at zero magnetic field, was governed by the intricate interplay between Heisenberg exchange interactions (J_{ij}), Dzyaloshinskii-Moriya interactions (DMI), and magnetocrystalline anisotropy energy (MAE). The spins of the Cr layer are spread into four sublattices, each of them hosting ferromagnetically aligned spins pointing either up or down, and can stabilize a ferromagnetic (FM) skyrmion within the sublattice. We systematically investigated the influence of varying parameters on the size of the AFM skyrmions, identifying a critical range of interaction strengths within which these novel solitons can be stabilized. Additionally, we examined the effects of external magnetic fields on the size of the AFM skyrmions. Moreover, our research investigated the catenation of AFM skyrmions, revealing that their overlap enhances their stability.

Taking a step forward, in chapter 5, we constructed a generic spin model designed to capture the fundamental magnetic interactions essential for AFM skyrmion formation on a triangular

lattice. Our model elucidates that the stabilization of the AFM skyrmions under investigation necessitates the incorporation of magnetic interactions extending up to the third nearest neighbors (n.n.). Crucially, the first n.n. Heisenberg exchange interaction (J_1) needs to be of an AFM nature, in addition to an out-of-plane (OOP) MAE, complemented by DMI, and FM Heisenberg exchange interactions with the third n.n. ($\mathbf{D}_3$, and J_3). The latter facilitate the formation of FM skyrmions at the sublattice level. We explored how altering those magnetic interactions affect the size and stability of the single and interchained AFM skyrmions. We then constructed the corresponding phase diagrams and identify the window where they can emerge. We have found that the external magnetic field enhances the thermal stability of those AFM soltions by increasing their energy barrier. These insights have enriched our theoretical framework and are expected to serve as a pivotal tool for experimentally identifying materials capable of hosting these distinctive AFM solitons.

In chapter 6, we replaced Cr with a Mn layer, which in contrast to Cr is characterized by an in-plane Néel state in all different magnetic layered systems, namely Mn/Ir(111), PdMn/Ir(111), MnPdFe/Ir(111), and $MnPd_2Fe$/Ir(111). Here, we found frustrated multimerons in the Mn ultrathin film, which combine for example in a hexa-meronic texture, when assuming periodic boundary conditions. Those multi-meronic solitons are characterized by FM meronic pairs with different topological charges occupying distinct sublattices. The intriguing outcome was the formation of hexa-meronic solitons, each bearing a total topological charge of 0, 1, or -1, and further higher excited states were found, such as dodeca-merons. Moreover, our investigation unveiled a critical insight into the role of topological charge at the sublattice level, profoundly influencing the behavior of these multi-meronic spin textures when subjected to an external OOP magnetic field. To deepen our understanding, we meticulously crafted a minimal spin model, intricately mapping the magnetic interactions necessary for the emergence of these AFM textures.

In chapter 7, we investigated the dynamical behavior of the single and interchained AFM skyrmions discussed in chapter 4. We have inspected the spin-polarized induced motion of the AFM skyrmions, when subjected to perpendicular-to-plane spin current with in-plane polarization. The AFM skyrmions show unexpected trajectories, showing an anisotropic skyrmion Hall effect (SkHE) stemming from the elliptical shape of the AFM skyrmions. The direction of the polarization of the current with respect to the axes of the skyrmions defines both the magnitude of the Hall angles and the skyrmion velocity. The skyrmions exhibit their highest (slowest) velocity when moving along their main (minor) axis, where the Hall angle vanishes. The interaction between the AFM skyrmions in Cr layer and the FM ones in the Fe interface gives rise to a rich energy profile. The FM skyrmions within the Fe layer serve as pinning sites, exerting a substantial influence on the trajectories and velocities of AFM skyrmions. These findings significantly enhance our understanding of AFM skyrmion dynamics and their intricate interplay with FM skyrmions. Such insights hold promise for the development of innovative spintronic devices, enabling the engineering of customized

racetracks by seeding pinned FM skyrmions at the Fe layer to create tailored paths for the AFM skyrmions.

In the last results chapter (chapter 8), we investigated the formation of topological solitons (AFM and FM) on diluted adatoms lattices of Cr, Mn, or Fe deposited on Nb(110) substrates. By adjusting the distance between the magnetic adatoms, it is possible to toggle the magnetic interactions from FM to AFM. We have examined two cases, the first one, where the adatoms are arranged in a rectangular lattice where the atoms at the corners are with 0.66 nm and 0.93 nm separation distances. The second lattice is rhombic, where the atoms are allocated at 0.87 nm separation. We have found that Mn (Fe) rectangular lattices can stabilize FM skyrmion (antiskyrmions), while their rhombic lattice does not stabilize topological solitons, with AFM spirals being the ground state. Whereas Cr rectangular lattice supports the formation of AFM antiskyrmion, in-plane or OOP, depending on the sign and magnitude of the MAE, while AFM skyrmions can emerge at the Cr rhombic lattice.

Our research significantly advances our understanding of AFM topological spin textures and paves the way for exploring the non-trivial effects of spin-polarized currents on the dynamics of elliptical AFM skyrmions. Notably, our predictions regarding Cr and Mn magnetic layers deposited on Ir(111) surfaces present an intriguing opportunity for the experimental community to realize entirely new types of zero-field AFM spin textures—a milestone that has remained elusive until now. This breakthrough holds profound implications for future research in the field. In summary, our findings have opened new avenues for designing experiments aimed at experimentally verifying the formation of these novel AFM solitons in thin layered systems and shaping the development of racetrack devices with controlled paths. However, the identification of AFM spin-textures requires specific experimental techniques. We expect the recently proposed all-electrical detection based on the tunneling spin-mixing magnetoresistance (TXMR) [193, 285], with its different possible modes [195] that can be enhanced by the proper implantation of atomic defects [255], to be useful for the exploration of AFM states. In this context, the predicted non-collinear Hall effect [286], the topological spin Hall effect for antiferromagnets [287] as well as the spin-resolved inelastic electron scattering approaches could be valuable [288, 289]. Obviously, spin-polarized scanning tunneling microscopy is capable of resolving AFM states via atomic resolution [290, 291] while enormous progress has been made with X-ray magnetic microscopy [91] and all-optical relaxometry with a scanning quantum sensor based on a single nitrogen-vacancy (NV) defect in diamond, which were applied for various synthetic AFM textures, among which skyrmions [90].

Although our study has uncovered significant insights, there remains ample room for future exploration. Our next steps involve a deeper investigation into the influence of spin-polarized currents on the motion of AFM Néel multimeronic solitons. Moreover, the prospect of exploring thicker films of Cr or Mn at the vicinity of Ir surface is appealing by offering the potential of exploring the evolution of the unveiled 2D spin-texture into 3D. This intricate stacking

of materials may yield emergent phenomena and exotic magnetic states, paving the way for exciting possibilities enabling entirely novel applications and technological paradigms.

A. Appendix for chapter 4

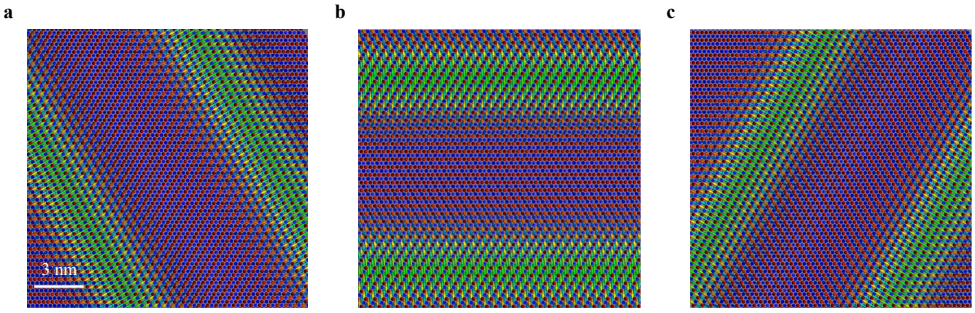

Figure **A-1**.: **AFM domain walls as metastable states in Cr layer deposited on PdFe/Ir(111). a**, **b** and **c** Snapshots of AFM domain walls emerging in Cr overlayer along different but equivalent orientations.

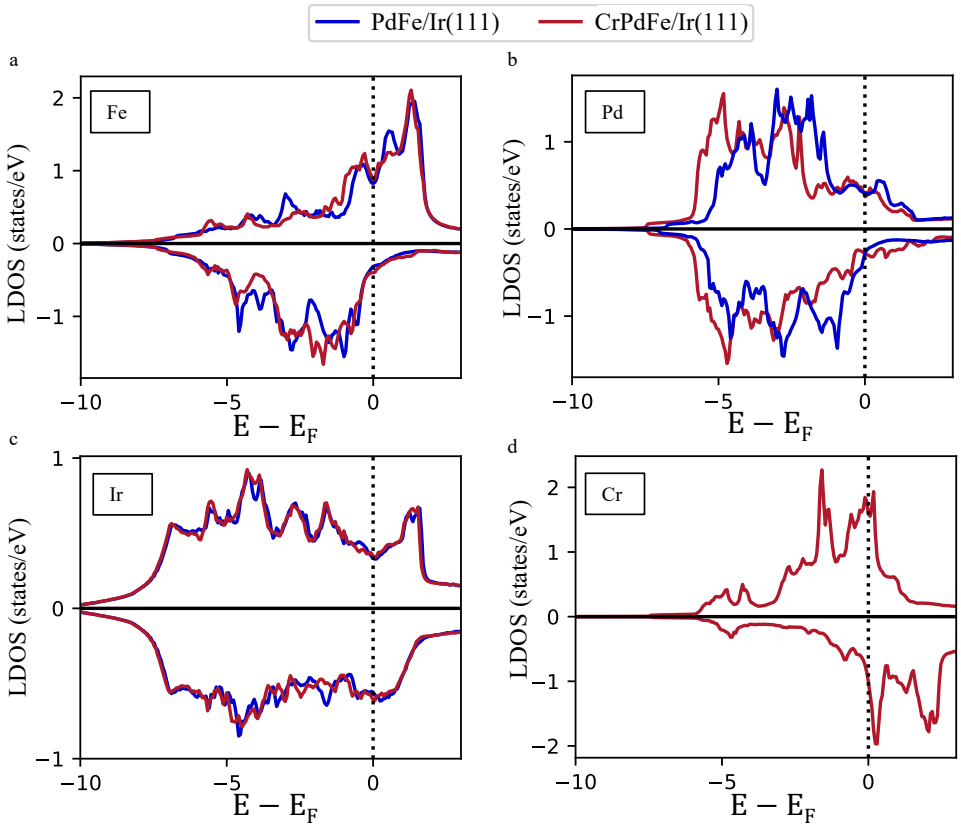

Figure **A-2**.: **Electronic structure of the CrPdFe trilayer and PdFe bilayer deposited on Ir(111) surface.** Spin-resolved local density of states (LDOS) of Fe, Pd, Ir and Cr. Red and blue colors correspond to the presence or not of the Cr overlayer. The assumed magnetic state is collinear with Cr moments aligned antiferromagnetically to those of Fe.

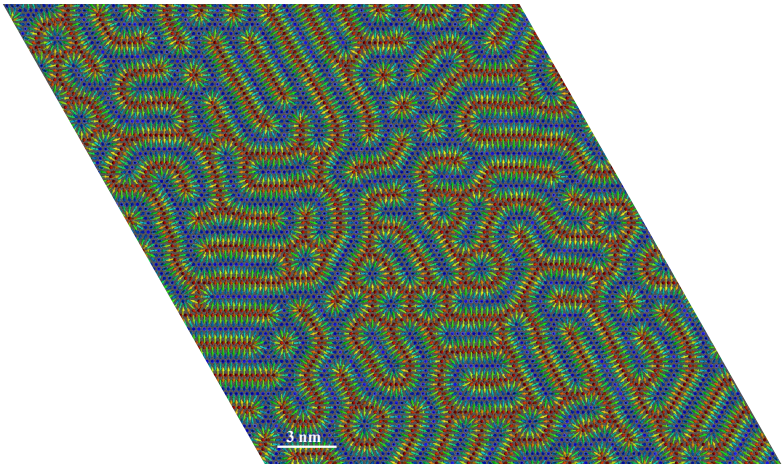

Figure **A-3**.: **Magnetic state of Fe layer when covered by the AFM Cr layer.** FM skyrmions emerge within the spin spirals hosted by the Fe layer without application of an external magnetic field.

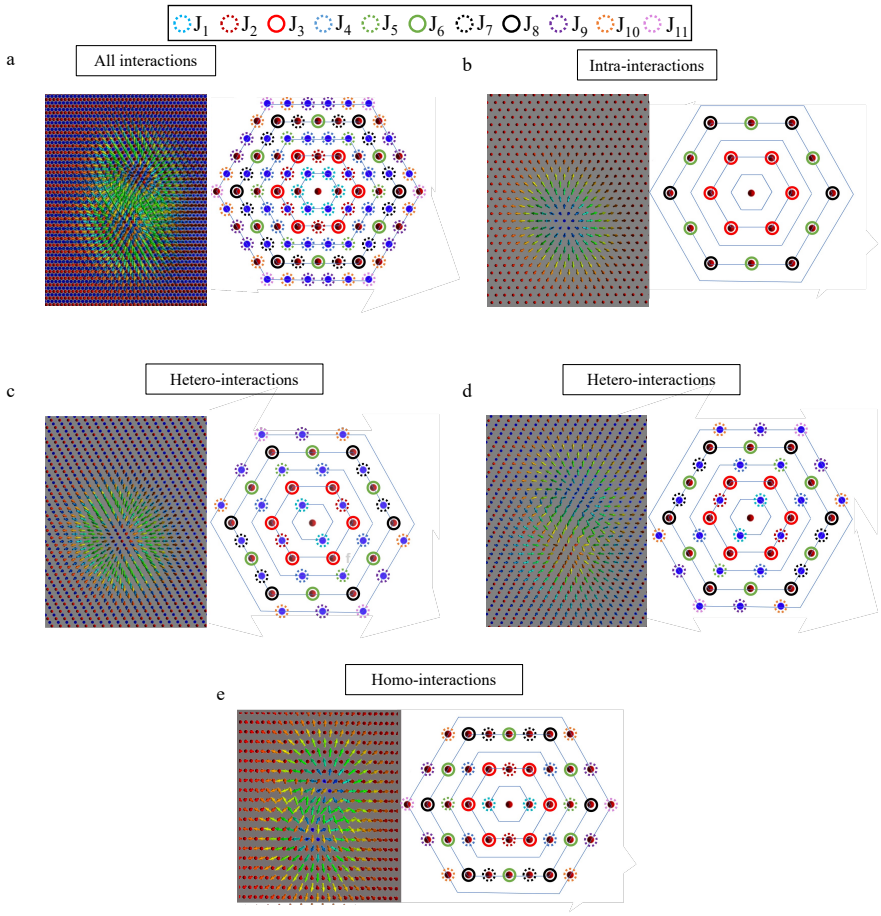

Figure **A-4.**: **Schematic representation of the interactions among the building blocks of the interchained AFM skyrmions.** Intra-interactions represent magnetic interactions within one sublattice. Hetero-interactions are associated to magnetic interactions between sublattices, which host skyrmions coupled antiferromagnetically. Homo-interactions mediate magnetic coupling between sublattices hosting skyrmions coupled ferromagnetically.

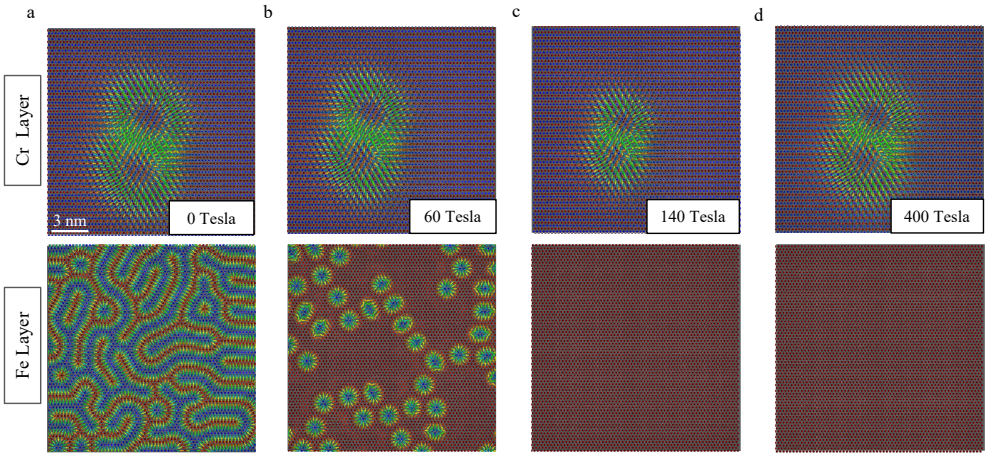

Figure **A-5**.: **Double AFM skyrmion – Impact of magnetic field on the magnetic state of both Cr and Fe layers.** The spin configuration in Cr (upper row) and Fe layers (lower row) for different magnetic fields applied perpendicular to the surface: 0, 60, 140 and 400 Tesla depicted at **a**, **b**, **c** and **d**, respectively.

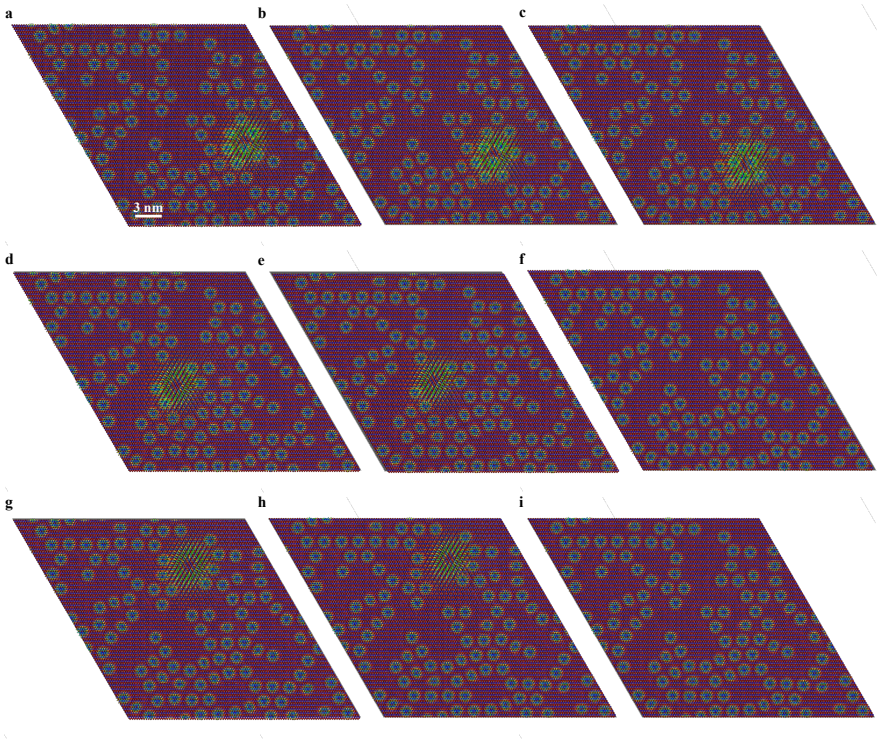

Figure **A-6**.: **Single AFM skyrmion – Stability Impacted by the magnetic inhomogeneity of Fe.** Snapshots of the evolution of the single AFM skyrmion upon shifts across the lattice under a magnetic field of 70 Tesla. The AFM skyrmion positioned directly above the FM Fe skyrmions and antiskyrmions in **a** survives; **b** shows an intermediate state while **c** represents the final converged configuration. In **d**, the AFM skyrmion is displaced to a rather collinear region such that the skyrmion edges are rather close to the Fe skyrmions. The AFM soliton shrinks as shown in **e** before disappearing in **f**. A similar faith occurs for the AFM skyrmion shifted to a larger collinear Fe area **g** (evolution illustrated in **h** and **i**).

B. Appendix for chapter 5

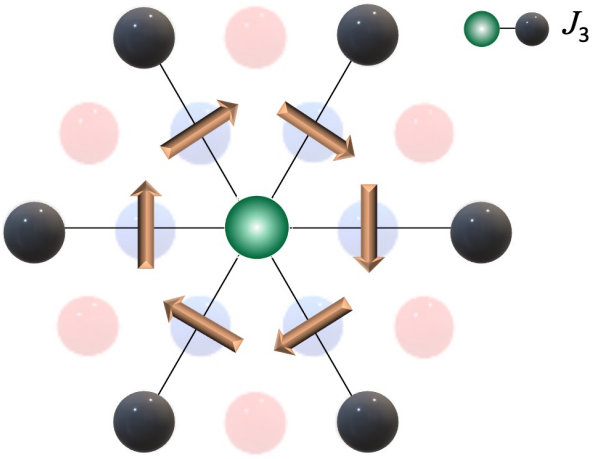

Figure **B-1**.: **Schematic representation of the DMI vectors among the third nearest neighbours sitting on the same sublattice $\mathbf{L}_i$.** The DMI vectors are assumed to be in-plane and experience a clock-wise rotation.

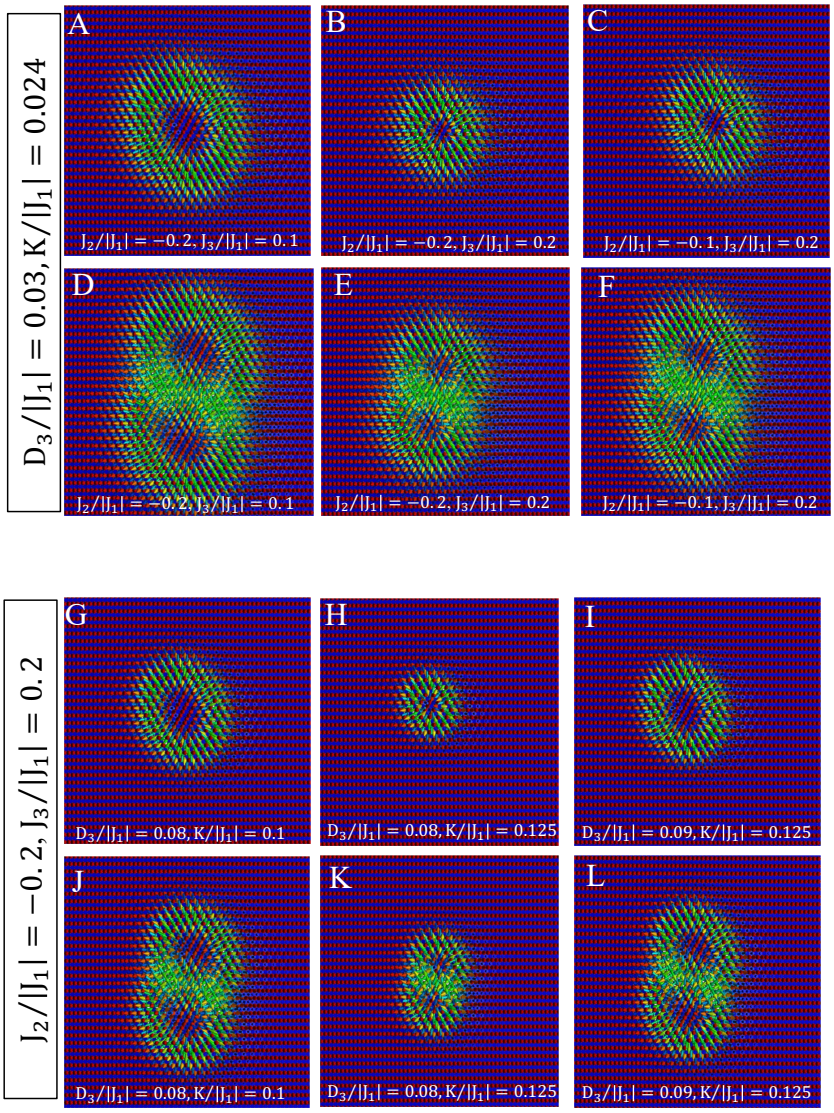

Figure **B-2**.: **Snapshots of single and interchained AFM skyrmions for different values of magnetic interactions at zero magnetic field**.

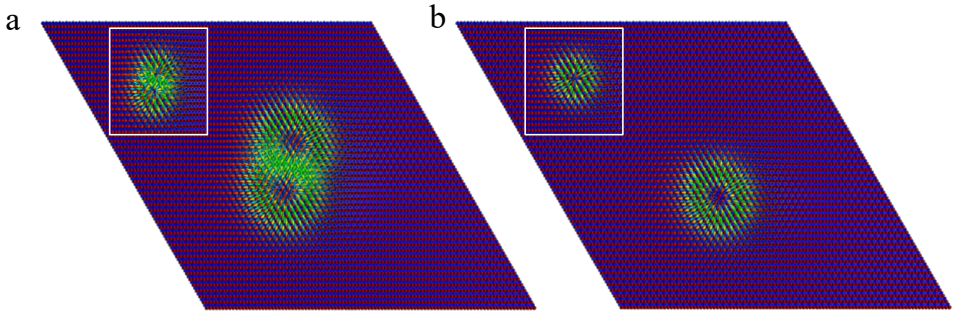

Figure **B-3**.: **Snapshots of the AFM skyrmions with in the inset the associated saddle points considered in the GNEB simulations**.

C. Appendix for chapter 6

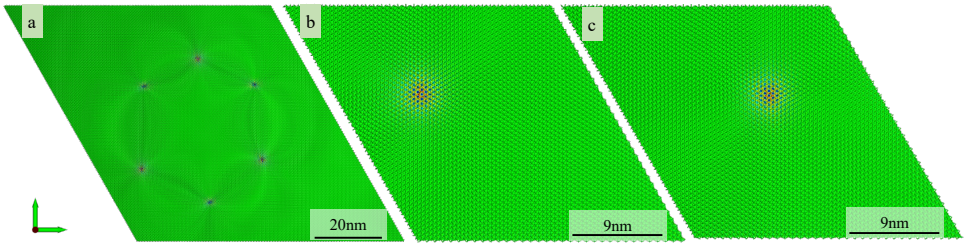

Figure **C-1**.: **Different AFM multi-meronic textures that emerge in the Mn layer.** **a** Excited state with six AFM meronic structures. **b, c** Single AFM meron, antimeron form on confined geometries.

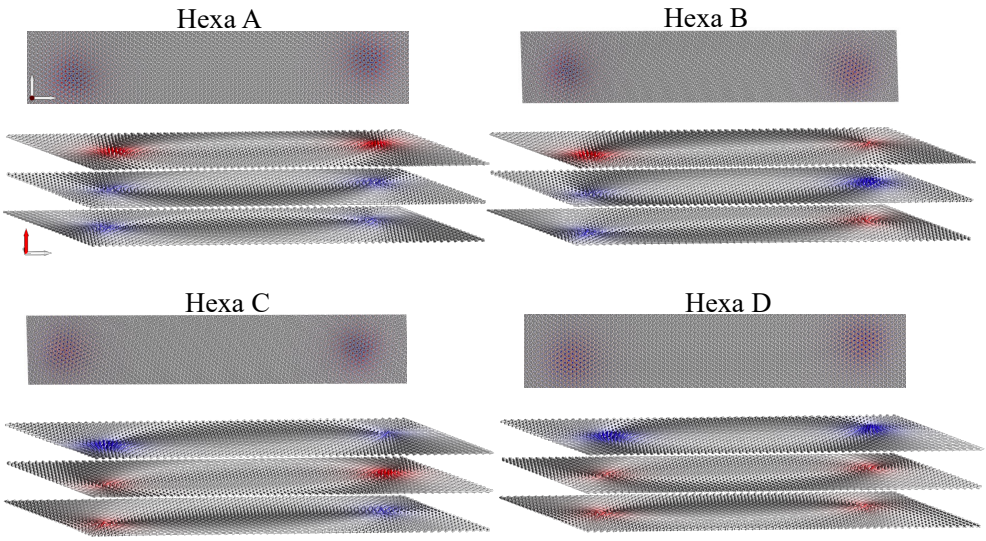

Figure **C-2**.: **Illustration of the initially degenerate topologically different hexa-meronic states.** Snapshots showing the hexa-merons (upper) and their FM meronic decomposition at the three sublattices (lower).

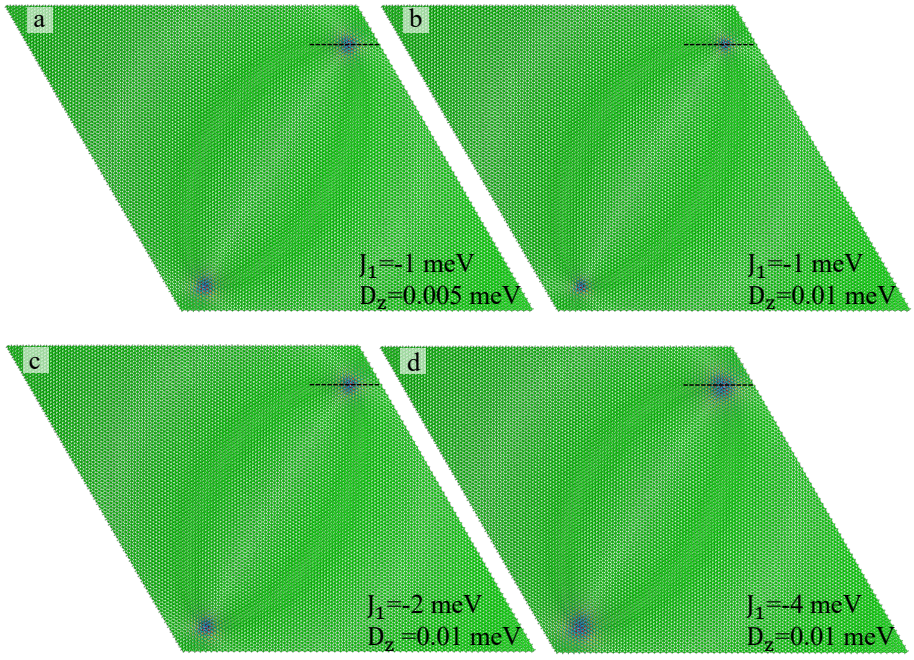

Figure **C-3**.: **Impact of the nearest neighboring magnetic interaction on the size of the AFM vortex-antivortex pairs.** Results obtained with a minimal spin model with the Heisenberg exchange interaction J_1 and out-of-plane component of DMI D_z. Snapshots for **a** D_z=0.005 meV, J_1=-1 meV, **b** D_z=0.01 meV, J_1=-1 meV, **c** D_z=0.01 meV, J_1=-2 meV, and **d** D_z=0.01 meV, J_1=-4 meV.

D. Appendix for chapter 7

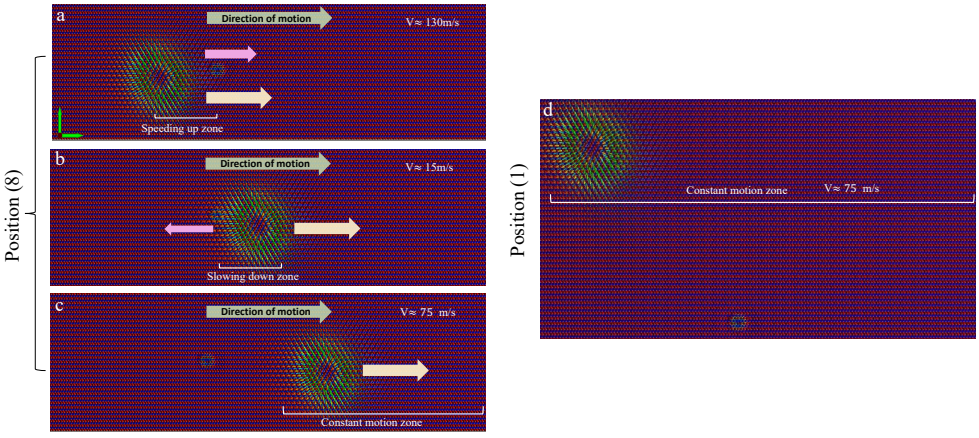

Figure **D-1**.: **Impact of a pinned FM skyrmion on the translational motion of AFM skyrmion in a synthetic AFM-FM skyrmion scenario. a-c** Snapshots showing the different regions where a current-driven AFM skyrmion (η/α= 0.0167 meV) interact with single FM skyrmion at Fe layer when located at position (1) in Fig. **7-4** d. **a** When the FM skyrmions lays ahead of the AFM skyrmions and it lays in its vicinity, both the attraction force works with the drag force causing the velocity increase of the AFM skyrmion , while when the AFM skyrmion passes the FM skyrmion, and it lays behind it, the attraction force acts against the drag force causing deceleration of the AFM skyrmion **b**. When the AFM skyrmion passes the interaction area, it gains constant motion speed **c**, similar to the velocity of the AFM skyrmion when moving away from the FM skyrmion **d** which represents the AFM skyrmion when located at position(8) in Fig. **7-4** d.

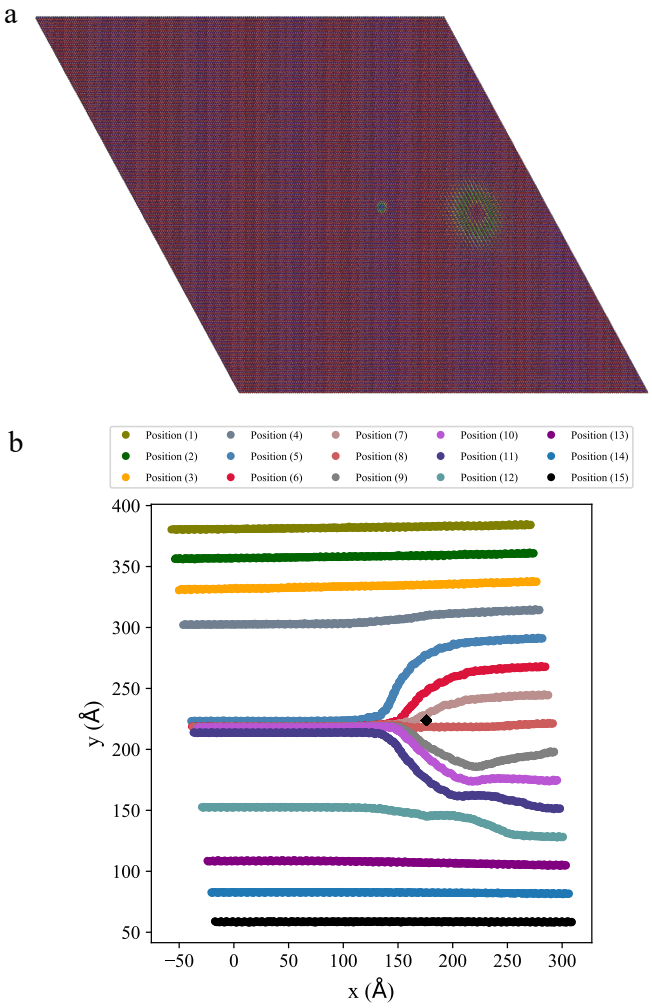

Figure **D-2**.: **Position dependent deflection of AFM skyrmions due to the presence of FM skyrmions at Fe layer assuming a driving motion from right to left. a** In contrast to Fig. **7-4** , the AFM skyrmion is positioned on the right hand side with respect to the FM skyrmion. **b** The trajectory of the single AFM skyrmion when moved toward pinned FM skyrmion at Fe layer from different positions from right to left, which shows deflections that depend on the relative position of the AFM skyrmion and the FM skyrmion.

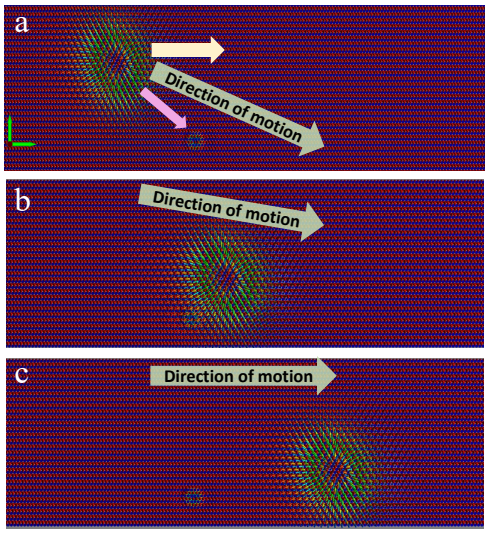

Figure **D-3**.: **Direction of motion of AFM skyrmion interacting with a FM skyrmion in a synthetic AFM-FM skyrmion scenario. a-c** Snapshots showing the trajectory of the AFM skyrmion when the FM skyrmion is not located along the path. A deflection occurs, followed by a straightforward motion. Here, the FM skyrmion is pinned.

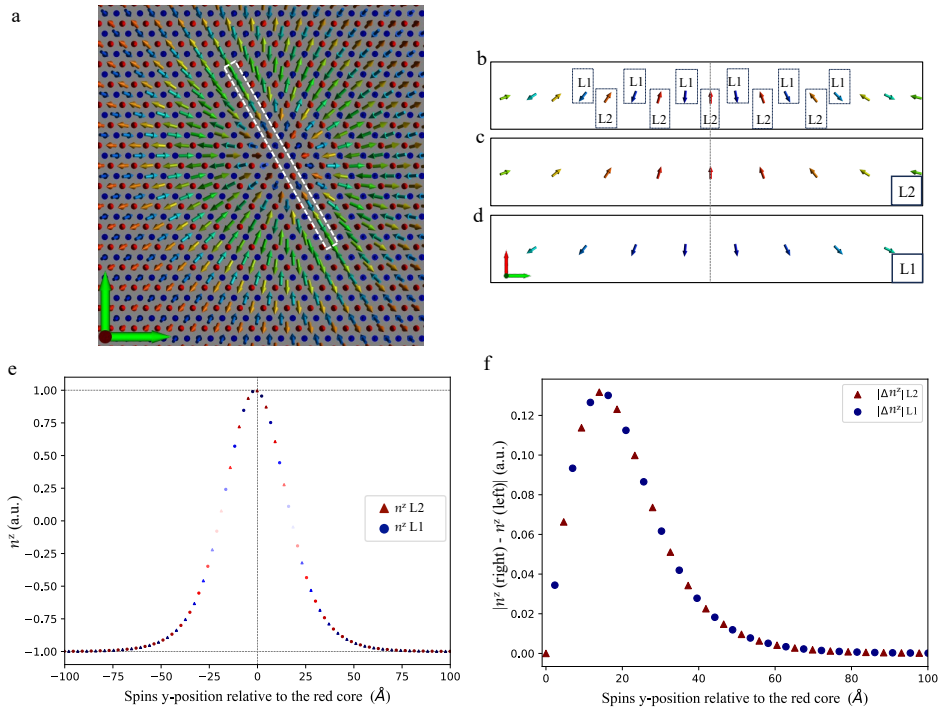

Figure **D-4**.: **Spin analysis along the line connecting the two FM building-block skyrmions of the single AFM skyrmion. a** Snapshot showing the AFM skyrmion. **b** Snapshot of the spins along the line connecting two centers of the AFM skyrmion. Two spirals belong to two sublattices L1 and L2 are shown separately in respectively **c** and **d**. Once, one sublattice hosts a skyrmion core, the adjacent spins rearrange themselves to accommodate the different magnetic interactions and produce a natural spin asymmetry with respect to the skyrmionc core. This asymmetry is quantified in the n^z profile **e**. **f** Taking the difference between right and left n^z highlights how the spin asymmetry develops away from the skyrmion core. It reaches a maximum at a distance of 1.4 nm.

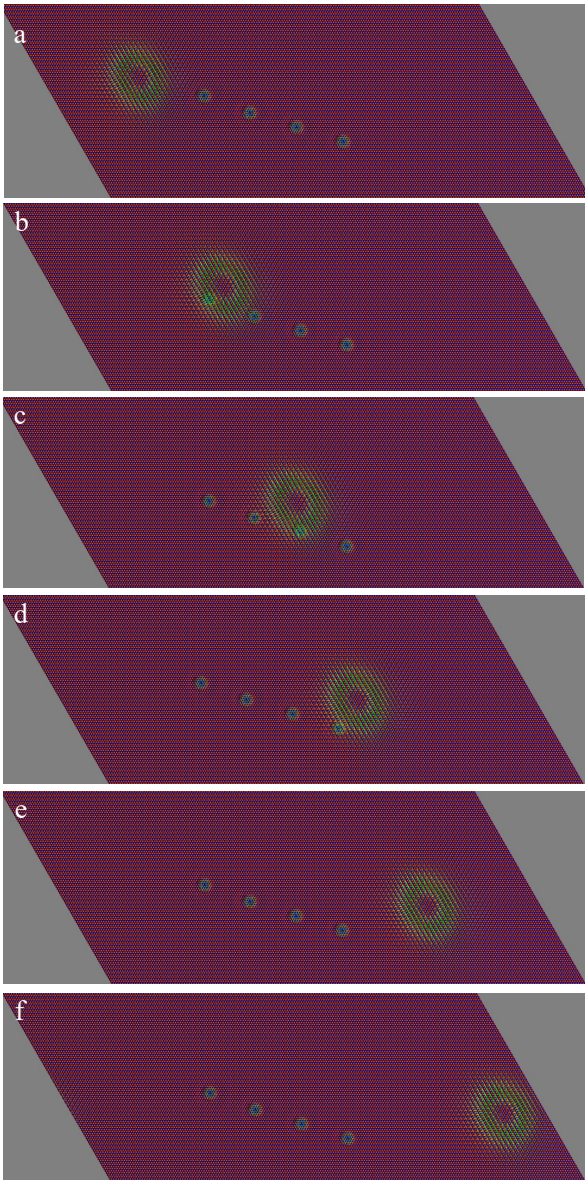

Figure **D-5**.: **Design of FM skyrmions for the motion control of AFM skyrmions. a-f** Snapshots vividly demonstrating the capacity to precisely steer the motion of AFM skyrmions by precisely arranging the positions of FM skyrmions within the Fe layer in a hybrid synthetic scenario of AFM and FM films. The figures obtained with a current parameter of η/α= 0.0167 meV.

Bibliography

[1] S. A. Wolf, A. Y. Chtchelkanova, and D. M. Treger, "Spintronics—a retrospective and perspective," *IBM J. Res. Dev.*, vol. 50, p. 101, 2006.

[2] J. Sinova, "Thinks globally but acts locally," *Nat. Mater.*, vol. 9, p. 880, 2010.

[3] L. Eeckhout, "Is Moore's law slowing down? what's next?," *IEEE Micro*, vol. 37, p. 4, 2017.

[4] R. Jansen, "Silicon spintronics," *Nat. Mater.*, vol. 11, p. 400, 2012.

[5] G. Binasch, P. Grünberg, F. Saurenbach, and W. Zinn, "Enhanced magnetoresistance in layered magnetic structures with antiferromagnetic interlayer exchange," *Phys. Rev. B*, vol. 39, p. 4828, 1989.

[6] M. N. Baibich, J. M. Broto, A. Fert, F. N. Van Dau, F. Petroff, P. Etienne, G. Creuzet, A. Friederich, and J. Chazelas, "Giant magnetoresistance of (001) Fe/(001) Cr magnetic superlattices," *Phys. Rev. Lett.*, vol. 61, p. 2472, 1988.

[7] M. Julliere, "Tunneling between ferromagnetic films," *Phys. Lett. A*, vol. 54, p. 225, 1975.

[8] T. Miyazaki and N. Tezuka, "Giant magnetic tunneling effect in Fe/Al_2O_3/Fe junction," *J. Magn. Magn. Mater.*, vol. 139, p. L231, 1995.

[9] J. S. Moodera, L. R. Kinder, T. M. Wong, and R. Meservey, "Large magnetoresistance at room temperature in ferromagnetic thin film tunnel junctions," *Phys. Rev. Lett.*, vol. 74, p. 3273, 1995.

[10] O. Gomonay, T. Jungwirth, and J. Sinova, "High antiferromagnetic domain wall velocity induced by Néel spin-orbit torques," *Phys. Rev. Lett.*, vol. 117, p. 017202, 2016.

[11] T. Jungwirth, X. Marti, P. Wadley, and J. Wunderlich, "Antiferromagnetic spintronics," *Nat. Nanotechnol.*, vol. 11, p. 231, 2016.

[12] V. Baltz, A. Manchon, M. Tsoi, T. Moriyama, T. Ono, and Y. Tserkovnyak, "Antiferromagnetic spintronics," *Rev. Mod. Phys.*, vol. 90, p. 015005, 2018.

[13] S. Mühlbauer, B. Binz, F. Jonietz, C. Pfleiderer, A. Rosch, A. Neubauer, R. Georgii, and P. Böni, "Skyrmion lattice in a chiral magnet," *Science*, vol. 323, p. 915, 2009.

[14] X. Yu, Y. Onose, N. Kanazawa, J. H. Park, J. Han, Y. Matsui, N. Nagaosa, and Y. Tokura, "Real-space observation of a two-dimensional skyrmion crystal," *Nature*, vol. 465, p. 901, 2010.

[15] X. Yu, Y. Tokunaga, Y. Kaneko, W. Zhang, K. Kimoto, Y. Matsui, Y. Taguchi, and Y. Tokura, "Biskyrmion states and their current-driven motion in a layered manganite," *Nat. Commun.*, vol. 5, p. 3198, 2014.

[16] W. Wang, Y. Zhang, G. Xu, L. Peng, B. Ding, Y. Wang, Z. Hou, X. Zhang, X. Li, E. Liu, *et al.*, "A centrosymmetric hexagonal magnet with superstable biskyrmion magnetic nanodomains in a wide temperature range of 100–340 K," *Adv. Mater.*, vol. 28, p. 6887, 2016.

[17] L. Peng, Y. Zhang, W. Wang, M. He, L. Li, B. Ding, J. Li, Y. Sun, X.-G. Zhang, J. Cai, *et al.*, "Real-space observation of nonvolatile zero-field biskyrmion lattice generation in MnNiGa magnet," *Nano Lett.*, vol. 17, p. 7075, 2017.

[18] X. Wang, A. Qaiumzadeh, and A. Brataas, "Current-driven dynamics of magnetic hopfions," *Phys. Rev. Lett.*, vol. 123, p. 147203, 2019.

[19] N. Kent, N. Reynolds, D. Raftrey, I. T. Campbell, S. Virasawmy, S. Dhuey, R. V. Chopdekar, A. Hierro-Rodriguez, A. Sorrentino, E. Pereiro, *et al.*, "Creation and observation of hopfions in magnetic multilayer systems," *Nat. Commun.*, vol. 12, p. 1562, 2021.

[20] M. Sallermann, H. Jónsson, and S. Blügel, "Stability of hopfions in bulk magnets with competing exchange interactions," *Phys. Rev. B*, vol. 107, p. 104404, 2023.

[21] F. Zheng, F. N. Rybakov, A. B. Borisov, D. Song, S. Wang, Z.-A. Li, H. Du, N. S. Kiselev, J. Caron, A. Kovács, *et al.*, "Experimental observation of chiral magnetic bobbers in B20-type FeGe," *Nat. Nanotechnol.*, vol. 13, p. 451, 2018.

[22] K. Ran, Y. Liu, Y. Guang, D. M. Burn, G. van der Laan, T. Hesjedal, H. Du, G. Yu, and S. Zhang, "Creation of a chiral bobber lattice in helimagnet-multilayer heterostructures," *Phys. Rev. Lett.*, vol. 126, p. 017204, 2021.

[23] M. Grelier, F. Godel, A. Vecchiola, S. Collin, K. Bouzehouane, A. Fert, V. Cros, and N. Reyren, "Three-dimensional skyrmionic cocoons in magnetic multilayers," *Nat. Commun.*, vol. 13, p. 6843, 2022.

[24] Y. Kharkov, O. Sushkov, and M. Mostovoy, "Bound states of skyrmions and merons near the Lifshitz point," *Phys. Rev. Lett.*, vol. 119, p. 207201, 2017.

[25] X. Yu, W. Koshibae, Y. Tokunaga, K. Shibata, Y. Taguchi, N. Nagaosa, and Y. Tokura, "Transformation between meron and skyrmion topological spin textures in a chiral magnet," *Nature*, vol. 564, p. 95, 2018.

[26] K. Shibata, X. Yu, T. Hara, D. Morikawa, N. Kanazawa, K. Kimoto, S. Ishiwata, Y. Matsui, and Y. Tokura, "Towards control of the size and helicity of skyrmions in helimagnetic alloys by spin–orbit coupling," *Nat. Nanotechnol.*, vol. 8, p. 723, 2013.

[27] N. Romming, C. Hanneken, M. Menzel, J. E. Bickel, B. Wolter, K. von Bergmann, A. Kubetzka, and R. Wiesendanger, "Writing and deleting single magnetic skyrmions," *Science*, vol. 341, p. 636, 2013.

[28] A. Fert, V. Cros, and J. Sampaio, "Skyrmions on the track," *Nat. Nanotechnol.*, vol. 8, p. 152, 2013.

[29] R. Tomasello, E. Martinez, R. Zivieri, L. Torres, M. Carpentieri, and G. Finocchio, "A strategy for the design of skyrmion racetrack memories," *Sci. Rep.*, vol. 4, p. 6784, 2014.

[30] F. Jonietz, S. Mühlbauer, C. Pfleiderer, A. Neubauer, W. Münzer, A. Bauer, T. Adams, R. Georgii, P. Böni, R. A. Duine, *et al.*, "Spin transfer torques in MnSi at ultralow current densities," *Science*, vol. 330, p. 1648, 2010.

[31] J. Iwasaki, M. Mochizuki, and N. Nagaosa, "Current-induced skyrmion dynamics in constricted geometries," *Nat. Nanotechnol.*, vol. 8, p. 742, 2013.

[32] S. Woo, K. Litzius, B. Krüger, M.-Y. Im, L. Caretta, K. Richter, M. Mann, A. Krone, R. M. Reeve, M. Weigand, *et al.*, "Observation of room-temperature magnetic skyrmions and their current-driven dynamics in ultrathin metallic ferromagnets," *Nat. Mater.*, vol. 15, p. 501, 2016.

[33] K. Litzius, I. Lemesh, B. Krüger, P. Bassirian, L. Caretta, K. Richter, F. Büttner, K. Sato, O. A. Tretiakov, J. Förster, *et al.*, "Skyrmion Hall effect revealed by direct time-resolved X-ray microscopy," *Nat. Phys.*, vol. 13, p. 170, 2017.

[34] M. A. Goerzen, S. von Malottki, G. J. Kwiatkowski, P. F. Bessarab, and S. Heinze, "Atomistic spin simulations of electric-field-assisted nucleation and annihilation of magnetic skyrmions in Pd/Fe/Ir (111)," *Phys. Rev. B*, vol. 105, p. 214435, 2022.

[35] J. Sampaio, V. Cros, S. Rohart, A. Thiaville, and A. Fert, "Nucleation, stability and current-induced motion of isolated magnetic skyrmions in nanostructures," *Nat. Nanotech.*, vol. 8, p. 839, 2013.

[36] X. Zhang, G. Zhao, H. Fangohr, J. P. Liu, W. Xia, J. Xia, and F. Morvan, "Skyrmion-skyrmion and skyrmion-edge repulsions in skyrmion-based racetrack memory," *Sci. Rep.*, vol. 5, p. 7643, 2015.

[37] S. S. P. Parkin, M. Hayashi, and L. Thomas, "Magnetic domain-wall racetrack memory," *Science*, vol. 320, p. 190, 2008.

[38] T. H. R. Skyrme, "A unified field theory of mesons and baryons," *Nucl. Phys.*, vol. 31, p. 556, 1962.

[39] A. Bogdanov and A. Hubert, "Thermodynamically stable magnetic vortex states in magnetic crystals," *J. Magn. Magn. Mater.*, vol. 138, p. 255, 1994.

[40] S. Heinze, K. Von Bergmann, M. Menzel, J. Brede, A. Kubetzka, R. Wiesendanger, G. Bihlmayer, and S. Blügel, "Spontaneous atomic-scale magnetic skyrmion lattice in two dimensions," *Nat. Phys.*, vol. 7, p. 713, 2011.

[41] N. Nagaosa and Y. Tokura, "Topological properties and dynamics of magnetic skyrmions.," *Nat. Nanotech.*, vol. 8, p. 899, 2013.

[42] I. Dzyaloshinsky, "A thermodynamic theory of "weak" ferromagnetism of antiferromagnetics," *J. Phys. Chem. Solids*, vol. 4, p. 241, 1958.

[43] T. Moriya, "Anisotropic superexchange interaction and weak ferromagnetism," *Phys. Rev.*, vol. 120, p. 91, 1960.

[44] X. Yu, N. Kanazawa, Y. Onose, K. Kimoto, W. Zhang, S. Ishiwata, Y. Matsui, and Y. Tokura, "Near room-temperature formation of a skyrmion crystal in thin-films of the helimagnet FeGe," *Nat. Mater.*, vol. 10, p. 106, 2011.

[45] S. Seki, X. Yu, S. Ishiwata, and Y. Tokura, "Observation of skyrmions in a multiferroic material," *Science*, vol. 336, p. 198, 2012.

[46] Y. Tokunaga, X. Yu, J. White, H. M. Rønnow, D. Morikawa, Y. Taguchi, and Y. Tokura, "A new class of chiral materials hosting magnetic skyrmions beyond room temperature," *Nat. Commun.*, vol. 6, p. 7638, 2015.

[47] A. Leonov and M. Mostovoy, "Multiply periodic states and isolated skyrmions in an anisotropic frustrated magnet," *Nat. Commun.*, vol. 6, p. 8275, 2015.

[48] S. Hayami, S.-Z. Lin, and C. D. Batista, "Bubble and skyrmion crystals in frustrated magnets with easy-axis anisotropy," *Phys. Rev. B*, vol. 93, p. 184413, 2016.

[49] S. von Malottki, B. Dupé, P. F. Bessarab, A. Delin, and S. Heinze, "Enhanced skyrmion stability due to exchange frustration," *Sci. Rep.*, vol. 7, p. 12299, 2017.

[50] T. Garel and S. Doniach, "Phase transitions with spontaneous modulation-the dipolar Ising ferromagnet," *Phys. Rev. B*, vol. 26, p. 325, 1982.

[51] H.-B. Braun, "Topological effects in nanomagnetism: From superparamagnetism to chiral quantum solitons," *Adv. Phys.*, vol. 61, p. 1, 2012.

[52] S. Rohart, J. Miltat, and A. Thiaville, "Path to collapse for an isolated Néel skyrmion," *Phys. Rev. B*, vol. 93, p. 214412, 2016.

[53] R. Wiesendanger, "Nanoscale magnetic skyrmions in metallic films and multilayers: A new twist for spintronics," *Nat. Rev. Mater.*, vol. 1, p. 16044, 2016.

[54] A. Fert, N. Reyren, and V. Cros, "Magnetic skyrmions: Advances in physics and potential applications," *Nat. Rev. Mater.*, vol. 2, p. 17031, 2017.

[55] X. Yu, N. Kanazawa, W. Zhang, T. Nagai, T. Hara, K. Kimoto, Y. Matsui, Y. Onose, and Y. Tokura, "Skyrmion flow near room temperature in an ultralow current density," *Nat. Commun.*, vol. 3, p. 988, 2012.

[56] K. Everschor-Sitte and M. Sitte, "Real-space berry phases: Skyrmion soccer," *J. Appl. Phys.*, vol. 115, p. 172602, 2014.

[57] A. Neubauer, C. Pfleiderer, B. Binz, A. Rosch, R. Ritz, P. Niklowitz, and P. Böni, "Topological Hall effect in the A phase of MnSi," *Phys. Rev. Lett.*, vol. 102, p. 186602, 2009.

[58] T. Schulz, R. Ritz, A. Bauer, M. Halder, M. Wagner, C. Franz, C. Pfleiderer, K. Everschor, M. Garst, and A. Rosch, "Emergent electrodynamics of skyrmions in a chiral magnet," *Nat. Phys.*, vol. 8, p. 301, 2012.

[59] A. N. Bogdanov and D. Yablonskii, "Thermodynamically stable "vortices" in magnetically ordered crystals. the mixed state of magnets," *J. Exp. Theor. Phys.*, vol. 95, p. 178, 1989.

[60] J. H. Han, J. Zang, Z. Yang, J.-H. Park, and N. Nagaosa, "Skyrmion lattice in a two-dimensional chiral magnet," *Phys. Rev. B*, vol. 82, p. 094429, 2010.

[61] E. Simon, K. Palotás, L. Rózsa, L. Udvardi, and L. Szunyogh, " Formation of magnetic skyrmions with tunable properties in PdFe bilayer deposited on Ir (111)," *Phys. Rev. B*, vol. 90, p. 094410, 2014.

[62] B. Dupé, M. Hoffmann, C. Paillard, and S. Heinze, "Tailoring magnetic skyrmions in ultra-thin transition metal films," *Nat. Commun.*, vol. 5, p. 4030, 2014.

[63] L. Rózsa, A. Deák, E. Simon, R. Yanes, L. Udvardi, L. Szunyogh, and U. Nowak, "Skyrmions with attractive interactions in an ultrathin magnetic film," *Phys. Rev. Lett.*, vol. 117, p. 157205, 2016.

[64] S. Woo, K. M. Song, X. Zhang, Y. Zhou, M. Ezawa, X. Liu, S. Finizio, J. Raabe, N. J. Lee, S.-I. Kim, *et al.*, "Current-driven dynamics and inhibition of the skyrmion Hall effect of ferrimagnetic skyrmions in GdFeCo films," *Nat. Commun.*, vol. 9, p. 959, 2018.

[65] I. L. Fernandes, J. Chico, and S. Lounis, "Impurity-dependent gyrotropic motion, deflection and pinning of current-driven ultrasmall skyrmions in PdFe/Ir (111) surface," *J. Phys.: Condens. Matter*, vol. 32, p. 425802, 2020.

[66] X. Zhang, Y. Zhou, K. M. Song, T.-E. Park, J. Xia, M. Ezawa, X. Liu, W. Zhao, G. Zhao, and S. Woo, "Skyrmion-electronics: writing, deleting, reading and processing magnetic skyrmions toward spintronic applications," *J. Phys.: Condens. Matter*, vol. 32, p. 143001, 2020.

[67] F. Büttner, I. Lemesh, and G. S. D. Beach, "Theory of isolated magnetic skyrmions: From fundamentals to room temperature applications," *Sci. Rep.*, vol. 8, p. 4464, 2018.

[68] W. Legrand, D. Maccariello, F. Ajejas, S. Collin, A. Vecchiola, K. Bouzehouane, N. Reyren, V. Cros, and A. Fert, "Room-temperature stabilization of antiferromagnetic skyrmions in synthetic antiferromagnets," *Nat. Mater.*, vol. 19, p. 34, 2020.

[69] S. Z. Lin, C. Reichhardt, C. D. Batista, and A. Saxena, "Particle model for skyrmions in metallic chiral magnets: Dynamics, pinning, and creep," *Phys. Rev. B*, vol. 87, p. 214419, 2013.

[70] W. Jiang, X. Zhang, G. Yu, W. Zhang, X. Wang, M. Benjamin Jungfleisch, J. E. Pearson, X. Cheng, O. Heinonen, K. L. Wang, *et al.*, "Direct observation of the skyrmion Hall effect," *Nat. Phys.*, vol. 13, p. 162, 2017.

[71] J. Iwasaki, M. Mochizuki, and N. Nagaosa, "Universal current-velocity relation of skyrmion motion in chiral magnets," *Nat. Commun.*, vol. 4, p. 1463, 2013.

[72] I. L. Fernandes, J. Bouaziz, S. Blügel, and S. Lounis, "Universality of defect-skyrmion interaction profiles," *Nat. Commun.*, vol. 9, p. 4395, 2018.

[73] X. Zhang, Y. Zhou, and M. Ezawa, "Antiferromagnetic skyrmion: Stability, creation and manipulation," *Sci. Rep.*, vol. 6, p. 24795, 2016.

[74] J. Barker and O. A. Tretiakov, "Static and dynamical properties of antiferromagnetic skyrmions in the presence of applied current and temperature," *Phys. Rev. Lett.*, vol. 116, p. 147203, 2016.

[75] Y. Hirata, D.-H. Kim, S. K. Kim, D.-K. Lee, S.-H. Oh, D.-Y. Kim, T. Nishimura, T. Okuno, Y. Futakawa, H. Yoshikawa, *et al.*, "Vanishing skyrmion Hall effect at the angular momentum compensation temperature of a ferrimagnet," *Nat. Nanotechnol.*, vol. 14, p. 232, 2019.

[76] A. Bogdanov, U. K. Roessler, M. Wolf, and K.-H. Müller, "Magnetic structures and reorientation transitions in noncentrosymmetric uniaxial antiferromagnets," *Phys. Rev. B*, vol. 66, p. 214410, 2002.

[77] H. D. Rosales, D. C. Cabra, and P. Pujol, "Three-sublattice skyrmion crystal in the antiferromagnetic triangular lattice," *Phys. Rev. B*, vol. 92, p. 214439, 2015.

[78] R. Keesman, M. Raaijmakers, A. Baerends, G. Barkema, and R. Duine, "Skyrmions in square-lattice antiferromagnets," *Phys. Rev. B*, vol. 94, p. 054402, 2016.

[79] X. Zhang, M. Ezawa, and Y. Zhou, "Thermally stable magnetic skyrmions in multilayer synthetic antiferromagnetic racetracks," *Phys. Rev. B*, vol. 94, p. 064406, 2016.

[80] B. Göbel, A. Mook, J. Henk, and I. Mertig, "Antiferromagnetic skyrmion crystals: Generation, topological Hall, and topological spin Hall effect," *Phys. Rev. B*, vol. 96, p. 060406, 2017.

[81] L. Shen, J. Xia, G. Zhao, X. Zhang, M. Ezawa, O. A. Tretiakov, X. Liu, and Y. Zhou, "Dynamics of the antiferromagnetic skyrmion induced by a magnetic anisotropy gradient," *Phys. Rev. B*, vol. 98, p. 134448, 2018.

[82] R. Silva, R. Silva, A. Pereira, and W. Moura-Melo, "Antiferromagnetic skyrmions overcoming obstacles in a racetrack," *J. Phys.: Condens. Matter*, vol. 31, p. 225802, 2019.

[83] R. Khoshlahni, A. Qaiumzadeh, A. Bergman, and A. Brataas, "Ultrafast generation and dynamics of isolated skyrmions in antiferromagnetic insulators," *Phys. Rev. B*, vol. 99, p. 054423, 2019.

[84] S. A. Díaz, J. Klinovaja, and D. Loss, "Topological magnons and edge states in antiferromagnetic skyrmion crystals," *Phys. Rev. Lett.*, vol. 122, p. 187203, 2019.

[85] R. Zarzuela, S. K. Kim, and Y. Tserkovnyak, "Stabilization of the skyrmion crystal phase and transport in thin-film antiferromagnets," *Phys. Rev. B*, vol. 100, p. 100408, 2019.

[86] P. Bessarab, D. Yudin, D. Gulevich, P. Wadley, M. Titov, and O. A. Tretiakov, "Stability and lifetime of antiferromagnetic skyrmions," *Phys. Rev. B*, vol. 99, p. 140411, 2019.

[87] M. N. Potkina, I. S. Lobanov, H. Jónsson, and V. M. Uzdin, "Skyrmions in antiferromagnets: Thermal stability and the effect of external field and impurities," *J. Appl. Phys.*, vol. 127, p. 213906, 2020.

[88] Z. Liu, M. dos Santos Dias, and S. Lounis, "Theoretical investigation of antiferromagnetic skyrmions in a triangular monolayer," *J. Phys.: Condens. Matter*, vol. 32, p. 425801, 2020.

[89] T. Dohi, S. DuttaGupta, S. Fukami, and H. Ohno, "Formation and current-induced motion of synthetic antiferromagnetic skyrmion bubbles," *Nat. Commun.*, vol. 10, p. 5153, 2019.

[90] A. Finco, A. Haykal, R. Tanos, F. Fabre, S. Chouaieb, W. Akhtar, I. Robert-Philip, W. Legrand, F. Ajejas, K. Bouzehouane, *et al.*, "Imaging non-collinear antiferromagnetic textures via single spin relaxometry," *Nat. Commun.*, vol. 12, p. 767, 2021.

[91] R. Juge, N. Sisodia, J. U. Larrañaga, Q. Zhang, V. T. Pham, K. G. Rana, B. Sarpi, N. Mille, S. Stanescu, R. Belkhou, *et al.*, "Skyrmions in synthetic antiferromagnets and their nucleation via electrical current and ultra-fast laser illumination," *Nat. Commun.*, vol. 13, p. 4807, 2022.

[92] R. Chen, Q. Cui, L. Han, X. Xue, J. Liang, H. Bai, Y. Zhou, F. Pan, H. Yang, and C. Song, "Controllable generation of antiferromagnetic skyrmions in synthetic antiferromagnets with thermal effect," *Adv. Funct. Mater.*, vol. 32, p. 2111906, 2022.

[93] S. Gao, H. D. Rosales, F. A. Gómez Albarracín, V. Tsurkan, G. Kaur, T. Fennell, P. Steffens, M. Boehm, P. Čermák, A. Schneidewind, E. Ressouche, D. C. Cabra, C. Rüegg, and O. Zaharko, "Fractional antiferromagnetic skyrmion lattice induced by anisotropic couplings," *Nature*, vol. 586, p. 37, 2020.

[94] A. Ross, R. Lebrun, C. Ulloa, D. A. Grave, A. Kay, L. Baldrati, F. Kronast, S. Valencia, A. Rothschild, and M. Kläui, "Structural sensitivity of the spin Hall magnetoresistance in antiferromagnetic thin films," *Phys. Rev. B*, vol. 102, p. 094415, 2020.

[95] H. Jani, J.-C. Lin, J. Chen, J. Harrison, F. Maccherozzi, J. Schad, S. Prakash, C.-B. Eom, A. Ariando, T. Venkatesan, and P. G. Radaelli, "Antiferromagnetic half-skyrmions and bimerons at room temperature," *Nature*, vol. 590, p. 74, 2021.

[96] O. Tretiakov and O. Tchernyshyov, "Vortices in thin ferromagnetic films and the skyrmion number," *Phys. Rev. B*, vol. 75, p. 012408, 2007.

[97] M. Ezawa, "Compact merons and skyrmions in thin chiral magnetic films," *Phys. Rev. B*, vol. 83, p. 100408, 2011.

[98] S.-Z. Lin, A. Saxena, and C. D. Batista, "Skyrmion fractionalization and merons in chiral magnets with easy-plane anisotropy," *Phys. Rev. B*, vol. 91, p. 224407, 2015.

[99] B. Göbel, A. Mook, J. Henk, I. Mertig, and O. A. Tretiakov, "Magnetic bimerons as skyrmion analogues in in-plane magnets," *Phys. Rev. B*, vol. 99, p. 060407, 2019.

[100] C. Phatak, A. Petford-Long, and O. Heinonen, "Direct observation of unconventional topological spin structure in coupled magnetic discs," *Phys. Rev. Lett.*, vol. 108, p. 067205, 2012.

[101] A. Tan, J. Li, A. Scholl, E. Arenholz, A. Young, Q. Li, C. Hwang, and Z. Qiu, "Topology of spin meron pairs in coupled Ni/Fe/Co/Cu (001) disks," *Phys. Rev. B*, vol. 94, p. 014433, 2016.

[102] X. Lu, R. Fei, L. Zhu, and L. Yang, "Meron-like topological spin defects in monolayer $CrCl_3$," *Nat. Commun.*, vol. 11, p. 4724, 2020.

[103] M. Augustin, S. Jenkins, R. F. Evans, K. S. Novoselov, and E. J. Santos, "Properties and dynamics of meron topological spin textures in the two-dimensional magnet $CrCl_3$," *Nat. Commun.*, vol. 12, p. 185, 2021.

[104] S. Hayami and R. Yambe, "Meron-antimeron crystals in noncentrosymmetric itinerant magnets on a triangular lattice," *Phys. Rev. B*, vol. 104, p. 094425, 2021.

[105] J. Xia, X. Zhang, X. Liu, Y. Zhou, and M. Ezawa, "Qubits based on merons in magnetic nanodisks," *Commun. Mater.*, vol. 3, p. 88, 2022.

[106] N. Romming, A. Kubetzka, C. Hanneken, K. von Bergmann, and R. Wiesendanger, "Field-dependent size and shape of single magnetic skyrmions," *Phys. Rev. Lett.*, vol. 114, p. 177203, 2015.

[107] A. Liechtenstein, M. Katsnelson, V. Antropov, and V. Gubanov, "Local spin density functional approach to the theory of exchange interactions in ferromagnetic metals and alloys," *J. Magn. Magn. Mater.*, vol. 67, p. 65, 1987.

[108] L. Udvardi, L. Szunyogh, K. Palotás, and P. Weinberger, "First-principles relativistic study of spin waves in thin magnetic films," *Phys. Rev. B*, vol. 68, p. 104436, 2003.

[109] E. C. Stoner, "Collective electron ferromagnetism," *Proc. R. Soc. London Ser. A-Math. Phys. Eng. Sci.*, vol. 165, p. 372, 1938.

[110] S. Alexander and P. Anderson, "Interaction between localized states in metals," *Phys. Rev.*, vol. 133, p. A1594, 1964.

[111] S. Blügel, M. Weinert, and P. Dederichs, "Ferromagnetism and antiferromagnetism of 3d-metal overlayers on metals," *Phys. Rev. Lett.*, vol. 60, p. 1077, 1988.

[112] A. Bogdanov and U. Rößler, "Chiral symmetry breaking in magnetic thin films and multilayers," *Phys. Rev. Lett.*, vol. 87, p. 037203, 2001.

[113] A. K. Nayak, V. Kumar, T. Ma, P. Werner, E. Pippel, R. Sahoo, F. Damay, U. K. Rößler, C. Felser, and S. S. Parkin, "Magnetic antiskyrmions above room temperature in tetragonal Heusler materials," *Nature*, vol. 548, p. 561, 2017.

[114] G. P. Müller, M. Hoffmann, C. Dißelkamp, D. Schürhoff, S. Mavros, M. Sallermann, N. S. Kiselev, H. Jónsson, and S. Blügel, "Spirit: Multifunctional framework for atomistic spin simulations," *Phys. Rev. B*, vol. 99, p. 224414, 2019.

[115] G. Chen, "Skyrmion Hall effect," *Nat. Phys.*, vol. 13, p. 112, 2017.

[116] R. Msiska, D. R. Rodrigues, J. Leliaert, and K. Everschor-Sitte, "Nonzero skyrmion Hall effect in topologically trivial structures," *Phys. Rev. Appl.*, vol. 17, p. 064015, 2022.

[117] X. Zhang, Y. Zhou, and M. Ezawa, "Magnetic bilayer-skyrmions without skyrmion Hall effect," *Nat. Commun.*, vol. 7, p. 10293, 2016.

[118] W. Heisenberg, Zur theorie des ferromagnetismus. Springer, 1928.

[119] P. A. M. Dirac, "Quantum mechanics of many-electron systems," *Proc. R. Soc. London Ser. A-Math. Phys. Eng. Sci.*, vol. 123, p. 714, 1929.

[120] N. Majlis, The Quantum Theory Of Magnetism. World Scientific Publishing, 2007.

[121] A. Fert, "Magnetic and transport properties of metallic multilayers," *Mater. Sci. Forum*, vol. 59, p. 439, 1990.

[122] A. Crépieux and C. Lacroix, "Dzyaloshinsky–Moriya interactions induced by symmetry breaking at a surface," *J. Magn. Magn. Mater.*, vol. 182, p. 341, 1998.

[123] P. Hohenberg and W. Kohn, "Inhomogeneous electron gas," *Phys. Rev.*, vol. 136, p. B864, 1964.

[124] W. Kohn and L. J. Sham, "Self-consistent equations including exchange and correlation effects," *Phys. Rev.*, vol. 140, p. A1133, 1965.

[125] P. Giannozzi, S. Baroni, N. Bonini, M. Calandra, R. Car, C. Cavazzoni, D. Ceresoli, G. L. Chiarotti, M. Cococcioni, I. Dabo, *et al.*, "QUANTUM ESPRESSO: A modular and open-source software project for quantum simulations of materials," *J. Phys.: Condens. Matter*, vol. 21, p. 395502, 2009.

[126] P. Giannozzi, O. Andreussi, T. Brumme, O. Bunau, M. B. Nardelli, M. Calandra, R. Car, C. Cavazzoni, D. Ceresoli, M. Cococcioni, *et al.*, "Advanced capabilities for materials modelling with Quantum ESPRESSO," *J. Phys.: Condens. Matter*, vol. 29, p. 465901, 2017.

[127] J. Korringa, "On the calculation of the energy of a Bloch wave in a metal," *Physica*, vol. 13, p. 392, 1947.

[128] W. Kohn and N. Rostoker, "Solution of the Schrödinger equation in periodic lattices with an application to metallic lithium," *Phys. Rev.*, vol. 94, p. 1111, 1954.

[129] N. Papanikolaou, R. Zeller, and P. Dederichs, "Conceptual improvements of the KKR method," *J. Phys.: Condens. Matter*, vol. 14, p. 2799, 2002.

[130] H. Ebert, D. Koedderitzsch, and J. Minar, "Calculating condensed matter properties using the KKR-Green's function method—recent developments and applications," *Rep. Prog. Phys.*, vol. 74, p. 096501, 2011.

[131] H. Ebert and S. Mankovsky, "Anisotropic exchange coupling in diluted magnetic semiconductors: *Ab initio* spin-density functional theory," *Phys. Rev. B*, vol. 79, p. 045209, 2009.

[132] L. Udvardi and L. Szunyogh, "Chiral asymmetry of the spin-wave spectra in ultrathin magnetic films," *Phys. Rev. Lett.*, vol. 102, p. 207204, 2009.

[133] R. M. Martin, Electronic Structure: Basic Theory and Practical Methods. Cambridge University Press, 2020.

[134] E. Engel, Density Functional Theory. Springer, 2011.

[135] J. Zabloudil, R. Hammerling, P. Weinberger, and L. Szunyogh, Electron Scattering in Solid Matter. Springer, 2005.

[136] D. S. G. Bauer, Development of a Relativistic Full-Potential First-Principles Multiple Scattering Green Function Method Applied to Complex Magnetic Textures of Nanostructures at Surfaces. PhD thesis, RWTH Aachen, 2014.

[137] J. C. Villanueva, "How many atoms are there in the universe," *Universe Today*, vol. 30, 2009.

[138] M. Born and W. Heisenberg, "Zur quantentheorie der molekeln," *Ann. Phys.-Berlin*, vol. 379, p. 1, 1924.

[139] S. H. Vosko, L. Wilk, and M. Nusair, "Accurate spin-dependent electron liquid correlation energies for local spin density calculations: a critical analysis," *Can. J. Phys.*, vol. 58, p. 1200, 1980.

[140] G. Ortiz and P. Ballone, "Correlation energy, structure factor, radial distribution function, and momentum distribution of the spin-polarized uniform electron gas," *Phys. Rev. B*, vol. 50, p. 1391, 1994.

[141] K. Capelle, "A bird's-eye view of density-functional theory," *Braz. J. Phys.*, vol. 36, pp. 1318–1343, 2006.

[142] J. P. Perdew, K. Burke, and M. Ernzerhof, "Generalized gradient approximation made simple," *Phys. Rev. Lett.*, vol. 77, p. 3865, 1996.

[143] J. P. Perdew, A. Ruzsinszky, G. I. Csonka, O. A. Vydrov, G. E. Scuseria, L. A. Constantin, X. Zhou, and K. Burke, "Restoring the density-gradient expansion for exchange in solids and surfaces," *Phys. Rev. Lett.*, vol. 100, p. 136406, 2008.

[144] F. Bloch, "Über die quantenmechanik der elektronen in kristallgittern," *Z. Phys.*, vol. 52, p. 555, 1929.

[145] U. Von Barth and C. Gelatt, "Validity of the frozen-core approximation and pseudopotential theory for cohesive energy calculations," *Phys. Rev. B*, vol. 21, p. 2222, 1980.

[146] W. E. Pickett, "Pseudopotential methods in condensed matter applications," *Computer Physics Reports*, vol. 9, p. 115, 1989.

[147] P. Schwerdtfeger, "The pseudopotential approximation in electronic structure theory," *ChemPhysChem*, vol. 12, p. 3143, 2011.

[148] D. Hamann, M. Schlüter, and C. Chiang, "Norm-conserving pseudopotentials," *Phys. Rev. Lett.*, vol. 43, p. 1494, 1979.

[149] G. B. Bachelet, D. R. Hamann, and M. Schlüter, "Pseudopotentials that work: From H to Pu," *Phys. Rev. B*, vol. 26, p. 4199, 1982.

[150] P. E. Blöchl, "Projector augmented-wave method," *Phys. Rev. B*, vol. 50, p. 17953, 1994.

[151] G. Kresse and D. Joubert, "From ultrasoft pseudopotentials to the projector augmented-wave method," *Phys. Rev. B*, vol. 59, p. 1758, 1999.

[152] P. Giannozzi, O. Baseggio, P. Bonfà, D. Brunato, R. Car, I. Carnimeo, C. Cavazzoni, S. De Gironcoli, P. Delugas, F. Ferrari Ruffino, *et al.*, "QUANTUM ESPRESSO toward the exascale," *J. Chem. Phys.*, vol. 152, p. 154105, 2020.

[153] A. Dal Corso, "Pseudopotentials periodic table: From H to Pu," *Comput. Mater. Sci.*, vol. 95, p. 337, 2014.

[154] K. Lejaeghere, G. Bihlmayer, T. Björkman, P. Blaha, S. Blügel, V. Blum, D. Caliste, I. E. Castelli, S. J. Clark, A. Dal Corso, *et al.*, "Reproducibility in density functional theory calculations of solids," *Science*, vol. 351, p. aad3000, 2016.

[155] B. H. Drittler, KKR-Greensche Funktionsmethode für das volle Zellpotential. PhD thesis, RWTH Aachen, 1990.

[156] N. Stefanou, H. Akai, and R. Zeller, "An efficient numerical method to calculate shape truncation functions for Wigner-Seitz atomic polyhedra," *Comput. Phys. Commun.*, vol. 60, p. 231, 1990.

[157] P. Rüßmann and JuDFTteam, "JuDFTteam/JuKKR: v3.6," *Zenodo*, 2022.

[158] A. Gonis, Theoretical Materials Science: Tracing the Electronic Origins of Materials Behavior. Materials Research Society, 2000.

[159] S. Heers, Effect of Spin-Orbit Scattering on Transport Properties of Low-Dimensional Dilute Alloys. PhD thesis, RWTH Aachen, 2011.

[160] R. Zeller, P. Dederichs, B. Újfalussy, L. Szunyogh, and P. Weinberger, "Theory and convergence properties of the screened Korringa-Kohn-Rostoker method," *Phys. Rev. B*, vol. 52, p. 8807, 1995.

[161] K. Wildberger, R. Zeller, and P. Dederichs, "Screened KKR-Green's-function method for layered systems," *Phys. Rev. B*, vol. 55, p. 10074, 1997.

[162] K. Wildberger, P. Lang, R. Zeller, and P. Dederichs, "Fermi-Dirac distribution in ab initio Green's-function calculations," *Phys. Rev. B*, vol. 52, p. 11502, 1995.

[163] A. R. Thieß, Development and Application of a Massively Parallel KKR Green Function Method for Large Scale Systems. PhD thesis, RWTH Aachen, 2013.

[164] M. Springford, Electrons at the Fermi Surface. Cambridge University Press, 1980.

[165] V. Heine, B. DW, R. Haydock, and K. MJ, Solid state physics: Advances in research and applications. Academic Press, 1980.

[166] P. Lloyd, "Wave propagation through an assembly of spheres: III. The density of states in a liquid," *Proc. Phys. Soc.*, vol. 90, p. 217, 1967.

[167] G. Daalderop, P. Kelly, and M. Schuurmans, "First-principles calculation of the magnetocrystalline anisotropy energy of iron, cobalt, and nickel," *Phys. Rev. B*, vol. 41, p. 11919, 1990.

[168] K. Krieger, J. Dewhurst, P. Elliott, S. Sharma, and E. Gross, "Laser-induced demagnetization at ultrashort time scales: Predictions of TDDFT," *J. Chem. Theory Comput.*, vol. 11, p. 4870, 2015.

[169] M. Stamenova, J. Simoni, and S. Sanvito, "Role of spin-orbit interaction in the ultrafast demagnetization of small iron clusters," *Phys. Rev. B*, vol. 94, p. 014423, 2016.

[170] G. P. Müller, H. Jonsson, C. Honerkamp, and S. Blügel, "Advanced methods for atomic scale spin simulations and application to localized magnetic states," tech. rep., Fachgruppe Physik, 2019.

[171] O. Eriksson, A. Bergman, L. Bergqvist, and J. Hellsvik, Atomistic Spin Dynamics: Foundations and Applications. Oxford University Press, 2017.

[172] J. P. Chico Carpio, Magnetization Dynamics on the Nanoscale: From First Principles to Atomistic Spin Dynamics. PhD thesis, Acta Universitatis Upsaliensis, 2016.

[173] U. Nowak, "Thermally activated reversal in magnetic nanostructures," *Annu. Rev. Comput. Phys.*, vol. 9, p. 105, 2001.

[174] J. Mentink, M. Tretyakov, A. Fasolino, M. Katsnelson, and T. Rasing, "Stable and fast semi-implicit integration of the Stochastic Landau–Lifshitz equation," *J. Phys.: Condens. Matter*, vol. 22, p. 176001, 2010.

[175] P. Depondt and F. Mertens, "Spin dynamics simulations of two-dimensional clusters with Heisenberg and dipole–dipole interactions," *J. Phys.: Condens. Matter*, vol. 21, p. 336005, 2009.

[176] A. V. Ivanov, V. M. Uzdin, and H. Jónsson, "Fast and robust algorithm for energy minimization of spin systems applied in an analysis of high temperature spin configurations in terms of skyrmion density," *Comput. Phys. Commun.*, vol. 260, p. 107749, 2021.

[177] J. C. Slonczewski, "Current-driven excitation of magnetic multilayers," *J. Magn. Magn. Mater.*, vol. 159, p. L1, 1996.

[178] P. Chureemart, R. Evans, and R. Chantrell, "Dynamics of domain wall driven by spin-transfer torque," *Phys. Rev. B*, vol. 83, p. 184416, 2011.

[179] D. C. B. Schürhoff, Atomistic Spin Dynamics with Real Time Control of Simulation Parameters and Visualizationx. PhD thesis, RWTH Aachen, 2016.

[180] C. Schieback, M. Kläui, U. Nowak, U. Rüdiger, and P. Nielaba, "Numerical investigation of spin-torque using the Heisenberg model," *Eur. Phys. J. B*, vol. 59, p. 429, 2007.

[181] P. F. Bessarab, V. M. Uzdin, and H. Jónsson, "Method for finding mechanism and activation energy of magnetic transitions, applied to skyrmion and antivortex annihilation," *Comput. Phys. Commun.*, vol. 196, p. 335, 2015.

[182] G. P. Müller, P. F. Bessarab, S. M. Vlasov, F. Lux, N. S. Kiselev, S. Blügel, V. M. Uzdin, and H. Jónsson, "Duplication, collapse, and escape of magnetic skyrmions revealed using a systematic saddle point search method," *Phys. Rev. Lett.*, vol. 121, p. 197202, 2018.

[183] K. Binder, D. W. Heermann, and K. Binder, Monte Carlo Simulation in Statistical Physics. Springer, 2010.

[184] A. Aldarawsheh, I. L. Fernandes, S. Brinker, M. Sallermann, M. Abusaa, S. Blügel, and S. Lounis, "Emergence of zero-field non-synthetic single and interchained antiferromagnetic skyrmions in thin films," *Nat. Commun.*, vol. 13, p. 7369, 2022.

[185] J. Xia, X. Zhang, M. Ezawa, Z. Hou, W. Wang, X. Liu, and Y. Zhou, "Current-driven dynamics of frustrated skyrmions in a synthetic antiferromagnetic bilayer," *Phys. Rev. Appl.*, vol. 11, p. 044046, 2019.

[186] P. Kurz, Non-collinear magnetism at surfaces and in ultrathin films. PhD thesis, RWTH Aachen, 2000.

[187] J. Spethmann, S. Meyer, K. von Bergmann, R. Wiesendanger, S. Heinze, and A. Kubetzka, "Discovery of magnetic single-and triple-Q states in Mn/Re (0001)," *Phys. Rev. Lett.*, vol. 124, p. 227203, 2020.

[188] J. Spethmann, M. Grünebohm, R. Wiesendanger, K. von Bergmann, and A. Kubetzka, "Discovery and characterization of a new type of domain wall in a row-wise antiferromagnet," *Nat. Commun.*, vol. 12, p. 3488, 2021.

[189] F. Y. Wu, "Knot theory and statistical mechanics," *Rev. Mod. Phys.*, vol. 64, p. 1099, 1992.

[190] D. B. Amabilino and J. F. Stoddart, "Interlocked and intertwined structures and superstructures," *Chem. Rev.*, vol. 95, p. 2725, 1995.

[191] P. Dabrowski-Tumanski and J. I. Sulkowska, "Topological knots and links in proteins," *Proc. Natl Acad. Sci. USA*, vol. 114, p. 3415, 2017.

[192] A. D. Bates, A. Maxwell, *et al.*, DNA Topology. Oxford University Press, 2005.

[193] D. M. Crum, M. Bouhassoune, J. Bouaziz, B. Schweflinghaus, S. Blügel, and S. Lounis, "Perpendicular reading of single confined magnetic skyrmions," *Nat. Commun.*, vol. 6, p. 8541, 2015.

[194] M. Bouhassoune and S. Lounis, "Friedel oscillations induced by magnetic skyrmions: From scattering properties to all-electrical detection," *Nanomaterials*, vol. 11, p. 194, 2021.

[195] I. Lima Fernandes, S. Blügel, and S. Lounis, "Spin-orbit enabled all-electrical readout of chiral spin-textures," *Nat. Commun.*, vol. 13, p. 1576, 2022.

[196] S. Rohart and A. Thiaville, "Skyrmion confinement in ultrathin film nanostructures in the presence of Dzyaloshinskii-Moriya interaction," *Phys. Rev. B*, vol. 88, p. 184422, 2013.

[197] D. Hinzke and U. Nowak, "Monte Carlo simulation of magnetization switching in a Heisenberg model for small ferromagnetic particles," *Comput. Phys. Commun.*, vol. 121, p. 334, 1999.

[198] A. Aldarawsheh, M. Sallermann, M. Abusaa, and S. Lounis, "A spin model for intrinsic antiferromagnetic skyrmions on a triangular lattice," *Front. Phys.*, vol. 11, p. 1175317, 2023.

[199] B. Hardrat, A. Al-Zubi, P. Ferriani, S. Blügel, G. Bihlmayer, and S. Heinze, "Complex magnetism of iron monolayers on hexagonal transition metal surfaces from first principles," *Phys. Rev. B*, vol. 79, p. 094411, 2009.

[200] X. Zhang, Y. Zhou, M. Ezawa, G. Zhao, and W. Zhao, "Magnetic skyrmion transistor: skyrmion motion in a voltage-gated nanotrack," *Sci. Rep.*, vol. 5, p. 11369, 2015.

[201] X. Wang, H. Yuan, and X. Wang, "A theory on skyrmion size," *Commun. Phys.*, vol. 1, p. 31, 2018.

[202] A. Aldarawsheh, M. Sallermann, M. Abusaa, and S. Lounis, "Intrinsic Néel antiferromagnetic multimeronic spin textures in ultrathin films," *J. Phys. Chem. Lett.*, vol. 14, p. 8970, 2023.

[203] N. Gao, S.-G. Je, M.-Y. Im, J. W. Choi, M. Yang, Q.-c. Li, T. Wang, S. Lee, H.-S. Han, K.-S. Lee, *et al.*, "Creation and annihilation of topological meron pairs in in-plane magnetized films," *Nat. Commun.*, vol. 10, p. 5603, 2019.

[204] C. Donnelly, K. L. Metlov, V. Scagnoli, M. Guizar-Sicairos, M. Holler, N. S. Bingham, J. Raabe, L. J. Heyderman, N. R. Cooper, and S. Gliga, "Experimental observation of vortex rings in a bulk magnet," *Nat. Phys.*, vol. 17, p. 316, 2021.

[205] A. Kolesnikov, V. Plotnikov, E. Pustovalov, A. Samardak, L. Chebotkevich, A. Ognev, and O. A. Tretiakov, "Composite topological structure of domain walls in synthetic antiferromagnets," *Sci. Rep.*, vol. 8, p. 15794, 2018.

[206] O. Amin, S. Poole, S. Reimers, L. Barton, A. Dal Din, F. Maccherozzi, S. Dhesi, V. Novák, F. Krizek, J. Chauhan, *et al.*, "Antiferromagnetic half-skyrmions electrically generated and controlled at room temperature," *Nat. Nanotechnol.*, vol. 18, p. 849, 2023.

[207] F. P. Chmiel, N. Waterfield Price, R. D. Johnson, A. D. Lamirand, J. Schad, G. van der Laan, D. T. Harris, J. Irwin, M. S. Rzchowski, C. B. Eom, *et al.*, "Observation of magnetic vortex pairs at room temperature in a planar α-Fe_2O_3/Co heterostructure," *Nat. Mater.*, vol. 17, p. 581, 2018.

[208] R. Fernandes, R. Lopes, and A. Pereira, "Skyrmions and merons in two-dimensional antiferromagnetic systems," *Solid State Commun.*, vol. 290, p. 55, 2019.

[209] P. Radaelli, J. Radaelli, N. Waterfield-Price, and R. Johnson, "Micromagnetic modeling and imaging of vortex— meron structures in an oxide— metal heterostructure," *Phys. Rev. B*, vol. 101, p. 144420, 2020.

[210] X. Li, L. Shen, Y. Bai, J. Wang, X. Zhang, J. Xia, M. Ezawa, O. A. Tretiakov, X. Xu, M. Mruczkiewicz, *et al.*, "Bimeron clusters in chiral antiferromagnets," *npj Comp. Mater.*, vol. 6, p. 169, 2020.

[211] L. Shen, J. Xia, X. Zhang, M. Ezawa, O. A. Tretiakov, X. Liu, G. Zhao, and Y. Zhou, "Current-induced dynamics and chaos of antiferromagnetic bimerons," *Phys. Rev. Lett.*, vol. 124, p. 037202, 2020.

[212] R. Silva, "Antiferromagnetic-bimeron dynamics driven by a spin-polarized current at an inhomogeneous racetrack," *Phys. Lett. A*, vol. 403, p. 127399, 2021.

[213] T. Shinjo, T. Okuno, R. Hassdorf, K. Shigeto, and T. Ono, "Magnetic vortex core observation in circular dots of permalloy," *Science*, vol. 289, p. 930, 2000.

[214] A. Rodríguez-Sota, V. Saxena, J. Spethmann, R. Wiesendanger, R. Lo Conte, A. Kubetzka, and K. von Bergmann, "Phase coexistence of Mn trimer clusters and antiferromagnetic Mn islands on Ir (111)," *ACS nano*, vol. 18, p. 3699, 2024.

[215] X. Liang, J. Xia, X. Zhang, M. Ezawa, O. A. Tretiakov, X. Liu, L. Qiu, G. Zhao, and Y. Zhou, "Antiferromagnetic skyrmion-based logic gates controlled by electric currents and fields," *Appl. Phys. Lett.*, vol. 119, 2021.

[216] M. Bhukta, T. Dohi, V. K. Bharadwaj, R. Zarzuela, M.-A. Syskaki, M. Foerster, M. A. Niño, J. Sinova, R. Frömter, and M. Kläui, "Homochiral antiferromagnetic merons, antimerons and bimerons realized in synthetic antiferromagnets," *Nat. Commun.*, vol. 15, p. 1641, 2024.

[217] X. Zhang, M. Ezawa, D. Xiao, G. Zhao, Y. Liu, and Y. Zhou, "All-magnetic control of skyrmions in nanowires by a spin wave," *Nanotechnology*, vol. 26, p. 225701, 2015.

[218] S. Komineas and N. Papanicolaou, "Skyrmion dynamics in chiral ferromagnets," *Phys. Rev. B*, vol. 92, p. 064412, 2015.

[219] L. Kong and J. Zang, "Dynamics of an insulating skyrmion under a temperature gradient," *Phys. Rev. Lett.*, vol. 111, p. 067203, 2013.

[220] C. Ma, X. Zhang, J. Xia, M. Ezawa, W. Jiang, T. Ono, S. Piramanayagam, A. Morisako, Y. Zhou, and X. Liu, "Electric field-induced creation and directional motion of domain walls and skyrmion bubbles," *Nano Lett.*, vol. 19, p. 353, 2018.

[221] R. Tomasello, S. Komineas, G. Siracusano, M. Carpentieri, and G. Finocchio, "Chiral skyrmions in an anisotropy gradient," *Phys. Rev. B*, vol. 98, p. 024421, 2018.

[222] H. Xia, C. Song, C. Jin, J. Wang, J. Wang, and Q. Liu, "Skyrmion motion driven by the gradient of voltage-controlled magnetic anisotropy," *J. Magn. Magn. Mater.*, vol. 458, p. 57, 2018.

[223] X. Wang, W. L. Gan, J. Martinez, F. N. Tan, M. Jalil, and W. S. Lew, "Efficient skyrmion transport mediated by a voltage controlled magnetic anisotropy gradient," *Nanoscale*, vol. 10, p. 733, 2018.

[224] J. Liang, J. Yu, J. Chen, M. Qin, M. Zeng, X. Lu, X. Gao, and J.-M. Liu, "Magnetic field gradient driven dynamics of isolated skyrmions and antiskyrmions in frustrated magnets," *New J. Phys.*, vol. 20, p. 053037, 2018.

[225] D. Cortés-Ortuño, W. Wang, M. Beg, R. A. Pepper, M.-A. Bisotti, R. Carey, M. Vousden, T. Kluyver, O. Hovorka, and H. Fangohr, "Thermal stability and topological protection of skyrmions in nanotracks," *Sci. Rep.*, vol. 7, p. 4060, 2017.

[226] C. Jin, C. Song, J. Wang, and Q. Liu, "Dynamics of antiferromagnetic skyrmion driven by the spin Hall effect," *Appl. Phys. Lett.*, vol. 109, p. 182404, 2016.

[227] S.-J. Lee, K.-W. Kim, H.-W. Lee, and K.-J. Lee, "Spin-orbit-torque-induced skyrmion dynamics for different types of spin-orbit coupling," *J. Magn. Magn. Mater.*, vol. 455, p. 14, 2018.

[228] A. Thiele, "Steady-state motion of magnetic domains," *Phys. Rev. Lett.*, vol. 30, p. 230, 1973.

[229] J. Xia, X. Zhang, M. Ezawa, Q. Shao, X. Liu, and Y. Zhou, "Dynamics of an elliptical ferromagnetic skyrmion driven by the spin–orbit torque," *Appl. Phys. Lett.*, vol. 116, 2020.

[230] S. Huang, C. Zhou, G. Chen, H. Shen, A. K. Schmid, K. Liu, and Y. Wu, "Stabilization and current-induced motion of antiskyrmion in the presence of anisotropic Dzyaloshinskii-Moriya interaction," *Phys. Rev. B*, vol. 96, p. 144412, 2017.

[231] J. Chen, J. Liang, J. Yu, M. Qin, Z. Fan, M. Zeng, X. Lu, X. Gao, S. Dong, and J. Liu, "Dynamics of distorted skyrmions in strained chiral magnets," *New J. Phys.*, vol. 20, p. 063050, 2018.

[232] A. A. Khajetoorians, W. D., O. A. F., and S. I., "Creating designer quantum states of matter atom-by-atom," *Nat. Rev. Phys.*, vol. 1, p. 703, 2019.

[233] S. E. Freeney, M. R. Slot, T. S. Gardenier, I. Swart, and D. Vanmaekelbergh, "Electronic quantum materials simulated with artificial model lattices," *ACS Nanosci. Au*, vol. 2, p. 198, 2022.

[234] M. F. Crommie, C. P. Lutz, and D. M. Eigler, "Confinement of electrons to quantum corrals on a metal surface," *Science*, vol. 262, p. 218, 1993.

[235] N. Nilius, T. M. Wallis, and W. Ho, "Development of one-dimensional band structure in artificial gold chains," *Science*, vol. 297, p. 1853, 2002.

[236] J. A. Stroscio, F. Tavazza, J. N. Crain, R. J. Celotta, and A. M. Chaka, "Electronically induced atom motion in engineered $CoCu_n$ nanostructures," *Science*, vol. 313, p. 948, 2006.

[237] M. Bouhassoune, B. Zimmermann, P. Mavropoulos, D. Wortmann, P. H. Dederichs, B. S., and S. Lounis, "Quantum well states and amplified spin-dependent Friedel oscillations in thin film," *Nat. Commun.*, vol. 5, p. 5558, 2014.

[238] M. Yankowitz, J. Xue, D. Cormode, J. D. Sanchez-Yamagishi, K. Watanabe, T. Taniguchi, P. Jarillo-Herrero, P. Jacquod, and B. J. LeRoy, "Emergence of superlattice Dirac points in graphene on hexagonal boron nitride," *Nat. Phys.*, vol. 8, p. 382, 2012.

[239] J. W. Park, H. S. Kim, T. Brumme, H. T., and Y. H. W., "Artificial relativistic molecules," *Nat. Commun.*, vol. 11, p. 815, 2020.

[240] M. R. Slot, T. S. Gardenier, P. H. Jacobse, G. C. P. van Miert, S. N. Kempkes, S. J. M. Zevenhuizen, C. M. Smith, D. Vanmaekelbergh, and I. Swart, "Experimental realization and characterization of an electronic Lieb lattice," *Nat. Phys.*, vol. 13, p. 372, 2017.

[241] S. Cheon, T.-H. Kim, S.-H. Lee, and H. W. Yeom, "Chiral solitons in a coupled double Peierls chain," *Science*, vol. 350, p. 182, 2015.

[242] . Drost, R., T. Ojanen, A. Harju, and P. Liljeroth, "Topological states in engineered atomic lattices," *Nat. Phys.*, vol. 13, p. 668, 2017.

[243] C. F. Hirjibehedin, P. L. Christopher, and A. J. Heinrich, "Spin coupling in engineered atomic structures," *Science*, vol. 312, p. 1021, 2006.

[244] S. Lounis, P. Mavropoulos, R. Zeller, P. H. Dederichs, and S. Blügel, "Noncollinear magnetism of Cr and Mn nanoclusters on Ni(111): Changing the magnetic configuration atom by atom," *Phys. Rev. B*, vol. 75, p. 174436, 2007.

[245] S. Lounis, P. H. Dederichs, and S. Blügel, "Magnetism of nanowires driven by novel even-odd effects," *Phys. Rev. Lett.*, vol. 101, p. 107204, 2008.

[246] S. Lounis, M. Reif, P. Mavropoulos, L. Glaser, P. H. Dederichs, M. Martins, S. Blügel, and W. Wurth, "Non-collinear magnetism of Cr nanostructures on $Fe_{3ML}/Cu(001)$: First principles and experimental investigations," *Europhys. Lett.*, vol. 81, p. 47004, 2008.

[247] P. Mavropoulos, S. Lounis, and S. Blügel, "Exchange coupling in transition-metal nanoclusters on Cu(001) and Cu(111) surfaces," *Phys. Status Solidi B*, vol. 247, p. 1187, 2010.

[248] S. Holzberger, T. Schuh, S. Blügel, S. Lounis, and W. Wulfhekel, "Parity effect in the ground state localization of antiferromagnetic chains coupled to a ferromagnet," *Phys. Rev. Lett.*, vol. 110, p. 157206, 2013.

[249] C. Holl, M. Knol, J. Pratzer, M. Chico, I. Lima Fernandes, S. Lounis, and M. Morgenstern, "Probing the pinning strength of magnetic vortex cores with sub-nanometer resolution," *Nat. Commun.*, vol. 11, p. 2833, 2020.

[250] I. G. Arjana, I. Lima Fernandes, J. Chico, and S. Lounis, "Sub-nanoscale atom-by-atom crafting of skyrmion-defect interaction profiles," *Sci. Rep.*, vol. 10, p. 14655, 2020.

[251] C. Reichhardt, C. J. O. Reichhardt, and M. V. Milošević, "Statics and dynamics of skyrmions interacting with disorder and nanostructures," *Rev. Mod. Phys.*, vol. 94, p. 035005, 2022.

[252] S. Brinker, M. dos Santos Dias, and S. Lounis, "Interatomic orbital magnetism: The case of $3d$ adatoms deposited on the Pt(111) surface," *Phys. Rev. B*, vol. 98, p. 094428, 2018.

[253] J. Bouaziz, M. d. S. Dias, F. S. M. Guimarães, S. Blügel, and S. Lounis, "Impurity-induced orbital magnetization in a Rashba electron gas," *Phys. Rev. B*, vol. 98, p. 125420, 2018.

[254] I. Lima Fernandes and S. Lounis, "Universal patterns of skyrmion magnetizations unveiled by defect implantation," *ArXiv:*, p. 2312.05903, 2023.

[255] I. L. Fernandes, M. Bouhassoune, and S. Lounis, "Defect-implantation for the all-electrical detection of non-collinear spin-textures," *Nat. Commun.*, vol. 11, p. 1602, 2020.

[256] F. Silly, M. Pivetta, M. Ternes, F. m. c. Patthey, J. P. Pelz, and W.-D. Schneider, "Creation of an atomic superlattice by immersing metallic adatoms in a two-dimensional electron sea," *Phys. Rev. Lett.*, vol. 92, p. 016101, 2004.

[257] N. N. Negulyaev, V. S. Stepanyuk, L. Niebergall, P. Bruno, M. Pivetta, M. Ternes, F. Patthey, and W.-D. Schneider, "Melting of two-dimensional adatom superlattices stabilized by long-range electronic interactions," *Phys. Rev. Lett.*, vol. 102, p. 246102, 2009.

[258] F. Meier, S. Lounis, J. Wiebe, L. Zhou, S. Heers, P. Mavropoulos, P. H. Dederichs, S. Blügel, and R. Wiesendanger, "Spin polarization of platinum (111) induced by the proximity to cobalt nanostripes," *Phys. Rev. B*, vol. 83, p. 075407, 2011.

[259] S. Lounis, A. Bringer, and S. Blügel, "Magnetic adatom induced skyrmion-like spin texture in surface electron waves," *Phys. Rev. Lett.*, vol. 108, p. 207202, 2012.

[260] M. A. Ruderman and C. Kittel, "Indirect exchange coupling of nuclear magnetic moments by conduction electrons," *Phys. Rev.*, vol. 96, p. 99, 1954.

[261] T. Kasuya, "A theory of metallic ferro- and antiferromagnetism on Zener's model," *Prog. Theor. Phys.*, vol. 16, p. 45, 1956.

[262] K. Yosida, "Magnetic properties of Cu-Mn alloys," *Phys. Rev.*, vol. 106, p. 893, 1957.

[263] H. Imamura, P. Bruno, and Y. Utsumi, "Twisted exchange interaction between localized spins embedded in a one- or two-dimensional electron gas with Rashba spin-orbit coupling," *Phys. Rev. B*, vol. 69, p. 121303, 2004.

[264] L. Zhou, J. Wiebe, S. Lounis, E. Vedmedenko, F. Meier, S. Blügel, P. H. Dederichs, and R. Wiesendanger, "Strength and directionality of surface Ruderman–Kittel–Kasuya–Yosida interaction mapped on the atomic scale," *Nat. Phys.*, vol. 6, p. 187, 2010.

[265] A. A. Khajetoorians, J. Wiebe, B. Chilian, S. Lounis, S. Blügel, and R. Wiesendanger, "Atom-by-atom engineering and magnetometry of tailored nanomagnets," *Nat. Phys.*, vol. 8, p. 497, 2012.

[266] A. Khajetoorians, M. Steinbrecher, M. Ternes, M. Bouhassoune, M. dos Santos Dias, S. Lounis, J. Wiebe, and R. Wiesendanger, "Tailoring the chiral magnetic interaction between two individual atoms," *Nat. Commun.*, vol. 7, p. 10620, 2016.

[267] J. Bouaziz, M. dos Santos Dias, A. Ziane, M. Benakki, S. Blügel, and S. Lounis, "Chiral magnetism of magnetic adatoms generated by Rashba electrons," *New J. Phys.*, vol. 19, p. 023010, 2017.

[268] J. Hermenau, S. Brinker, M. Marciani, M. Steinbrecher, M. dos Santos Dias, R. Wiesendanger, S. Lounis, and J. Wiebe, "Stabilizing spin systems via symmetrically tailored RKKY interactions," *Nat. Commun.*, vol. 11, p. 2833, 2020.

[269] U. K. Roessler, A. Bogdanov, and C. Pfleiderer, "Spontaneous skyrmion ground states in magnetic metals," *Nature*, vol. 442, p. 797, 2006.

[270] G. Finocchio, F. Büttner, R. Tomasello, M. Carpentieri, and M. Kläui, "Magnetic skyrmions: From fundamental to applications," *J. Phys. D: Appl. Phys.*, vol. 49, p. 423001, 2016.

[271] K. Everschor-Sitte, J. Masell, R. M. Reeve, and M. Kläui, "Perspective: Magnetic skyrmions—overview of recent progress in an active research field," *J. Appl. Phys.*, vol. 124, 2018.

[272] Y. Zhou, "Magnetic skyrmions: Intriguing physics and new spintronic device concepts," *Natl. Sci. Rev.*, vol. 6, p. 210, 2019.

[273] A. B. Odobesko, S. Haldar, S. Wilfert, J. Hagen, J. Jung, N. Schmidt, P. Sessi, M. Vogt, S. Heinze, and M. Bode, "Preparation and electronic properties of clean superconducting Nb (110) surfaces," *Phys. Rev. B*, vol. 99, p. 115437, 2019.

[274] L. Schneider, P. Beck, T. Posske, D. Crawford, E. Mascot, S. Rachel, R. Wiesendanger, and J. Wiebe, "Topological Shiba bands in artificial spin chains on superconductors," *Nat. Phys.*, vol. 17, p. 943, 2021.

[275] L. Schneider, P. Beck, J. Neuhaus-Steinmetz, L. Rózsa, T. Posske, J. Wiebe, and R. Wiesendanger, "Precursors of Majorana modes and their length-dependent energy oscillations probed at both ends of atomic Shiba chains," *Nat. Nanotechnol.*, vol. 17, p. 384, 2022.

[276] F. Küster, S. Brinker, R. Hess, D. Loss, S. S. P. Parkin, J. Klinovaja, S. Lounis, and P. Sessi, "Non-Majorana modes in diluted spin chains proximitized to a superconductor," *Proc. Natl Acad. Sci. USA*, vol. 119, p. e2210589119, 2022.

[277] A. Odobesko, D. Di Sante, A. Kowalski, S. Wilfert, F. Friedrich, R. Thomale, G. Sangiovanni, and M. Bode, "Observation of tunable single-atom Yu-Shiba-Rusinov states," *Phys. Rev. B*, vol. 102, p. 174504, 2020.

[278] F. Küster, A. M. Montero, F. S. Guimarães, S. Brinker, S. Lounis, S. S. Parkin, and P. Sessi, "Correlating Josephson supercurrents and Shiba states in quantum spins unconventionally coupled to superconductors," *Nat.commun.*, vol. 12, p. 1108, 2021.

[279] F. Küster, S. Brinker, S. Lounis, S. S. Parkin, and P. Sessi, "Long range and highly tunable interaction between local spins coupled to a superconducting condensate," *Nat.commun.*, vol. 12, p. 6722, 2021.

[280] P. Beck, L. Schneider, L. Rózsa, K. Palotás, A. Lászlóffy, L. Szunyogh, J. Wiebe, and R. Wiesendanger, "Spin-orbit coupling induced splitting of Yu-Shiba-Rusinov states in antiferromagnetic dimers," *Nat. commun.*, vol. 12, p. 2040, 2021.

[281] S. Brinker, F. Küster, S. S. P. Parkin, P. Sessi, and S. Lounis, "Anomalous excitations of atomically crafted quantum magnets," *Sci. Adv.*, vol. 8, p. abi7291, 2022.

[282] M. O. Soldini, F. Küster, G. Wagner, S. Das, A. Aldarawsheh, R. Thomale, S. Lounis, S. S. Parkin, P. Sessi, and T. Neupert, "Two-dimensional shiba lattices as a possible platform for crystalline topological superconductivity," *Nat. Phys.*, vol. 19, p. 1848, 2023.

[283] S. Rex, I. V. Gornyi, and A. D. Mirlin, "Majorana bound states in magnetic skyrmions imposed onto a superconductor," *Phys. Rev. B*, vol. 100, p. 064504, 2019.

[284] S. A. Díaz, J. Klinovaja, D. Loss, and S. Hoffman, "Majorana bound states induced by antiferromagnetic skyrmion textures," *Phys. Rev. B*, vol. 104, p. 214501, 2021.

[285] C. Hanneken, F. Otte, A. Kubetzka, B. Dupé, N. Romming, K. Von Bergmann, R. Wiesendanger, and S. Heinze, "Electrical detection of magnetic skyrmions by tunnelling non-collinear magnetoresistance," *Nat. Nanotechnol.*, vol. 10, p. 1039, 2015.

[286] J. Bouaziz, H. Ishida, S. Lounis, and S. Blügel, "Transverse transport in two-dimensional relativistic systems with nontrivial spin textures," *Phys. Rev. Lett.*, vol. 126, p. 147203, 2021.

[287] K. Nakazawa, K. Hoshi, J. J. Nakane, J.-i. Ohe, and H. Kohno, "Topological spin Hall effect in antiferromagnets driven by vector Néel chirality," *arXiv preprint arXiv:2304.02850*, 2023.

[288] F. J. Dos Santos, M. dos Santos Dias, F. S. M. Guimaraes, J. Bouaziz, and S. Lounis, "Spin-resolved inelastic electron scattering by spin waves in noncollinear magnets," *Phys. Rev. B*, vol. 97, p. 024431, 2018.

[289] F. J. Dos Santos, M. dos Santos Dias, and S. Lounis, "Modeling spin waves in noncollinear antiferromagnets: Spin-flop states, spin spirals, skyrmions, and anti-skyrmions," *Phys. Rev. B*, vol. 102, p. 104436, 2020.

[290] D. Wortmann, S. Heinze, P. Kurz, G. Bihlmayer, and S. Blügel, "Resolving complex atomic-scale spin structures by spin-polarized scanning tunneling microscopy," *Phys. Rev. Lett.*, vol. 86, p. 4132, 2001.

[291] M. Schmitt, P. Moras, G. Bihlmayer, R. Cotsakis, M. Vogt, J. Kemmer, A. Belabbes, P. M. Sheverdyaeva, A. K. Kundu, C. Carbone, *et al.*, "Indirect chiral magnetic exchange through Dzyaloshinskii–Moriya-enhanced RKKY interactions in manganese oxide chains on Ir (100)," *Nat. Commun.*, vol. 10, p. 2610, 2019.

Band / Volume 273
Analysis of the signal transduction cascade tuning the 2-oxoglutarate dehydrogenase activity in *Corynebacterium glutamicum*
L. Sundermeyer (2023), VI, 119 pp
ISBN: 978-3-95806-722-6

Band / Volume 274
Multicellular defense against phage infection in *Streptomyces* – impact of secondary metabolites and mycelial development
L. Kever (2023), iv, 246 pp
ISBN: 978-3-95806-724-0

Band / Volume 275
Investigation of the electronic band structure of 2D transition metal dichalcogenides via angle-resolved photoemission spectroscopy
B. Parashar (2023), xvii, 156 pp
ISBN: 978-3-95806-725-7

Band / Volume 276
Strain- and process engineering for polyketides production with *Pseudomonas taiwanensis* VLB120 in two-phase cultivations
T. P. Schwanemann (2023), 230 pp
ISBN: 978-3-95806-726-4

Band / Volume 277
Quantitative atomic-level investigation of solid materials through multidimensional electron diffraction measurements
H. L. Lalandec-Robert (2024), xxi, 152 pp
ISBN: 978-3-95806-735-6

Band / Volume 278
Studies on the cAMP-responsive regulatory network of *Corynebacterium glutamicum*
N. Wolf (2024), iii, 122 pp
ISBN: 978-3-95806-736-3

Band / Volume 279
Rare-earth atoms on two-dimensional materials: ab initio investigation of magnetic properties
J. P. Carbone (2024), 235 pp
ISBN: 978-3-95806-740-0

Band / Volume 280
**Communities of Niche-optimized Strains (CoNoS) –
a novel concept for improving biotechnological production**
R. Zuchowski (2024), VIII, 168 pp
ISBN: 978-3-95806-743-1

Schriften des Forschungszentrums Jülich
Reihe Schlüsseltechnologien / Key Technologies

Band / Volume 281
Enabling mixed microbial upcycling of plastic monomers
Y. S. Ackermann (2024), XVI, 203 pp
ISBN: 978-3-95806-749-3

Band / Volume 282
Folding and structural studies of *saccharomyces cerevisiae* Phosphoglycerate Kinase
N. Bustorff (2024), xxvi, 126 pp
ISBN: 978-3-95806-754-7

Band / Volume 283
The role of cellular development in multicellular antiphage defense of *Streptomyces*
T. Luthe (2024), vi, 173 pp
ISBN: 978-3-95806-768-4

Band / Volume 284
Probing the Transformation from Transition Metal Complexes to Extended Two-Dimensional Nanostructures
D. Baranowski (2024), XII, 103 pp
ISBN: 978-3-95806-772-1

Band / Volume 285
Neutron Scattering
Lectures of the JCNS Laboratory Course held at Forschungszentrum Jülich and at the Heinz-Maier-Leibnitz Zentrum Garching
edited by S. Förster, K. Friese, M. Kruteva, S. Nandi, M. Zobel, R. Zorn (2024), ca. 365 pp
ISBN: 978-3-95806-774-5

Band / Volume 286
***Ab initio* investigation of intrinsic antiferromagnetic solitons**
Amal Jawdat Nayef Aldarawsheh (2024), xv, 164 pp
ISBN: 978-3-95806-785-1

Weitere ***Schriften des Verlags im Forschungszentrum Jülich*** unter
http://wwwzb1.fz-juelich.de/verlagextern1/index.asp

Schlüsseltechnologien / Key Technologies
Band / Volume 286
ISBN 978-3-95806-785-1

Mitglied der Helmholtz-Gemeinschaft

JÜLICH
Forschungszentrum